



## D3.3

# Intermediate integrated report about the new circular building prototypes

*Lead beneficiary:* SOPR

Due date: 30.10.2021 (M18)

Type of deliverable: R

<i>Dissemination level</i>		
PU	Public	X
PP	Restricted to other programme participants	
RE	Restricted to a group specified by the consortium	
CO	Confidential, only for members of the consortium	

The project has received funding from the European Union's Horizon 2020 research and innovation program under grant agreement No 869336.

The content of this report does not reflect the official opinion of the European Union. Responsibility for the information and views expressed in the therein lies entirely with the author(s)

### History of changes

Version	Date	Organisation	Modifications
1	19/10/2021	SOPREMA	Creation
2	26/10/2021	VITO	Comments on the part Eco-hybrid cement
3	28/10/2021	SOPREMA	Add VITO part
4	08/11/2021	SOPREMA	Final update

### Main author(s) (in alphabetical order)

Name	Surname	Organisation
Berrak	Avcioğlu	CIMS
Vincent	Barraud	SOPR
Jérémie	Boucher	SOPR
İpek	Bulut	CIMS
José Francisco	Fernández Lozano	CSIC
Özge	Gökçe Gümüşbas	CIMS
Vicente Luis	Guaita Delgado	KERA
Sibel	Hacioglu	TEPE
Hadi	Kazemi Kamyab	VITO
Poppy	Krassa	MEGA
Tatiana	Lovato	GYPS
Sonia	Marín Cortés	CSIC
Peter	Nielsen	VITO
Peter	Nielsen	VITO
Mohamed	Osmani	LU
Oğuzhan	Öztürk	HU
Bill	Parker	GYPS
Kanda	Philippe	KEEY
William	René	SOPR
Francisco	Ruiz	KEEY

Alexandru	Sarbu	SOPR
Ioannis	Stamatopoulos	MEGA
Peter	Vanmierlo	ORBI

ICEBERG website: [www.iceberg-project.eu](http://www.iceberg-project.eu)

#### Legal Disclaimer

The information in this document is provided “as is”, and no guarantee or warranty is given that the information is fit for any particular purpose. The above referenced consortium members shall have no liability for damages of any kind including without limitation direct, special, indirect, or consequential damages that may result from the use of these materials subject to any liability which is mandatory due to applicable law. © 2020 by ICEBERG Consortium.

## Executive Summary

This deliverable overviews a set of activities carried out in 18 months of the ICEBERG project dealing with the development of new pre-industrial prototypes from the waste of demolition building or industrial sources. The aim in the WP3 was to develop, optimize and test at the pre-industrial stage prototypes with raw material from the WP2.

These prototypes are:

- 1) Cement- and Concrete-based products (Eco-Hybrid Cement, Structural concrete elements, Ultra-lightweight non-structural wall, green wood chip concrete panels and demountable pre-cast carbonated blocks),
- 2) Ceramic based product (circular ceramic-based tiles),
- 3) Wooden product (circular wood fiber insulation panels),
- 4) Gypsum-based product (circular plasterboards)
- 5) PU-based product (PU aerogels and circular PU insulation panels)

This report describes the results of research and workshops held within the framework of WP3. The collected information will be used to define GO or NO GO strategies that will be carried out in the tasks of WP4.



## Table of contents

Executive Summary .....	4
List of figures .....	8
List of tables .....	15
1 Introduction .....	18
2 Eco-Hybrid Cement .....	18
2.1 Preliminary Studies for developing and optimizing eco-hybrid cement and assessing technical performance according to EN 196 standards .....	18
2.1.1 Introduction .....	18
2.1.2 Materials and Methodology .....	20
2.1.3 Results and Discussions.....	31
2.1.4 References.....	33
3 Structural precast recycled concrete elements .....	34
3.1 Optimized concrete recipes considering regulations, requirements and needs .....	34
3.1.1 Introduction .....	34
3.1.2 Materials and Methodology .....	36
3.1.3 Results and Discussion .....	45
3.1.4 Conclusion and Future Studies .....	58
3.1.5 References.....	60
3.2 Concrete building elements and their connections .....	63
Abstract .....	63
3.2.1 Introduction .....	63
3.2.2 Current Practice In Structural Engineering .....	65
3.2.3 Demountable Dry Connections .....	68
3.2.4 Further Proposed Developments of Demountable Dry Connections.....	75
3.2.5 Summary and partial conclusions .....	85
3.3 Experimental Studies on Demountable Concrete Structures.....	87
3.3.1 Experimental Tests on Demountable Reinforced Concrete.....	87
3.3.2 Experimental Tests On Demountable Reinforced Concrete Slabs .....	94
3.3.3 References.....	100
3.4 Development of numerical models of concrete elements .....	102
3.4.1 Introduction .....	102
3.4.2 Beam tests .....	104
3.4.3 Details of numerical models .....	131
3.4.4 References.....	142
4 Ultra-lightweight non-structural wall elements and green wood chip concrete panels.....	142

4.1	Introduction to lightweight concretes .....	142
4.1.2	Materials and Methodology.....	148
4.1.3	Results and Discussion .....	152
4.1.4	Conclusion .....	162
4.1.5	References.....	163
4.2	Circular woodchip concrete panels to produce interior wall elements and roof slab	166
4.2.1	Introduction.....	166
4.2.2	Materials and methodology .....	166
4.2.3	Results and discussion.....	173
4.2.4	Conclusion .....	181
4.2.5	References.....	182
5	Demountable precast hollow-core blocks produced by accelerated carbonation.....	183
5.1	Fine fraction upcycling.....	183
5.2	References .....	185
6	Adjustment of formulations and pre-industrial prototypes of circular ceramic wall tiles.....	187
6.1	Description of the problem. ....	187
6.2	State of the art/technology. ....	187
6.3	Extended methodology.....	188
6.4	Materials .....	189
6.5	Activities in progress.....	193
6.6	Planning for the rest of the activities .....	205
6.7	Preliminary conclusions.....	206
6.8	References .....	207
7	Adjustment of formulations and pre-industrial prototypes of circular wooden based panels .....	207
7.1	Phenolic resin formulation and up-scale production using the bio-oil .....	207
7.2	Thermal insulation panels containing >50 wt% of high-quality recovered wood fibers and 2.5 wt% of biophenolic resin .....	210
7.2.1	C&D waste wood for defibrating operation in insulation fiber board process	210
7.2.2	First specimens from C&D raw materials.....	211
7.2.3	New development of C&D wood waste shredding for getting pin chips	212
8	Formulations and pre-industrial prototype of circular plasterboards .....	213
8.1	Assessment of the industrial impact of increasing the recycled gypsum content to 35 wt% from a productivity standpoint .....	213
8.2	Evaluation of productivity and rejection percentage with 10 wt% recycled content gypsum plasterboards.....	214
8.3	Assessment for circular plasterboard including circular silica aerogels to enhance thermal properties of the product. ....	214

8.4	Assessment and optimization of the binding system used to attach the plasterboard to the wall to facilitate assembly and disassembly .....	215
8.5	Characterization of the ICEBERG plasterboards .....	215
9	Adjustment of formulations and pre-industrial prototypes of circular PU based products.....	217
9.1	Circular PU-based granular aerogels .....	217
9.1.1	Pre-screen recycled polyols by analysing their molecular weight, functional group, purity and solubility.....	217
9.1.2	Integration of selected recycled polyols (>10 wt%) in the current formulation of PU aerogel.....	218
9.1.3	Optimization of the reaction conditions of recycled polyol-based PU aerogels	220
9.1.4	Adjustment of the percentage of recycled polyols in the formulation for PU aerogel .....	221
9.1.5	Characterization of the recycled polyol-based PU aerogels.....	222
9.1.6	Validation and large batch manufacturing.....	222
9.2	Circular PU-based panels .....	222
9.2.1	Establish a polyol book of specifications containing the desired physical and chemical characteristics.....	222
9.2.2	Screen different polyol iterations to identify the most suitable candidates via lab foam trials.....	223
9.2.3	Results and Discussions.....	235

## List of figures

Figure 2-1 Photographs and SEM Images of CDW-based materials:, (a) Hollow Brick, (b) Concrete Waste, (c) Glass Waste .....	20
Figure 2-2 XRD analysis of Mix1, Mix2 Blended cements .....	23
Figure 2-3 XRD analysis of Mix 3 and Mix 8 Blended cements .....	24
Figure 2-4 XRD analysis of lab scale produced CSA cement .....	25
Figure 2-5 XRD analysis of CSA clinker powder .....	25
Figure 2-6 4x4x16 cm Cement Mortar Mold.....	27
Figure 2-7 Cement Mortar Compressive Strength Test.....	27
Figure 2-8 Vicat Tool .....	28
Figure 2-9 Cement Mortar Setting time test.....	29
Figure 2-10 Cement Flow table test .....	30
Figure 2-11 Soundness of cement Le chatlier's Test Apparatus .....	31
Figure 3-1 The images of RCA's collected from different demolition regions. ...	37
Figure 3-2 Sieves used for aggregate gradation. ....	37
Figure 3-3 Recycled Coarse and Fine Aggregates.....	38
Figure 3-4 Sulphate soundness test equipment photo .....	41
Figure 3-5 Gradation curve graphs of the aggregates.....	42
Figure 3-6 The visuals of the cubic and cylinder specimens.....	44
Figure 3-7 7-days compressive strength results of Portland cement-based mixtures.....	47
Figure 3-8 14-days compressive strength results of Portland cement-based mixtures.....	48
Figure 3-9 28-days compressive strength results of Portland cement-based mixtures.....	49
Figure 3-10 7-days splitting-tensile strength results of Portland cement-based mixtures.....	50
Figure 3-11 14-days splitting-tensile strength results of Portland cement-based mixtures.....	51
Figure 3-12 28-days splitting-tensile strength results of Portland cement-based mixtures.....	52
Figure 3-13 7-days compressive strength results of Eco-hybrid cement-based mixtures.....	54
Figure 3-14 14-days compressive strength results of Eco-hybrid cement-based mixtures.....	55

Figure 3-15 28-days compressive strength results of Eco-hybrid cement-based mixtures.....	56
Figure 3-16 7-days splitting-tensile strength results of Eco-hybrid cement-based mixtures.....	57
Figure 3-17 14-days splitting-tensile strength results of Eco-hybrid cement-based mixtures.....	57
Figure 3-18 28-days splitting-tensile strength results of Eco-hybrid cement-based mixtures.....	58
Figure 3-19 Dowel connection between a column and the foundation of a reinforced precast concrete structure: (a) before the grout injection; and (b) after the grout injection. Reprinted from Metelli et al. [26].	66
Figure 3-20 Moment-resisting semi-dry connection, with welded continuity reinforcement, between a beam and a column of a precast reinforced concrete structure. Reprinted from Xiao et al. [27].	67
Figure 3-21 Three types of concrete beam/column dry connections with pretensioned threaded bolts and a steel end plate: (a) outlook; and (b) detailed view. Reprinted from Aninthaneni et al. [29].	67
Figure 3-22 Concrete beam/column dry connection with embedded steel plates and threaded bolts: (a) view of the disassembled form; and (b) view of the assembled form. Reprinted from Pul and Şentürk et al. [30].	70
Figure 3-23 Concrete wall/wall dry connection with a horizontal steel connector and high-strength bolts. Reprinted from Sun et al. [31].	71
Figure 3-24 Schematic representation of a beam/column concrete dry connection – solution 1.....	77
Figure 3-25 Schematic representation of a beam/column concrete dry connection – solution 2.....	79
Figure 3-26 Schematic representation of a column/column concrete dry connection.....	80
Figure 3-27 Schematic representation of a slab/slab concrete dry connection – solution 1.....	83
Figure 3-28 Schematic representation of a slab/slab concrete dry connection – solution 2.....	84
Figure 3-29 Schematic representation of beam/slab concrete dry connection.....	85
Figure 3-30 Demountable Column 1 .....	88
Figure 3-31 Dimensions of connection point of demountable column 1 .....	89
Figure 3-32 Demountable Column 2 .....	90
Figure 3-33 Dimensions of connection point of demountable column 2 .....	91
Figure 3-34 Grid modelling .....	91
Figure 3-35 Details of Grid .....	92
Figure 3-36 Dimensions of connection point of demountable column 3 .....	92

Figure 3-37 Modelling of demountable column-4 (a) During placing, (b) After Placing ..... 93

Figure 3-38 Details of connection point of demountable column 4 ..... 93

Figure 3-39 Reference slab (monolithic slab with no connection) ..... 95

Figure 3-40 Connection with no key and no embedded steel block ..... 96

Figure 3-41 Connection with no key and with an embedded steel block ..... 97

Figure 3-42 Connection with a key and no embedded steel block ..... 98

Figure 3-43 Connection with a key and with an embedded steel block ..... 99

Figure 3-44 Reinforcement Details of the Test Specimens ..... 106

Figure 3-45 Test Setup and Instrumentation ..... 107

Figure 3-46 Test Results of Beam Specimens with  $a/d=0.50$ : (a) Total vertical load-midspan displacement, (b) the moment-curvature curve from left LVDTs, (b) the moment-curvature curve from mid-LVDTs, and (d) the moment-curvature curve from right LVDTs ..... 108

Figure 3-47 Observed Crack Patterns of Beam Specimens with  $a/d=0.50$ ..... 109

Figure 3-48 Test Results of Beam Specimens with  $a/d=1.00$ : (a) Total vertical load-midspan displacement, (b) the moment-curvature curve from left LVDTs, (b) the moment-curvature curve from mid-LVDTs, and (d) the moment-curvature curve from right LVDTs ..... 111

Figure 3-49 Observed Crack Patterns of Beam Specimens with  $a/d=1.00$ ..... 112

Figure 3-50 Test Results of Beam Specimens with  $a/d=1.65$ : (a) Total vertical load-midspan displacement, (b) the moment-curvature curve from left LVDTs, (b) the moment-curvature curve from mid-LVDTs, and (d) the moment-curvature curve from right LVDTs ..... 113

Figure 3-51 Observed Crack Patterns of Beam Specimens with  $a/d=1.65$ ..... 114

Figure 3-52 Test Results of Beam Specimens with  $a/d=0.50$ : (a) the moment-curvature curve from left LVDTs, (b) the moment-curvature curve from mid-LVDTs, (c) the moment-curvature curve from right LVDTs, and (d) Total vertical load-midspan vertical displacement ..... 118

Figure 3-53 Observed Crack Patterns of Test Specimens with  $a/d=0.50$  ..... 120

Figure 3-54 Test Results of Beam Specimens with  $a/d=1.00$ : (a) the moment-curvature curve from left LVDTs, (b) the moment-curvature curve from mid-LVDTs, (c) the moment-curvature curve from right LVDTs, and (d) Total vertical load-midspan vertical displacement ..... 123

Figure 3-55 Observed Crack Patterns of Test Specimens with  $a/d=1.00$  ..... 124

Figure 3-56 Test Results of Beam Specimens with  $a/d=1.65$ : (a) the moment-curvature curve from left LVDTs, (b) the moment-curvature curve from mid-LVDTs, (c) the moment-curvature curve from right LVDTs, and (d) Total vertical load-midspan vertical displacement ..... 126

Figure 3-57 Observed Crack Patterns of Beam Specimens with  $a/d=1.65$ ..... 127

Figure 3-58 Close look-up to the final state of shear cracks of test specimens with an a/d ratio of 0.49 ..... 129

Figure 3-59 Close look-up to the final state of shear cracks of test specimens with an a/d ratio of 1.65 ..... 130

Figure 3-60 Numerical model: (a) 3D solid model and (b) Steel reinforcements ..... 132

Figure 3-61 Numeric Model for a/d ratio = 0.50 ..... 133

Figure 3-62 Load Displacement Curves (a/d = 0.50) ..... 133

Figure 3-63 Estimated Crack Pattern (a/d = 0.50) ..... 134

Figure 3-64 Numeric Model for a/d ratio = 1.00 ..... 134

Figure 3-65 Load Displacement Curves (a/d = 1.00) ..... 135

Figure 3-66 Estimated Crack Pattern (a/d = 1.00) ..... 135

Figure 3-67 Numeric Model for a/d ratio = 1.65 ..... 136

Figure 3-68 Load Displacement Curves (a/d = 1.65) ..... 136

Figure 3-69 Estimated Crack Pattern (a/d = 1.65) ..... 137

Figure 3-70 Load Displacement Curves (a/d = 0.50) ..... 137

Figure 3-71 Estimated Crack Pattern (a/d = 0.50) ..... 138

Figure 3-72 Load Displacement Curves (a/d = 1.00) ..... 138

Figure 3-73 Estimated Crack Pattern (a/d = 1.00) ..... 139

Figure 3-74 Load Displacement Curves (a/d = 1.65) ..... 139

Figure 3-75 Estimated Crack Pattern (a/d = 1.65) ..... 140

Figure 4-1 Images of the coarse and fine perlite aggregate (a) coarse fraction, (b) fine fraction ..... 149

Figure 4-2 Images of the coarse and fine pumice aggregate (a) coarse fraction, (b) fine fraction ..... 149

Figure 4-3 Image of the used molds for production of samples ..... 151

Figure 4-4 Images of the 1<sup>st</sup> group samples produced within the scope of preliminary studies ..... 153

Figure 4-5 Density values of the 1<sup>st</sup> group samples produced within the scope of preliminary studies ..... 154

Figure 4-6 Images of the 2<sup>nd</sup> group samples produced with the foam generated by 2.5% foaming agent ..... 155

Figure 4-7 Density values of the 2<sup>nd</sup> group samples produced with the foam generated by 2.5% foaming agent ..... 156

Figure 4-8 Images of the 2<sup>nd</sup> group samples produced with the foam generated by 0.5% foaming agent ..... 157

Figure 4-9 Density values of the 2<sup>nd</sup> group samples produced with the foam generated by 0.5% foaming agent ..... 158



Figure 4-10 Images of the 3 <sup>rd</sup> group samples produced within the scope of preliminary studies .....	160
Figure 4-11 Density values of the 3 <sup>rd</sup> group samples .....	162
Figure 4-12 Result of sieve analysis of recycle aggregates. ....	167
Figure 4-13 Wood-chip fibers .....	168
Figure 4-14 a) concrete mixer (pan type) b) Mixing of wood-chip c) Adding aluminium sulphate ( $Al_2(SO_4)$ ) solution d) adding sodium silicate ( $Na_2SiO_3$ ) e) Adding recycle aggregate f) Adding eco-hybrid cement .....	171
Figure 4-15 g) Press machine and pre-mold h) specimen before pressing i) specimen after pressing j) water curing at 85 °C k) cure pool l) specimen .....	172
Figure 4-16 m) Three-point flexural test machine n) Compression test machine .....	173
Figure 4-17 Results of three-point flexural tests .....	174
Figure 4-18 Flexural load-deformation curve of different recycle aggregate content. ....	175
Figure 4-19 Flexural load-deformation curve of different eco-hybrid cement content. ....	175
Figure 4-20 Flexural load-deformation curve of different chemical admixture content. ....	176
Figure 4-21 Results of toughness for flexural stress-deformation curve.....	177
Figure 4-22 Flexural stress-deformation curve of different recycle aggregate content. ....	178
Figure 4-23 Flexural stress-deformation curve of different eco-hybrid cement content. ....	178
Figure 4-24 Flexural stress-deformation curve of different chemical admixture content. ....	179
Figure 4-25 Results of compression tests .....	180
Figure 4-26 Results of density values .....	181
<i>Figure 5-1. Carbonated cylinders made by hydraulic compaction of the RCF (left), RCA (right).</i> .....	184
Figure 5-2 - Compressive strength (MPa) as function of density( $g/cm^3$ ) before carbonation, dry bulk density ( $g/cm^3$ ) before carbonation, and porosity (%) for RCA and RCF prisms made with the Vibro-press. ....	185
Figure 6-1. Pictures of the chosen construction materials: Ceramics, gypsums and cements groups.....	190
Figure 6-2. Single-house material proportion and only ceramic material proportion. ....	192
Figure 6-3. Sintered samples: mixtures containing common brick as ceramic fraction. ....	194



Figure 6-4. Sintered samples: mixtures containing porcelain tile as ceramic fraction. .... 195

Figure 6-5. Final density, linear shrinkage and mass loss for brick-based samples containing 20, 10 and 5% of mortar, cement, drywall or plaster. .... 196

Figure 6-6. Final density, linear shrinkage and mass loss for porcelain tile-based samples containing 20, 10 and 5% of mortar, cement, drywall or plaster. .... 197

Figure 6-7. Comparison of XRD patterns of mixtures and individual starting material. Mixtures containing common brick as major material. .... 198

Figure 6-8. Comparison of XRD patterns of mixtures and individual starting material. Mixtures containing porcelain tile as majority material. .... 199

Figure 6-9 Final density (g/cm<sup>3</sup>) of the porcelain with mortar or plasterboard mixtures with 30, 10 and 5 % content of clay 1 and 2. .... 200

Figure 6-10 Photographic Image of Porcelain/mortar mixtures with clay 1 fractions of 30, 10, 5 % and no clay fraction, 0%, treated at 1150 °C with a dwelling time of 1 h. .... 201

Figure 6-11 Density (g/cm<sup>3</sup>) of the porcelain (a) and brick (b) based materials with 5% of clay and 10% of the following impurities: mortar, plasterboard and mixture of mortar and plasterboard. Dwelling time = 1h. .... 203

Figure 6-12 Brick based materials after thermal treatment at 950 and 1050 °C with a dwelling time of 1 h. .... 203

Figure 6-13 Density variation, water absorption and flexural strength for brick-based materials (left) and porcelain based ones (right). .... 205

Figure 6-14 Photographic image of porcelain-based and brick-based materials after the sintering at 1150 and 1100 °C during 6 min respectively. .... 205

Figure 7-1. Synthetic view of the wood insulation fiberboard process. .... 210

Figure 7-2 The first six kind of shredded C&D wood waste sample send from VTT. .... 211

Figure 7-3. At left standard soft wood pin chips; at right wood fiber obtained from standard raw material. .... 211

Figure 7-4. At left Raw materials from Purkupiha, at right mixed C&D wood waste .... 212

Figure 7-5. At left sorting and pre-crushing; on center and right, sort of Pin chips obtained for defibrating. .... 212

Figure 8-1. Flow diagram of the plasterboard manufacturing process at British Gypsum (GYPS). .... 213

Figure 9-1 Polyols PUR\_V4 .... 218

Figure 9-2 Polyaddition between polyols and polyisocyanates .... 219

Figure 9-3 Obtained PU aerogels with different polyols .... 220

Figure 9-4. Polyol book of specifications .... 223

Figure 9-5. Pictures of the polyols synthesized by RAMPF. .... 225

Figure 9-6. Viscosity measurements of the first series of 6 polyols received . 226

Figure 9-7. Viscosity measurements of the second series of 6 polyols received ..... 226

Figure 9-8. a. Foamat equipment and b. example of curves obtained..... 228

Figure 9-9. Examples of expansion curves obtained from the recycling of PUR and PIR foams..... 229

Figure 9-10. Expansion curves of the first series of polyols at 10 % substitution ..... 229

Figure 9-11. Expansion curves of the first series of polyols at 25 % substitution ..... 230

Figure 9-12. Expansion curves of the first series of polyols at 50 % substitution ..... 230

Figure 9-13. Pictures of the foams resulting from the evaluation of the first series of 6 polyols ..... 231

Figure 9-14. Expansion curves of the second series of polyols at 10 % substitution ..... 232

Figure 9-15. Expansion curves of the second series of polyols at 25 % substitution ..... 232

Figure 9-16. Expansion curves of the second series of polyols at 50 % substitution ..... 233

Figure 9-17. Pictures of the foams resulting from the evaluation of second series of 6 polyols ..... 234

## List of tables

Table 2-1 Compressive strength of brick substituted Portland cement concrete .....	19
Table 2-2 XRF analysis of CDW-based materials .....	21
Table 2-3 XRF analysis of Cem I 42.5 cement .....	21
Table 2-4 Blended cement trial mixes rates .....	21
Table 2-5 XRF analysis of Blended cements.....	22
Table 2-6 Blaine and density of Blended cements and Cem I 42.5 R cement..	22
Table 2-7 XRF analysis of CSA clinker powder.....	26
Table 2-8 Blaine and density of Blended cements and CSA clinker powder ....	26
Table 2-9 Eco-hybrid cement trial mixtures .....	26
Table 2-10 Setting Time and Flow of Blended cements and CEM I 42.5 R cement .....	31
Table 2-11 Mortar Compressive Strength of Blended cements and CEM I 42.5 R cement .....	32
Table 2-12 Setting Time and Flow of CSA clinker powder, Eco-hybrid cement and CEM I 42.5 R cement .....	32
Table 2-13 Mortar Compressive Strength of CSA clinker powder, Eco-hybrid cement and CEM I 42.5 R cement .....	32
Table 2-14 Soundness of CSA clinker powder, Eco-hybrid cement and CEM I 42.5 R cement.....	32
Table 3-1 The chemical composition of Portland cement.....	36
Table 3-2 Densities of recycled aggregates .....	39
Table 3-3 Water absorption of aggregates .....	40
Table 3-4 Aggregate soundness test results .....	41
Table 3-5 Properties of the aggregates .....	42
Table 3-6 Mixture designs of the preliminary study .....	45
Table 3-7 Slump values of the mixtures .....	46
Table 3-8 Mixture designs of the eco-hybrid cement based mixes.....	52
Table 3-9 Slump values of the mixtures .....	53
Table 3-10 Summary of the achievements and aspects that need further development in precast concrete dry connections.....	73
Table 3-11 Test specimen details.....	94
Table 3-12 Summary of Test Specimens .....	105
Table 3-13 Summary of Test Results .....	110
Table 3-14 Estimation Performance of Code Proposed Equations .....	116

Table 3-15 Summary of Test Results .....	121
Table 3-16 Prediction Performance of Code Equations .....	131
Table 3-17 Crack parameter values of geopolymer concrete .....	132
Table 3-18 Summary of Numerical Estimations (Shear-critical beams) .....	140
Table 3-19 Summary of Numerical Estimations (Flexure-critical beams) .....	141
Table 4-1 Technical properties of the foaming agent .....	150
Table 4-2 LINSEIS HFM300 device specifications .....	152
Table 4-3 1 <sup>st</sup> group samples produced within the scope of preliminary studies .....	153
Table 4-4 First part of the 2 <sup>nd</sup> group samples produced within the scope of preliminary studies .....	155
Table 4-5 Second part of the 2 <sup>nd</sup> group samples produced within the scope of preliminary studies .....	157
Table 4-6 3 <sup>rd</sup> group samples produced within the scope of preliminary studies .....	160
Table 4-7 Sieve analysis table of recycle aggregates. ....	167
Table 4-8 Properties of wood-chip fibers .....	168
Table 4-9 Properties of aluminum sulphate (Al <sub>2</sub> (SO <sub>4</sub> ) <sub>3</sub> ) .....	168
Table 4-10 Properties of sodium silicate (Na <sub>2</sub> SiO <sub>3</sub> ) .....	169
Table 4-11 Experimental designs and amount of materials used in mixtures. ....	169
Table 6-1. Composition in equivalent oxides of the materials obtained by XRF. N.d.: Non detected. Lol.: Loss-of-ignition. ....	191
Table 6-2. Particle size distributions (d <sub>50</sub> and d <sub>90</sub> ) of the pattern materials after conventional milling and sieving. ....	191
Table 6-3. Composition in equivalent oxides of the two industrial clays obtained by XRF. (In bold those present in >2%). Lol.: Loss-of-ignition. ....	192
Table 6-4 Temperatures of start of densification, maximum and densification percentage of brick with plasterboard or mortar mixtures, obtained by hot-stage microscopy. ....	201
Table 6-5 Percentage of mass loss and temperature range for brick with plasterboard or mortar mixtures, obtained by TG analysis. ....	202
Table 6-6 Gant diagram with the planning for the rest of activities. ....	206
Table 7-1 Characterization results of resins. ....	209
Table 7-2 Characterization results of resins .....	<b>¡Error! Marcador no definido.</b>
Table 8-1 Composition and amount of rejected products for the new ICEBERG plasterboard (35 wt% recycled gypsum) and BAU plasterboard (15 wt% recycled gypsum) .....	214

Table 8-2 Properties of the new ICEBERG plasterboard (35 wt% recycled gypsum), with and without circular silica aerogel, and BAU plasterboard (15 wt% recycled gypsum). .....	215
Table 9-1 The specifications of each polyols .....	217
Table 9-2 The conditions of PU aerogels prepared by varying the solid content.....	221
Table 9-3 The conditions of PU aerogels prepared by adjusting the wt.% of polyols	222
Table 9-4. Properties of the recycled polyols synthesized.....	224
Table 9-5. Reaction times of the first series of 6 polyols .....	227
Table 9-6. Reaction times of the second series of 6 polyols .....	227

## 1 Introduction

During the first 18 months of the ICEBERG project, an interaction between Work package 2 and 3 was established in order to provide formulations and pre-industrial prototypes of new circular green building products. This document presents an update of these activities according to the state of progress.

## 2 Eco-Hybrid Cement

### 2.1 Preliminary Studies for developing and optimizing eco-hybrid cement and assessing technical performance according to EN 196 standards

#### 2.1.1 Introduction

For many years, a number of material substitutions have been made in Portland cement concretes in order to manipulate their fresh and hardened properties. These materials, which are generally called Supplementary cementitious materials (SCM), have been used frequently and successfully in various applications thanks to some physical and chemical properties. For example, fly ash, a by-product of coal combustion in power plants, has a positive effect on the workability of concrete mixtures due to its spherical grain structure. Blast furnace slag, which is a by-product in the steel industry, increases the mechanical performance of the mixture by contributing to the formation of extra C-S-H gel in the matrix by showing pozzolanic activity when included in Portland cement systems. In addition, it is known that blast furnace slag is frequently used in mass concrete applications such as dams by substituting certain proportions of cement by reducing the heat of hydration. The SCM substitutions of Portland cement concretes are not only limited to improving the fresh properties, mechanical properties, and durability properties of the mixes, but also various environmental purposes have been pursued in the use of these materials. In this context, the gradual increase in construction and demolition applications due to increasing urbanization has caused a large amount of waste material to be released into the environment. Currently, the European construction sector produces 820 million tons of construction and demolition waste (CDW) every year, which is around 46% of the total amount of total waste generated according to Eurostat (Eurostat, 2017). Considering the damage caused by these construction and demolition wastes to the environment, studies on recycling by researchers have accelerated in recent years. Significant work has been initiated on the recycling of brick, tile, glass and concrete wastes, which are produced as a result of construction and demolition waste, by substituting Portland cement systems at certain rates.

Research has been conducted by Abdelghani Naceri (2009) to show the impact of waste brick as a partial replacement of cement in mortar. Clinker was replaced by waste brick in different proportions (0%, 5%, 10%, 15% and 20%) by weight of the cement. The result showed that the grinding time of cement was unchanged for 5% brick replacement and decreased 5% for 10% brick replacement and

decreased 10% for 15% and 20% brick replacement. The results demonstrated that the specific gravity values tended to decrease by 0.9%, 3.1%, 4.4% and 5% compared to the reference sample at the 5%, 10%, 15% and 20% waste brick replacement rate, respectively. Also, it was observed that the increase of the quantity or percentage of the waste brick incorporated in the cement increases the amount of water needed to have a normal consistency of the cement paste. It was noticed that setting times decrease proportionally with the increase in the quantity of waste brick. According to the shrinkage performance of the waste brick replacement, it was concluded that increasing waste brick content leads to an increase in the shrinkage values. It was observed that the increase in the waste brick replacement rate in the mixtures decreased the 7 and 28 day mechanical performances of the samples. However, in 90-day mechanical performances, higher strength and resistance values were observed in mixtures where the brick replacement rate was up to 10% due to the variation of the content of SiO<sub>2</sub> and Al<sub>2</sub>O<sub>3</sub> and the ratio CaO/SiO<sub>2</sub>.

In a study conducted by Sanjay Raj et al., (2018), the fresh and hardened properties of concrete mixes in which crushed rock powder was used as aggregate and waste brick was substituted for cement at rates of 0%, 5%, 10%, 15% and 20% were investigated. The 7, 14 and 28 days compressive strength results of the reference sample and the mixtures produced with waste brick.

Table 2-1 Compressive strength of brick substituted Portland cement concrete

<b>Compressive Strengths (Mpa)</b>	<b>M40 normal concrete</b>	<b>5% waste brick</b>	<b>10% waste brick</b>	<b>15% waste brick</b>	<b>20% waste brick</b>
<b>7 days</b>	26.84	26.62	27.21	20.18	20.51
<b>14 days</b>	28.58	31.18	38.03	24.07	23.29
<b>28 days</b>	48.4	41.85	49.18	33.99	35.33

According to the results, the compressive strengths of the mixtures in which the brick waste is replaced by 5% and 10% were higher than the reference sample at all ages. However, a significant decrease in compressive strength was observed in the mixtures where the brick ratio was used as 15% and 20%. When the split tensile strengths are examined, it was found that the cylinder samples performed better than 10% waste brick substitution rate, and higher substitution rates had a negative effect on the splitting tensile strengths. The authors emphasized that this was due to the high rate of water absorption of the brick waste in the ambient cured samples.

Calcium sulfoaluminate (CSA) cement has attracted the attention of researchers in recent years as a substitute for conventional Portland cement systems. CSA cement was first developed in China in the 1970s and is produced by heating together limestone, gypsum and bauxite. Researchers found that the mechanical performance was improved and the autogenous shrinkage was considerably reduced in concretes using CSA cement. In this context, Yoo et al., (2019) showed that CSA cement provides a significant reduction in the expansive strain values of ultra-high performance concretes. In another study, Song et al., (2021) found that the autogenous shrinkage in ultra-high performance concretes



developed with 15% CSA cement was 123% lower than the reference sample. In a study by Shen et al., (2020), it was concluded that the addition of 5% CSA-CaO significantly improves the compressive and flexural strengths at early ages.

### 2.1.2 Materials and Methodology

Eco-Hybrid Cement is produced through the combination of CSA cement and Blended Cement with minimum 30 wt% of diverse Recycled Building Materials (RBM; brick, concrete, glass and gypsum). It has a 35% lower CO<sub>2</sub> footprint and it is 25% more cost effective when compared to the current patented solutions.

For the blended cement, CDW based materials were collected by BESE from an urban transformation area located in Ankara and earthquake zones in Turkey. Hacettepe University made chemical and physical analysis of these materials (concrete waste (CW), glass waste (GW) and masonry units which include red clay brick (RCB), hollow brick (HB) and roof tile (RT)). After analysis it was understood that amorphous and high alumina-silica content materials can be used as additives for blended cement.

Concrete waste, glass waste and brick waste were used as RBM in blended cement.

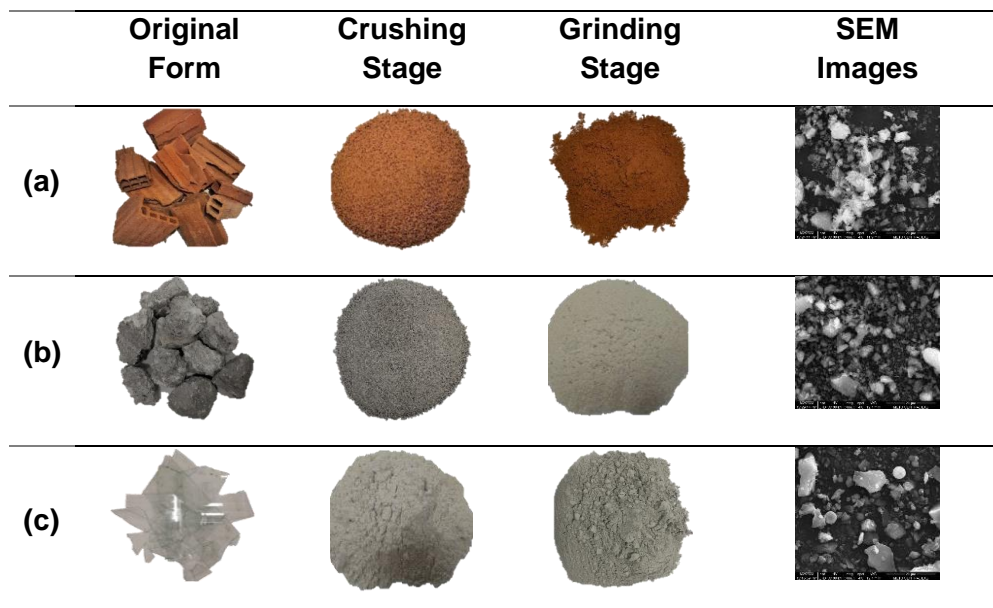


Figure 2-1 Photographs and SEM Images of CDW-based materials: (a) Hollow Brick, (b) Concrete Waste, (c) Glass Waste



Table 2-2 XRF analysis of CDW-based materials

Chemical analysis										
Composition (%)	SiO <sub>2</sub>	Al <sub>2</sub> O <sub>3</sub>	Fe <sub>2</sub> O <sub>3</sub>	CaO	MgO	K <sub>2</sub> O	Na <sub>2</sub> O	SO <sub>3</sub>	TiO <sub>2</sub>	LOI
<b>Brick waste</b>	42.85	13.86	16.49	11.09	5.74	1.25	2.08	0.91	2.77	2.3
<b>Concrete waste</b>	34.82	4.09	3.63	27.07	4.65	0.69	0.62	0.5	0.27	23.5
<b>Glass waste</b>	70.25	0.88	0.43	9.37	3.83	0.19	13.91	0.08	0.11	0.6
<b>Gypsum</b>	3.43	1.09	0.51	30.33	1.43	0.19	0.01	41.87	-	20.83

Çimsa Cem I 42.5 R portland cement was used in blended cement trials. As EN 197-1 standard, it consists of Portland cement clinker and limestone. It is suitable for general use. It is appropriate to use it in the circumstances where the early mould must be taken.

Table 2-3 XRF analysis of Cem I 42.5 cement

Chemical analysis										
Composition (%)	SiO <sub>2</sub>	Al <sub>2</sub> O <sub>3</sub>	Fe <sub>2</sub> O <sub>3</sub>	CaO	MgO	K <sub>2</sub> O	Na <sub>2</sub> O	SO <sub>3</sub>	TiO <sub>2</sub>	LOI
<b>Cem I 42.5 R cement</b>	19.37	5.12	2.79	63.51	2.58	0.87	0.28	3.05	-	2.65

Eight blended cement mortar trials were done with different combinations of these materials. In these studies, commercial gypsum was used instead of waste gypsum.

Table 2-4 Blended cement trial mixes rates

Blended Cement Mix Ratios (min %30 EBM)									
Materials (%)	Mix1	Mix2	Mix3	Mix4	Mix5	Mix6	Mix7	Mix8	
<b>Cem I 42,5 Cement</b>	70%	70%	70%	70%	70%	70%	70%	66%	
<b>Brick waste</b>	30%	-	-	-	15%	15%	10%	19.5%	
<b>Glass waste</b>	-	30%	-	15%	15%	-	10%	-	
<b>Concrete waste</b>	-	-	30%	15%	-	15%	10%	12.5%	
<b>Gypsum</b>	-	-	-	-	-	-	-	2%	

The first three mixtures (mix1, mix2, mix3) were designed to examine how the CDW-based materials work separately. The next four mixtures (mix4, mix5, mix6, mix7) were also designed in equal amounts to examine how the CDW-based materials works together. Mix 8 was designed according to stated RBM ratios in the proposal (19.5% of glass or brick, 12.5% of concrete and 2% of gypsum). XRF, Blaine measurement and density measurement analysis were carried out for all mixtures. XRD analyses were carried out for mix1, mix2, mix3 and mix8.

With XRD analysis the presence and amounts of minerals in cement samples was determined as well as identify phases. With XRF analysis, the chemical composition of cement samples was determined. The fineness of cement was

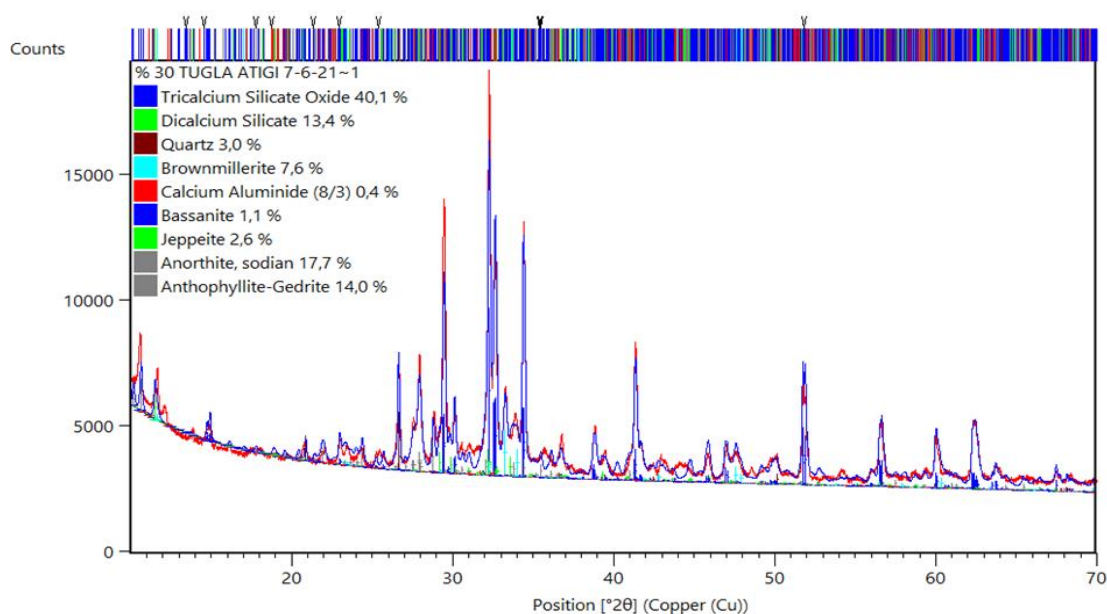
measured as specific surface. Specific surface is expressed as the total surface area in square meters of all the cement particles in one kilogram of cement. The higher the specific surface is, the finer cement will be. The fineness of cement was measured with Blaine's air permeability method. Specific gravity (density) is the mass of the void-free volume of a material. To determine the specific gravity of cements, a Le Chatelier balloon and a precision balance are required. The specific gravity ( $\rho$ ) value is the mass divided by the volume calculated with the help of a pycnometer.

Table 2-5 XRF analysis of Blended cements

Chemical analysis										
Composition (%)	SiO <sub>2</sub>	Al <sub>2</sub> O <sub>3</sub>	Fe <sub>2</sub> O <sub>3</sub>	CaO	MgO	K <sub>2</sub> O	Na <sub>2</sub> O	SO <sub>3</sub>	TiO <sub>2</sub>	LOI
<b>Mix1</b>	27.18	7.61	6.02	46.46	3.46	0.98	0.86	2.58	0.83	2.73
<b>Mix2</b>	34.5	3.72	2.42	46.79	2.9	0.68	4.2	2.03	0.24	2.2
<b>Mix3</b>	24.38	4.64	3.08	51.83	3.13	0.84	0.45	2.13	0.27	9
<b>Mix4</b>	29.55	4.24	2.79	49.78	3.04	0.77	2.32	2.1	0.26	5.65
<b>Mix5</b>	31.11	5.72	4.16	47.55	3.17	0.89	2.46	2.14	0.51	2.74
<b>Mix6</b>	26.09	6.19	5.01	49.43	3.28	0.97	0.63	2.22	0.53	6.11
<b>Mix7</b>	29.19	5.36	3.8	49.17	3.19	0.88	1.83	2.15	0.43	4.68
<b>Mix8</b>	26.49	6.46	4.94	48.49	3.39	0.93	0.71	2.12	0.62	5.75

Table 2-6 Blaine and density of Blended cements and Cem I 42.5 R cement

Mixes	Mix1	Mix2	Mix3	Mix4	Mix5	Mix6	Mix7	Mix8	Control (Cem I 42.5)
<b>Blaine (cm<sup>2</sup>/g)</b>	3325	2480	3410	3070	3230	3200	3010	3290	3400
<b>Density (g/cm<sup>3</sup>)</b>	2.62	2.56	2.69	2.71	2.79	2.56	2.62	2.56	3.15



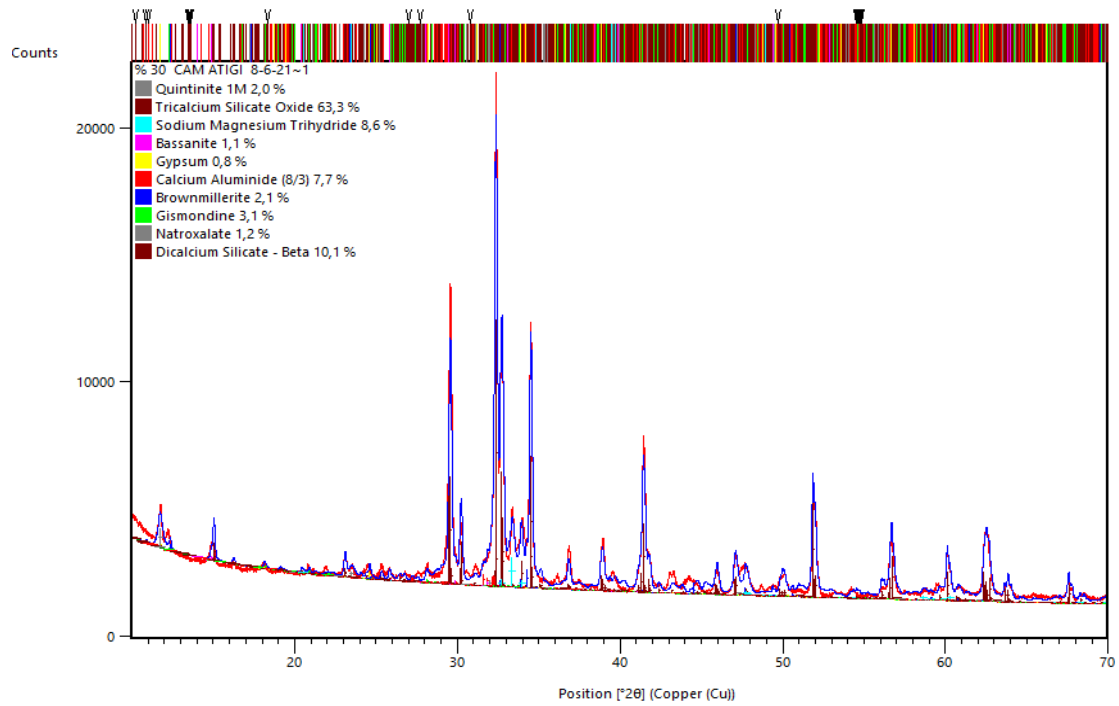
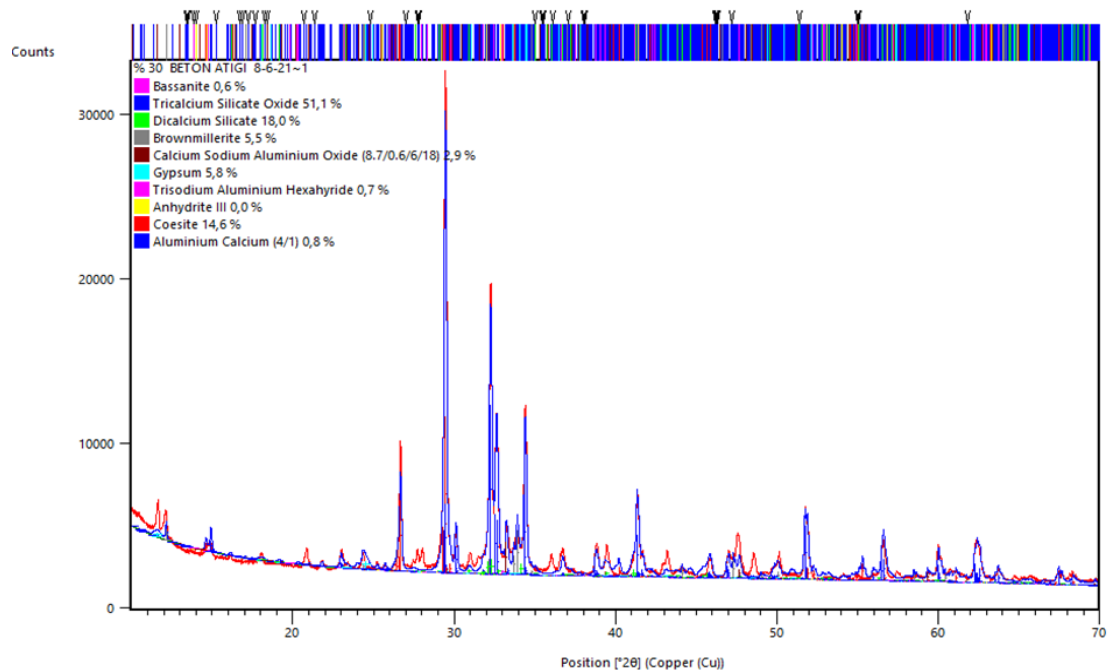


Figure 2-2 XRD analysis of Mix1, Mix2 Blended cements



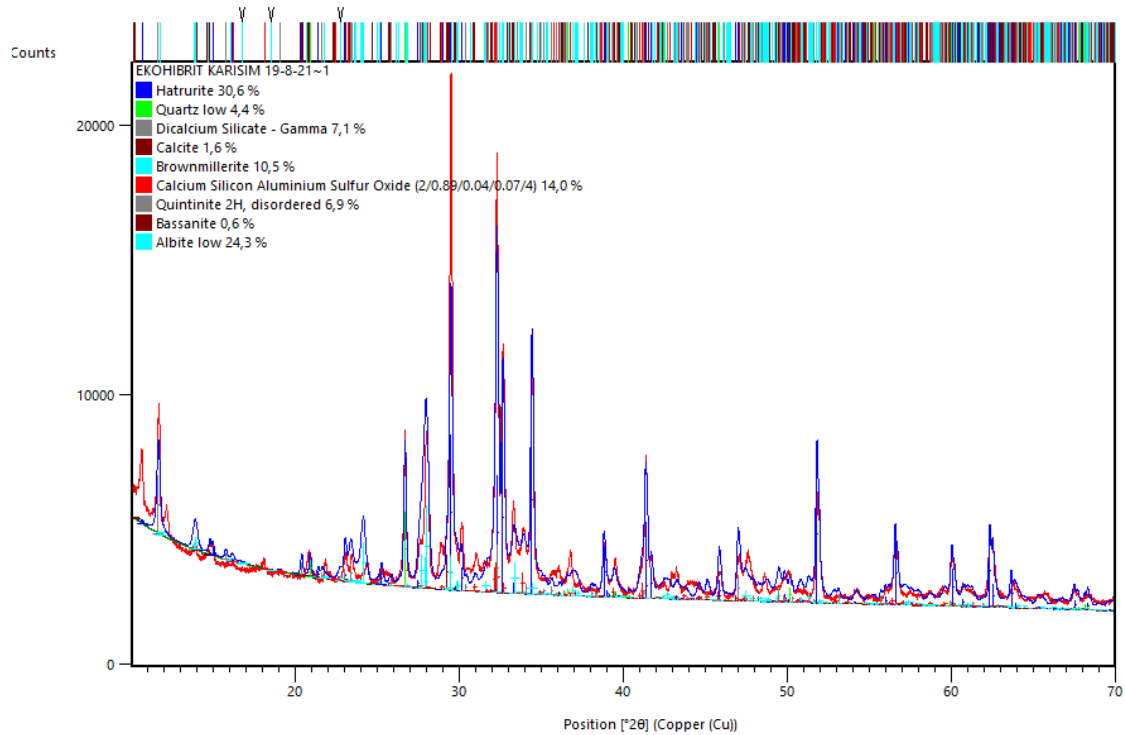


Figure 2-3 XRD analysis of Mix 3 and Mix 8 Blended cements

Calcium Sulfo-Aluminate (CSA) cements have been optimized over the last decades as a substitute of Ordinary Portland Cement (OPC) due to the mechanical improvements regarding the rapid hardening and the reduction in CO<sub>2</sub> emissions (burnt at lower temperature than OPC). It was conducted 25 different trial experiments with different raw material sources (limestone, clay, gypsum and bauxite) for CSA cement formulation in lab scale. The required yeelimite phase for CSA cement production was obtained in lab scale.

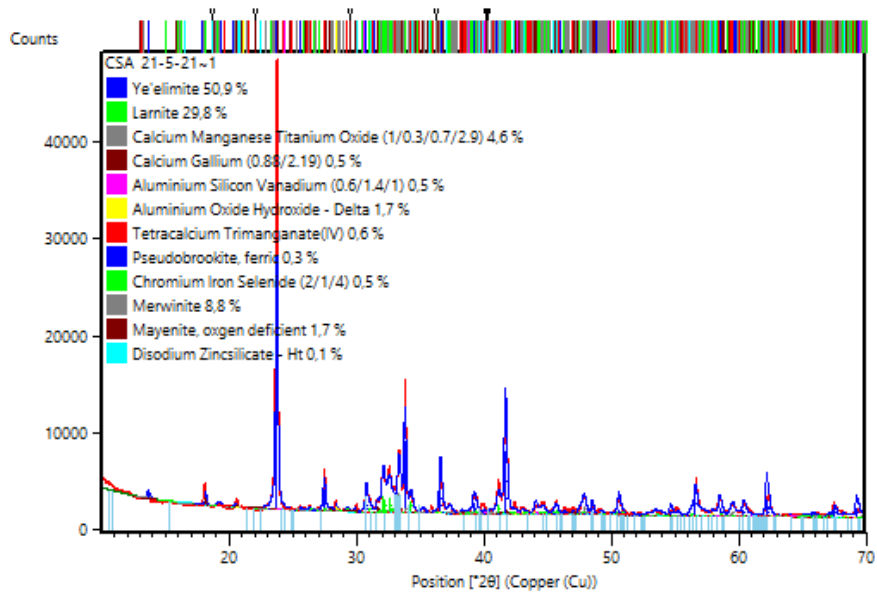


Figure 2-4 XRD analysis of lab scale produced CSA cement

In lab scale production, the amount of CSA cement was inadequate for eco-hybrid cement formulation. CSA clinker powder for eco-hybrid cement trials was purchased and chemical and physical analysis was performed on it.

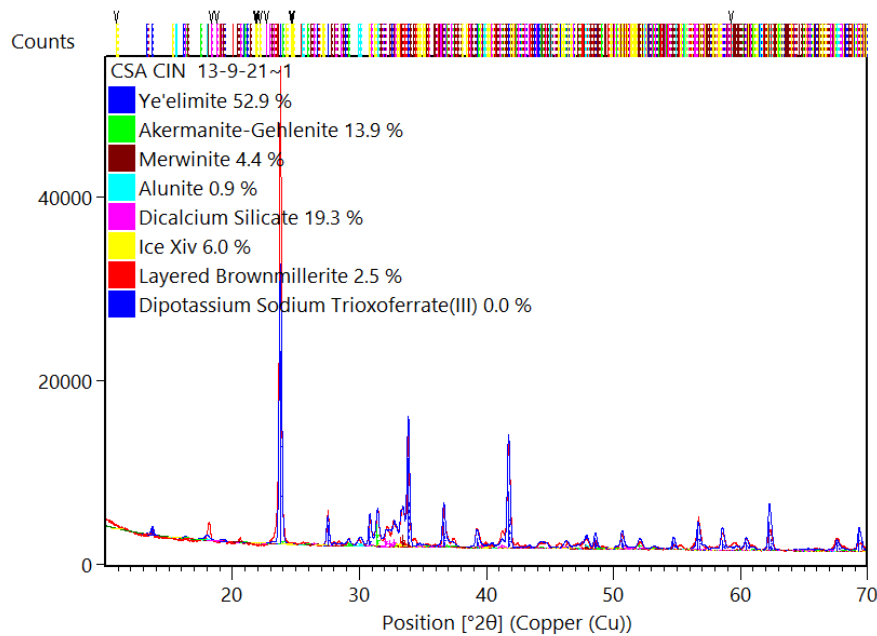


Figure 2-5 XRD analysis of CSA clinker powder

Table 2-7 XRF analysis of CSA clinker powder.

Chemical analysis										
Composition (%)	SiO <sub>2</sub>	Al <sub>2</sub> O <sub>3</sub>	Fe <sub>2</sub> O <sub>3</sub>	CaO	MgO	K <sub>2</sub> O	Na <sub>2</sub> O	SO <sub>3</sub>	TiO <sub>2</sub>	LOI
CSA cement	7.77	35.72	2.69	42.31	1.18	0.23	0.07	7.85	1.86	0.33

Table 2-8 Blaine and density of Blended cements and CSA clinker powder

Material	CSA clinker powder
Blaine (cm <sup>2</sup> /g)	5000
Density (g/cm <sup>3</sup> )	3.12

Eco-hybrid cement trials were done with combination of CSA and Blended cement incorporating high amount of RBM 19.5% of brick, 12.5% of concrete and 2% of gypsum (Mix 9). For this study 5% of Cem I 42.5 cement was replaced with CSA cement to obtain Eco-hybrid cement. Mix 8 and Mix 9 were sent to Hacettepe University and Tepe Betopan for obtaining concrete elements.

Table 2-9 Eco-hybrid cement trial mixtures

Eco-hybrid cement (CSA+ Blended Cement (min %30 EBM))		
Materials	Mix8	Mix9
Cem I 42,5 cement	66%	61%
CSA cement	-	5%
Brick waste	19.5%	19.5%
Glass waste	-	-
Concrete waste	12.5%	12.5%
Gypsum	2%	2%

All blended cement mixtures and Eco-hybrid cement mixture were tested according to EN standards. Mortar compressive strengths, setting time, flow measured for all mixtures, soundness of cement (volume expansions) were measured for mixture 8 and mixture 9 (Eco-hybrid cement trials).

For the measurement of cement compressive strength, mixtures were prepared by mixing with a mortar mixer consisting of 450±2g cement, 1350±5g standard sand and 225±1g water according to EN 196-1 standard. Prepared mortars were

carefully placed in three-compartment mortar molds with dimensions of 4x4x16cm. The three prismatic samples prepared are stored in a moisture-saturated curing room or in lime-saturated water at  $20\pm 1^{\circ}\text{C}$  until the test date. Each prismatic sample was first divided into 2 separate parts by performing a bending test in the test press. Thus, 6 pressure samples were obtained from 3 prism samples. A metal breaking head of 4x4 cm was placed on the lower and upper surfaces of each half sample and subjected to a pressure test in the test press. The half prism between the crushing heads behaves like a cube sample of 4x4x4cm. The compressive strength of the sample was obtained by dividing the cross-sectional area by the fracture force  $P$ . After this test was performed on all 6 samples, the arithmetic average of the results was taken and the compressive strength of the cement for the desired age (2, 7, 28 days) was obtained. With the results of the compressive strength, the suitability of whether the cement provides the desired strength class was checked.



Figure 2-6 4x4x16 cm Cement Mortar Mold



Figure 2-7 Cement Mortar Compressive Strength Test

The amount of water required for the cement paste to be of normal consistency is determined with the help of the vicat tool. The Vicat tool consists of a flat table and a gooseneck holding the cylinder shaft adjusted to the axis of the table. The total mass of the movable shaft should be  $300\pm 1$  grams. In order to determine the normal consistency, two mortars are obtained by adding 5% water according to the mortar sample prepared in the spreading test and the cement used. The probe (needle) attached to the vicat device for the experiment is lowered to the base plate and adjusted to read zero on the scale indicator. The bottom plate



glass and the inner surface of the sample ring are lubricated with mineral oil. Freshly mixed cement paste is placed in the ring without compaction and vibration. Excesses are removed with the help of spatula. The tip of the probe is lowered and released until it touches the upper surface of the cement paste in the middle of the prepared vicat ring. The probe enters the cement paste with its own weight. If the water used with normal consistency is sufficient, the probe descends to the glass plate until it remains 5-7 mm in half a minute. This process is repeated with different amounts of water to determine the amount of water required for cement. Reading is carried out in two ways. For the probe that is still sinking, the value read after 4 minutes is the sinking depth, assuming its release is zero. The probe, whose sinking is completed before 4 minutes, should be read 30 seconds after it stops. The value giving the distance between the bottom face of the probe and the base plate is read and this value is recorded together with the water content of the paste, expressed as a percentage by the mass of cement. The probe is cleaned after each immersion. The test was carried out with pastes containing varying amounts of water, between the probe and the base plate. This is repeated until the distance is  $6\pm 1$  mm. The water amount of the cake that has reached the standard consistency is recorded with an accuracy of 0.5%, as the amount of water required for the standard consistency.



*Figure 2-8 Vicat Tool*

For the setting time test, the needle attached to the vicat device is lowered onto the base plate and the needle vicat device is set to zero on the scale indicator. Then the needle is lifted up and taken to the standing position. The Vicat mold is filled with cement paste of standard consistency and leveled. The Vicat needle is lowered slowly until it comes into contact with the paste. Then the arm is released and the cake is inserted into it. After the needle is inserted into the cake (or 30s



later), the values are taken. This value, which gives the distance between the tip of the needle and the base plate, is recorded together with the time elapsed from the zero moment. The process of inserting the needle into the same sample is repeated with a distance of at least 10 mm between the points where the needle is inserted into the cake or from the edge of the mold, and at appropriate time intervals of 10 minutes. The vicat needle should be cleaned after each immersion. The time elapsed from the starting time, which is accepted as zero, until the distance between the needle and the base plate is  $4\pm 1$  mm, is rounded to the nearest 5 minutes, recorded as the initial setting time. The used solid mold on the base plate is inverted to determine final setting time. Thus, the determination of the final setting time is made on the surface of the paste that initially comes into contact with the base plate. Values are taken as in the experiment of determining the initial setting time. The time intervals between immersion operations can be increased, for example up to 30 minutes. The vicat needle should be cleaned immediately after each immersion. The time when the needle sinks in for the first 0.05 mm and the time considered zero are rounded off to the nearest 15 minutes and recorded as the final setting time. (EN 196-3).



*Figure 2-9 Cement Mortar Setting time test*

A Cement Flow Table is used for spreading (fluidity) tests of mortar, lime and cement samples (EN 1015-3). It is aimed to determine the fresh consistency and flow value of the mortar containing mineral binder and dense aggregate or light aggregate immediately after mixing. The wet sample, which is placed on the flow table of standard shape and size, with the help of a mold of standard shape and size, is subjected to vibration by turning the arm of the device. The arm lifts the spreading table upwards and lowers it by releasing it from a certain height. The flow value of the fresh mortar sample is determined by measuring the mean diameter of the flow of mortar sample.



Figure 2-10 Cement Flow table test

If there is a large amount of free lime (CaO) or magnesium oxide (MgO) in the cement content, it causes the cement paste to expand. The reactions of CaO and MgO in the cement with water occur months after the cement paste or concrete hardens. As a result of the hydration of these oxides, expansion occurs in the hardened cement paste, and internal stresses and cracks may occur in concrete structures. This expansion is determined with the help of Le Chatelier device. Cement paste of normal consistency is prepared for the experiment. (the remaining mortar from the consistency analysis test can be used) The test is performed on two samples from the same cement paste mixture at the same time.

The oiled Le Chatelier mold is placed on the lightly oiled glass plate and filled with cement paste without compressing or vibrating, the level of the upper surface is adjusted by hand or using a straight edge spatula, if desired. In order to prevent the slit of the mold from opening during filling, it is lightly squeezed with fingers or the ends are tied or attached with a suitable rubber band. The top of the mold is covered with a lightly oiled glass plate, additional mass is added if necessary and the whole device is immediately placed in the humidity cabinet. It is stored here for  $24 \pm 0.5$  hours at  $20 \pm 1^\circ\text{C}$  and at a relative humidity of not less than 98%. After a period of  $24 \pm 0.5$  hours, the distance (A) between the indicator tips is measured to the nearest 0.5mm. Then, the mold is heated to boiling temperature in  $30 \pm 5$  minutes and the water bath is kept at boiling temperature for 3 hours  $\pm 5$  minutes. At the end of the boiling time, the distance (B) between the indicator tips can be measured to the nearest 0.5mm. The mold is expected to cool down to  $20 \pm 2^\circ\text{C}$ . The distance (C) between the indicator tips is measured to the nearest 0.5mm. The (A) and (C) measurements are recorded for each sample and the (C-A) difference is calculated. It is calculated by rounding the average of the two values of (C-A) to the nearest 0.5 mm. This expansion value should be less than 10mm (EN 196-3).

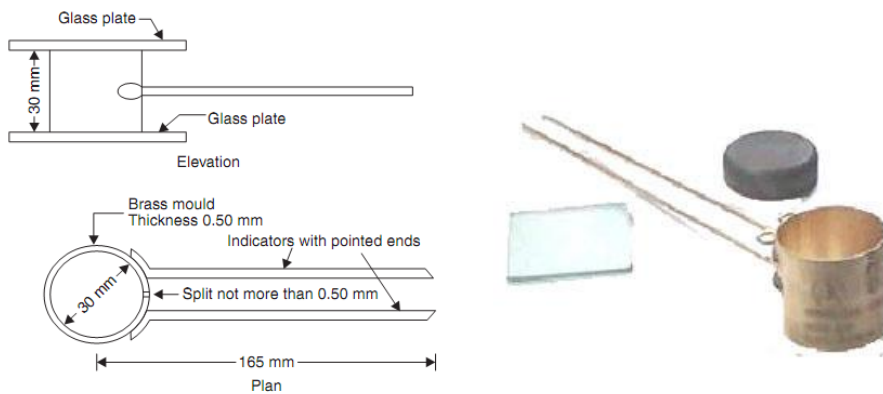


Figure 2-11 Soundness of cement Le chatlier's Test Apparatus

### 2.1.3 Results and Discussions

As stated above, blended cement tests were carried out. All mixtures were compared with reference CEM I 42.5 R cement. For this preliminary study, the target blended cement is mix 8. It was prepared by using waste at the rates specified in the project proposal (about 19.5% of glass or brick, 12.5% of concrete and 2% of gypsum).

When compared to CEM I 42.5 initial and final setting times are extended. The water amount is slightly increased. Flow results remained stable.

2 days, 7 days, 28 days compressive strengths of all mixtures are as follows in Table 2-11 Mortar Compressive Strength of Blended cements and CEM I 42.5 R cement. Accordingly, when the compressive strengths of all mixtures are examined, lower compressive strength was obtained than the CEM I 42.5 R cement. Low results are normal, because as the ratio of waste additives in cement increases, cement strength decreases. As a next step, further grinding and calcination steps will be performed to improve the reactive of the CDW-based materials.

Table 2-10 Setting Time and Flow of Blended cements and CEM I 42.5 R cement

Setting time and flow	Mix1	Mix2	Mix3	Mix4	Mix5	Mix6	Mix7	Mix8	Control (CEM I 42.5)
Initial setting time(min)	180	185	160	175	195	185	190	200	175
Final setting time (min)	270	290	260	290	305	295	300	240	220
Water amount for setting(%)	30.6	31	30.6	31.4	31	31.6	31.4	30.2	29.4
Flow(cm)	15	15	15	15	15	15	15	15	15

Table 2-11 Mortar Compressive Strength of Blended cements and CEM I 42.5 R cement

Mortar Compressive Strength (MPa)									
Time	Mix1	Mix2	Mix3	Mix4	Mix5	Mix6	Mix7	Mix8	Control (CEM I 42.5)
2 days	21.6	15.2	18.5	15.5	18	16.6	16.6	19.5	30.5
7 days	31.5	23	29.4	25.2	26	26.7	27.8	27.83	41.7
28 days	40	29.1	36.7	31.2	32.3	33.9	33.6	33.2	51.2

After having blended cement results, for eco-hybrid cement mixture 8 was blended with CSA cement. Eco-hybrid cement (mix 9) is obtained.

Table 2-12 Setting Time and Flow of CSA clinker powder, Eco-hybrid cement and CEM I 42.5 R cement

Setting time and flow	CSA clinker powder	Eco-hybrid Cement (mix9)	Control (CEM I 42.5)
Initial setting time(min)	275	115	175
Final setting time (min)	330	200	220
Water amount for setting(%)	28	33.4	29.4
Flow(cm)	20	12	15

Table 2-13 Mortar Compressive Strength of CSA clinker powder, Eco-hybrid cement and CEM I 42.5 R cement

Mortar Compressive Strength (MPa)			
Time	CSA clinker powder	Eco-hybrid Cement (mix9)	Control (CEM I 42.5)
2 days	67.8	17.5	30.5
7 days	86.2	27.5	41.7
28 days	90.5	33.3	51.2

Table 2-14 Soundness of CSA clinker powder, Eco-hybrid cement and CEM I 42.5 R cement

Soundness (Expansion) mm	CSA clinker powder	Eco-hybrid Cement (mix9)	Control (CEM I 42.5)
	0.1	10	1

When comparing Eco-hybrid cement with CEM I cement, initial and final setting times decreased, water amount for setting increased, flow decreased and expansion increased. When the results are examined, it can be concluded that CEM I 42.5 R cement with stated ratios CDW, equivalent CEM I 32.5 N cement can be obtained.

For further studies;

- CSA clinker and cement will be produced in Çimsa plant and will be used in eco-hybrid cement production.
- Different waste and CSA cement ratios will be examined.
- With different mixture trials expansion and compressive strength values will be optimized.

#### 2.1.4 References

Naceri, A., & Hamina, M. C. (2009). Use of waste brick as a partial replacement of cement in mortar. *Waste management*, 29(8), 2378-2384.

Preeti, D. B., Kumar, A., & Mangraj, A. (2018). Strength Characteristics by Partial Replacement of Cement with Brick Powder. *International Journal of Applied Engineering Research*, 13(7), 94-99.

Eurostat, B. (2017). Generation of waste by waste category, hazardousness and NACE Rev. 2 activity.

Pitroda, J., Zala, L. B., & Umrigar, F. S. (2012). Experimental Investigations on Partial Replacement of Cement with Fly ash in design mix concrete. *International Journal of Advanced Engineering Technology*, IJAET, 3(4), 126-129.

P. Shen, L. Lu, Y. He et al., "Investigation on expansion effect of the expansive agents in ultra-high performance concrete," *Cement and Concrete Composites*, vol. 105, p. 103425, 2020.

D.-Y. Yoo, S. Kim, J.-Y. Lee, I. You, and S.-J. Lee, "Implication of calcium sulfoaluminate-based expansive agent on tensile behavior of ultra-high-performance fiber-reinforced concrete," *Construction and Building Materials*, vol. 217, pp. 679–693, 2019.

Song, M., Wang, C., Cui, Y., Li, Q., & Gao, Z. (2021). Mechanical Performance and Microstructure of Ultra-High-Performance Concrete Modified by Calcium Sulfoaluminate Cement. *Advances in Civil Engineering*, 2021.

### 3 Structural precast recycled concrete elements

#### 3.1 Optimized concrete recipes considering regulations, requirements and needs

##### 3.1.1 Introduction

In the development of green concrete, it is of great importance that the components that make up the structural material are suitable for recycling and can be recycled repeatedly. It is known that brick and tile-based masonry, roof elements, concrete and glass are recyclable and it is possible to produce building elements again under suitable conditions (Hansen, 1992). The use of concrete, which constitutes a very large part of construction and demolition waste (CDW), both as a cement substitute and as aggregate in recycling is a matter that should be considered for the production of sustainable green building materials. As it is known, aggregates constitute 60-75% by volume and 80-85% by weight of Portland cement concrete mixes (Mehta and Monteiro, 1993). In this context, a proper analysis of the properties of recycling aggregates to be obtained from waste concrete and their use as an aggregate source in the production of green concrete will be a paradigm shift in the construction sector.

Recycling operations for CDW aggregates have been set up in many countries. In general, waste concrete elements are crushed mechanically into small pieces (<40 mm) for the production of recycled concrete aggregates (RCA). After the crushing processes, different sized fractions are screened using a sieving device. RCAs with better-quality and proper crushing processes exhibit better properties. More crushing decreases the amount of adhered mortar in the coarser aggregates, which influences positively to the characteristics of RCA (Nagataki et al. 2004). However, the amount of crushing in this way also brings higher costs. Some researchers have reported that the amount of adhered mortar increases with the decrease of grain size (Etxeberria et al. 2007a; Katz 2003; Zaharieva et al. 2003). For this reason, it is very important to provide the most suitable crushing-obtaining processes for waste concrete by making an optimization in terms of cost and quality.

Since the aggregate occupies a large volume in the concrete, its density affects many properties of the concrete. The density of RCA is lower than that of natural aggregate (NA) due to the existence of porous and adhered mortar on the RCA surface. It was already reported that an increase in adhered mortar amount on the aggregate leads to a lesser density of the RCA (De Juan and Gutiérrez 2009). In addition to the density properties of RCAs, the amount of adhered mortar greatly affects the water absorption of RCA. RCA aggregates have much higher water absorption capacity than NA due to the high water absorption capacity of adhered mortar. RCA aggregates have much higher water absorption capacity than NA due to the high water absorption capacity of adhered mortar. De Juan (2004) found that while natural aggregates have a water absorption between 0 and 4%, the water absorption of RCA is between 0.8 and 13%. Additionally, water



absorption increases as the grain size decreases as a result of the fine-sized recycled aggregates of the RCA has a higher amount of adhered mortar than the coarse-sized recycled aggregates (Zaharieva et al., 2003). However, the influence of waste concrete sources on the RCA properties is still discussed. Nagataki et al. (2004) state that as the grade of source concrete increases, the water absorption rate decreases, while Padmini et al. (2009) state that water absorption rate increases as the grade of source concrete increases. Since the water/cement (w/c) ratio directly affects the adhered mortar amount, RCA obtained from concrete with a low w/c ratio has low water absorption capacity (Hansen and Narud 1983; Santos et al. 2002b).

The fact that the properties of RCA are quite different from NA, leads to differences in the fresh and hardened properties of the concretes produced with these aggregates. The properties of fresh concrete are greatly affected by factors such as density and workability, and the workability of fresh concrete can be measured with the slump test. In studies on workability, the slump values of concrete produced with RCA are not the same as those of concrete produced with NA because RCA has a considerably higher water absorption capacity than NA. Topçu (1997) observed a 75 mm slump in concrete produced with RCA while the concrete produced with NA was 100 mm. Additionally, Poon et al. (2004) reported that an increase of RCA amount in the mixture decreases the slump value. Also, the same authors stated that as the amount of RCA increases, the effect of moisture content of RCA on the slump value becomes considerable. As the amount of RCA increases, the slump value decreases, and the water requirement increases significantly. However, to meet this enormous water demand and increase workability, superplasticizer can be used (Evangelista and de Brito 2007). Many researchers have found that concrete produced with RCA has lower slump values than concrete produced with NA (Khan 1984; Mukai et al., 1978; Buck 1977; Hansen and Narud 1983). The density of fresh concrete depends on many variables such as aggregate, cement type, water content, and air content. Fresh concrete containing RCA is slightly less dense than fresh concrete containing NA due to the presence of adhered mortar (Gonzalez-Fonteboa et al., 2011). Further, the density of fresh concrete affects numerous hardened-state properties of concrete. The fresh density of concrete containing RCA is less than that of normal aggregate concrete. The adhered mortar, which is permeable and has a high water absorption value on the surface of the RCA, causes a decrease in its density (Gonzalez-Fonteboa et al., 2011). Also, Katz (2003) found no significant differences in densities of concrete mixes incorporating RCA made from old concrete of three different ages (1, 7 and 28 days), implying that the amount of adhered mortar in the various concrete aggregates was identical independent of crushing age.

With the addition of RCA, the compressive strength of concrete generally reduces (Topcu and Sengel 2004; Kou and Poon 2008; Oliveira and Vazquez 1996) and the reduction in compressive strength of the concrete may reach 40% (Katz 2003; Chen et al. 2003). Topcu and Sengel (2004) observed that the strength of the concrete produced by RCA decreased by 33% in C16 concrete and 23.5% in C20 concrete compared to normal concrete. According to Etxeberria et al. (2007a), the compressive strength of the concrete produced with 100% coarse RCA was 20-25% lower than normal concrete. However, it has been shown that the use of

RCA up to 30% does not affect the compressive strength (Gomez-Soberon 2002; Li et al. 2009; Limbachiya et al. 2004, 2012; Rao et al. 2011; Yang et al. 2011). Since the RCA has adhered mortar which is permeable and has high water absorption, these properties increase the porosity and decrease the aggregate-matrix interface bond strength (Kwan, Ramli et al. 2012). The splitting tensile strength of concrete containing RCA is typically lower than that of conventional concrete and increasing the amount of RCA lowers the compressive strength gradually. According to Kou et al. (2011a), the 28-day splitting tensile strength of concrete containing coarse RCA was found to be 10% and 7% lower than that of ordinary concrete. However, Yong and Teo (2009) found that replacing 100% of natural aggregate with normal or saturated surface dry coarse RCA improved the splitting tensile strength of concrete in the early stages of curing (up to 28 days). Similar to the compressive strength and splitting tensile strength, flexural strength decreases as the amount of RCA in concrete increases. Yang et al. (2011) observed a 3% and 9% decrease in 7 and 28 days of flexural strength, respectively. However, Safiuddina, Alengaramb et al. (2011) observed no difference between normal concrete and concrete produced with RCA, although a 12% decrease in compressive strength was reported. Furthermore, Chen et al. (2010) found that replacing up to 40% of coarse NA with RCA resulted in a slightly increase in flexural strength, with equal values to conventional concrete above the replacement threshold.

### 3.1.2 Materials and Methodology

In this section, the materials and their properties that are used within the scope of development of "green" concrete recipes were presented. Moreover, mixture designs, casting, curing and testing methods were also explained in detail.

#### 3.1.2.1 Materials

##### Portland Cement

CEM I 42,5 R - Portland cement used in the preliminary studies was supplied by CÍMSA. The chemical composition of cement was given in Table 3.1.

Table 3-1 The chemical composition of Portland cement

Property (%)	Lol	SiO <sub>2</sub>	Al <sub>2</sub> O <sub>3</sub>	Fe <sub>2</sub> O <sub>3</sub>	CaO	MgO	SO <sub>3</sub>	Na <sub>2</sub> O	K <sub>2</sub> O	Cl <sup>-</sup>	Insoluble residue
<b>CEM I 42.5 R</b>	3.59	18.90	5.15	3.36	63.59	1.57	2.65	0.40	0.77	0.02	0.91

Lol: Loss of Ignition



## Eco-hybrid cement

Within the scope of the study, eco-hybrid cement was used for the development and optimization of green concrete recipes. The chemical and physical properties of Eco-hybrid cement were given in the previous section.

## Aggregates

In the first stage of the study, natural aggregate and recycled concrete aggregate were used together in preliminary studies in order to determine the optimum replacement rates of the recycled concrete aggregate. In order to determine the properties of different RCAs collected from different sources, three concrete waste samples were collected from different demolition regions (coded as X, Y and Z). The images of that RCAs' were shown in Figure 3-1.



Figure 3-1 The images of RCA's collected from different demolition regions.

Concrete waste samples were crushed from two different openings in a laboratory-type jaw crusher to produce fine and coarse recycled aggregates. Later, the aggregates were separated into fine and coarse aggregates with the help of sieves.



Figure 3-2 Sieves used for aggregate gradation.

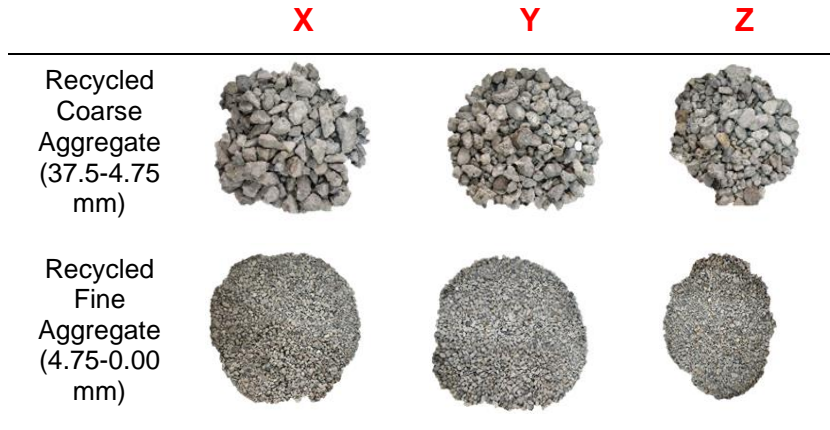


Figure 3-3 Recycled Coarse and Fine Aggregates

### Properties of Recycled Aggregates

The properties of recycled aggregates collected from different regions are presented in this section. In this context, the densities, water absorption capacity and chemical content of the recycled aggregates were analyzed.

#### Density

The densities of aggregates were determined following TS EN 1097 standard. The samples were kept immersed in water at 20°C for 24 hours. This way, all the pores of the aggregate were filled with water. A 500 gr sample was used for fine aggregates and 2 kg sample was used for coarse aggregates. Secondly, the weight of the coarse aggregates in water was measured (M2) and the weight of the empty basket in which the aggregate was placed was measured (M3). M2 and M3 were calculated by pycnometer for fine aggregates. Then, the aggregates were brought to a surface saturated dry (SSD) state and weighed (M1). Finally, the aggregates were dried in an oven at 115°C until they reached a constant mass, and their weights were measured (M4). All values measured in g. Densities of aggregates ( $\rho_a$ ,  $\rho_{rd}$  and  $\rho_{SSD}$ ) were calculated using the following formulas:

$$\rho_a = \rho_w \frac{M4}{M4 - (M2 - M3)} \quad (1)$$

$$\rho_{rd} = \rho_w \frac{M4}{M1 - (M2 - M3)} \quad (2)$$

$$\rho_{SSD} = \rho_w \frac{M1}{M1 - (M2 - M3)} \quad (3)$$

where,

$\rho_a$ : Apparent density, g/cm<sup>3</sup>

$\rho_{rd}$ : Oven Dry density, g/cm<sup>3</sup>

$\rho_{SSD}$ : SSD density, g/cm<sup>3</sup>

$\rho_w$ : Density of water, g/cm<sup>3</sup>

Density values for coarse and fine recycled aggregate for X, Y, and Z are presented in Table 3.2. In general, it is observed that the density decreases as the grain size decreases, regardless of aggregate source.

Table 3-2 Densities of recycled aggregates

Properties	X		Y		Z	
	Coarse	Fine	Coarse	Fine	Coarse	Fine
pa	2.64	2.62	2.63	2.60	2.65	2.56
prd	2.25	2.04	2.14	2.05	2.31	1.99
pssd	2.40	2.28	2.33	2.26	2.44	2.17

According to the density values of recycled aggregates given in Table 3.2, the apparent density range of fine recycled aggregate was found as 2.56-2.62, oven-dry density range 1.99-2.05 and SSD density range 2.17-2.28. The apparent density range of coarse recycled aggregate was 2.63-2.65, oven-dry density range was 2.14-2.31 and SSD density range was 2.33-2.44. These ranges showed that the change in the source of aggregate collected from the demolition zones was quite similar in terms of density ranges. As it is known, density is one of the key parameters of aggregate and is important to design concrete mixtures and control several properties of the resulting concrete. In this context, it was concluded that the recycled aggregates produced with the waste concrete collected from different demolition zones are practically applicable regardless of the region.

In general, recycled aggregates have a lower density than normal aggregates. The main reason for this situation is that the cement mortar adhered to the recycled aggregate has a porous and less dense structure (J De Brito and N Saikia, 2012).

### Water Absorption

The water absorption values of recycled aggregates were determined following TS EN 1097 standart and presented in Table 3.3. The M1 and M4 values obtained from the density experiment were calculated using the formula given below.

$$WA_{24} = \frac{100(M1-M4)}{M4} \quad (4)$$

where,

$WA_{24}$  = Water absorption

Table 3-3 Water absorption of aggregates

WA24	Coarse	Fine
X	6.56	11.79
Y	8.65	12.35
Z	5.56	11.39

According to the water absorption values presented in Table 3-3 Water absorption of aggregates, the coarse recycled aggregates exhibited a water absorption value in the range of 5.56-8.65%, while the fine recycled aggregates exhibited a water absorption value in the range of 10.35-11.79%. The water absorption performances of the recycled aggregates from different regions were generally consistent with the density results presented in the previous section. As it is known, the most important reason for this consistency is the amount of adhered mortar in the recycled aggregate. Adherent mortar on the aggregate surface is porous by nature and therefore can absorb high amounts of water. Thus, increasing the amount of adhered mortar decreases the aggregate density and increases the water absorption rate. Besides these, the variation of water absorption capacity reported in various references is due to the variation of cement paste content in aggregate as well as the content of other components such as crushed clay brick and tiles, which have very high water absorption capacity (De Juan, 2004).

### Sulfate Soundness

The soundness test determines the resistance of an aggregate to degradation through decomposition and, especially freeze-thaw cycles. Durable (weather resistant) aggregates are less likely to deteriorate on site. In the soundness test, the aggregates are repeatedly immersed in sodium/magnesium sulphate solution. As a result of that process, salty crystals are formed in the porous parts of the aggregate. These crystal compositions create internal forces that will cause the aggregate disintegration by force pressure. After a certain immersing and drying cycles, the soundness test ends by determining the percentage of material loss.

The soundness test for aggregates was carried out by the methods specified in ASTM-C88 standards for the recycled aggregates. The test equipment photo and the results were presented in Figure 3-4 and Table 3-4, respectively.



Figure 3-4 Sulphate soundness test equipment photo

Table 3-4 Aggregate soundness test results

<b>Sulphate Soundness (%)</b>	<b>Coarse</b>	<b>Fine</b>
<b>X</b>	16.03	12.61
<b>Y</b>	17.45	13.24
<b>Z</b>	15.78	12.95

According to the results presented in Table 3.4, it was observed that weight loss rates of coarse aggregates depended on between 15.78-17.45% and weight loss rates of fine aggregates depended on between 12.61-13.24%. These weight loss values demonstrated that recycled aggregates exhibited similar sulfate soundness performance regardless of their source. As is known, the sulfate soundness property of recycled aggregates, as well as its density and water absorption capacity, is largely controlled by the amount of adhered mortar it contains. The large variation in the sulfate soundness properties of recycled aggregates in the literature is highly dependent on both the amount and quality of the adhered mortar. In addition, components such as hydrated cement, ceramics and natural aggregates in the recycled aggregate, unlike normal aggregates, are also at the forefront in determining these properties. In this context, as a result of the researches in the literature, Zaharieva et al. (2003) found the weight loss of recycled coarse aggregates as 26.4% as a result of the sulfate soundness test, while the weight loss of recycled fine aggregates was found to be 25.7%. In another work, Lin et al. (2004) found the weight loss of recycled coarse aggregates to be 17.9%, while the weight loss of recycled fine aggregates was found to be 10.8%. Since these variations greatly affect the fresh and hardened properties of concrete produced with recycled aggregate, it is of great importance to investigate the sulfate soundness of recycled aggregates and to apply treatment processes to aggregates if necessary to reduce their negative effect.



### Select and design of the aggregates

The properties of the aggregates selected to be used within the scope of the study were presented in Table 3.5. In addition, gradation curve graphs of aggregates used in the mixture were also presented in Figure 3-5.

Table 3-5 Properties of the aggregates

Property	Recycled Aggregates		Natural Aggregates	
	Coarse	Fine	Coarse	Fine
Size				
Dry Specific Gravity (g/cm <sup>3</sup> )	2.25	1.86	2.68	2.64
SSD Specific Gravity (g/cm <sup>3</sup> )	2.32	2.11	2.69	2.67
Apparent Specific Gravity (g/cm <sup>3</sup> )	2.49	2.51	2.71	2.72
Water Absorption (%)	5.30	11.80	0.29	1.24
Loose unit weight (g/cm <sup>3</sup> )	1.22	1.44	1.47	1.67
Dense unit weight (g/cm <sup>3</sup> )	1.35	1.58	1.54	1.80
Sulfate Soundness (%)	15.36	12.91	3.12	1.56

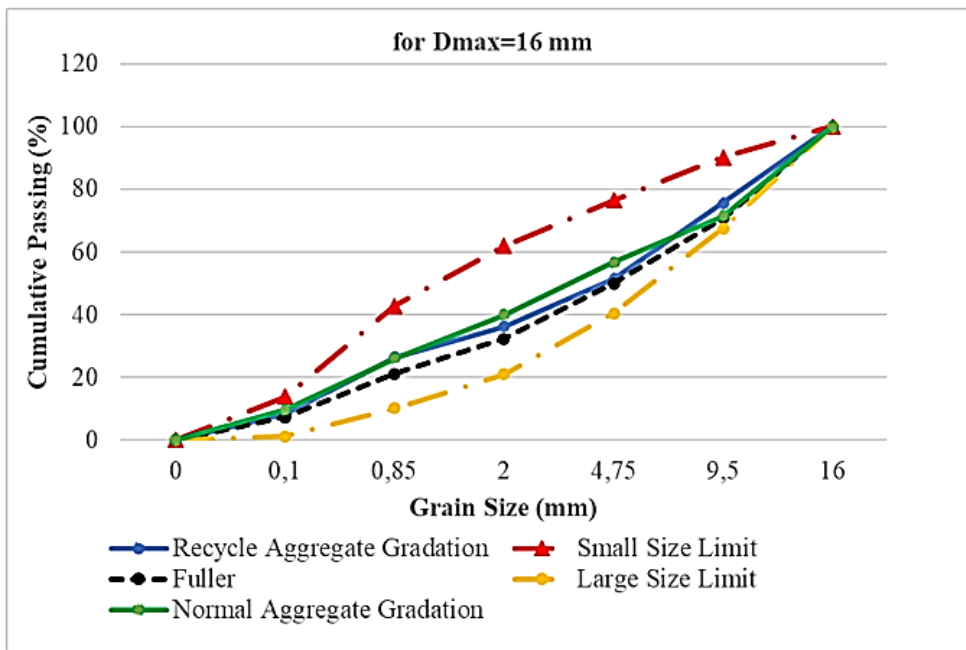


Figure 3-5 Gradation curve graphs of the aggregates

### 3.1.2.2 Methodology

In this section, studies such as mixture designs, casting and placing processes, curing conditions and test methods carried out within the scope of the development of green concrete with eco-hybrid cement and recycled aggregates were presented in detail.

#### Preparation of the Mixtures

Within the scope of the study, the traditional Portland cemented concrete mixture design was made with a variety of recycled aggregate and cement rates. Within the scope of this preliminary study, the cement dosage was designed to be 310.8 kg/m<sup>3</sup>, 383.3 kg/m<sup>3</sup> and 425.9 kg/m<sup>3</sup> of the mixture. The amount of water used in these mixtures was kept constant. Different rates of superplasticizer (SP) were added to the mixtures with low workability. In the mixtures produced by each cement dosage, five different recycled aggregate replacement ratios such as 0%, %60, 75%, 90% and 100% were used. Any pre-saturating process was not applied to the recycled aggregates. The solid materials used in the mixtures were weighed on a 0.1 g precision scale and poured into the Hobart mixer vessel.

#### Casting and Placing

All mixtures designed within the scope of the study were mixed via Hobart mixer. Mixing processes were initially performed for 1 minute in such a way that the cement and both natural and recycled aggregates were mixed homogeneously. Then water was added to the mixture and the mixer was launched at high speed for 5 minutes. The material produced after mixing was cast into 100x100x100 mm cubic molds for concrete samples and 100 mm diameter and 50 mm height cylindrical (Ø100x50 mm) molds for cylinder samples. The casting was carried out in two stages, firstly the slurry was divided into three equal layers and 25 strokes were applied to each of these layers. Secondly, after placing the slurry into molds, the compaction process was applied to the specimens via the vibration table for 1 minute. After the casting process is finished, the samples were covered with a plastic bag for 1 day and then subjected to water curing until the testing day. Pictures of the samples produced after casting were presented below. The contents of all these mixtures prepared within the scope of the study were presented in the experimental results and discussion section.

#### Curing and Testing

Firstly, the slump test was carried out to measure the workability of the mixtures before they were placed in the molds. After the casting and slump test of the mixtures was completed, the samples were molded and kept in the water tank until the test day. Within the scope of the study, 3 cubic specimens of each age with 100x100x100 mm dimensions were prepared from each of the concrete



mixtures to determine the 7-, 14- and 28-days compressive strength. The compressive strength test was performed on cubic specimens using a 100 ton capacity test device at a loading speed of 0.9 kN/sec in accordance with ASTM C39 (2003) standard. The compressive strength result was calculated by averaging the results obtained from the 3 specimens produced. In splitting-tensile strength test, 3 cylinder specimens of each age with 50 mm thickness and 100 mm diameter ( $\varnothing 100 \times 50$  mm) were prepared from each of the concrete mixtures to determine the 7-, 14- and 28-days splitting-tensile strength. Similar with compressive strength, the splitting-tensile strength result was calculated by averaging the results obtained from the 3 specimens produced.



a) Cube and cylinder specimens produced with Portland cement

b) Cube and cylinder specimens produced with Eco-hybrid cement

Figure 3-6 The visuals of the cubic and cylinder specimens

### 3.1.3 Results and Discussion

#### 3.1.3.1 Preliminary Studies

Within the scope of the study, a series of mixture designs were made in order to determine the optimum replacement ratio of recycled aggregates using Portland cement in the first stage. The contents of the mixtures produced by using various cement dosages and 0%, 60%, 75%, 90% and 100% ratios of recycled aggregates were presented in Table 3-6. As seen in Table 3-6. As it is known, due to the high water absorption capacity of the recycled aggregates, the workability of the mixtures decreased significantly as the amount of recycled aggregate increased in the mixtures with the same water/binder ratio. In order to overcome this problem, it is aimed to ensure the mixtures to similar workability by adding SP instead of water. However, according to the slump values of the mixtures presented in Table 3-7, although the mixtures were cast when it reaches sufficient workability, differences were found between the slump values. Even so, with the experience obtained from the slump values determined according to the recycled aggregate replacement ratios and SP amounts, the next stage of the study, the mixture designs with similar slump values to each other for eco-hybrid cement productions were made.

Table 3-6 Mixture designs of the preliminary study

Mix ID	RCA Rep. (%)	Portland Cement	FNA	CNA	FRCA	CRCA	Water	SP	w/c
<b>C30</b>	0	310.8	751.6	1082	0	0	230	0	0.74
	60		300.64	432.8	450.96	649.2		0	
	75		187.9	270.5	563.7	811.5		0	
	90		75.16	108.2	676.44	973.8		0.83	
	100		0	0	751.6	1082		2.5	
<b>C40</b>	0	383.3	792.3	968.4	0	0	230	0	0.6
	60		316.92	387.36	475.38	581.04		0	
	75		198.075	242.1	594.225	726.3		0	
	90		79.23	96.84	713.07	871.56		0.83	
	100		0	0	792.3	968.4		2.5	
<b>C50</b>	0	425.9	670.1	1048	0	0	230	0	0.54
	60		268.04	419.2	402.06	628.8		0	
	75		167.525	262	502.575	786		1.66	
	90		67.01	104.8	603.09	943.2		1.66	
	100		0	0	670.1	1048		2.5	

**Note:** All units were given in kg/m<sup>3</sup>, FNA: Fine natural aggregate, CNA: Coarse natural aggregate, FRCA: Fine recycled concrete aggregate, CRCA: Coarse recycled concrete aggregate, SP: Superplasticizer

## Workability Test

In order to determine the workability of the mixtures, the slump test was carried out on the mixtures before casting. According to the slump values presented in Table 3-7, mixtures without RCA had the highest slump values regardless of cement dosage as expected. Afterwards, it was observed that the increase in the amount of RCA used in the mixtures caused a gradual decrease in the slump values of the mixtures. Especially in C30/75% and C40/75% mixtures produced without using SP, there was a serious decrease in slump values, resulting in 30 mm and 25 mm, respectively. Considering this decrease in slump values, SP was added to the mixture produced with 90% RCA replacement. However, although SP addition did not increase the slump values of the mixtures as much as the mixture without RCA replacement, a high decrease in slump values was not observed according to the trend in decreasing slump values with the increase of RCA addition. Based on these results, the amount of SP added in the final mixtures containing 100% RCA was further increased, and slump values of 80 mm and 150 mm were reached, respectively, in C30 and C40 coded mixtures. Although these slump values are still below from to the 100% NA based mixtures, it has been observed that the mixtures reach a sufficiently workability. Another point to note is that the slump value of the mixture with 60% RCA replacement of the C50 coded serie showed a very high decrease compared to the 100% NA-based mixture. In this line, the amount of SP added to the 75%, 90% and 100% RCA replacement mixtures produced in the C50 coded serie was kept higher. Although the results were variable, the mixtures reached a workable level according to the slump values.

Table 3-7 Slump values of the mixtures

C30	%0 RCA	%60 RCA	%75 RCA	%90 RCA	%100 RCA
	145	60	30	20	80
C40	%0 RCA	%60 RCA	%75 RCA	%90 RCA	%100 RCA
	185	40	25	25	150
C50	%0 RCA	%60 RCA	%75 RCA	%90 RCA	%100 RCA
	160	25	170	55	45

**Note:** All units were given in mm.

## Compressive Strength Test

Within the scope of the preliminary studies, the 7-, 14- and 28-days compressive strength results of the mixtures produced with Portland cement were presented in Figure 3-7, Figure 3-8 and Figure 3-9, respectively. According to the 7-day compressive strength results, the relationship between the recycled aggregate

replacement ratios and compressive strength values of the mixtures produced with three different cement dosages was different from each other. Considering the results of the C30 coded series, it was observed that the increase in the recycled aggregate replacement rate led to a slight increase in the compressive strengths. In particular, the C30/100 coded mixture, which was the produced with 100% recycled aggregate, was exhibited the highest compressive strength of the series with 33.7 MPa at the end of 7 days of curing. A similar trend between recycled aggregate replacement rates and compressive strengths was also observed in C40 coded mixtures. In this series, especially the compressive strengths of the C40/90 and C40/100 coded mixtures were found to be considerably higher than the other mixtures with lower recycled aggregate replacement rate. This situation has been reported in the literature as it can contribute to the development of compressive strength by having a better bond strength and interlocking characteristics, especially at an early age, due to the high water absorption capacity of the adhered mortar content of the recycled aggregate (Rao et al., 2011). This was explained by the fact that, due to the high water absorption capacity of the recycled aggregate, it may consume a large amount of free water in the system at an early age, leading to an increase in compressive strength up to a certain threshold (Gonzalez-Fonteboa and Martinez-Abella (2005). Another result that can be shown as evidence for this situation can be stated as the decrease in compressive strength as the recycled aggregate ratio increases in the C50 series produced with lower water/binder than the other series. Within the scope of this study, since processes such as pre-saturation applied to recycled aggregates or adding extra water to reach similar water consumptions with NA were not carried out, so this behaviour was interpreted as the consumption of a part of the water required for full hydration by the recycled aggregates and therefore the decrease in compressive strength. Although the workability of the mixtures has been brought to sufficient levels by using SP, it is thought that this decrease in compressive strength is due to the hydration efficiency.

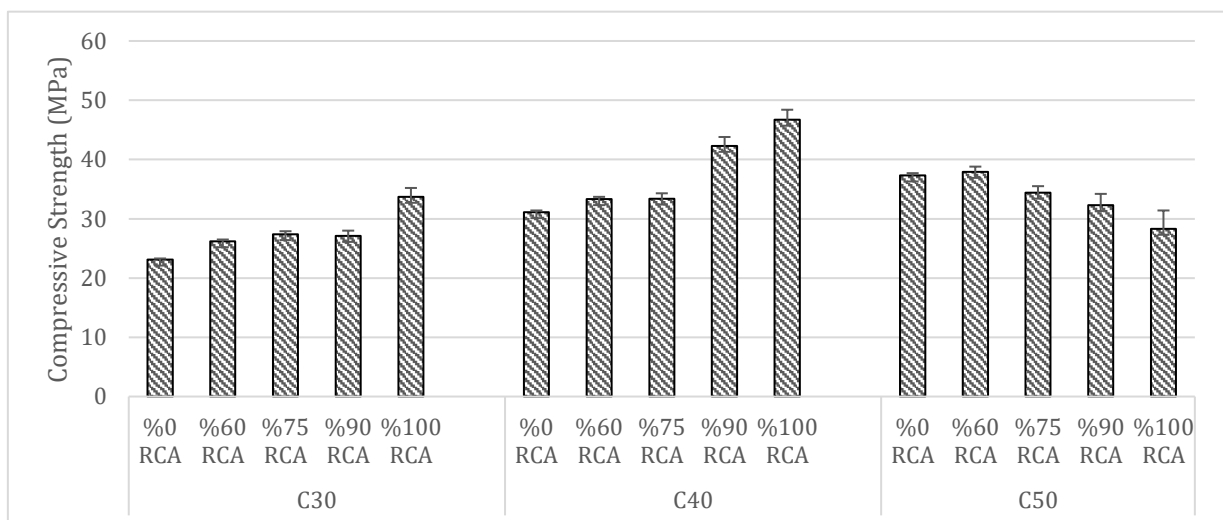


Figure 3-7 7-days compressive strength results of Portland cement-based mixtures

When the 14-days compressive strength results of the Portland cement-based mixtures were examined, the relationship between the compressive strength and the recycled aggregate replacement rate was quite similar to the 7-days compressive strengths, as expected. At the end of 14-days of curing, the compressive strength of the C40 coded mixtures was generally higher than the mixtures coded C30 and C50. Although it is expected that the increase in cement dosage will lead to an increase in the compressive strength, different results were seen due to the fact that the recycled aggregate replacement affects many parameters in the mixture. The point that supports this is that the increase in cement dosage increased the compressive strength only in mixtures using 100% NA. Among the mixtures after 14 days of curing, the C40/90 and C40/100 coded mixtures exhibited the highest results with a compressive strength of 45.7 and 46.95 MPa, respectively. On the other hand, it was observed that the increase in the replacement rate in C50 coded mixtures affected the compressive strengths negatively, even if it was not linear. This situation is related to the fact that the recycled aggregates in this series, which were produced with a lower water/binder ratio compared to other series, consumed some of the water required for fully hydration and causes a weaker matrix formation during the ongoing hydration.

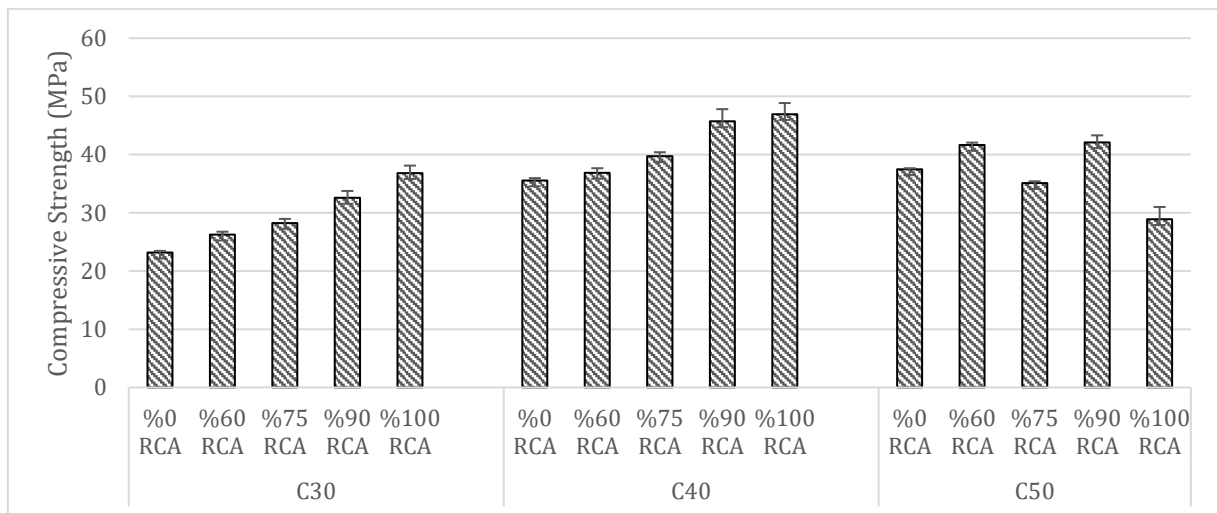


Figure 3-8 14-days compressive strength results of Portland cement-based mixtures

According to the 28-days compressive strength results of the mixtures produced with Portland cement and recycled aggregates, C40 coded samples exhibited the highest compressive strength results. In this context, the mixture coded C40/100, which was produced with 100% recycled aggregate replacement ratio in the series coded C40, showed the highest performance with a compressive strength of 47.3 MPa at the end of 28 days. In the C30 coded series, as in the previous ages, the increase in the recycled aggregate replacement led to a continuous increase in the compressive strength, while a similar trend was not observed in the C50 coded series. In this context, the mixture produced with 90% recycling aggregate replacement in the C50 series showed the highest compressive



strength, while the mixture produced with 100% recycled aggregate showed the lowest compressive strength. As mentioned before, although the mixture brought to certain workability with SP, full hydration could not be achieved due to excessive water absorption of the recycled aggregate and it had an inhomogeneous matrix compared to other mixtures. As it is known, extra water is added to the mixtures in order to ensure adequate workability in concretes produced with recycled aggregates in general. Although this extra water is consumed by the recycled aggregates and does not change the amount of water required for full hydration of the mixture, it creates weak zones with low density and high water/binder ratio in the interfacial transition zone around the recycled aggregates. This creates extra interfacial transition zones and heterogeneous structures in the mixture, reducing the compressive strength in general. However, in recycled aggregate-based concretes, in order to minimize the negative properties of the recycling aggregate without any improvement process, the following steps can be utilized: i) the water required for full hydration is calculated and first mixed with cement, ii) then the recycled aggregates are added to the mixture, iii) and finally admixtures can be used such as SP for sufficient workability. In these mixtures designed within the scope of the study, the aim was to observe this behavior and to observe the highest recycled aggregate usage rate with sufficient workability without any loss of mechanical performance. These results provided an important idea for the optimum workability/recycled aggregate ratio/mechanical performance for the eco-hybrid cement-based mixtures to be produced in the rest of the study.

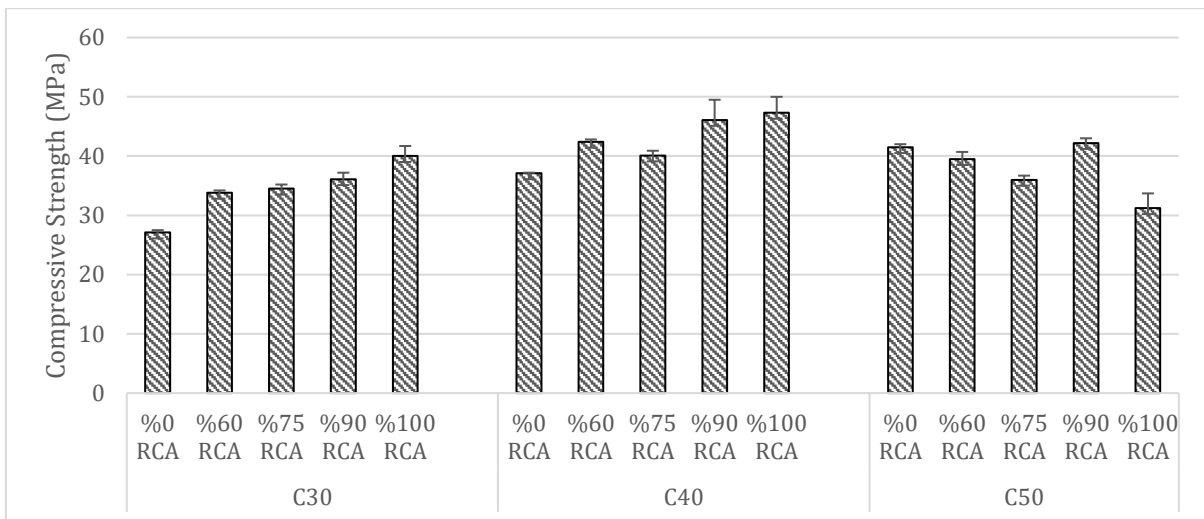


Figure 3-9 28-days compressive strength results of Portland cement-based mixtures

### Splitting-Tensile Strength Test

Within the scope of the preliminary studies, the 7-, 14- and 28-days splitting-tensile strength results of the mixtures produced with Portland cement were presented in Figure 3-10, Figure 3-11 and Figure 3-12, respectively. According to the 7-days splitting-tensile strength results of the mixtures presented in Figure D.1, a continuous increase was observed in the splitting-tensile strengths with

the increase of the recycled aggregate replacement ratio in the C30 coded mixtures. While this increase was 22.7% in the C30/60 coded mixture containing 60% recycled aggregate replacement ratio, it was 42.6% in the C30/100 coded mixture containing 100% recycled aggregate replacement ratio compared to the reference sample. Similar to the compressive strengths, in the C30 coded series produced with a higher water/binder ratio compared to the other series, this behavior was again related to the fact that the recycled aggregates consumed more than the water required for the full hydration of the cement and the matrix had a more compact structure. This situation is similar to the finding of an increase in splitting-tensile strength in a study by Kou and Poon (2006) by substituting recycled aggregate for natural aggregate in mixtures with a higher water/binder ratio. In addition, the authors showed in another study that higher splitting-tensile strength is expected to be found in concrete produced with recycled aggregates, since there may be stronger cement paste-aggregate bonds up to a certain replacement ratio (Kou and Poon 2008). However, studies in the literature are highly variable as they depend on many parameters such as the source, production quality, surface texture of the CDW-based recycled aggregate. However, the common opinion reached by many researchers is that recycled aggregate has a very small effect on splitting-tensile strength compared to its effect on compressive strength (De Brito and Saikia, 2012). Considering the splitting-tensile strength results of the mixtures produced in the C40 coded series, quite variable results were found. As an example, the highest splitting-tensile strength result was exhibited by the C40/100 coded mixture, followed by the C40/60 coded mixture. Another point to note here is that all recycled aggregate replacement rates exhibited better performance than the reference mixture. However, in contrast to the behavior in the C30 and C40 series, the recycled aggregate substitution in the C50 mixtures had a negative effect when compared to the splitting-tensile strength of the reference mixture. As mentioned in the compressive strength results, this was associated with reasons such as the insufficient amount of water for hydration, poor workability, and relatively higher porosity resulting from the use of recycling aggregate.

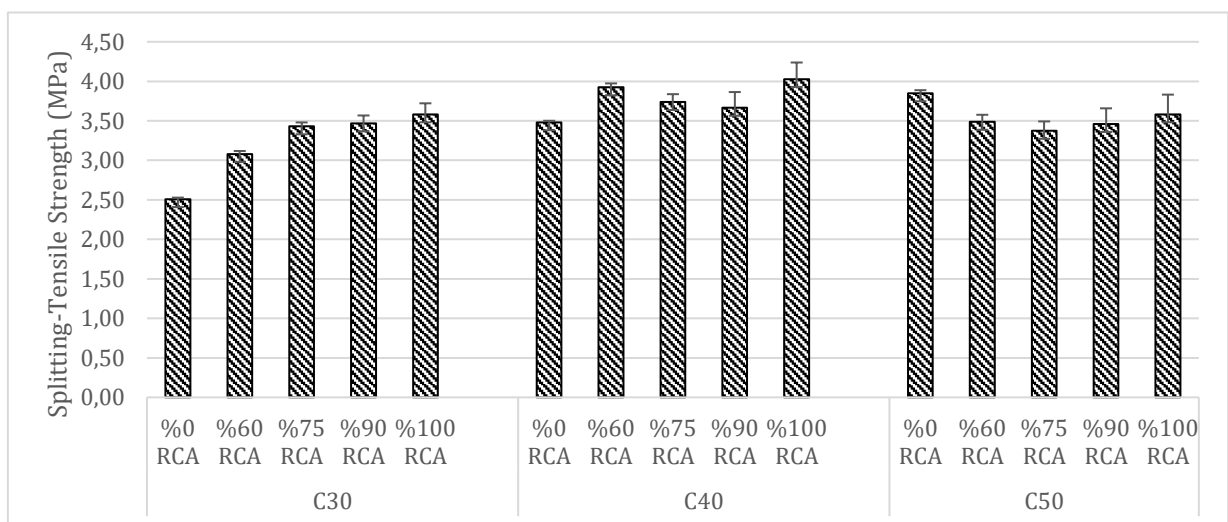


Figure 3-10 7-days splitting-tensile strength results of Portland cement-based mixtures



Considering the 14-days splitting tensile strength results of the Portland cement-based mixtures, it was seen an increment of around 6% according to the 7-days splitting-tensile strengths generally. Also, the trend seen in 7-days results from the usage of recycled aggregate was similar in this age.

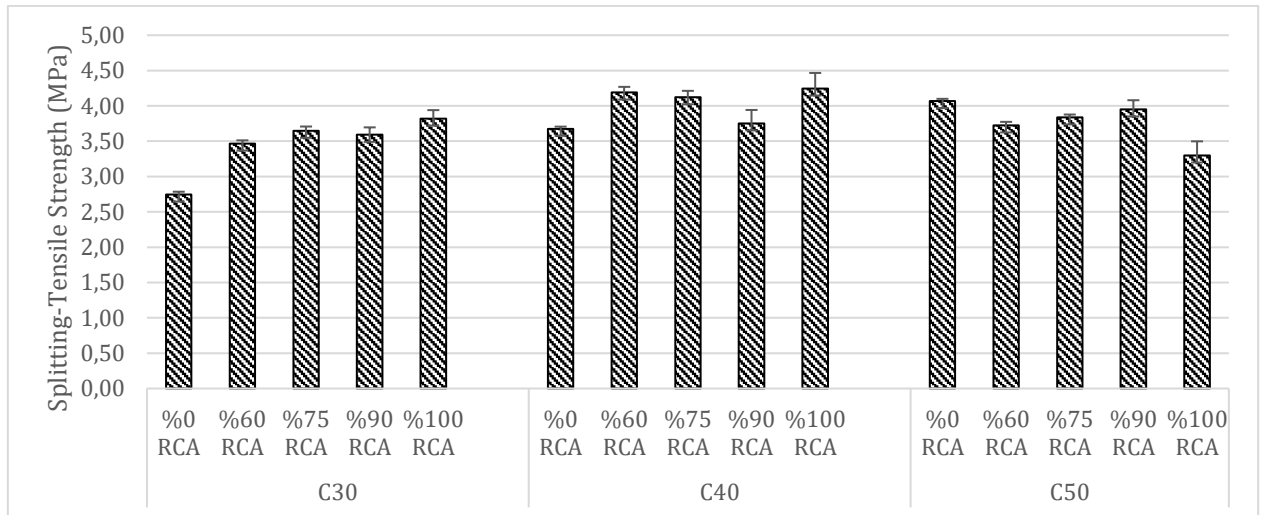


Figure 3-11 14-days splitting-tensile strength results of Portland cement-based mixtures

Finally, according to the 28-days, splitting-tensile strengths of the mixtures presented in Figure 3-12, C40/100 coded mixture exhibited the highest performance with 4.27 MPa, while this result was followed by C40/75 and C50/0 with splitting-tensile strength of 4.26 MPa and 4.16 MPa, respectively. According to the results obtained by all ages of the splitting-tensile strengths, the negative effect of the recycled aggregate substitution could be minimized with the proper mixture design and optimize water/cement ratios, cement dosages and adequate sufficient workability. In the later stages of the study which containing eco-hybrid cement-based mixture designs, all the outcomes obtained by Portland cement-based designs will be considered. Although the properties and chemical composition of the eco-hybrid cement are different from traditional Portland cement, the effect and behaviour of the recycled aggregate substitution will be expected to be similar and reasonable.

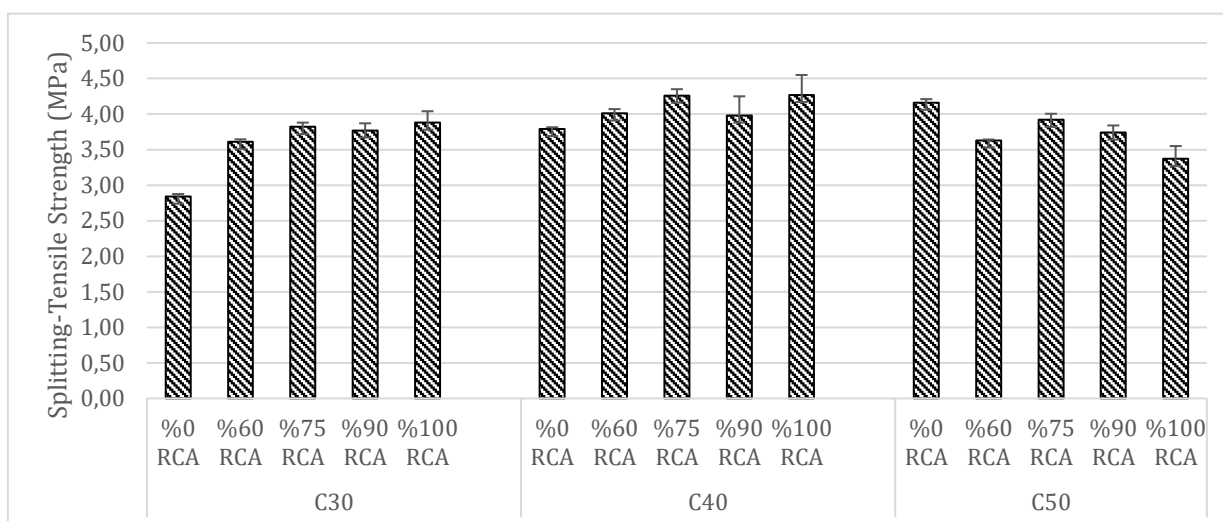


Figure 3-12 28-days splitting-tensile strength results of Portland cement-based mixtures

### 3.1.3.2 Development of Eco-hybrid cement based concrete

Within the scope of the study, mixture designs using completely Eco-hybrid cement and recycled concrete aggregates with various ratios were presented in Table 3-8. Unlike the mixtures designed in the same way as C30, C40 and C50 coded mixtures produced with Portland cement, only 60% recycled aggregate replacement ratio was not used. In addition to this, slightly higher amounts of SP were used in an effort to keep the workability of the mixtures similar.

Table 3-8 Mixture designs of the eco-hybrid cement based mixes.

Mix ID	RCA Rep. (%)	Eco-hybrid Cement	FNA	CNA	FRCA	CRCA	Water	SP	w/c
EC-1	0	310.8	751.6	1082	0	0	230	0	0.74
	75		187.9	270.5	563.7	811.5		5.83	
	90		75.16	108.2	676.44	973.8		6.66	
	100		0	0	751.6	1082		7.5	
EC-2	0	383.3	792.3	968.4	0	0	230	0	0.6
	75		198.075	242.1	594.225	726.3		5.83	
	90		79.23	96.84	713.07	871.56		7.5	
	100		0	0	792.3	968.4		8.33	
EC-3	0	425.9	670.1	1048	0	0	230	0	0.54
	75		167.525	262	502.575	786		5.83	
	90		67.01	104.8	603.09	943.2		7.5	
	100		0	0	670.1	1048		8.33	

**Note:** All units were given in kg/m<sup>3</sup>, FNA: Fine natural aggregate, CNA: Coarse natural aggregate, FRCA: Fine recycled concrete aggregate, CRCA: Coarse recycled concrete aggregate, SP: Superplasticizer

## Workability Test

In order to determine the workability of the mixtures, the slump test was carried out on all mixtures in the fresh stage. In this context, slump values of the mixtures were presented in Table 3-9. According to the results, reference samples produced with 100% natural aggregates exhibited similar slump values between 55-80 mm. The mixtures designed with 75% recycled aggregate replacement ratio were produced with 5.83 kg/m<sup>3</sup> SP and slump values of these mixtures were calculated as 50 mm, 65 mm and 180 mm, respectively. According to these results, it was seen that EC-3/75 coded mixture produced with the highest cement dosage among all mixtures showed better workability properties. In the EC-1 coded mixtures, the highest slump value was calculated as 80 mm in the 90% recycled aggregate replacement ratio although the amount of SP was gradually increased. In the EC-2 coded mixtures, the highest slump values were calculated as 170 mm and 190 mm in the 90% and 100% recycled aggregate replacement ratios, respectively. In the EC-3 coded mixtures, whereas the SP amount was gradually increased, the slump values were not increased continuously. In this context, the EC-3/100 coded mixture exhibited the lowest slump value with 35 mm. It should be also noted that due to not being desired the diverge the casting and placing standards, additional SP was not added to the mixtures in order to provide the same workability of the mixtures. Also, the effect of the workability on the compressive and splitting-tensile strength of the mixtures was discussed below.

Table 3-9 Slump values of the mixtures

EC-1	%0 RCA	%75 RCA	%90 RCA	%100 RCA
	60	50	80	55
EC-2	%0 RCA	%75 RCA	%90 RCA	%100 RCA
	55	65	170	190
EC-3	%0 RCA	%75 RCA	%90 RCA	%100 RCA
	80	180	195	35

**Note:** All units were given in mm.

## Compressive Strength Test

The 7-, 14- and 28-day compressive strength results of the mixtures produced with Eco-hybrid cement are presented in Figure 3-13, Figure 3-14 and Figure 3-15, respectively. According to the 7-days compressive strengths of the mixtures, it was seen that compressive strengths of the specimens increased with the increase of recycled aggregate replacement ratio in EC-1 coded mixtures. These results had similar trend with Portland cement-based mixtures. The compressive

strength of the EC-1/0 coded mixture was calculated as 15.7 MPa after 7-days. According to this result, a 32% decrease was observed compared to the 7-days compressive strength of the mixture produced with Portland cement-based and 100% natural aggregate designed in the previous series. This behaviour showed that Eco-hybrid cement exhibited lower performance than Portland cement as expected in concrete production. It showed that materials such as waste brick and waste concrete used in the production of Eco-hybrid cement do not show any reaction at an early age and do not contribute to the compressive strength, but are only inert in the matrix and have the filler effect. On the other hand, the increase in recycled aggregate had a very positive effect on the compressive strengths, especially in EC-2 coded mixtures. In this context, the EC-2/100 coded mixture produced with Eco-hybrid cement and 100% recycled aggregate showed a compressive strength of 35.9 MPa at the end of 7 days. While EC-3/75 and EC-3/90 coded mixtures showed the best strength performance in the mixtures produced in the EC-3 coded series, the EC3-0 and EC3-100 coded mixtures showed a slightly lower strength result. One of the reasons for this contradictory result is related to the fact that better workability had a positive effect on the compressive strength according to the slump values presented in Table 3-9. In addition, it has been observed that the recycled aggregate substitution has similar behavior with the Portland cement mixtures in the mixtures produced with Eco-hybrid cement, slightly different from the EC-3 coded series. In the EC-3 coded series, on the other hand, with the increase of recycled aggregate substitution, the compressive strength increased up to 100% recycling aggregate replacement rate.

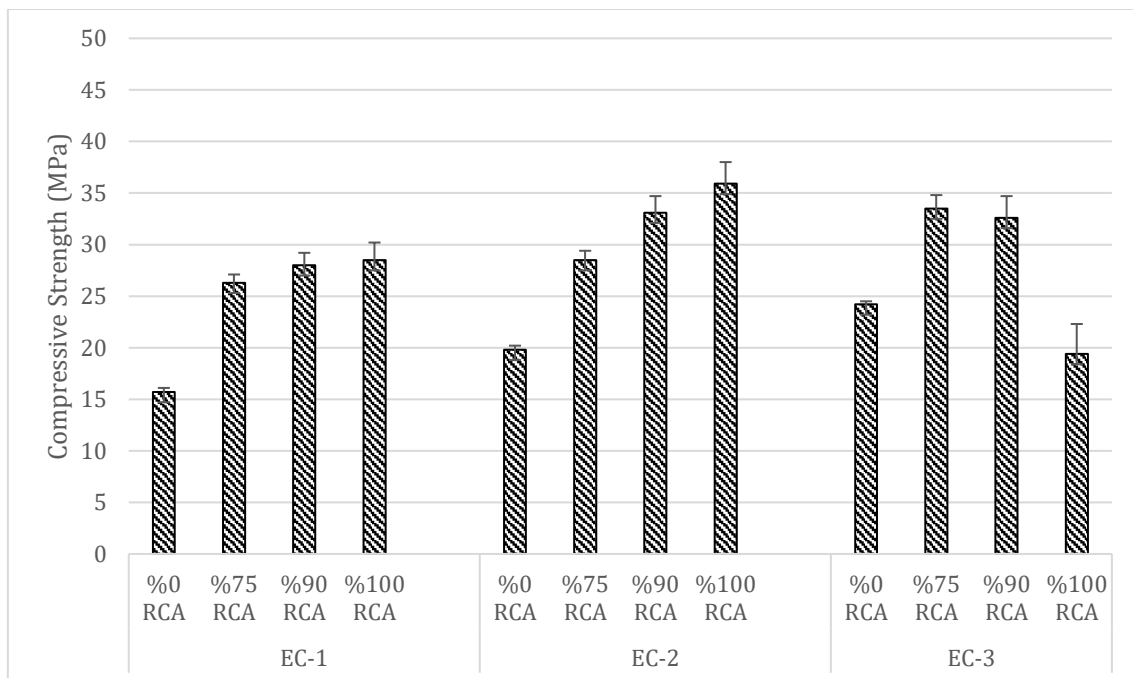


Figure 3-13 7-days compressive strength results of Eco-hybrid cement-based mixtures

The 14-days compressive strength results of the series produced with Eco-hybrid cement are presented in Figure 3-14. According to the results, the trend in the

effect of recycled aggregate substitution on compressive strengths was similar to the 7-day results. Here, the mixture coded EC-2/100 showed the highest compressive strength result with 44.05 MPa, followed by mixtures coded EC-3/90 and EC-3/75 with 40.85 MPa and 39 MPa, respectively. Another point to be mentioned here is that, unlike the Portland cement series, higher cement usage dosages are needed to obtain high compressive strength with Eco-hybrid cement. Although the EC-2/100 coded mixture exhibited the best performance in terms of compressive strength, the EC-3 code series achieved better average mechanical performance. Additionally, the increase in the compressive strengths from 7-days to 14-days was seen higher in the mixtures produced with recycled aggregate substitution.

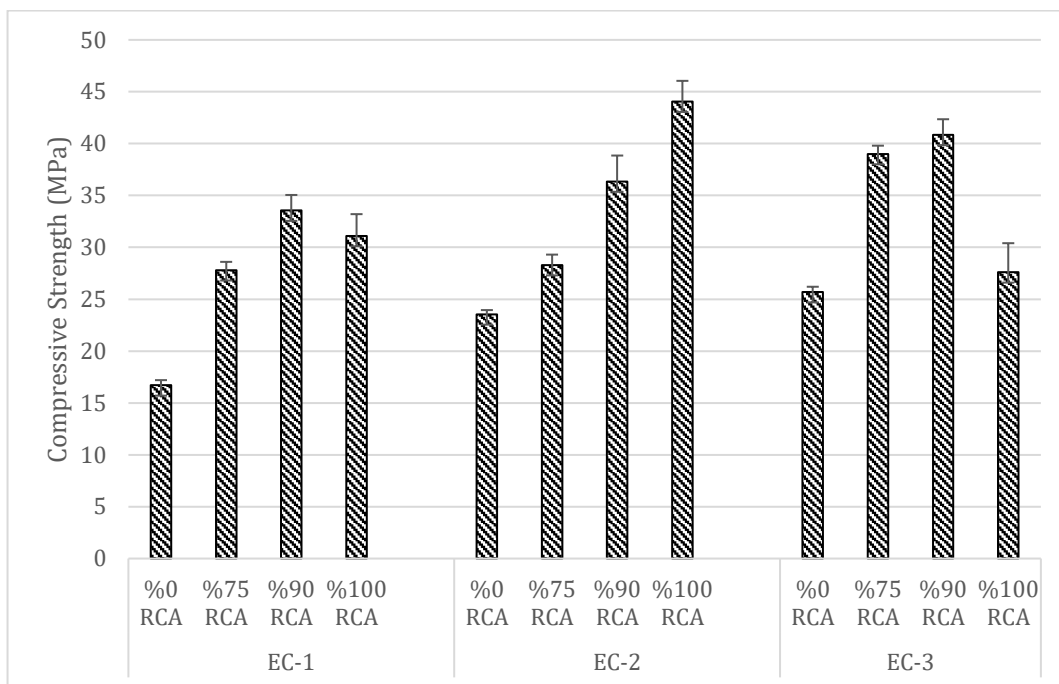


Figure 3-14 14-days compressive strength results of Eco-hybrid cement-based mixtures

According to the 28-days compressive strength results of the Eco-hybrid cement-based mixtures, the highest compressive strength result was obtained from the EC-3/75 coded mixture with 48.14 MPa. Afterward, EGC-2/90 and EGC-2/100 coded mixtures exhibited quite high compressive strength results after 28-days with 47.23 MPa and 45.70 MPa, respectively. In contrast to the reference mixtures produced with 100% natural aggregate, these mixtures exhibited similar or higher compressive strengths than the mixes produced with Portland cement. This result may be related to the fact that sufficient workability in concretes containing recycled aggregate is provided by the addition of an optimum amount of SP instead of extra water, thus minimizing the negative effect of the recycling aggregate. In addition, it is thought that aluminosilicate-based brick waste and concrete waste with high calcium content may contribute to the compressive strength by showing a pozzolanic characteristic at later ages. As a result, concrete mixtures that can reach 48 MPa compressive strength values at the end of 28 days have been successfully developed with the ECO-hybrid cement

developed within the scope of the ICEBERG project and the recycled aggregate replacement rate of up to 100%.

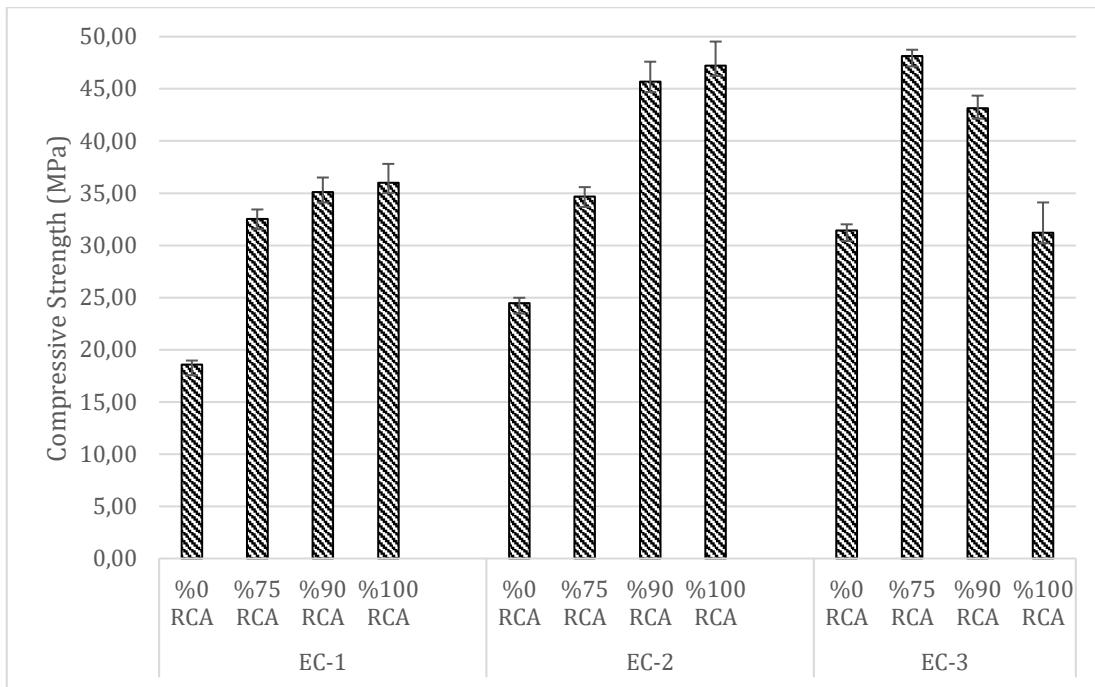


Figure 3-15 28-days compressive strength results of Eco-hybrid cement-based mixtures

### Splitting-Tensile Strength Test

Within the scope of the preliminary studies, the 7-, 14- and 28-days splitting-tensile strength results of the mixtures produced with Eco-hybrid cement were presented in Figure 3-16, Figure 3-17 and Figure 3-18, respectively. According to the 7-days splitting-tensile strength results of the mixtures, it was observed that the splitting-tensile strengths increased continuously as the recycled aggregate replacement rate increased in the EC-1 coded series. In this context, the EC-1/0 coded mixture produced with 100% natural aggregate exhibited a splitting-tensile strength result of 2.41 MPa, while the EC-1/100 coded mixture produced with 100% recycled aggregate exhibited a splitting-tensile strength result of 3.87 MPa. This behavior is due to the high volume of recycled aggregates used in mixtures with high water/binder content, as explained previously, consuming more than the water required for complete hydration, resulting in a more compact and denser matrix. On the other hand, a similar trend was observed in the EC-2 coded series, but not in the EC-3 coded series. Although all mixtures using recycled aggregate in the EC-3 coded series exhibited higher splitting-tensile strength than the reference mixture, it was observed that the increase in the recycled aggregate replacement rate decreased the splitting-tensile strength.

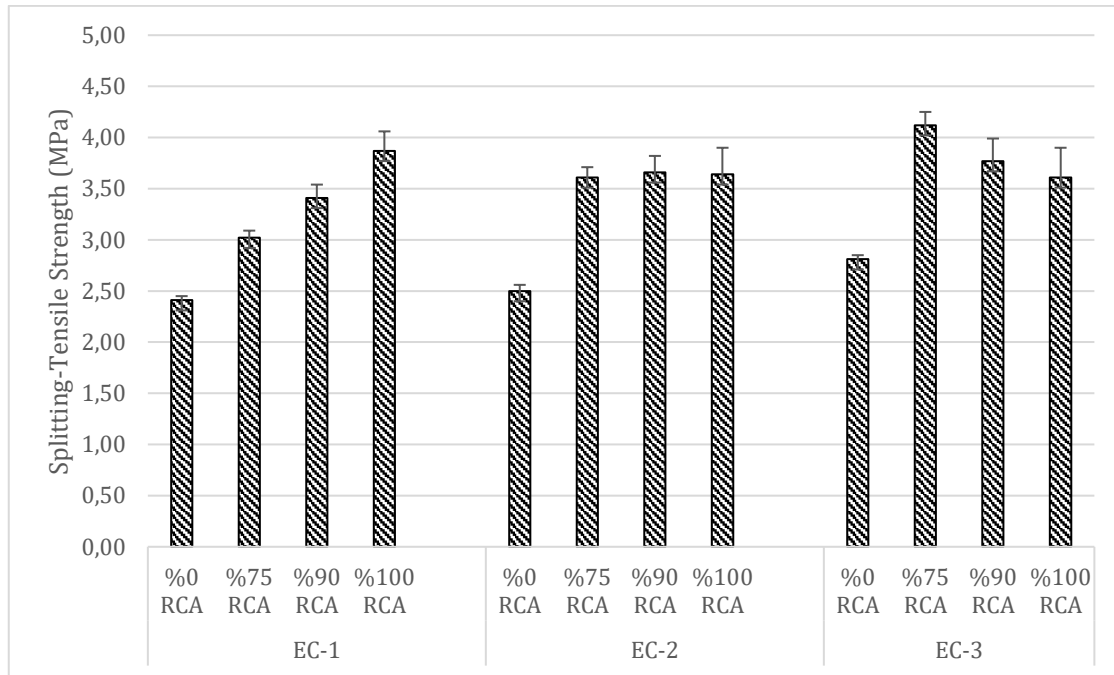


Figure 3-16 7-days splitting-tensile strength results of Eco-hybrid cement-based mixtures

Considering the 14-days splitting-tensile strength results of the series produced with Eco-hybrid cement, it was seen that the results are similar to the trend in the 7-days splitting-tensile results, as expected. In addition, at the end of 14 days, the splitting-tensile strength of the mixtures showed an average increase of around 7% compared to the 7-days results. However, this increase was observed at very low levels in some mixtures (EC-1/90, EC-2/75, EC-3/90, EC-3/100).

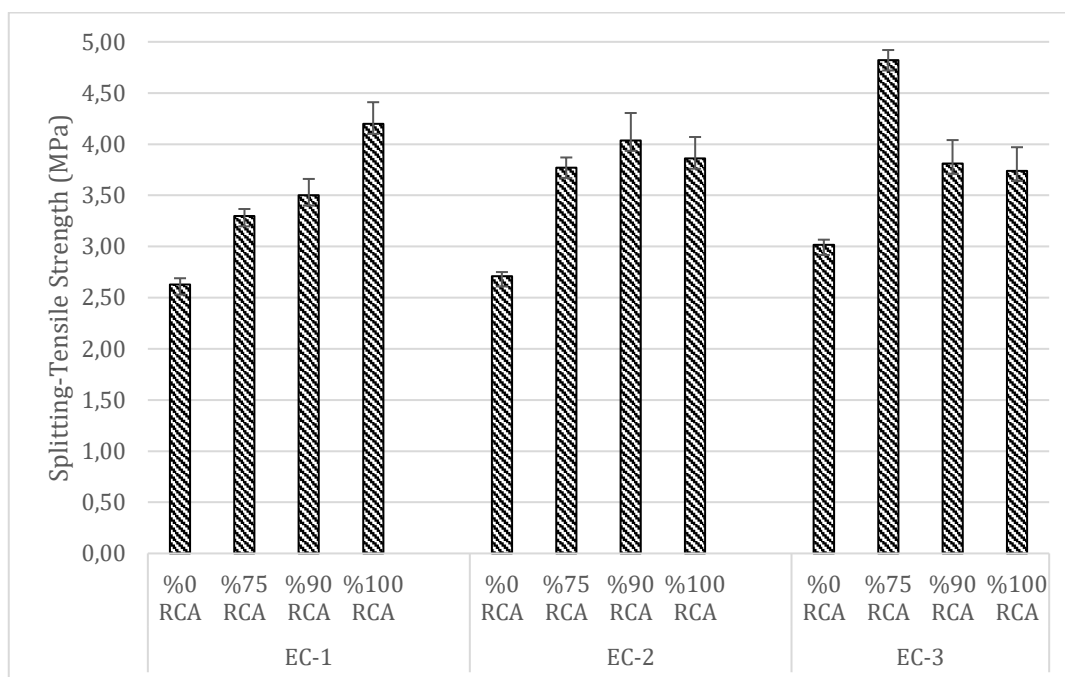


Figure 3-17 14-days splitting-tensile strength results of Eco-hybrid cement-based mixtures



Considering the 28-days splitting-tensile strength results of the series produced with Eco-hybrid cement, it was seen that the mixture with the highest splitting-tensile strength result was the EC-3/75 coded mixture with 4.89 MPa. This mixture was followed by the EC-1/100 coded mixture with a splitting-tensile strength of 4.22 MPa. As in the compressive strength results, higher splitting-tensile strength results were obtained in these mixtures produced with Eco-hybrid cement compared to the series produced with Portland cement.

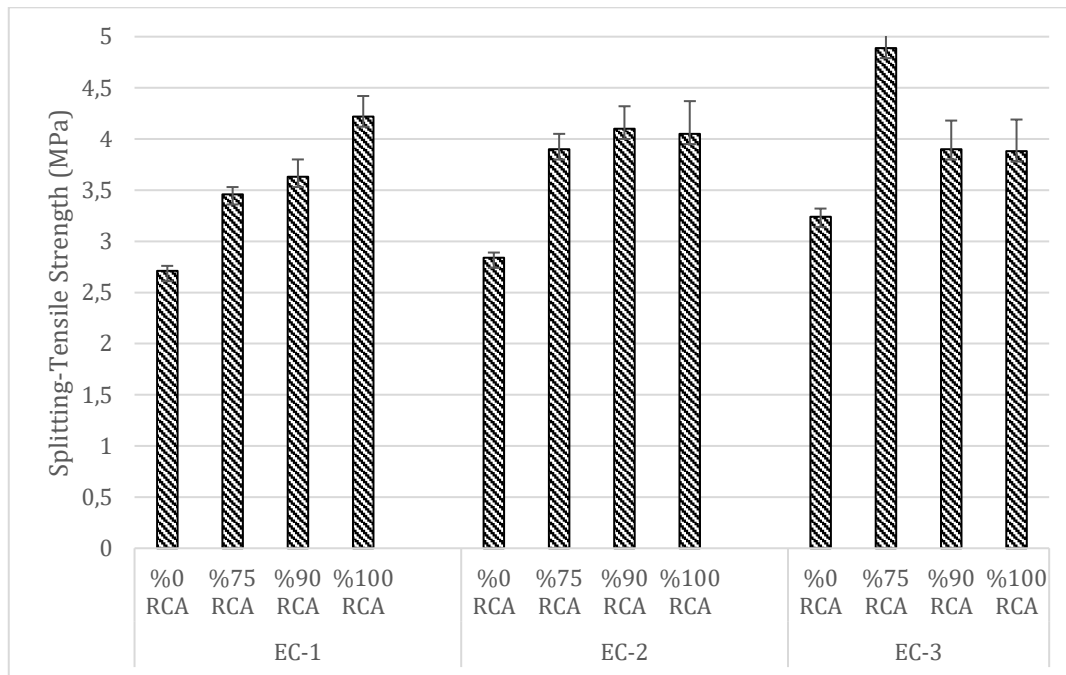


Figure 3-18 28-days splitting-tensile strength results of Eco-hybrid cement-based mixtures

### 3.1.4 Conclusion and Future Studies

The aim of this study within the scope of ICEBERG Project "TASK 3.3 Adjustment of formulations and pre-industrial prototypes of new circular green cement and concrete-based building products" was optimized concrete recipes considering regulations, requirements and needs for "TASK 4.3: Case study demonstrating circular cement-based products (CCS2)". In this study, the recycled aggregate was produced by crushing the concrete wastes collected from different demolition zones in various sizes as fine and coarse, and various properties of these aggregates were examined in the first stage. In the following stage, a study was carried out to examine the fresh and hardened properties of the concrete mixtures produced with Portland cement and Eco-hybrid cement with recycled aggregate. In this context, 3 different cement dosages and 5 different recycled aggregate replacement ratios as 0%, 60%, 75%, 90% and 100% were applied in the design of the Portland cement-based mixtures. In the Eco-hybrid cement-based mixtures, 3 different cement dosages were applied similarly, but a 60% recycled aggregate ratio was not applied differently. The workability loss caused by the

use of recycled aggregates of the mixtures was tried to be compensated by using a superplasticizer. In this context, the outcomes obtained as a result of the study can be drawn as follows:

- Within the scope of the study, an average of 7% deviation was found between both the oven-dry density and saturated surface densities of the recycling aggregates collected from different demolition zones. On the other hand, while there was a water absorption capacity variability between 5.56% and 8.65% for coarse recycled aggregates, a water absorption capacity variability of 11.39-12.35% was found for fine recycled aggregates. When the sulfate soundness results of the recycling aggregates are examined, a range of 15.76-17.45% for coarse recycling aggregates and 12.61-13.24% for fine recycling aggregates has been reached. According to the findings observed in the literature studies, it was seen that the physical properties of the recycled aggregates obtained from the construction sites were quite similar.
- In the preliminary study produced with Portland cement, the compressive strengths of C30 and C40 coded mixtures generally increased with the increase of the recycled aggregate replacement ratio, while the C50 coded mixtures decreased. According to the 28-days compressive strength results, the mixture showing the highest compressive strength was the mixture coded C40/100 with a value of 47.3 MPa.
- In the preliminary study produced with Portland cement, it was seen that the splitting-tensile strength results of the mixtures had a very similar trend with the compressive strengths of the mixtures. C40/100 coded mixture showed the highest performance with 4.27 MPa split-tensile strength at the end of 28 days.
- Although there are some deviations in the series produced with Eco-hybrid cement, it has been observed that the increase in the recycled aggregate replacement rate in the EC-1 and EC-2 series has a positive effect on the compressive strengths. EC-3/75 and EC-3/90 coded mixtures exhibited the highest compressive strength in the EC-3 coded series. At the end of 28 days, the mixture with the code EC-3/75 showed the highest compressive strength result with 48.14 MPa.
- The splitting-tensile strength of the Eco-hybrid cement-based mixtures generally increased as the recycled aggregate substitution increased. After 28 days of curing, the EC-3/75 coded mixture exhibited the highest performance with a splitting-tensile strength of 4.89 MPa.

In future studies, with the final development of Eco-hybrid cement, the studies for the development of the final concrete recipes will continue with the results of optimum workability/recycled aggregate replacement ratio/compressive and splitting-tensile strength obtained as a result of this study. In addition, it is planned to perform various chemical and durability tests on concrete mixtures that exhibit the best mechanical performance.

### 3.1.5 References

- Buck, A. D. (1976). Recycled concrete as a source of aggregate.
- Chen H-J, Yen T, Chen K-H (2003) Use of building rubbles as recycled aggregates. *Cem Concr Res* 33(1):125–132
- Chen ZP, Huang KW, Zhang XG, Xue JY (2010) Experimental research on the flexural strength of nrecycled coarse aggregate concrete, International conference on mechanic automation and control engineering (MACE) 2010, Wuhan, PR China, pp 1041–1043
- Chen, Z.-p., et al. (2010). Experimental research on the flexural strength of recycled coarse aggregate concrete. 2010 international conference on mechanic automation and control engineering, IEEE.
- De Brito, J., & Saikia, N. (2012). *Recycled aggregate in concrete: use of industrial, construction and demolition waste*. Springer Science & Business Media.
- De Juan MS (2004) Study on the use of recycled aggregates in structural concrete production (in Spanish), PhD thesis, Polytechnic University of Madrid, Madrid
- De Juan, M. S. and P. A. Gutiérrez (2009). "Study on the influence of attached mortar content on the properties of recycled concrete aggregate." *Construction and building materials* 23(2): 872-877.
- Etxeberria M, Mari A, Vázquez E (2007a) Recycled aggregate concrete as structural material. *Mater Struct* 40(5):529–541
- Etxeberria, M., et al. (2007). "Recycled aggregate concrete as structural material." *Materials and structures* 40(5): 529-541.
- Evangelista L, de Brito J (2007). Mechanical behaviour of concrete made with fine recycled concrete aggregates. *Cem Concr Compos* 29(5):397–401.
- Gomez-Soberon JMV (2002) Porosity of recycled concrete with substitution of recycled concrete aggregate: an experimental study. *Cem Concr Res* 32(8):1301–1311.
- Gonzalez-Fonteboá, B., Martínez-Abella, F., Eiras-Lopez, J., & Seara-Paz, S. (2011). Effect of recycled coarse aggregate on damage of recycled concrete. *Materials and structures*, 44(10), 1759-1771.
- Hansen, T. C. (Ed.). (1992). *Recycling of demolished concrete and masonry*. CRC Press.
- Hansen, T. C. and H. Narud (1983). "Strength of recycled concrete made from crushed concrete coarse aggregate." *Concrete international* 5(1): 79-83.

Katz A (2003) Properties of concrete made with recycled aggregate from partially hydrated old concrete. *Cem Concr Res* 33(5):703–711

Khan, A. (1984). "Recycled concrete—a source for new aggregate." *Cement, concrete and aggregates* 6(1): 17-27.

Kou S, Poon C (2008) Mechanical properties of 5-year-old concrete prepared with recycled aggregates obtained from three different sources. *Mag Concr Res* 61(1):57–64

Kou S, Poon C, Etxeberria M, (2011a) Influence of recycled aggregate on the long term mechanical properties and pore size distribution of concrete, *Cement Concr Compos* 33(2):286–291

Kwan, W. H., et al. (2012). "Influence of the amount of recycled coarse aggregate in concrete design and durability properties." *Construction and building materials* 26(1): 565-573.

Li J, Xiao H, Zhou Y (2009) Influence of coating recycled aggregate surface with pozzolanic powder on properties of recycled aggregate concrete. *Constr Build Mater* 23(3):1287–1291

Limbachiya M, Meddah MS, Ouchagour Y (2012) Use of recycled concrete aggregate in fly-ash concrete. *Constr Build Mater* 27(1):439–449

Limbachiya MC, Koulouris A, Roberts JJ, Fried AN (2004) Properties of recycled aggregate concrete, in RILEM international symposium on environment-conscious materials and systems for sustainable development, RILEM publication SARL, pp 127–136.

Lin Y-H, Tyan Y–Y, Chang T-P, Chang C-Y (2004) An assessment of optimal mixture for concrete made with recycled concrete aggregates. *Cem Concr Res* 34(8):1373–1380

Mehta and Monteiro. (1993) *Concrete Structure, Properties, and Materials*, Prentice-Hall, Inc., Englewood Cliffs, NJ

Mukai, T., Kikuchi, M., & Koizumi, H. (1978). Fundamental study on bond properties between recycled aggregate concrete and steel bars. *Cement Association of Japan*, 32.

Nagataki, S., et al. (2004). "Assessment of recycling process induced damage sensitivity of recycled concrete aggregates." *Cement and concrete research* 34(6): 965-971.

Oliveira MB, Vázquez E (1996) The influence of retained moisture in aggregates from recycling on the properties of new hardened concrete. *Waste Manage (Oxf)* 16(1–3):113–117

Padmini, A.K.; Ramamurthy, K.; Mathews, M.S. (2009) Influence of parent concrete on the properties of recycled aggregate concrete. *Constr. Build. Mater.*, 23 [2], 829–836. <http://dx.doi.org/10.1016/j.conbuildmat.2008.03.006>

Poon, C. S., Shui, Z. H., Lam, L., Fok, H., & Kou, S. C. (2004). Influence of moisture states of natural and recycled aggregates on the slump and compressive strength of concrete. *Cement and concrete research*, 34(1), 31-36.

Rao CM, Bhattacharyya SK, Barai SV (2011) Influence of field recycled aggregate on properties of concrete. *Mater Struct* 44(1):205–220

Safiuddin M, Alengaram UJ, Salam MA, Jumaat MZ, Jaafar FF, Saad HB (2011) Properties of high-workability concrete with recycled concrete aggregate. *Mater Res* 14(2):248–255

Safiuddina, M., et al. (2011). "Properties of High-Workability Concrete with Recycled Concrete Aggregate." *Materials Research* 14(2): 248-255.

Santos, J., et al. (2002). Use of coarse recycled concrete aggregates in the production of new concrete. *Structures*.

Topcu, I. B. (1997). "Physical and mechanical properties of concretes produced with waste concrete." *Cement and concrete research* 27(12): 1817-1823.

Topcu, I. B. and S. Şengel (2004). "Properties of concretes produced with waste concrete aggregate." *Cement and concrete research* 34(8): 1307-1312.

Yang J, Du Q, Bao Y (2011) Concrete with recycled concrete aggregate and crushed clay bricks. *Constr Build Mater* 25(4):1935–1945

Yong PC, Teo DCL (2009) Utilization of recycled aggregate as coarse aggregate in concrete. *UNIMAS E-J Civil Eng* 1(1):1–6

Zaharieva R, Buyle-Bodin F, Skoczylas F, Wirquin E (2003) Assessment of the surface permeation properties of recycled aggregate concrete. *Cem Concr Compos* 25(2):223–232.

Zaharieva, R., et al. (2003). "Assessment of the surface permeation properties of recycled aggregate concrete." *Cement and Concrete Composites* 25(2): 223-232.

Rao CM, Bhattacharyya SK, Barai SV (2011) Influence of field recycled aggregate on properties of concrete. *Mater Struct* 44(1):205–220

Gonzalez-Fontboa B, Martinez-Abella F (2005) Recycled aggregates concrete: aggregates and mix properties. *Materiales de Construcción* 55(279):53–6

Kou S, Poon C (2006) Compressive strength, pore size distribution and chloride-ion penetration of recycled aggregate concrete incorporating class-F fly ash. *J Wuhan Univ Technol Mater Sci Edition* 21(4):130–136

De Brito, J., & Saikia, N. (2012). *Recycled aggregate in concrete: use of industrial, construction and demolition waste*. Springer Science & Business Media.

Kou S, Poon C (2008) Mechanical properties of 5-year-old concrete prepared with recycled aggregates obtained from three different sources. *Mag Concr Res* 61(1):57–64

## 3.2 Concrete building elements and their connections

### Abstract

In the current practice, at the end of life of a reinforced concrete structure, it is destructively demolished, and the demolition waste is landfilled or recycled. This approach is clearly wasteful of energy, creating serious environmental pollution and at high cost. However, design for demountability/deconstruction (DfD) of reinforced concrete structures would facilitate the future reuse of structural elements at the end of their life, potentially achieving a significant reduction in embodied energy of structures as well as giving the clients the benefit of retaining the value of their assets. The main focus was on connections that should be designed in such a way to allow demounting. The main achievements are outlined, for each type of dry and semi dry connections, along with the aspects that still need to be developed. It is concluded that only semi-dry connections are currently implemented but information available in the literature on dry connections between structural elements is still very scarce of DfD in concrete construction.

### 3.2.1 Introduction

The construction sector remains nowadays as one of the main contributors to the worldwide carbon and heavy metal gas emissions, and consequently greenhouse gas pollution [1]. The emissions are mainly caused by the extraction and production of materials, especially Portland cement, accounting for 5 to 8% of total human-driven CO<sub>2</sub> emissions [2, 3] (i.e. 1000 to 1200 kg of CO<sub>2</sub> are emitted due to the fabrication of every 1000 kg of Portland cement [4]). There is also a very significant environmental impact related to the construction waste storage and treatment in landfills. An impact reflected in air pollution (due to the dust released [5]), water contamination (due to natural radioactive and toxic elements present [6]) and a detrimental effect on the local ecosystems [7]. Construction waste represents about half of overall landfill volumes [8] of which cement-based materials like concrete represent about one quarter [9].

The substantial impact of the construction sector in public health and ecology represents a major challenge, so new solutions can be developed towards "green construction" [10]. In terms of structural engineering, the current challenges mainly rely on two themes: 1 – the incorporation of waste products in materials, so a full recycled production can be achieved [11]; and 2 – the conception of structural configurations in which the structural elements (beams, slabs, columns and foundations) can be disassembled and reused in new structures [12]. The



accomplishment of these objectives would dramatically reduce the amount of natural (raw) resources extracted, the need to produce new materials and the accumulation of waste in landfills [13].

Traditionally, steel is the material more suitable to fulfil the demand for more sustainable construction with less ecological impact. However, the use of structural steel frequently turns out to be less economical, due its more complex production requiring intensive energy and less availability compared to concrete [14]. Consequently, research has started to be carried out more intensively in the last decade on topics such as concrete recycling [15-17] and concrete structural design for deconstruction and material reuse [18-20]. Along research, common practice in structural engineering already applies recycled raw materials in concrete production [21] and semi-dry connections between reinforced concrete structural elements [22]. These advances are not only motivated by an increased environmental awareness in society, which tends to be reflected in legislation and public funding, but also by the speed and economic benefits (value of the assets is retained for longer time) compared to new construction [23].

The question of how best to join the many parts of a structure is probably as old as building construction itself. Clearly, the principal role of any structural connection is to transfer forces safely between various components meeting at that joint. Therefore in the design of connections a clear understanding of load paths, i.e. the mechanism by which various components of the joint itself transfer loads through the connection, is essential. On the other hand, connections in DfD need also to be designed in such a way to allow demounting of structural elements undamaged, permitting their reuse in other structures.

In semi-dry connections, small portions of cast-in-place concrete are used to connect precast elements. Therefore, conditions for structural disassembly and reutilization are more favourable compared to pure wet connections, in which reutilization is not possible. Although semi-dry connections represent a step forward towards sustainability in construction, the path clearly leads to the achievement and implementation of totally dry connections [22]. In dry connections, the precast structural elements are directly connected to each other and no cast-in-place concrete is used. Consequently, reutilization can be easily carried out at the end of the structure's life, without a need for wasting or even recycling, potentially achieving more than 50% reduction in embodied energy of structures.

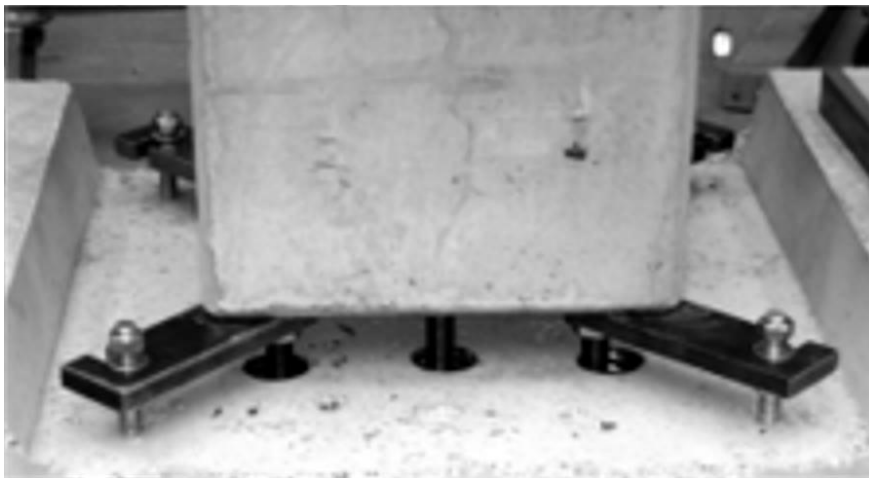
Few investigations have focused on demountable composite steel-concrete constructions using various types of bolted shear studs, rather than welded, allowing the reuse of the steel beams. However, this technique would not currently permit the reuse of concrete slabs that are generally demolished. Various bolts, including friction-grip bolts [24], threaded bolts tightened by exterior nuts [25] and exterior nut-tightened threaded bolts with single embedded nuts [26], have been studied with different degrees of success in achieving the shear transfer forces between the concrete slab and steel beams. However, the demountable shear connectors are rarely used in composite construction in practice due to the lack of detailed design rules concerning their behaviour.



### 3.2.2 Current Practice In Structural Engineering

Currently, at the end of life of a structure, although all the steel and concrete materials remain serviceable, the structure is demolished destructively, large steel elements are recycled by energy-intensive melting [27], and the rest of materials are rather landfilled or recycled. This approach is clearly wasteful of energy, creating serious emissions and potentially costly. To drastically reduce such waste as well as reducing the embodied energy of structures, it should become the norm that structures be designed and constructed for reuse after service. However, that goal is still to be achieved in the case of RC structures, that generally dominate the construction market worldwide [14]. The lack of knowledge on the structural behaviour of easily demountable (dry) connections between RC elements [22], including safety and structural strength, is still limiting its practical application.

Therefore, current practice of demountable structures relies mainly on reinforced precast concrete structures with semi-dry connections between structural elements. Deconstruction of RC structures with semi-dry connections, although feasible, is not an easy procedure. Parts of cast-in-place concrete or injected grout need to be mechanically destroyed and removed as well as cutting of steel reinforcement. Then, reconstruction follows the inverse path: parts of cast-in-place concrete need to be added and some reinforcing bars welded. Since the application of these semi-dry connections in new Civil engineering constructions is still not distant in time [22], most of the structures containing semi-dry concrete connections are still within their service life cycle. However, deconstruction/reconstruction has not been practiced so far. Nowadays, there are mainly two types of semi-dry connections in RC structures: 1 – dowel shear connections; and 2 – moment-resisting connections with continuity bars.



(a)



(b)

Figure 3-19 Dowel connection between a column and the foundation of a reinforced precast concrete structure: (a) before the grout injection; and (b) after the grout injection. Reprinted from Metelli *et al.* [26].

### 3.2.2.1 Dowel shear connections

Dowel shear connections are the most commonly used semi-dry connection between precast RC elements [28]. Thus, recent research carried out on concrete semi-dry connections does not usually address dowel shear connections. In this type of connections, typically, the precast concrete elements contain pre-drilled holes that are crossed by a bolt. The connection is filled and established when grout is injected in the remaining clearance in the holes. Another way to establish a dowel connection is depicted in Figure 3-19, from the work of Metelli *et al.* [29], showing the case of a dowel connection between a column and the foundation of a precast RC structure. As can be seen, continuity reinforcement extends beyond the end of the column and enters the pre-drilled holes in the foundation (Figure 3-19(a)). The connection is later established when grout is injected, in order to fill the remaining clearance in the holes and the gap between the column and the foundation as depicted in Figure 3-19(b).

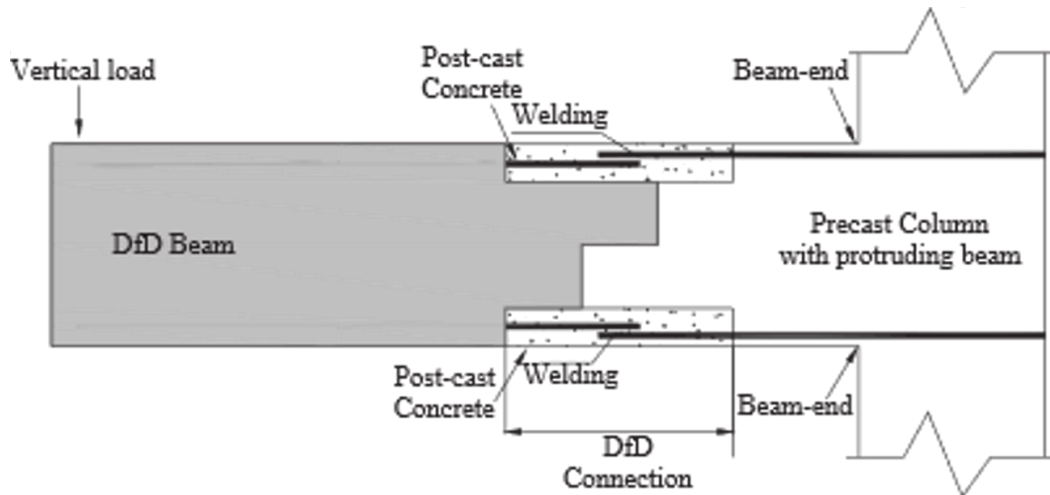


Figure 3-20 Moment-resisting semi-dry connection, with welded continuity reinforcement, between a beam and a column of a precast reinforced concrete structure. Reprinted from Xiao et al. [27].

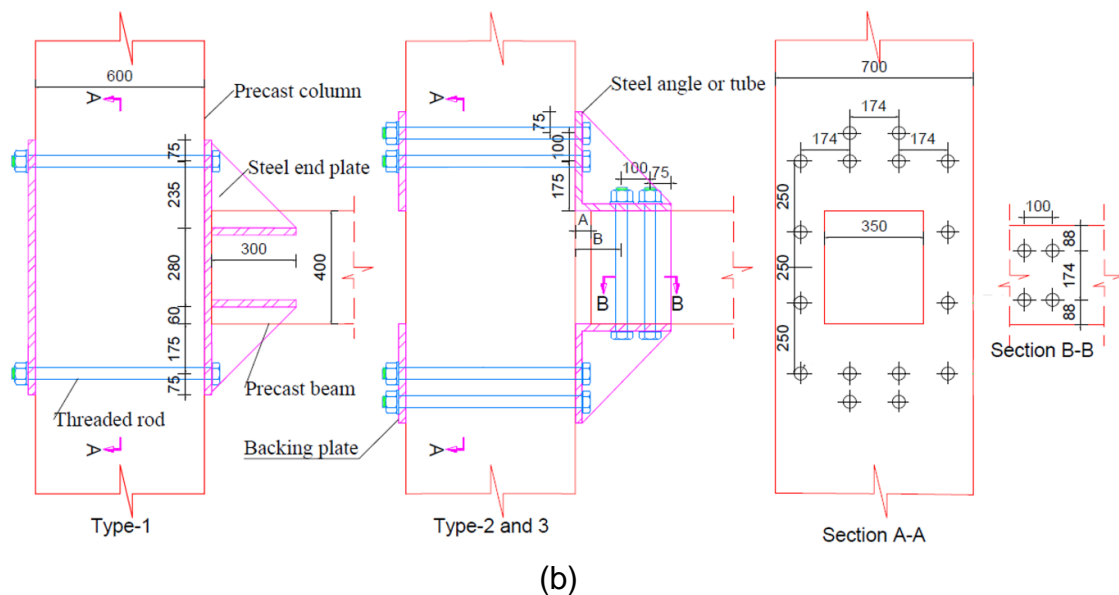
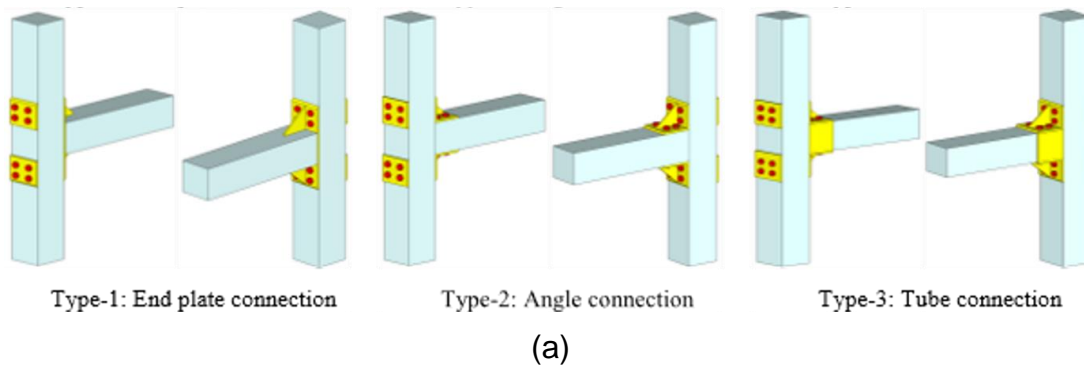


Figure 3-21 Three types of concrete beam/column dry connections with pretensioned threaded bolts and a steel end plate: (a) outlook; and (b) detailed view. Reprinted from Aninthaneni et al. [29].

### 3.2.2.2 Moment-resisting connections with continuity bars

In beam/beam or beam/column connections, flexural stress needs to be transferred between the structural elements connected. Therefore, in these cases, dowel shear connections are not feasible, and a different moment-resisting connection solution is implemented. The most typical configuration can be seen in Figure 3-20, taken from the study published by Xiao *et al.* [30], where continuity reinforcement extending beyond the top and bottom ends of the elements (beam and column) is welded. The connection is then established when cast-in-place concrete is added in order to cover the top and bottom welded reinforcement. In turn, shear is transferred through a shear key created by the fitting of the beam and column ends.

### 3.2.3 Demountable Dry Connections

Research performed on demountable dry connections in RC structures is still scarce and recent. The idea of demountable concrete structures was initially introduced by Reinhardt [31] in 1976 and a few systems were developed in the construction sector. However, their use and application were very limited due to the lack of knowledge and physical testing of such systems. The key to success of reusable structural components is to make the structural system easily demountable at the end of life. Only a few connection solutions were tested, and even fewer were subjected to finite element analysis and parametric studies. Consequently, a more precise understanding of the strength mechanisms involved in this type of connections, their structural behaviour and capacity, is still limited. Due to that fact, there is an absence of safe and optimized design recommendations in the norms, so structural engineers can opt for demountable RC dry connections in their practices.

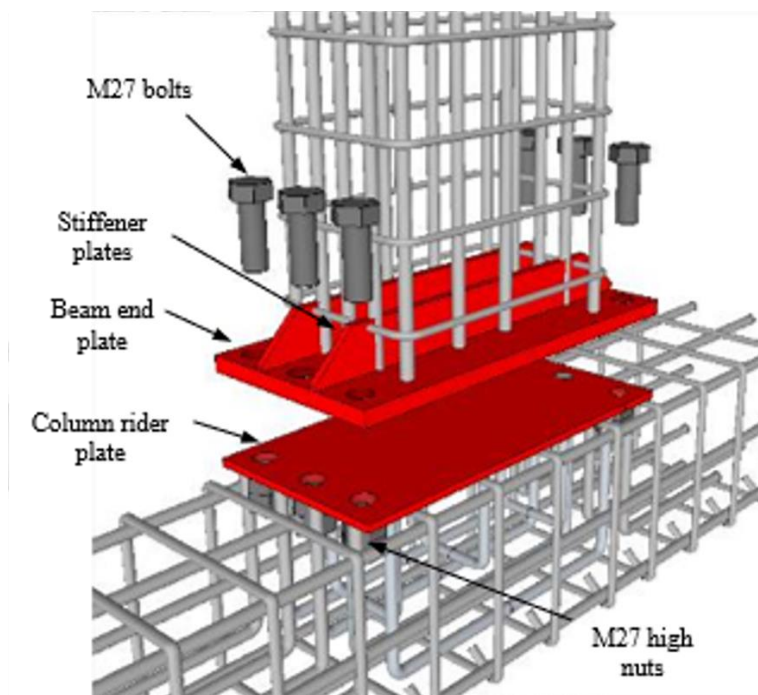
In this section, the research carried out on RC dry connections is detailed and discussed. Since the design of such connections depends on the elements being connected, the structure of the section is organized and divided in each type of connection studied so far in the literature.

#### 3.2.3.1 Beam/column connections

Due to the type of stresses transferred, bending and shear, beam/column connections are normally the most challenging to materialize and problematic type of connections in precast RC structures [32]. In 2016, Aninthaneni *et al.* [34, 33] proposed three non-prestressed solutions (see Figure 3-21) for a dry connection between a beam and a column of a precast RC structure, which incorporates threaded pre-tensioned bolts and a steel end plate. In turn, the beam and column have embedded threaded rods to accommodate the bolts. The main feature of these 3 connections is in the connecting element that is a steel end plate embedded in the beam in Type-1 connection (end plate connection), an

angle plate in Type-2 (angle connection) and the steel end angle plate encases the beam in Type-3 (tube connection). The connection types, along with a monolithic connection, were subjected to the same seismic action to assess their behaviour. Furthermore, four types of fill material for the gaps in the beam/column contact zone were examined: natural rubber sheets, grout, a dental plaster and epoxy resin. The use of a fill material in these connections assures that the pretension load applied in the bolts has a more uniform distribution.

The results obtained showed a similar behaviour for Type-1 connection compared to the monolithic connection. The location of the plastic hinge occurred away from the beam end and in front of the steel end plate, showing that the connection segment was stronger than the beam capacity itself. However, Type-2 and Type-3 exhibited less stiffness and strength compared with the control specimen as well as Type-1. Compared to Type-2 and Type-3, Type-1 connection has the beam's main reinforcement welded to the steel end plate and, consequently, the tensile force in the reinforcement was easily transmitted via the connection.



(a)



(b)

Figure 3-22 Concrete beam/column dry connection with embedded steel plates and threaded bolts: (a) view of the disassembled form; and (b) view of the assembled form. Reprinted from Pul and Şentürk et al. [30].

While the maximum lateral load of Type-1 connection varied between 175 kN and 185 kN, for a lateral drift of approximately 4%, the maximum lateral load of Type-2 connection varied between 110 and 155 kN, for a lateral drift of approximately 2%. In Type-2 connection, tensile force in the beam's main reinforcement is transferred to the steel end plate through the surrounding concrete and the bolts (strut and tie mechanism), which is a more sinuous path compared to the Type-1 stress transfer, highlighting the causes of strength and ductility reduction, and the severe cracks observed in the connection area during the tests of Type-2 connection. In turn, Type-3 connection behaviour was similar to Type-2, with strength varying from 110 kN to 140 kN for a lateral drift of approximately 2%. It was concluded therefore that the steel plate encasement does not largely influence the connection strength and ductility. Type-2 and Type-3 connections also revealed a structural behaviour more dependent on the fill material used. In this context, the rubber sheets and the epoxy resin caused premature slip in the connection, and thus their application as fill material is not recommended.



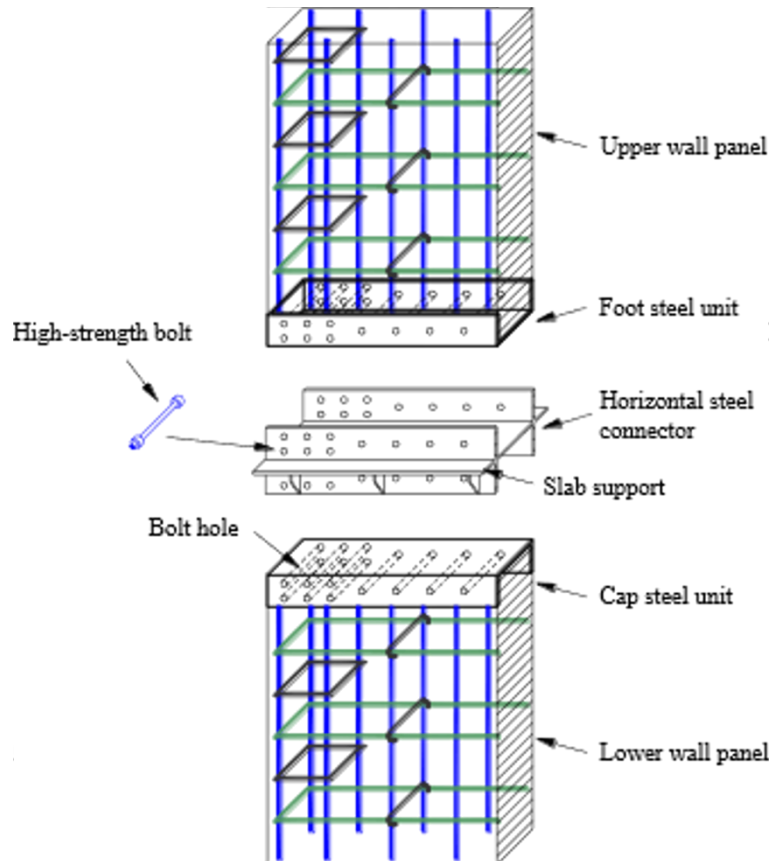


Figure 3-23 Concrete wall/wall dry connection with a horizontal steel connector and high-strength bolts. Reprinted from Sun *et al.* [31].

Although the results obtained for Type-1 connection were very encouraging, there are still few aspects about the experimental tests of Aninthaneni *et al.* [33, 34] that are relevant and deserve to be addressed, namely:

- different behaviour could have been observed if a less stiff column (0.70 x 0.60 m<sup>2</sup> in this study) had been considered compared to the beam (0.40 x 0.35 m<sup>2</sup>). Since no steel plate is embedded in the column as it is in the beam, a less stiff column would not be so capable to anchor the steel end plate, and cracking could appear in the concrete surrounding the bolts in the column. Similarly to what was depicted in the beams of Type-2 connection;
- only the pre-tensioned bolts provide shear strength to these connections. This substantially increases stress concentration in the bolts and tensile stresses in the column. Consequently, it can cause an increase in the number of bolts embedded in the column or an increase in the column dimensions. Thus, it would be interesting to study the introduction of a shear key in the column and assess its effect on the shear transfer in the connection; and
- development of a finite element model to Type-1 connection so a better understanding of the strength mechanisms involved, and the structural behaviour of the connection, could be achieved. A finite element model

calibrated to the experimental results could be used to perform parametric analyses of the connection and optimize it (i.e. through the design of smaller ribs in the main ribs of the steel plates to enhance steel/concrete stress transfer).

More recently, Pul and Şentürk [35] studied a beam/column precast dry connection, in which embedded steel plates are used along with threaded bolts. As can be seen in Figure 3-22(a), the steel plate embedded in the beam (end plate) is welded to the beam's main reinforcement and the steel plate embedded in the column (ride plate) is welded to the column's stirrups. Also welded to the column's ride plate are high nuts that act as steel threaded ducts to accommodate the bolts and establish the connection (see Figure 3-22 (b)). The connection was subjected to flexural and shear stresses in experimental tests and the results showed a very satisfactory structural behaviour, similar to the monolithic connection, also tested in the same experimental campaign. For example, the bearing capacity of bolted specimen was approximately 20% higher than the capacity of monolithic one. Furthermore, the shear and moment capacity of bolted joint has increased.

Compared with Type-1 connection studied by Aninthaneni *et al.* [33, 34], which also achieved a very good performance, one of the differences is that the connection of Pul and Şentürk [35] does not have pretension applied to the bolts. However, this fact does not seem to compromise shear transfer, since the bolts are connected to the ride plate embedded in the column, instead of being anchored directly to the column's concrete as they are in the Aninthaneni *et al.* [33, 34] solution. Besides these two aspects, apparently self-balanced in terms of structural behaviour, the connections are designed in a similar way and both achieved good results.

Table 3-10 Summary of the achievements and aspects that need further development in precast concrete dry connections.

Connection type	Achievements	Further developments
beam/column	<ul style="list-style-type: none"> <li>• a non-prestressed solution was achieved with a similar behaviour compared to the monolithic connection</li> <li>• prestress can be replaced by bolts and embedded steel plates with very good results</li> <li>• behaviour of prestressed solutions was close to the monolithic connection</li> </ul>	<ul style="list-style-type: none"> <li>• optimization of the solutions proposed through nonlinear finite element modelling and parametric analyses</li> <li>• inclusion of a shear key in the connection to prevent slip more effectively</li> <li>• definition of design recommendations</li> </ul>
wall/wall and wall/foundation	<ul style="list-style-type: none"> <li>• a solution was achieved where failure occurred away from the connection zone, with a good performance in terms of ductility</li> <li>• a finite element model was implemented to assess and verify the structural behaviour</li> </ul>	<ul style="list-style-type: none"> <li>• there is still a significant margin for optimization of the connection through parametric analyses</li> <li>• the definition of design recommendations</li> </ul>
beam/beam, column/column, beam/slab, slab/slab and column/foundation	<ul style="list-style-type: none"> <li>• no research could be found on these connections</li> </ul>	

### 3.2.3.2 Wall/wall and wall/foundation connections

Connections between precast wall panels or columns are mainly subjected to compression stresses, easily transferred between the elements without the need of any physical joinery. Consequently, the compression in the connection mobilizes friction and shear stress transfer is also facilitated. For these reasons, the design of wall/wall or column/column connections is not so challenging and complex as the design of beam/column connections. However, most connections between walls or columns still have flexural stress, implying that mechanical joinery is needed.

In this regard, a concrete wall/wall connection proposed by Sun *et al.* [36] in 2016 is illustrated in Figure 3-23, where a robust H-shaped steel connector is used

along with high-strength pre-tensioned bolts and top (foot) and bottom (cap) steel units. The H-shape is especially effective in providing buckling resistance to the steel connector, which embraces both sides of the wall. In turn, the pretension in the high-strength bolts mobilized shear strength by friction on the contact surface between the concrete walls and the steel connector. The top and bottom steel units contain steel ducts to accommodate the bolts and have the walls' main reinforcement welded. The units are placed during casting of the walls and act as confinement for the concrete in the connection zone, along with the stress provided by the pretension in the bolts.

The connection was subjected to a monotonic horizontal load in experimental tests [36], and a very satisfactory behaviour was observed. Failure occurred in the walls away from the connection zone, with a good performance in terms of ductility (with the ultimate measured displacement being 4 to 6 times of the yield displacement). A finite element model was also developed to verify and confirm the load transfer mechanism, failure modes and integrity of the connection. Slippage of the connection due to the surpassing of the shear friction strength was identified both experimentally and numerically for approximately 40% of the maximum load sustained by the connection. After slippage, the shear strength of the bolts, bearing capacity of the steel parts and concrete compressive strength were the main mechanisms responsible for the connection capacity. Although an advanced (nonlinear) finite element model was conceived and materialized to analyse the connection, the realization of parametric studies was left for further developments. It was concluded that there is still a significant margin for optimization of the connection configuration and dimensions, particularly the steel H-shaped connector.

Besides proposing a solution for a dry connection between wall precast elements, Sun *et al.* [36] also developed a similar solution for a dry connection between a wall and a foundation. The solution is similar to the one depicted in Figure 3-23, in which the bottom steel unit encases the short wall and is embedded on the foundation with ribs to enhance the anchoring bond between the steel and concrete. Cai *et al.* [37] have also conducted a preliminary study on demountable connections consisting of steel bolts and a steel plates for prefabricated shear walls in low-rise buildings, consisting of three reinforced concrete blocks. The number of steel bolts, the tightening process of the bolts and concrete compressive strength exhibited a significant effect on the overall performance and capacity of the connections. The investigation also identified possible failure modes of the steel bolted joints, including concrete crushing, shearing and tensile fracture of steel bolts, pull-out of steel bolts as well as fracture of steel plates.

### 3.2.4 Further Proposed Developments of Demountable Dry Connections

In the previous section, all concrete dry connections proposed in the literature were detailed and analysed. Moreover, the results obtained in each study were reviewed, through the outline and discussion of the main achievements along with the aspects that need further development as summarized in Table 3.10. The test specimens include a total of 11 reinforced concrete simply supported slabs. All slabs have the same total length of 5200 mm, span between supports = 5000mm, height = 160 mm and width = 500 mm.

The materials used are geopolymer (Cemfree) concrete having a compressive strength of 35 MPa and stainless steel reinforcing bars (1.4362) with a minimum yield tensile strength of 500 MPa. In turn, the steel block and plates correspond to a normal structural steel S355 JR, and the bolts and nuts to normal steel class 10.9.

2 of the 11 slabs are fully monolithically cast in one piece and considered as reference specimens. The other 9 slabs are composed of 2 segments and have a demountable connection at mid span. The demountable connection is materialized mainly using bolts and steel plates as explained below.

4 types of demountable connections are assessed, differing on the existence of a key to enhance strength or the inclusion of a steel block to improve the stress transfer in the connection. Moreover, for each type of connection, the number and diameter of bolts differ.

The slabs will be cast in two phases (6 + 5 specimens). The following table briefly details the properties of each slab.

Table 3-11, where, for all types of connections, important targets remain unachieved, in the path to make structural engineers apply these solutions in current practice.

While, in some cases, no configuration for the connection has been proposed, in other cases, a solution has been developed but still contains significant margin for improvement, including relevant changes in the configuration of the connection to transfer the stresses more effectively, experimental tests to be carried out, finite element modelling to be implemented or parametric analyses to be made. This section will focus on the first part, that is the configuration and conception of dry connections, since it represents the basis on which more advanced studies would be required. Table 3.11 presents new configurations and proposed further developments for concrete dry connections between various structural elements. In this context, configurations proposed by the authors of the

present paper (Figure 3-24 to Figure 3-29) will be illustrated and described. Besides the necessary validation by further experimental and numerical studies, it is also relevant to mention that the success of these connections in practice depends significantly on geometric and quality control during the manufacturing phase of the precast elements. Furthermore, availability of a standardization of the position of holes and bolts in different structural elements would facilitate their future reuse in similar applications.

#### 3.2.4.1 Beam/column connections

Figure 3-24 and Figure 3-25 present two schematic proposals for a precast concrete beam/column dry connection that is proposed to include a shear key, which is an aspect outlined in Table 3-10 as a further development in the conception of a new configuration for this type of connection. With the inclusion of the shear key, no bolts in the compression side of the connection are generally required. Furthermore, the first solution presented (Figure 3-24) has additional smaller ribs to the main ribs to enhance steel/concrete bond. This solution is based on the Aninthaneni *et al.* [33, 34] connection depicted in Figure 3-21 which proved to perform well.



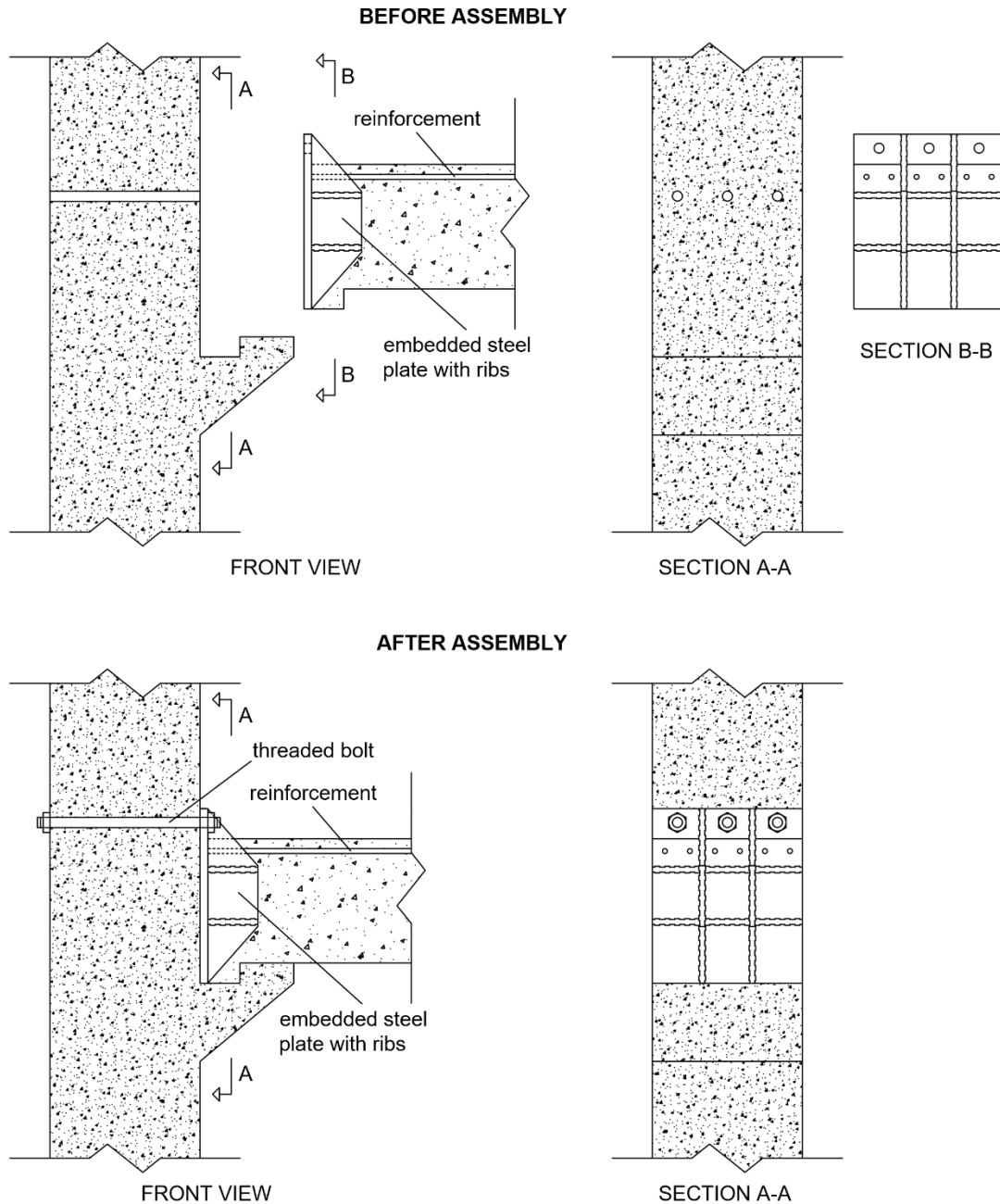


Figure 3-24 Schematic representation of a beam/column concrete dry connection – solution 1.

The second solution (Figure 3-25) is inspired by the connection studied by Pul and Şentürk *et al.* [35] (Figure 3-24), that also showed a very satisfactory performance, with a steel plate embedded in one of the surfaces of the column. The steel plate is welded to the column's stirrups so a more effective stress transfer to the column can be materialized. In turn, threaded ducts formed by nuts are welded to the steel plate in the column and accommodate the bolts that are connected to the beam's end steel plate, which has the beam's main reinforcement welded. Compared with solution 1, apart from the anchorage system of the bolts in the column, the main differences in solution 2 are the additional row of bolts in the tensioned area (materialized through the existence of openings in the beam's end to allow placement of the bolts and application of

the torque) and the absence of ribs in the beam's steel end plate. The beam end plate in the two connections shown in Figure 3-24 and Figure 3-25 has another welded plates with ribs embedded into the beam during casting to allow stresses transfer through the connection.

In the study of concrete beam/column dry connections, these two solutions represent different approaches, and, for that reason, they were chosen to be illustrated and described in more details in this section. Nevertheless, other solutions combining the two approaches are believed to be worth investigating as well of being explored in further research works. Furthermore, the two proposals presented in Figure 3-24 and Figure 3-25 may produce more effective performance than those in Figure 3-21 and Figure 3-22 but they are more complex and, consequently, expensive to construct.

#### 3.2.4.2 Wall/wall and column/column connections

It was mentioned that the concrete dry connection between precast walls studied by Sun *et al.* [36] achieved good results, so further developments of this type of connection should only be focused on optimization and design recommendations. For that reason, it seems plausible to consider a similar solution for a concrete dry connection between precast columns, with an H-shaped steel connector (welded to the wall's reinforcement) and pretensioned bolts. Especially in connections with significant flexural stress, since the H-shaped connector is particularly effective in transferring stresses on the edges of the column section.

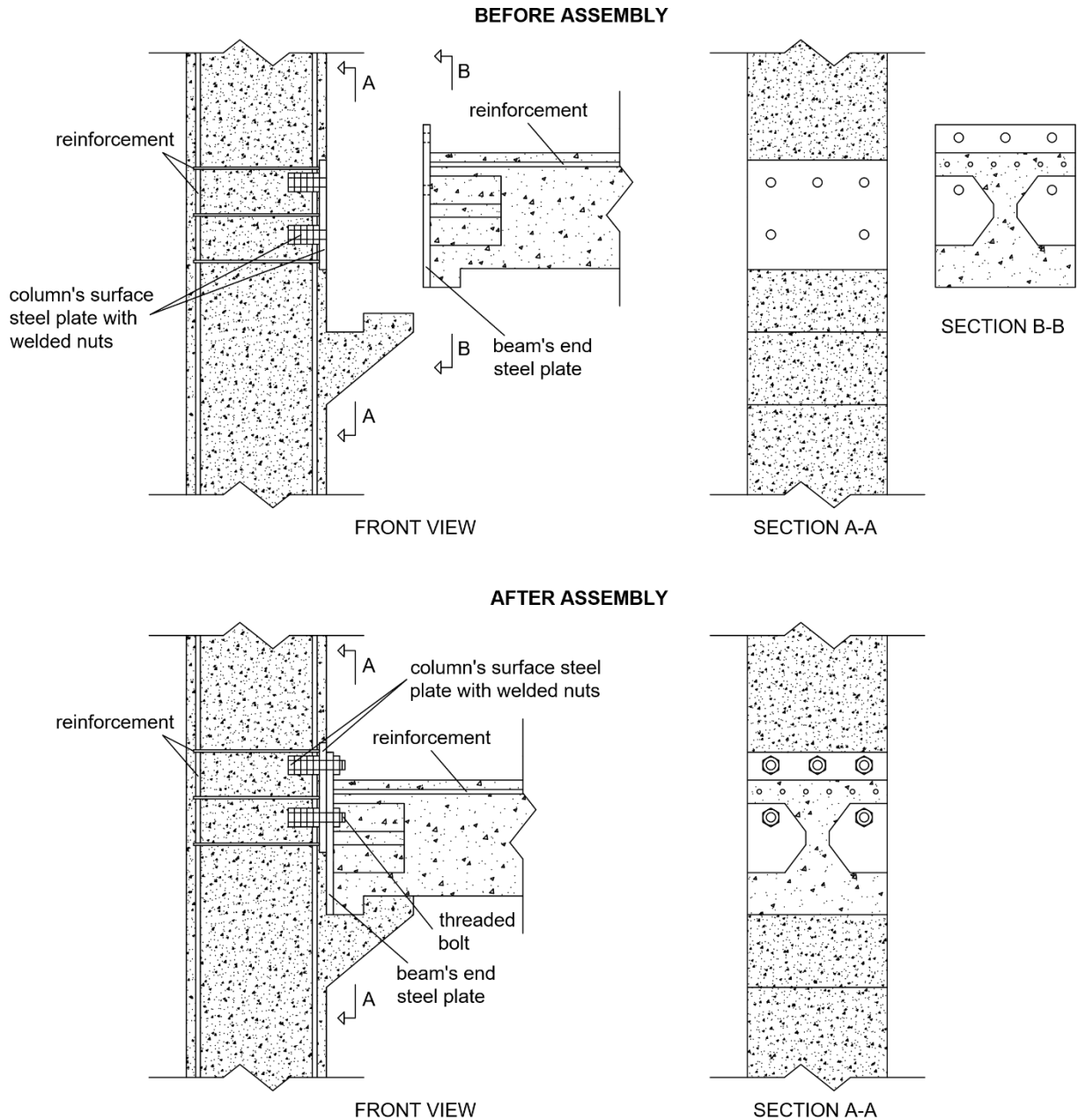


Figure 3-25 Schematic representation of a beam/column concrete dry connection – solution 2.

In cases where shear stresses are predominant, the inclusion of embedded steel plates in the columns seems to be preferable instead of the H-shaped connector. Figure 3-26 shows a schematic representation of that kind of solution, whose configuration follows the same concept of the beam/column connection illustrated in Figure 3-24.

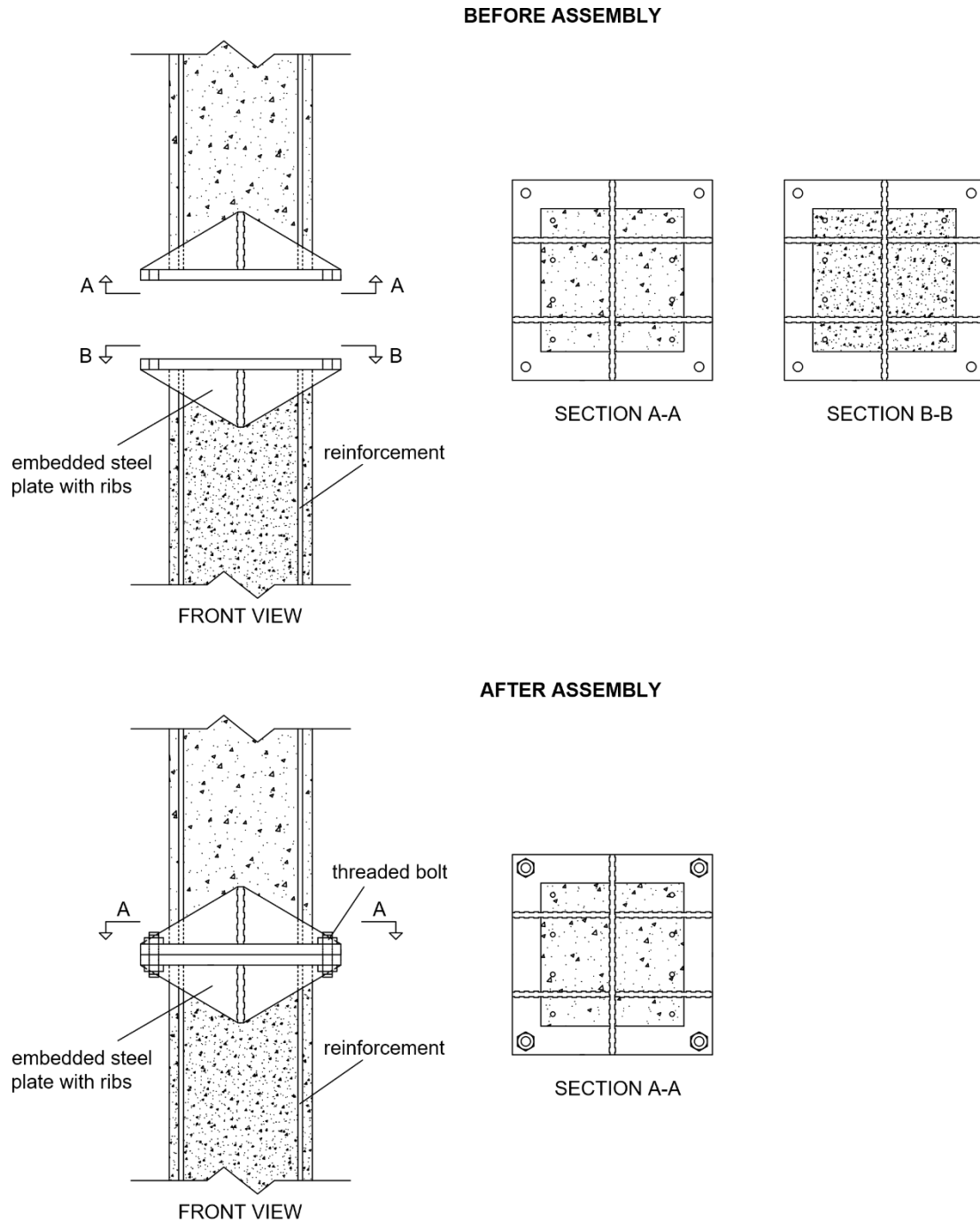


Figure 3-26 Schematic representation of a column/column concrete dry connection

### 3.2.4.3 Wall/foundation and column/foundation connections

The precast concrete wall/foundation dry connection assessed by Sun *et al.* [36] (Figure 3-23), equally to the wall/wall connection assessed by the same authors, displayed a very good performance and further developments should only be focused on optimization and design recommendations. In terms of concrete dry connections between a column and a foundation, no research studies could be

found so far in the literature. However, and since the type of stresses transferred is similar, the beam/column connection of Pul and Şentürk *et al.* [35] Figure 3-22 seems to be a solution that could be easily applicable to a column/foundation connection as it showed a structural behaviour similar to the monolithic connection.

#### 3.2.4.4 Slab/slab and beam/beam connections

In The test specimens include a total of 11 reinforced concrete simply supported slabs. All slabs have the same total length of 5200 mm, span between supports = 5000mm, height = 160 mm and width = 500 mm.

The materials used are geopolymer (Cemfree) concrete having a compressive strength of 35 MPa and stainless steel reinforcing bars (1.4362) with a minimum yield tensile strength of 500 MPa. In turn, the steel block and plates correspond to a normal structural steel S355 JR, and the bolts and nuts to normal steel class 10.9.

2 of the 11 slabs are fully monolithically cast in one piece and considered as reference specimens. The other 9 slabs are composed of 2 segments and have a demountable connection at mid span. The demountable connection is materialized mainly using bolts and steel plates as explained below.

4 types of demountable connections are assessed, differing on the existence of a key to enhance strength or the inclusion of a steel block to improve the stress transfer in the connection. Moreover, for each type of connection, the number and diameter of bolts differ.

The slabs will be cast in two phases (6 + 5 specimens). The following table briefly details the properties of each slab.

Table 3-11, it is mentioned that research on precast concrete dry connections between slab elements is scarce and further research work should rely on the conception and study of solutions that can effectively transfer flexural stress. Aiming to accomplish a solution on that regard, Figure 3-27 displays a configuration that includes a shear key sewed by threaded bolts. The bolts are anchored on a steel plate that carries tension stress at the bottom surface of the slab. Compression stresses at the top side of the slab can be either transferred by bearing or preferably by providing a similar steel plate at the top surface.

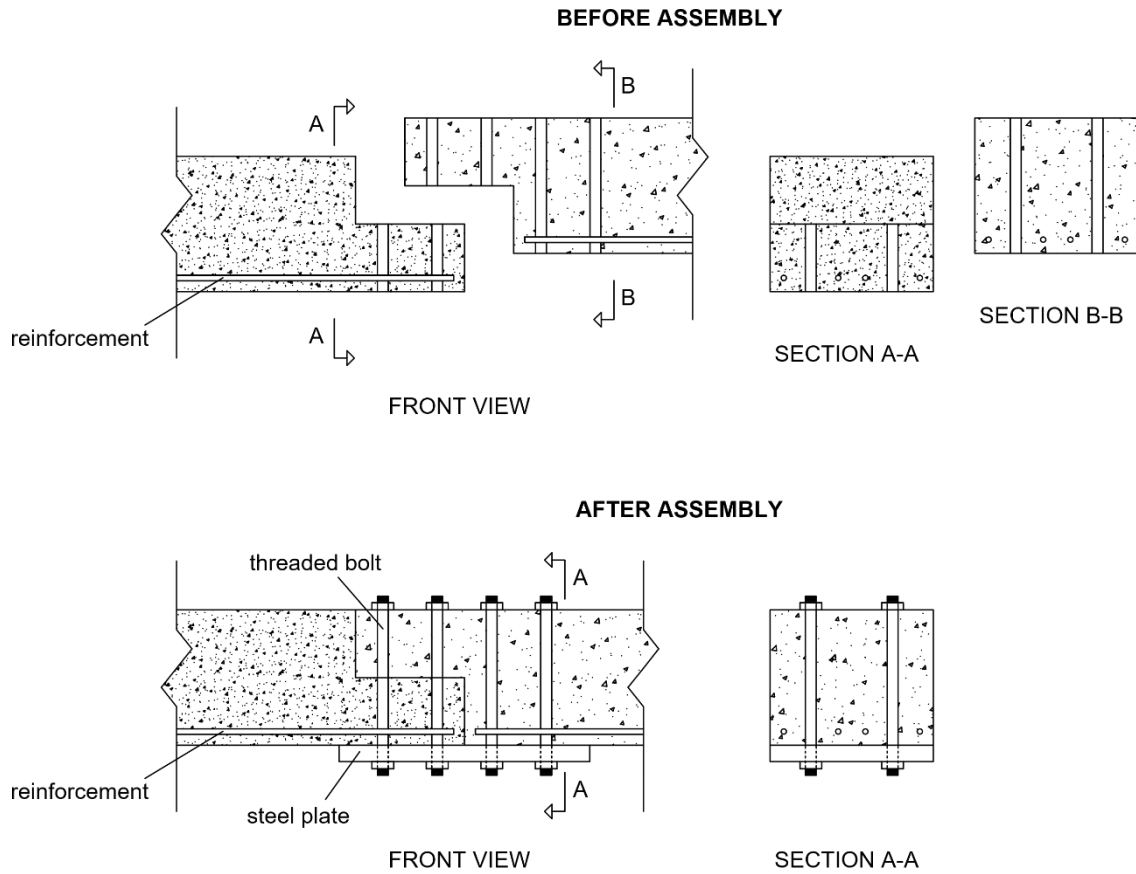
Stresses acting on slabs can vary significantly between the transversal and longitudinal directions depending on where the slab supports are placed. Consequently, while in one direction the connections can be less stiff, on other direction the same connections can be insufficient to transfer stresses. In Figure 3-28, a more robust joint is presented, having on each slab an additional embedded steel plate with ribs. Those steel plates are welded to the tensioned reinforcement at the bottom of the slabs. In this solution, the tensile stress is more easily transferred in the connection, since it is directly transmitted from the reinforcement to the steel plates. The solution of Figure 3-28 can also be applied in structural elements with significant shear and flexural stresses as beams. However, the presence of embedded steel plates and through slab bolts may weaken the slab section, leading to failure in concrete.

#### 3.2.4.5 Beam/slab connections

Beam/slab dry connections in precast concrete structures should be designed to prevent slip in the interface (contact) areas between the beam and slab elements, so the flexural capacity of the composite structure can be the same as in a monolithic structure. To achieve that full composite flexural strength, shear transfer needs to be effectively transferred in the interface areas. In this regard, a first sketch for a beam/slab concrete dry connection was divulged by Aninthaneni and Dhakal [34], where steel angle plates are used along with bolts. In this solution, shear stress is not directly transferred through the interface area, which is not ideal.

An enhanced connection is believed to be achieved in Figure 3-29 where an embedded steel plate (or connector) with ribs is considered in the interface area. In the presented configuration, the shear stress is transferred directly along the beam/slab interface, since it is mainly carried by the embedded steel instead of being forced to make a trajectory through the surrounding concrete. The conception of the steel plate is inspired in the wall/wall joint of Sun *et al.* [36] (Figure 3-23), especially in the way it embraces and links to the beam. It also resembles the beam/column joint of Aninthaneni *et al.* [33] (Figure 3-21) in the design of the embedded ribs. As can be seen in Figure 3-29 the solution depicted also allows the establishment of the slab/slab connections illustrated more in Figure 3-27 and Figure 3-28.





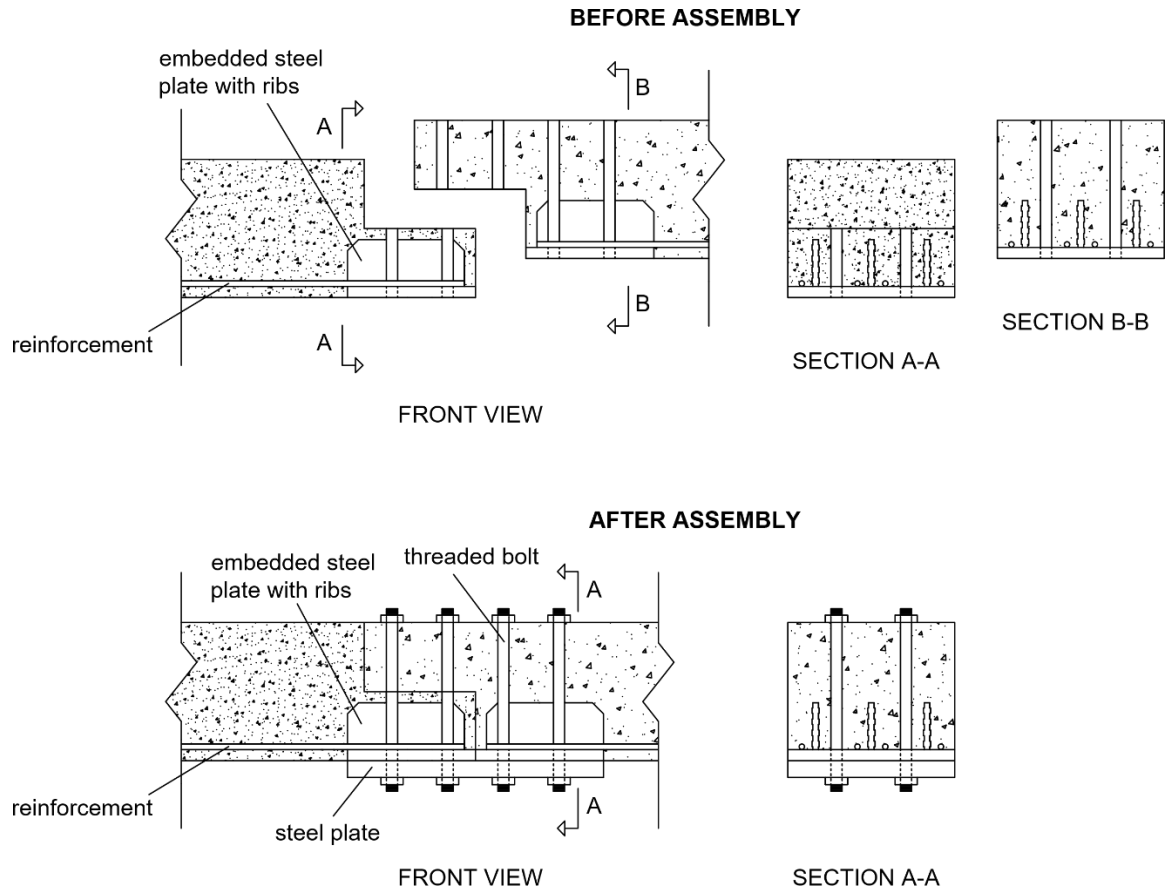


Figure 3-28 Schematic representation of a slab/slab concrete dry connection – solution 2.

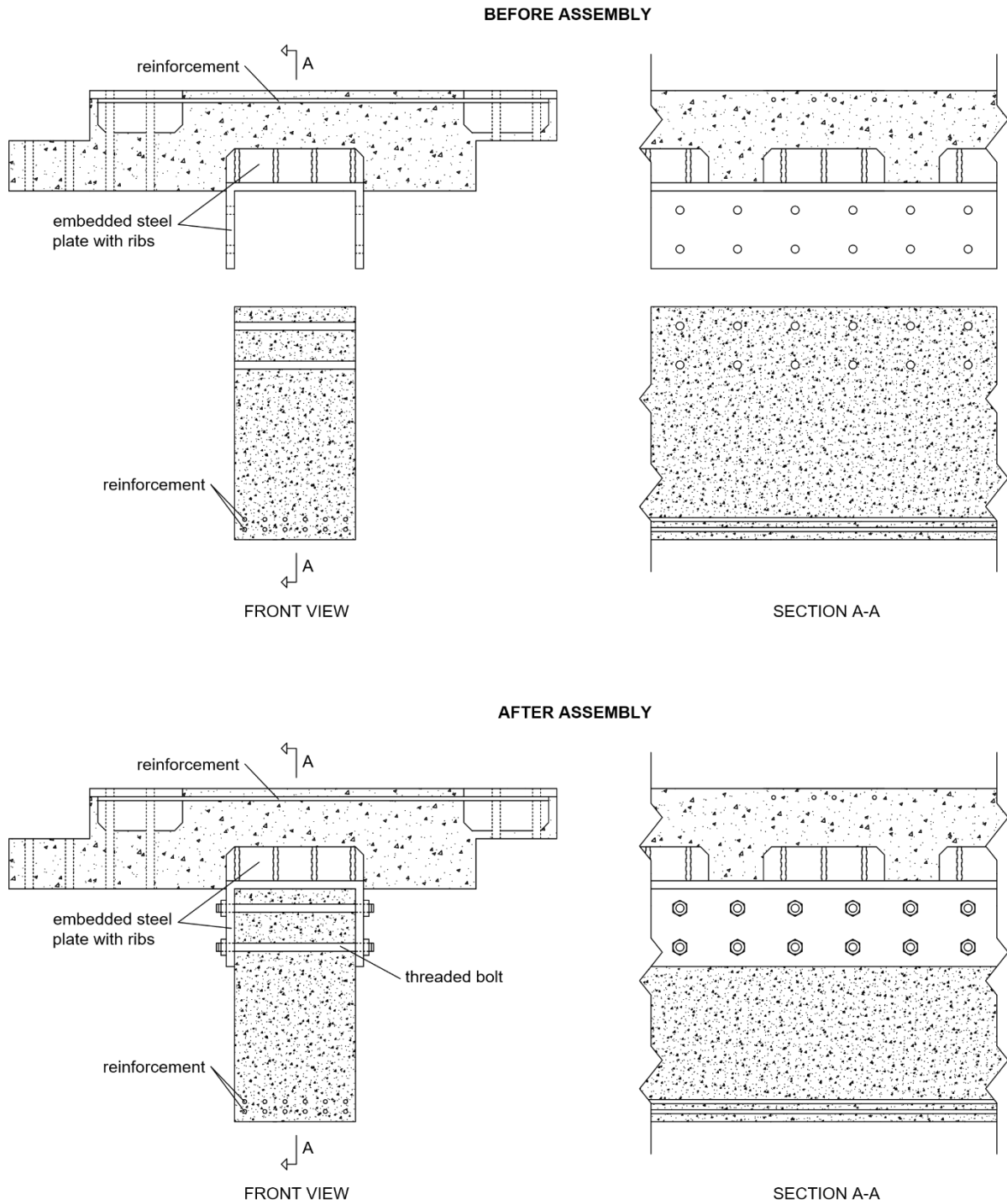


Figure 3-29 Schematic representation of beam/slab concrete dry connection.

### 3.2.5 Summary and partial conclusions

The review confirmed that the current knowledge on dry connections in precast concrete structures is still very scarce and incomplete, hindering the application

of this type of connections in structures. Current practice on dry connections relies traditionally on steel structures and steel/concrete composite structures.

In the past few years, semi-dry connection between precast concrete elements has started to be implemented more frequently, in which reuse is possible after mechanical removal of the cast-in-place parts. Two types of semi-dry connections can be found: dowel shear connection (more common) and moment-resisting connection with continuity bars. Although these semi-dry connections represent a step forward, the deconstruction and reconstruction of the structure elements is time-consuming and not an easy procedure to undertake.

Besides benefits related to time saving and smaller budgets, the achievement of dry connection solutions in precast concrete structures, and its application in the current practice, would have substantial advantages in terms of the environmental impact that the construction sector continuously inflicts. The construction sector is still one of the main contributors to the global carbon emissions and waste storage in landfills. Furthermore, concrete is the most used material nowadays in the construction sector. Therefore, the positive environmental contribution is evident and significant.

Although the current knowledge on precast concrete dry connections is very scarce, some research studies on the subject could be found in the literature. Almost all of them are very recent and the main conclusions derived from their review are the following:

- The main connecting elements include steel plates and bolts; however, the existence of bolts in concrete would reduce the concrete strength as well as create a stress concentration at concrete near the bolts.
- The available knowledge focused mainly on connections between a beam and a column. In this context, very good results have been obtained, in which the structural behaviour was similar to that of a monolithic connection. The best results were achieved for non-prestressed joint configurations, with embedded steel plates and pretensioned threaded bolts;
- Significant advances were also accomplished for connections between walls and between walls and foundations. A solution proposed in the literature could attain the same behaviour of a monolithic connection. The solution used an H-shaped steel connector (made of welded steel plates) and pretensioned threaded bolts. In wall/foundation joints, the H-shaped steel connector had ribs and embedded in the foundation.
- For other types of connection (i.e. column/column, beam/beam and beam/slab connections), no research could be found in the literature. For foundation/foundation and slab/slab connections only preliminary studies were published.
- Numerical modelling and simulation to explore load transfer mechanism, failure modes and integrity of demountable connections are very limited. The main challenges are in the modelling of compatibility of various elements as proposed for demountable connections, including concrete

elements, steel plates and bolts. Such numerical models need to be calibrated to the experimental results and, eventually, used to perform parametric analyses of the connection and optimize the connection configuration and dimensions.

- Although the initial cost of dry demountable connections would be higher than that of monolithic or semi dry connections, the life cycle cost analysis would significantly highlight the potential benefits of demountable connections. Such connections would facilitate the future reuse of structural elements at the end of their life, potentially achieving a significant reduction in embodied energy of structures, saving landfills as well as giving the clients the benefit of retaining the value of their assets. However, no life cycle cost analysis studies of demountable connections were found in the literature.

Despite the advances already made on the study of precast concrete dry connections, the current state-of-the-art is still far from being sufficient to allow engineers to design structures containing these connections. Therefore, future research on this subject is encouraged, possibly based on the proposed solutions in this review.

### 3.3 Experimental Studies on Demountable Concrete Structures

#### 3.3.1 Experimental Tests on Demountable Reinforced Concrete

##### Column

It is of great importance to develop connections that can be demountable in order to improve the sustainability and economy of reinforced concrete structures and to reduce the damage they cause to the environment. For this reason, in this part of the project, the new type was demountable and the connection details suitable for reuse were developed.

Before starting the connection designs, a literature review was made. As a result of the research, it was decided to fix the columns with rods. Research has been made on the basis of cost and workmanship issues, and the realization of designs that will reduce labor and cost has been emphasized.

In this context, steel plates are used for most of the column bottoms. One of the frequently encountered problems in the steel plates used is buckling. Column connection points are exposed to many different combinations of many different loads in the structure in which they are used.

Although a reinforcement plate is added to prevent buckling of steel plates under different loads, it is difficult to prevent buckling because different points are subjected to stress concentration. Therefore, if steel plate is to be used at the connection point, it must be surrounded very well.

Overdesigning in slabs is a very critical issue from an economic perspective. In general, it is designed as a flat plate with high stress concentration and considering many points, which triggers overdesign.

In addition, the adhesion of the concrete and the steel plate becomes critical here, since the highest moment and axial load will be exerted on the steel plates at the connection points of the columns. Since the adhesion of steel plate and concrete will be less than that of concrete, the connection point must either be replaced or designed to increase adhesion.

In the light of the above information, 4 different types of demountable column connections have been designed. The 4 columns designed will now be discussed.

### Design of Demountable Column-1

Since the endpoint of the longitudinal reinforcement was too large for the column shoe in demountable column 1, the assembly method of rebars by welding rather than bending was chosen. The points to be noted at this stage are that the margins of error increase in combining welding and reinforcement. It will be difficult to achieve a standard this way. Since it is both economical and feasible to design the connection point with a shoe in this way, a separate study can be made for the connection point design using the welding method with the reinforcements, and a separate system can be created to connect the welding work to the standard and a system can be developed for it.



Figure 3-30 Demountable Column 1



In demountable column 1, 6 pieces of 10-gauge reinforcement were used instead of 5 due to the relatively low height in the strong direction. In order to reduce the margin of error in the shoe, the longitudinal and transverse reinforcements are welded in 2 pieces. The 6-gauge reinforcements used in the weak direction surrounded the 10-gauge reinforcements. Again, these reinforcements were welded to each other by spot welding. The total height is designed as 90 mm. At this connection point, the reinforcements in the shoe are designed close to the holes of the studs. In this way, it will be easier to transfer the force that will flow from the column to the foundation.

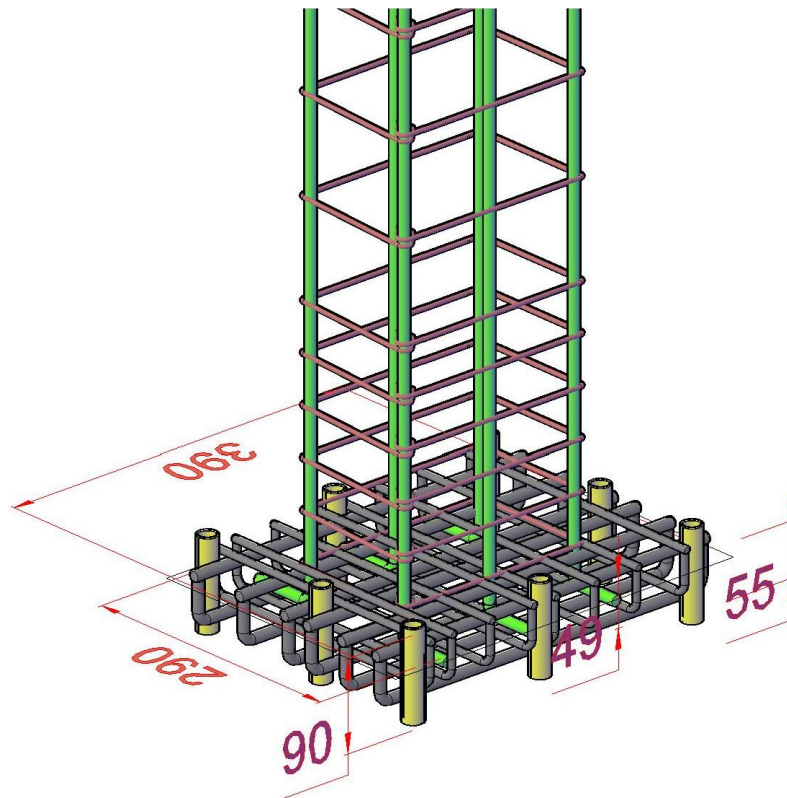


Figure 3-31 Dimensions of connection point of demountable column 1

### Design of Demountable Column-2

Similar connection points were designed in demountable column 2 and column 3. It was decided to use a grid, which is widely used in the market and used in water drains, at the connection point used in demountable column 2-3.

2 mm thick and 30 mm high steel plates were used in the strong direction of the grating. The distance between steel plates and reinforcements used in both directions is 28 mm. Including 2 mm steel plates, a total of 30 mm intervals were used. In the weak direction, a bar like a 6-gauge rebar was used. It was built in a place that manufactures the grill used here.



*Figure 3-32 Demountable Column 2*

The dimensions of the grid are 300\*400\*30 mm. The concrete cover was designed to be 15 mm in all directions. Again, using the guide, the connector hole pipes were attached to the grid by welding. Since the total height of the shoe used in demountable column-2 is 60 mm, the longitudinal reinforcements of the column are well welded to the steel plates of the grating, in order to ensure that the force from the column is transferred to the foundation with the rods without any problems. The force on these steel plates will be transferred to other plates by the reinforcements on them extending in the weak direction. These reinforcements connect the steel plates by spot welding.

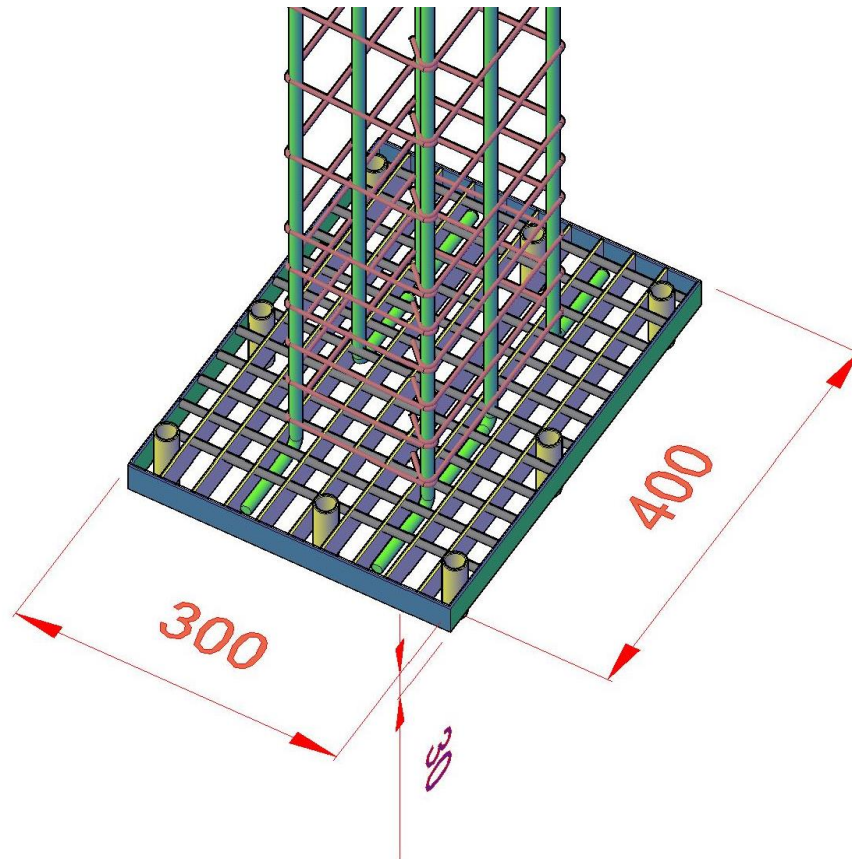


Figure 3-33 Dimensions of connection point of demountable column 2

### Design of Demountable Column-3

Similar pathways were followed in demountable column 3 with the previous column. Differently, steel plate was used in the weak direction. The plates are interlocked and joined with a point. In this way, the transfer of force to each other will be much more effective.

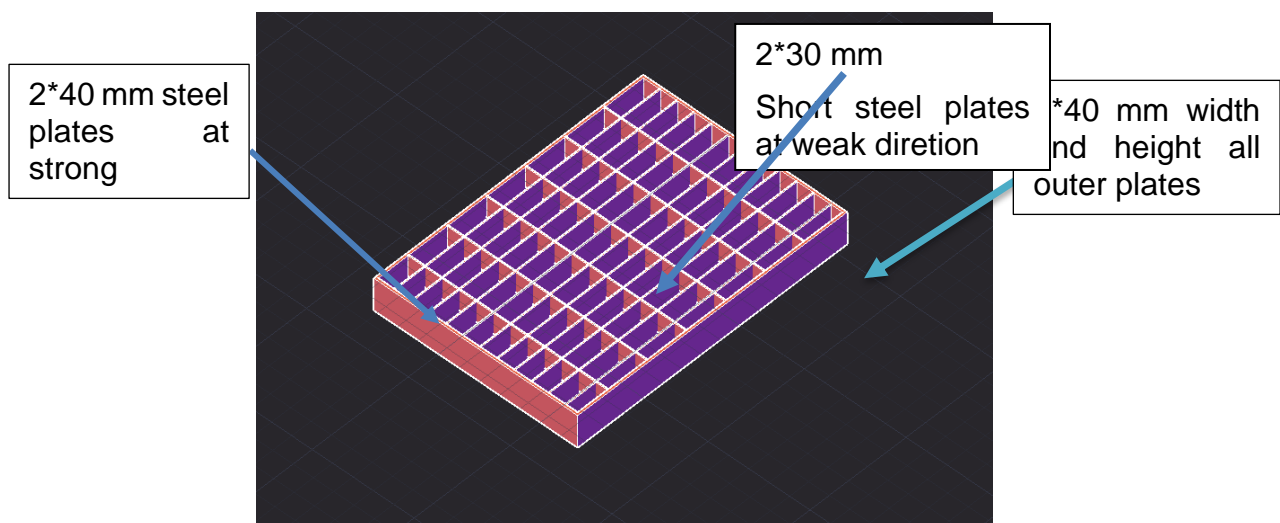


Figure 3-34 Grid modelling



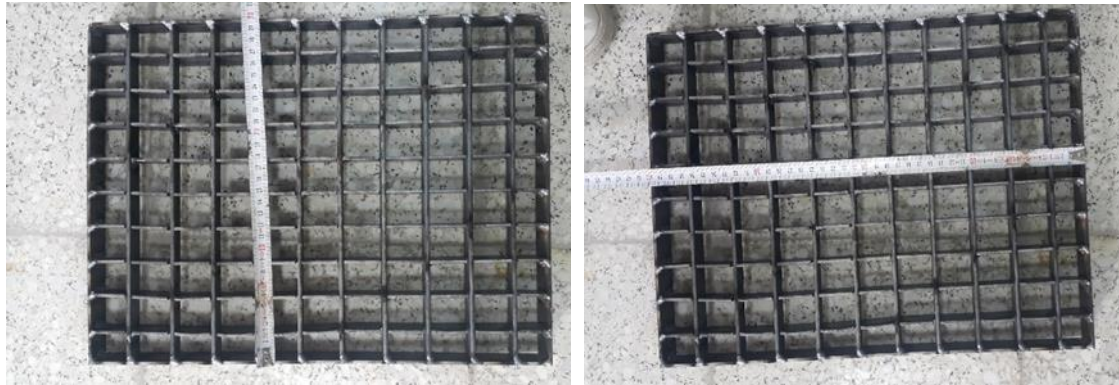


Figure 3-35 Details of Grid

In addition, it is necessary to mention the advantages of the connection points designed in the form of this grid. The adhesion of such connection points with concrete is very good. In other words, it is not possible for concrete and steel plates to separate and create weakness. Here, the effect of the column being attached to the foundation and tightening the concrete under it by tightening was great. That is, the disadvantage of designing the attachment point with only a flat steel plate is overcome in this way. In addition, since the edges of the steel plates are filled with concrete, the possibility of buckling of the plates is eliminated. The longitudinal reinforcements of the column are well welded to the grid, as in the previous grid.

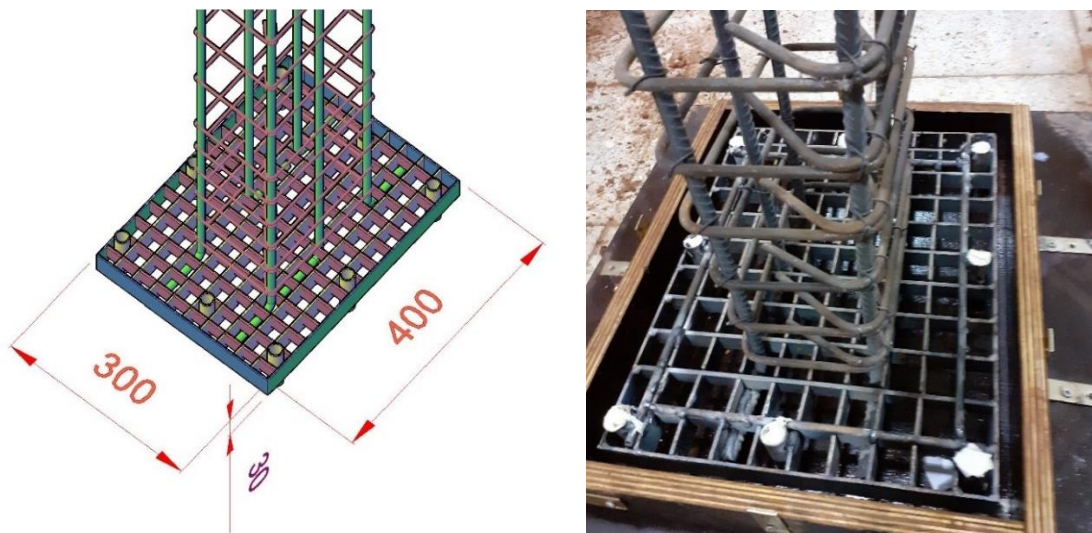


Figure 3-36 Dimensions of connection point of demountable column 3

### Design of Demountable Column-4

The way to design it in demountable column 4 includes many different divisions of work, such as cutting, drilling and welding the plate. Plates of different

thicknesses were used to form the shoe part of the columns. Firstly, 3D modeling was carried out to place the plates and reinforcements in the correct dimensions. The plates of the connection detail, whose 3D modeling was performed, were cut with CNC laser cutting.

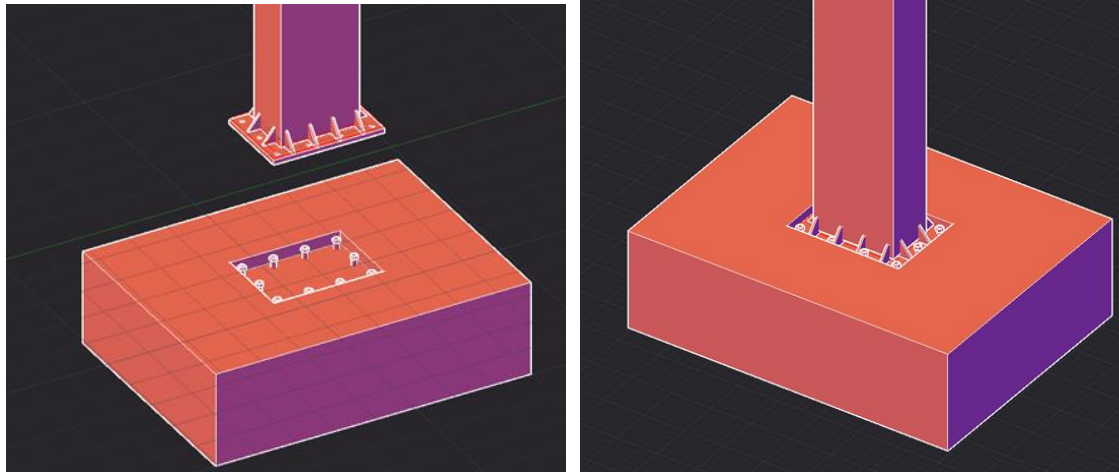


Figure 3-37 Modelling of demountable column-4 (a) During placing, (b) After Placing



Figure 3-38 Details of connection point of demountable column 4

Reinforcements with a diameter of 10 mm for the studs using demountable column 4 and 6 mm for stirrups were selected. A plate of 250\*350\*10mm was used to form the base part of the shoe, and 8 pieces of 8 mm thick reinforcement plates were used in the weak and strong directions to increase the rigidity of the connection point. In order to prevent joint cracking caused by weak adhesion, which is the disadvantage of composite materials, the ends of the columns are covered with 50 mm high and 3 mm thick plates. In order to carry out the load transfer between the shoe and the column in a homogeneous and safe manner, 8 pieces of 250 mm long 8 mm diameter rods were used between the longitudinal reinforcements. The ends of the connector are bent inward about 15 degrees to avoid shell shedding. In order to ensure the connection of the longitudinal reinforcements to the bottom plate, holes with a diameter of 13 mm were drilled

on the plates, the outer parts of the drilled holes were enlarged in a conical form, thus increasing the welding area. In the same way, holes with a diameter of 9 mm were drilled to fix the rods to the plate. Longitudinal reinforcement and rods were fixed to the bottom plate using ASKAYNAK MIG350 gas welding machine. 15 mm space is used in the columns.

### 3.3.2 Experimental Tests On Demountable Reinforced Concrete Slabs

The test specimens include a total of 11 reinforced concrete simply supported slabs. All slabs have the same total length of 5200 mm, span between supports = 5000mm, height = 160 mm and width = 500 mm.

The materials used are geopolymer (Cemfree) concrete having a compressive strength of 35 MPa and stainless steel reinforcing bars (1.4362) with a minimum yield tensile strength of 500 MPa. In turn, the steel block and plates correspond to a normal structural steel S355 JR, and the bolts and nuts to normal steel class 10.9.

2 of the 11 slabs are fully monolithically cast in one piece and considered as reference specimens. The other 9 slabs are composed of 2 segments and have a demountable connection at mid span. The demountable connection is materialized mainly using bolts and steel plates as explained below.

4 types of demountable connections are assessed, differing on the existence of a key to enhance strength or the inclusion of a steel block to improve the stress transfer in the connection. Moreover, for each type of connection, the number and diameter of bolts differ.

The slabs will be cast in two phases (6 + 5 specimens). The following table briefly details the properties of each slab.

Table 3-11 Test specimen details

TEST SPECIMEN DETAILS									
number of the slab	slab ID	connection type	key at the connection	embedded steel block	number of parts	equal parts	number of bolts	bolts diameter (mm)	casting
1	REF	-	-	-	1	-	-	-	first
2	C-5-16-NK-NB	2	no	no	2	yes	5	16	first
3	C-4-16-NK-NB	2	no	no	2	yes	4	16	first
4	C-5-12-NK-NB	2	no	no	2	yes	5	12	first
5	C-4-20-NK-B	3	no	yes	2	yes	4	20	second
6	C-4-16-NK-B	3	no	yes	2	yes	4	16	second
7	C-5-16-K-NB	4	yes	no	2	no	5	16	first
8	C-4-16-K-NB	4	yes	no	2	no	4	16	first
9	C-5-12-K-NB	4	yes	no	2	no	5	12	second
10	C-4-20-K-B	5	yes	yes	2	no	4	20	second
11	REF	-	-	-	1	-	-	-	second



**Reference slab (monolithic slab with no connection)**

Simply supported (5 m span)

Quantity = 2

Length = 5200 mm; Height = 160 mm; Width = 500 mm

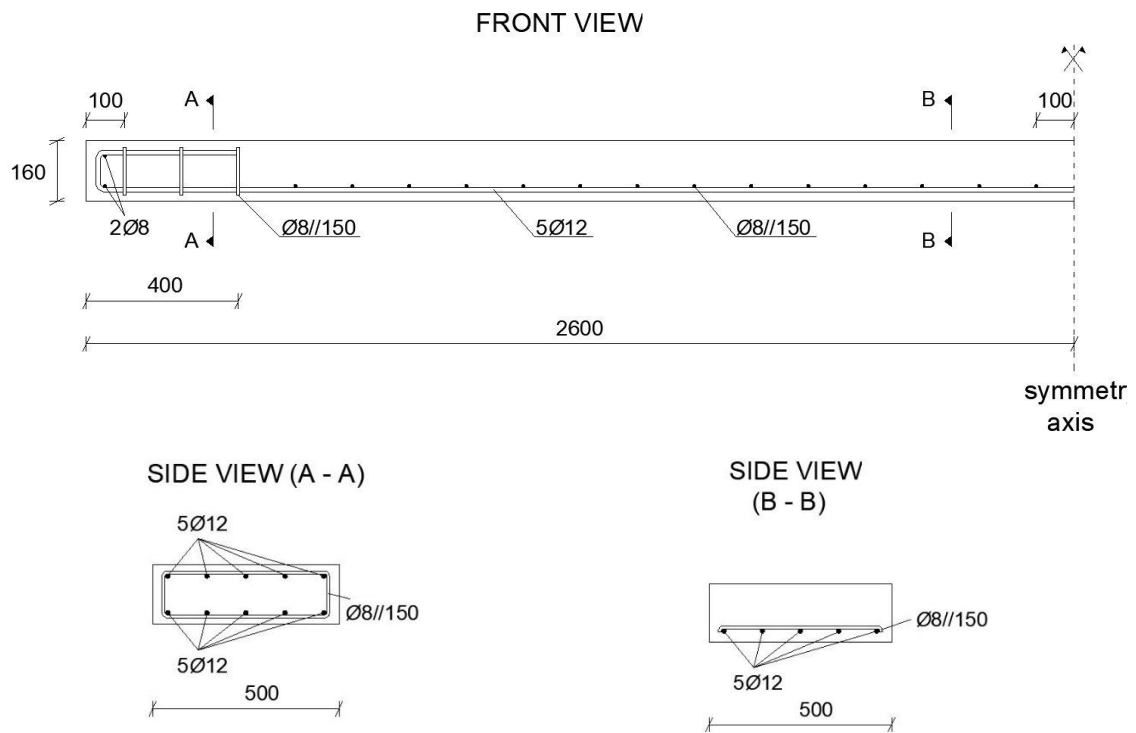


Figure 3-39 Reference slab (monolithic slab with no connection)

### Connection with no key and no embedded steel block

Simply supported (5 m span with connection at mid span)

Quantity = 3 (varying the diameter and the number of the bolts)

4 or 5 bolts of 16 mm or 20 mm

Length of each segment = 2600 mm; Height = 160 mm; Width = 500 mm

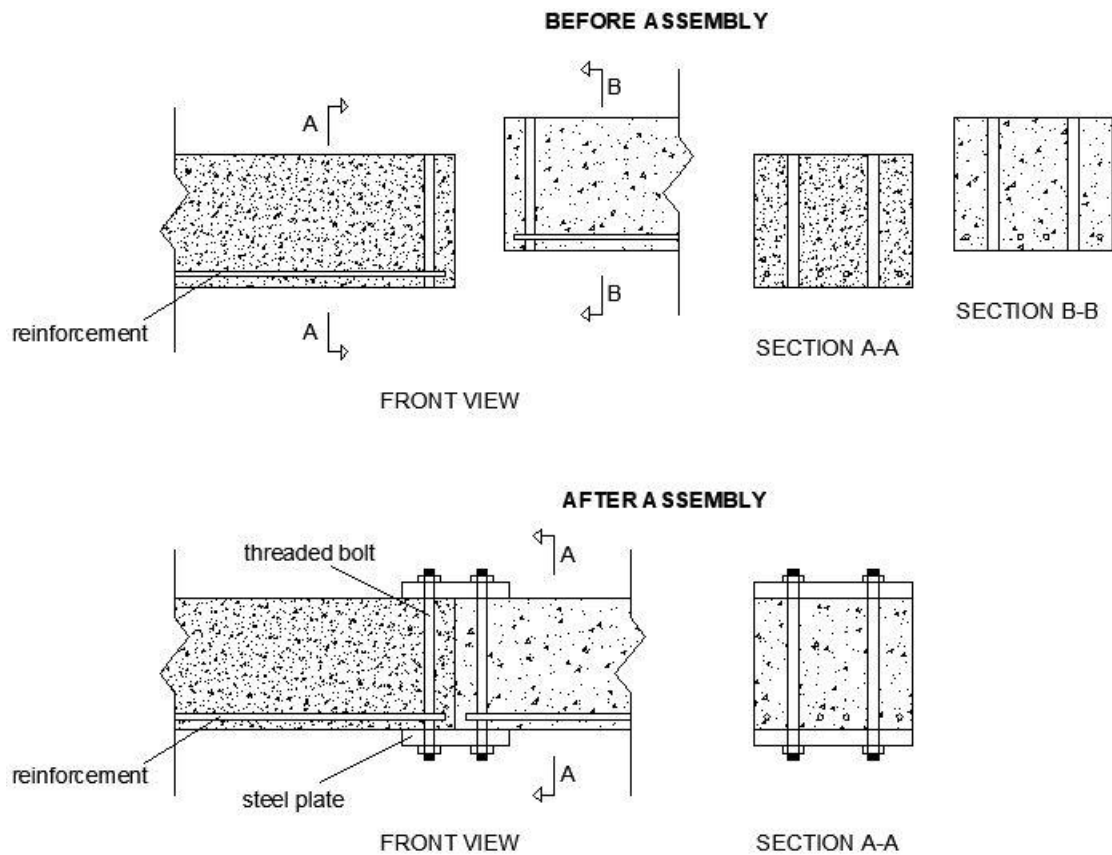


Figure 3-40 Connection with no key and no embedded steel block

### Connection with no key and with an embedded steel block

Simply supported (5 m span with connection at mid span)

Quantity = 2 (varying the diameter of the bolts)

4 bolts of 16 mm or 20 mm

Length of each segment = 2600 mm; Height = 160 mm; Width = 500 mm

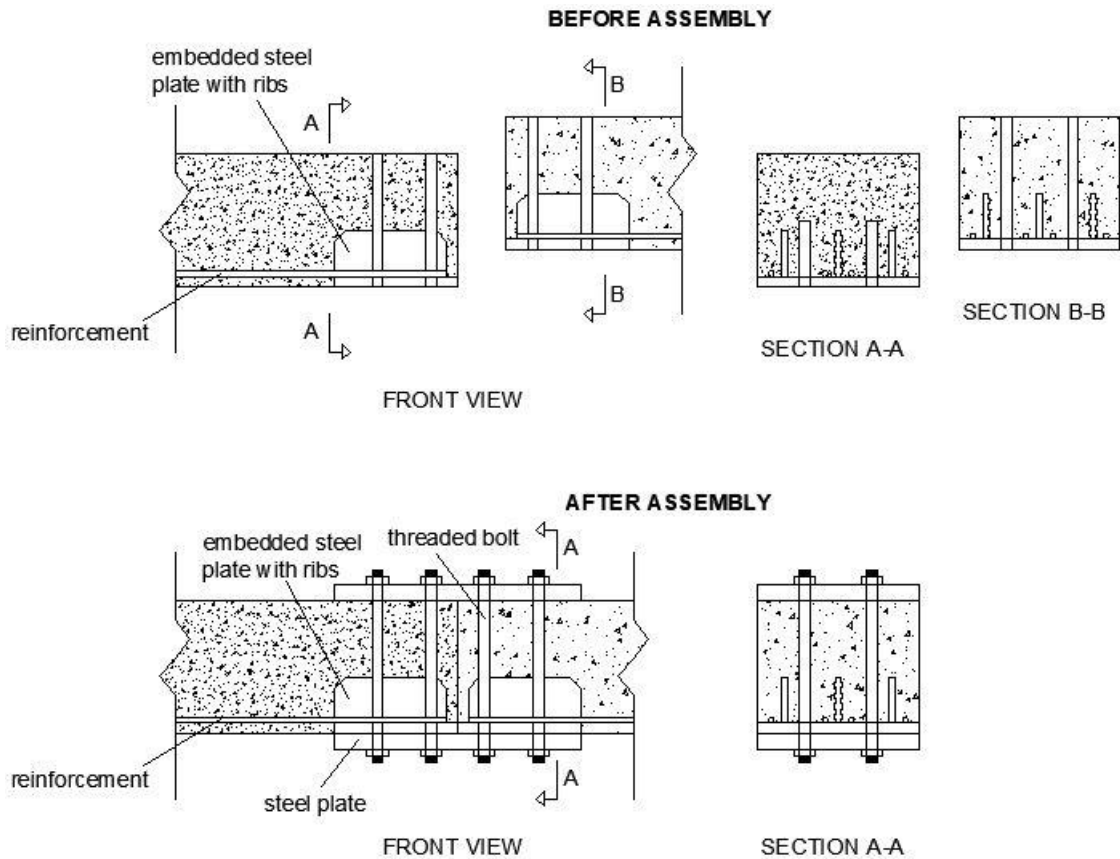


Figure 3-41 Connection with no key and with an embedded steel block

### Connection with a key and no embedded steel block

Simply supported (5 m span with connection at mid span)

Quantity = 3 (varying the diameter and the number of the bolts)

4 or 5 bolts of 16 mm or 20 mm

Length of each segment  $\approx$  2600 mm; Height = 160 mm; Width = 500 mm

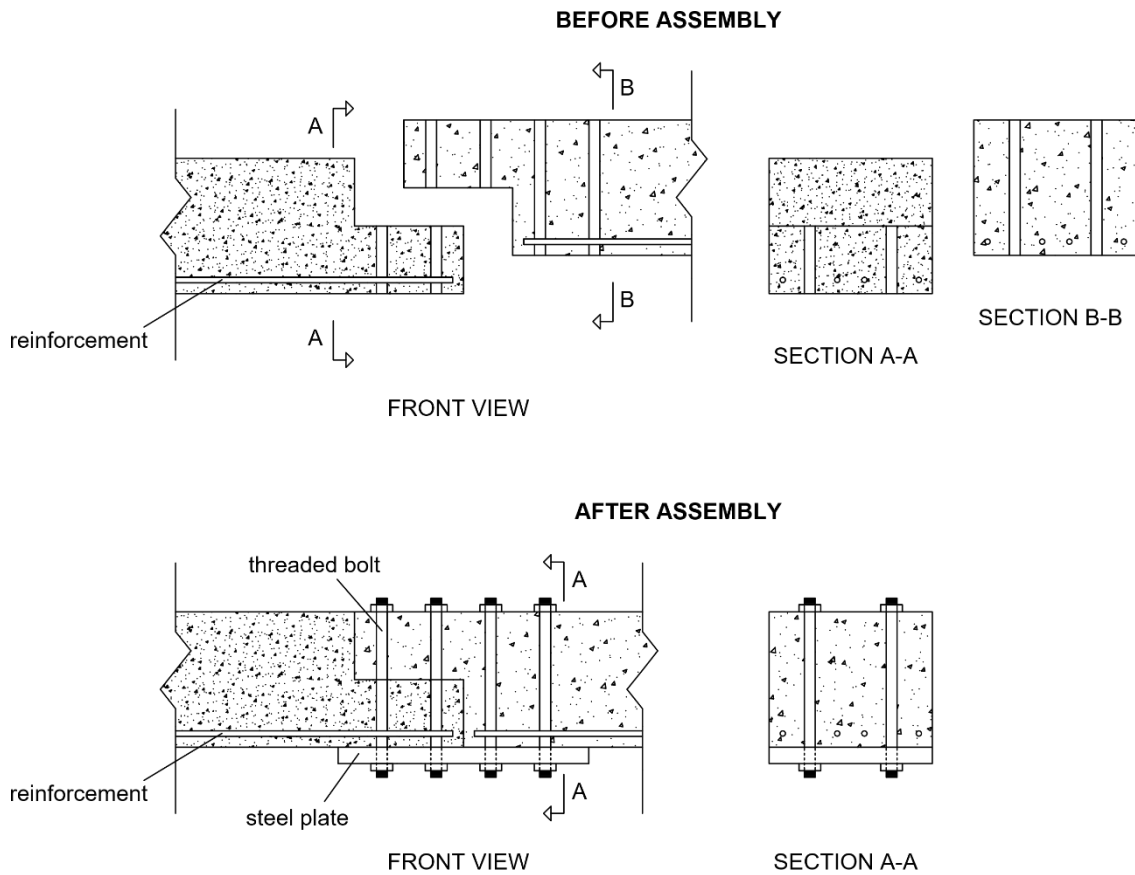


Figure 3-42 Connection with a key and no embedded steel block

### Connection with a key and with an embedded steel block

Simply supported (5 m span with connection at mid span)

Quantity = 1

4 bolts of 20 mm

Length of each segment  $\approx$  2600 mm; Height = 160 mm; Width = 500 mm

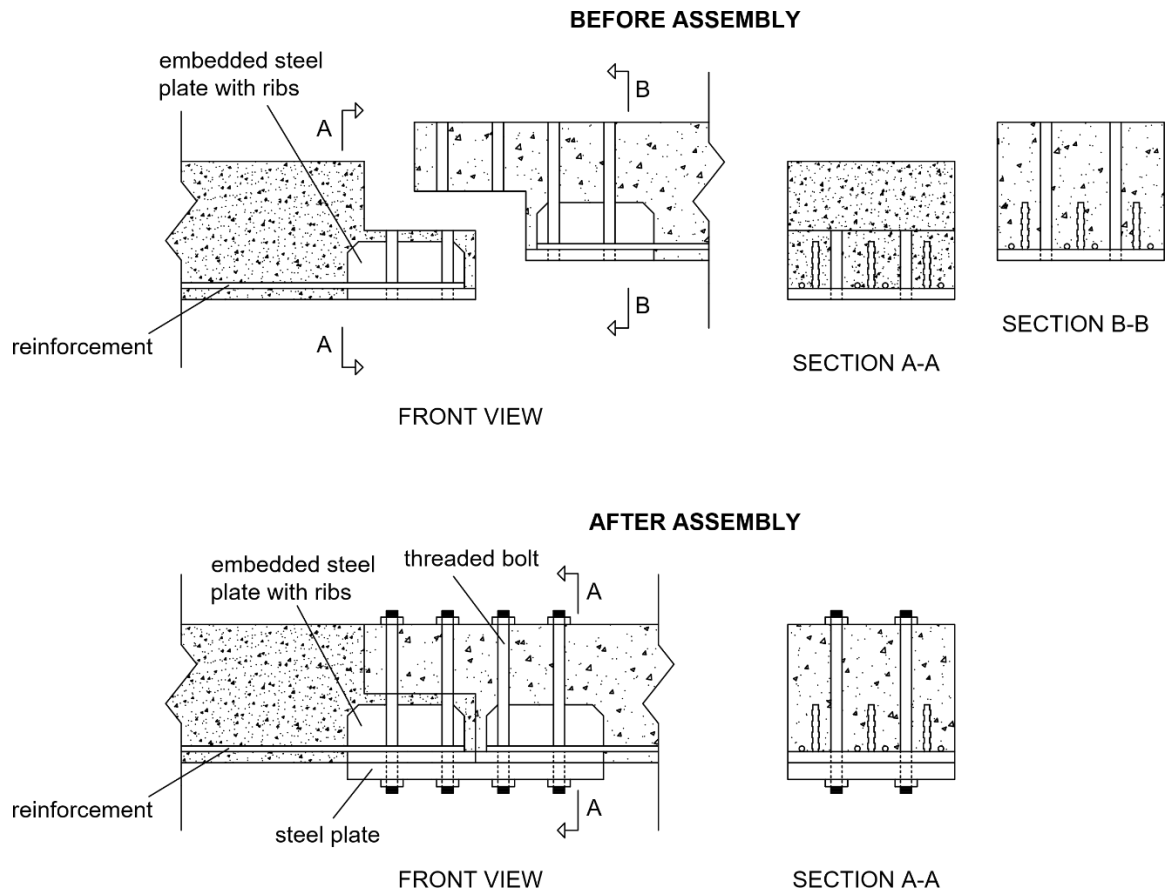


Figure 3-43 Connection with a key and with an embedded steel block

### 3.3.3 References

1. Huang, L., G. Krigsvoll, F. Johansen, Y. Liu and X. Zhang (2018). *Carbon emission of global construction sector*. Renewable and Sustainable Energy Reviews. 81: p. 1906-1916.
2. Andrew, R. M. (2018). *Global CO 2 emissions from cement production*. Earth System Science Data. 10: p. 195-217.
3. Scrivener, K. L. and R. J. Kirkpatrick (2008). *Innovation in use and research on cementitious material*. Cement and Concrete Research. 38(2): p. 128-136.
4. Swamy, R. N. (1998). *Designing concrete and concrete structures for sustainable development*, in *Proceedings of CANMET/ACI International Symposium*. Sustainable Development of the Cement and Concrete Industry. Ottawa (Canada). p. 245-255.
5. Yamamoto, R., N. Nagai, N. Koizumi and R. Nimomiya (1999). *Dust concentration around the sites of demolition work after the Great Hanshin-Awaji Earthquake*. Environmental Health and Preventive Medicine. 3(4): p. 207-214.
6. Ademola, J. A. and P. O. Oguneletu (2005). *Radionuclide content of concrete building blocks and radiation dose rates in some dwellings in Ibadan, Nigeria*. Journal of Environmental Radioactivity. 81(1): p. 107-113.
7. Mattiello, A., P. Chiodini, E. Bianco, N. Forgiione, I. Flammia, C. Gallo, R. Pizzuti and S. Panico (2013). *Health effects associated with the disposal of solid waste in landfills and incinerators in populations living in surrounding areas: a systematic review*. International Journal of Public Health. 58(5): p. 725-735.
8. Kibert, C. J., A. R. Chini and J. Languell (2001). *Deconstruction as an essential component of sustainable construction*, in *CIB World Building Congress*. NOV 54, Wellington (New Zealand).
9. Hogland, W., M. Marques and S. Nimmermark (2004). *Landfill mining and waste characterization: a strategy for remediation of contaminated areas*. Journal of material Cycles and Waste management. 6(2): p. 119-124.
10. Flager, F. L. (2003). *The design of building structures for improved life-cycle performance*. M.Sc. Thesis, Massachusetts Institute of Technology.
11. Durmisevic, E. and J. Brouwer (2002). *Design aspects of decomposable building structures*, in *Proceedings of the CIB Task Group*. Delft University of Technology, Department of Building Technology.
12. Tingley, D. D. and B. Davison (2011). *Design for deconstruction and material reuse*. Proceedings of the Institution of Civil Engineers - Energy. 164(4): p. 195-204.
13. Zabihi, H., F. Habib and L. Mirsaeedie (2013). *Towards green building: sustainability approach in building industrialization*. International Journal of Architecture and Urban Development. 3(3): p. 49-56.
14. Meyer, C. (2009). *The greening of the concrete industry*. Cement and Concrete Composites. 31(8): p. 601-605.



15. Lotfi, S., M. Eggimann, E. Wagner, R. Mróz and J. Deja (2015). *Performance of recycled aggregate concrete based on a new concrete recycling technology*. Construction and Building Materials. 95: p. 243-256.
16. Gastaldi, D., F. Canonico, L. Capelli, L. Buzzi, E. Boccaleri and S. Irigoien (2015). *An investigation on the recycling of hydrated cement from concrete demolition waste*. Cement and Concrete Composites. 61: p. 29-35.
17. Tam, V. W. (2008). *Economic comparison of concrete recycling: A case study approach*. Resources, Conservation and Recycling. 52(5): p. 821-828.
18. Durmisevic, E., O. Ciftcioglu and C. J. Anumba (2003). *Knowledge model for assessing disassembly potential of structures*, in CIB Task Group 39.
19. Guy, B., S. Shell and H. Esherick (2006). *Design for deconstruction and materials reuse*. Proceedings of the CIB Task Group. 39(4): p. 189-209.
20. Akinade, O., L. O. Oyedele, S. O. Ajayi, M. Bilal, H. A. Alaka, H. A. Owolabi, S. A. Bello, B. E. Jaiyeoba and K. O. Kadir (2017). *Design for Deconstruction (DfD): Critical success factors for diverting end-of-life waste from landfills*. Waste management. 60: p. 3-13.
21. Jin, R. and Q. Chen (2015). *Investigation of concrete recycling in the US construction industry*. Procedia Engineering. 118: p. 894-901.
22. Ding, T., J. Xiao, Q. Zhang and A. Akbarnezhad (2018). *Experimental and numerical studies on design for deconstruction concrete connections: An overview*. Advances in Structural Engineering. 21(14): p. 2198-2214.
23. Tingley, D. D. and B. Davison (2012). *Developing an LCA methodology to account for the environmental benefits of design for deconstruction*. Building and Environment. 57: p. 387-395.
24. Lee M S and Bradford M A, 2013. Sustainable composite beam behaviour with deconstructable bolted shear connectors, Composite Construction in Steel and Concrete, VII, 445–455.
25. Lam D, Dai X and Saveri E, 2013. Behaviour of demountable shear connectors in steel-concrete composite beams, Composite Construction in Steel and Concrete, VII, 618–631.
26. Lawan M M, Tahir M M and Mirza J, 2016. Bolted Shear connectors performance in selfcompacting concrete integrated with cold-formed steel section, Latin American Journal of Solids and Structures, 13, 731–749.
27. Gomer, C. R., D. Dulieu, K. W. Tupholme and G. J. Butterworth (1990). *The feasibility of recycling activated steel first wall/blanket materials from fusion reactors*. Fusion engineering and design. 11(4): p. 423-440.
28. Belleri, A., E. Brunesi, R. Nascimbene, M. Pagani and P. Riva (2014). *Seismic performance of precast industrial facilities following major earthquakes in the Italian territory*. Journal of Performance of Constructed Facilities. 29(5): 04014135.
29. Metelli, G., C. Beschi and P. Riva (2011). *Cyclic behaviour of a column to foundation joint for concrete precast structures*. European Journal of Environmental and Civil Engineering. 15(9): p. 1297-1318.
30. Xiao, J., T. Ding and Q. Zhang (2017). *Structural behavior of a new moment-resisting DfD concrete connection*. Engineering Structures. 132: p. 1-13.
31. Reinhardt, H.W., Kolpa, J.J., Stroband, J. Building with Demountable Precast Concrete Components in the Netherlands, Part 2. (1984) Betonwerk und Fertigteil-Technik/Concrete Precasting Plant and Technology, 50 (2), pp. 105-110.

32. fib (2008). *Structural connections for precast concrete buildings*. fib Bulletin 43, fédération internationale du béton.
33. Aninthaneni, P. K., R. P. Dhakal, J. Marshall and J. Bothara (2016). *Experimental investigation of dry beam-column moment connections for demountable precast concrete frame buildings*, in *New Zealand Society for Earthquake Engineering Annual Conference (NZSEE)*.
34. Aninthaneni, P. K. and R. P. Dhakal (2016). *Demountable precast RC frame building system for seismic regions*, in *Proceedings of the International Conference on Earthquake Engineering and Seismology (IZIIS-50)*, New Zealand.
35. Pul, S. and M. Şentürk (2017). *A bolted moment connection model for precast column beam joint*, in *Proceedings of the 2<sup>nd</sup> World Congress on Civil, Structural, and Environmental Engineering (CSEE'17)*. ICSENM 129. Barcelona (Spain).
36. Sun, J., H. Qiu and Y. Lu (2016). *Experimental study and associated numerical simulation of horizontally connected precast shear wall assembly*. *The structural design of tall and special buildings*. 25: p. 659-678.
37. Cai, G., Xiong, F., Yong, X., Larbi, A., Lu, Y. and Yoshizawa, M. (2019) *A Demountable Connection for Low-Rise Precast Concrete Structures with DfD for Construction Sustainability-A Preliminary Test under Cyclic Loads*. *Sustainability*. 2019, 11(13), doi:10.3390/su11133696.

### 3.4 Development of numerical models of concrete elements

#### 3.4.1 Introduction

In the previous studies conducted by the Hacettepe University (HU) team on the experimental analysis and numerical modeling of structural elements, traditional Portland cement reinforced concrete and structural elements produced entirely by recycling construction and demolition wastes were analyzed. In this context, the structural performances of these elements, which exhibit similar compressive strength and splitting-tensile strength, were experimentally compared with each other. In the continuation of the study, an effort was made on numerical modeling to simulate the cracking and crushing mechanics of structural elements using the ANSYS (2016) program. It was concluded that the numerical modeling developed in this context is quite successful in simulating experimental studies, as discussed in the subsections. Thus, within the scope of Task 3.3, when the final Eco-hybrid cement is procured in large quantities from CİMSA and the final recipe for Eco-hybrid cement-based concrete is determined, the production of large-scale structural elements already developed will begin and the validation of the numerical modeling that successfully worked will be made. Within the scope of the ICEBERG project, at this stage, both connection designs and numerical modeling development studies continue without any problems and with success.

The finite element method is frequently used to analyze materials with a highly heterogeneous behavior and complex structure, such as reinforced concrete structural materials. It is very important to accurately analyze the response of structures against loads such as reinforced concrete, which are exposed to many loads throughout their service life. As it is known, the behavior of reinforced concrete structures against the loads they are exposed to during their service life depends on many parameters. Experimentally analyzing each of these parameters causes very high labor and cost. For this reason, it is very necessary to accurately numerically model these loads with computer-based modeling systems and to successfully simulate experimental results.

In recent years, due to environmental concerns, studies have been carried out on the numerical modeling of reinforced concrete elements produced with recycled materials, especially from construction and demolition wastes. Dong Teng et al. (2021) conducted an analysis on numerically simulating the flexural failure of concretes with basalt fiber recycling aggregates. The authors analyzed the elements they produced both experimentally and using the ANSYS program. According to their results, it was concluded that the use of fiber in various ratios did not have much effect on crack distribution and propagation.

Zhou Jinghai et al. (2017) developed numerical modeling to measure the effect of changes in various parameters on the mechanical performance of recycled concretes by using the ANSYS program. According to the results obtained by the authors, it was observed that the increase in the adhesion of the mortar, the use of smaller aggregates and the use of less recycling aggregates had a positive effect on the mechanical properties.

Lu Bo et al. (2013) analyzed the cube and prism compressive strengths of fly ash concretes in a study they conducted. The authors performed the analyzes by combining ANSYS finite element method with Monte Carlo and Fuller grading methods. According to the results obtained as a result of the study, the authors reported that the microcracks first formed in the interfacial transition zone at the junction of aggregate and cement mortar.

Xiao et al. (2012) carried out a study on modeling the compressive and flexural strengths of recycled concretes using an improved lattice model. According to their results, they reported that crack formation under load first occurs in the interfacial transition zone. In the case of continued loading, they stated that the cracks widened around the old hardened mortar and finally spread around the new hardened mortar.

In this part of the Project, component tests to unveil the performance of the newly developed novel connections will be presented. The component tests on beams will be presented. Each specimen was produced with the new generation material

developed in the scope of this project. The tests will summarize both the capacity curves and the observed crack patterns.

### 3.4.2 Beam tests

Beam tests will be utilized to investigate the probable changes in the flexural and shear response of the developed new generation concrete material (CVC-RA) from the conventional concrete (CVC-NA). In addition, geopolymer concrete specimens were also tested (i.e., GPC-NA and GPC-RA). To this end, two different test protocols were applied. In the first tests, flexural performance of adequately detailed beam elements was examined. In the second phase, the shear performance was studied by testing inadequately detailed beams.

#### 3.4.2.1 Definition of Test Specimens and Test Setup

The geometrical and reinforcement details of the tested specimen were selected from the first-story central-internal bay of the three-story prototype RC building designed according to the Turkish Earthquake Code (TEC2018). The cross-section of the prototype beam was 300 × 500mm, which represented typical values in RC frames built in Turkey. Due to the facility limitations, specimens were scaled by  $\frac{1}{2}$  (i.e., all tested rectangular beam specimens had a width of 150mm and a height of 250mm.). In addition, fine and coarse aggregates have been used in the production of geopolymer concrete. The maximum aggregate size (MAS) was selected as 10mm in order not to violate the laws of similitude since the MAS of the prototype CVC was 20mm. In other words, the scaling process was aimed to generate the same stress demands on both the prototype and the scaled specimens but the fracture energy of the prototype and scaled concrete mixtures should be the same for accurate testing. It was proved that the fracture energy of the concrete was inversely proportional to the fracture process zone, which could be reduced to its half value by scaling down the aggregate size. To this end, MAS was also reduced by the selected scale factor during the specimen production. The target compressive strength was selected as 35 MPa, and uniaxial cylinder compressive strength and splitting tensile strength of the test specimens are given in Table 3.12 (i.e., 150 × 300mm cylinders). The yield and ultimate strength of the 10 mm (6.5 mm) bars were 456 MPa (330 MPa) and 716 MPa (449 MPa), respectively. Tie spacing was 100 mm over the beam length for the first set of specimens (i.e, flexure behaviour) and was 200mm for the first set of specimens (i.e, shear behaviour). All the ties were anchored to the core using 135° hooks to simulate code-compliant detailing.

Three different concrete shear-span-to-depth ( $a/d$ ) ratios (i.e., 0.50, 1.00, and 1.65) were used in the testing program in order to observe the change in the

failure pattern depending on the critical loading effects (i.e., shear-dominant behavior and flexure-dominant behavior). The beam specimens have the same reinforcement arrangements to examine the impact of the application of the geopolymer concrete and the recycled aggregate on the performance. All the reinforcement details are in compliance with the current seismic code in Turkey (i.e., TEC2018). The details of reinforcements used for all specimens are given in Figure 3-44.

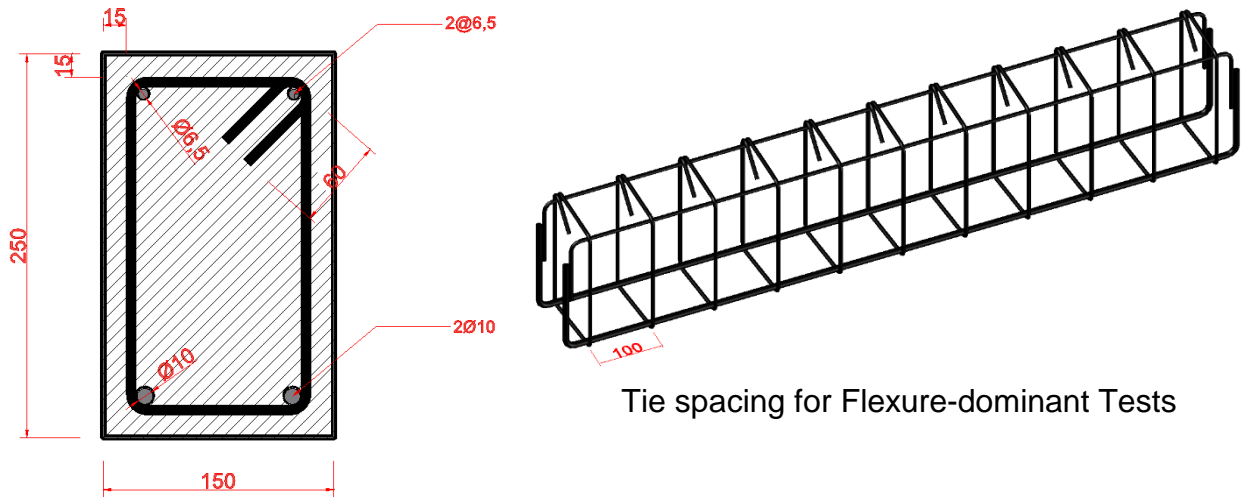
Table 3-12 Summary of Test Specimens

Specimens	Average Concrete Compressive Strength (MPa)	Average Concrete Splitting Tensile Strength (MPa)
GPC-NA and NGC Specimens	37.50 (2.83)*	2.56 (0.29)
GPC-RA and NGC-R Specimens	36.60 (2.06)	2.37 (0.31)
CVC and C Specimens	34.10 (1.32)	2.45 (0.15)
CVC and C-R Specimens	35.20 (1.60)	2.21(0.17)

\*: Numbers in parantheses are standard deviations.

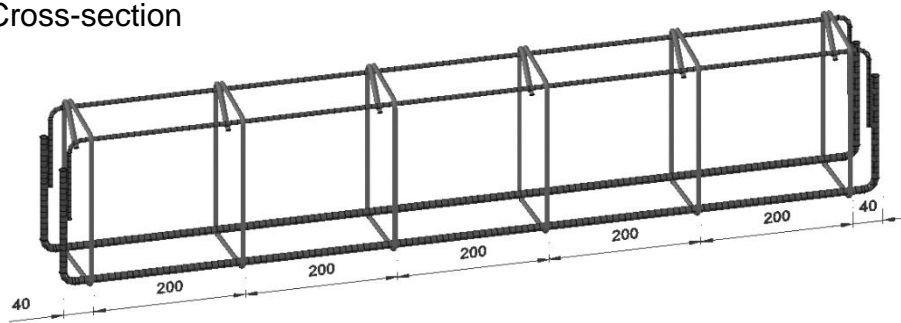
The test setup is shown in Figure 3-45. Vertical loads were applied by a displacement-controlled hydraulic actuator. All specimens were tested under a four-point loading system, i.e., subjected to two-point loads and supported on pin supports at both ends. The clear span of each specimen was 1000mm. For all specimens, applied vertical forces were monitored with a load cell. The midspan vertical displacement was measured using Linear Variable Differential Transformers (LVDTs) placed at the center of the beam. The average curvature response of all specimens was also determined by placing lateral LVDTs (Figure 3-45). Lateral LVDTs were placed in beam specimens at 100-mm, 50-mm, and 100-mm intervals for left span, midspan, and right span, respectively (Figure 3-45). All beam specimens were tested under a four-point bending test shown in Figure 3-45. Load deflection curves, moment-curve curves, and crack patterns were determined in order to compare the performance of geopolymer concrete.



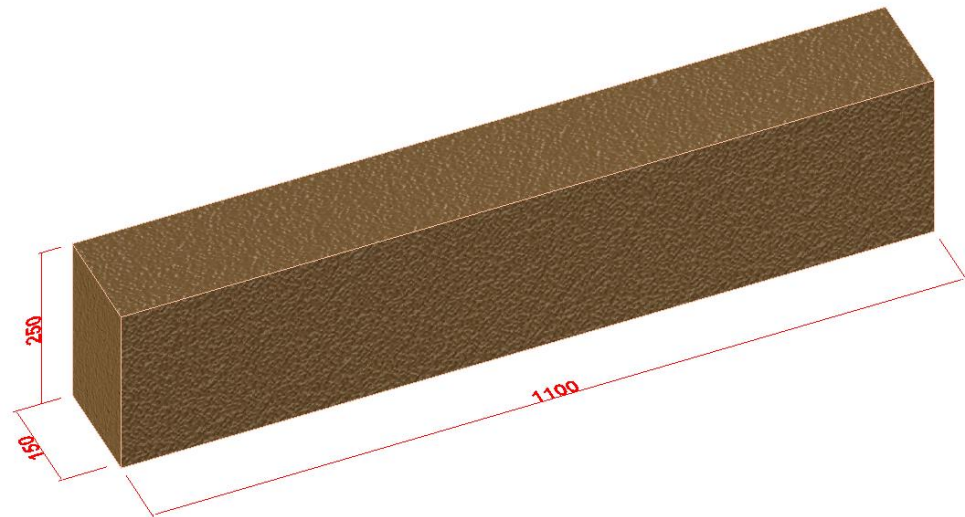


Cross-section

Tie spacing for Flexure-dominant Tests



Tie spacing for Shear-dominant Tests



Dimensions of Beam Specimens

Figure 3-44 Reinforcement Details of the Test Specimens

\* All dimensions are given in mm.



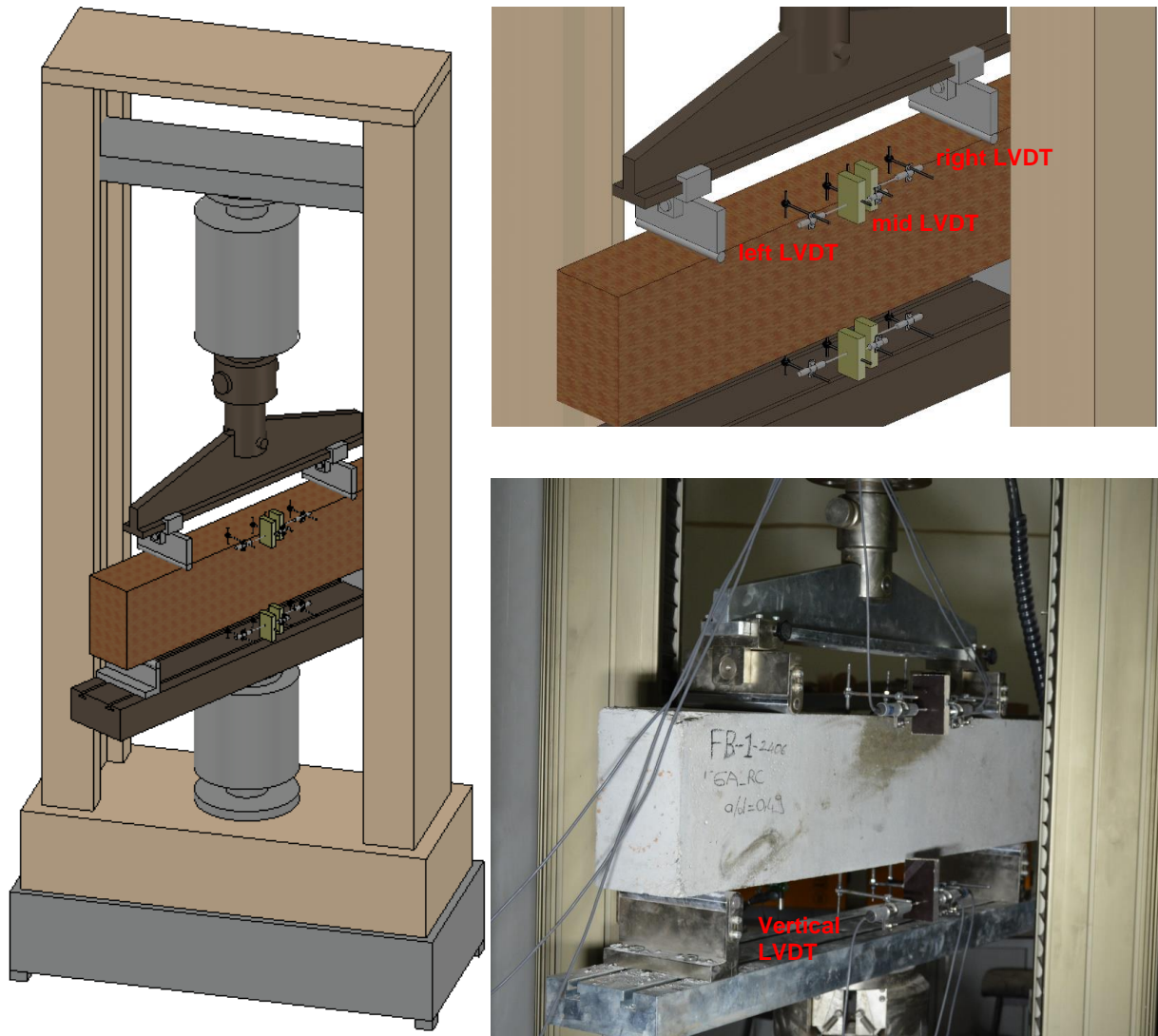


Figure 3-45 Test Setup and Instrumentation

### 3.4.2.2 Flexural Behaviour

In this section, the test results and the observed crack patterns during each flexure-dominant specimen were documented. To this end, the vertical load-midspan displacement and the moment-curvature responses of all specimens are drawn and compared with different materials for a constant  $a/d$  ratio. For the sake of clarity, the ultimate force ( $F_u$ ), ultimate displacement ( $u_u$ : displacement corresponding to the end of the test or the 20% capacity drop), the yield force, and displacement ( $F_y$  and  $u_y$  determined by using the bilinearization procedure in FEMA356), the displacement ductility ( $\mu_u$ :  $u_u / u_y$ ), the ultimate curvature ( $\phi_u$ : curvature corresponding to the end of the test or the 20% capacity drop), the yield curvature ( $\phi_y$ : yield curvature determined by using the bilinearization procedure in FEMA356), the curvature ductility ( $\mu_\phi$ :  $\phi_u / \phi_y$ ), the energy dissipation capacity

( $E_t$ ) and the normalized energy capacity ( $E_n: E_t / (F_y \times u_y / 2)$ ) measured during the tests are tabulated. The damage photographs at different displacement levels are also presented. The compressive strength and splitting tensile strength of each specimen were determined on the test day. Average strengths and their standard deviations are presented in Table 3-12.

### Test Results of Beam Specimens with $a/d = 0.50$

The total vertical load-midspan displacement and the moment-curvature responses of CVC-NA-0.50, CVC-RA-0.50, GPC-NA-0.50, and GPC-RA-0.50 are given in Figure 3-46. It could easily be inferred from Figure 3-46 that the response of all specimens is brittle. Limited or no post-yield response was observed. This observation was also validated by the determined crack patterns (Figure 3-47). It is apparent from Figure 3-47 that all specimens failed by a shear – crack reaching the support. The yield and ultimate loads, yield and ultimate displacements, as well as the ductility indices, were presented in Table 3-13.

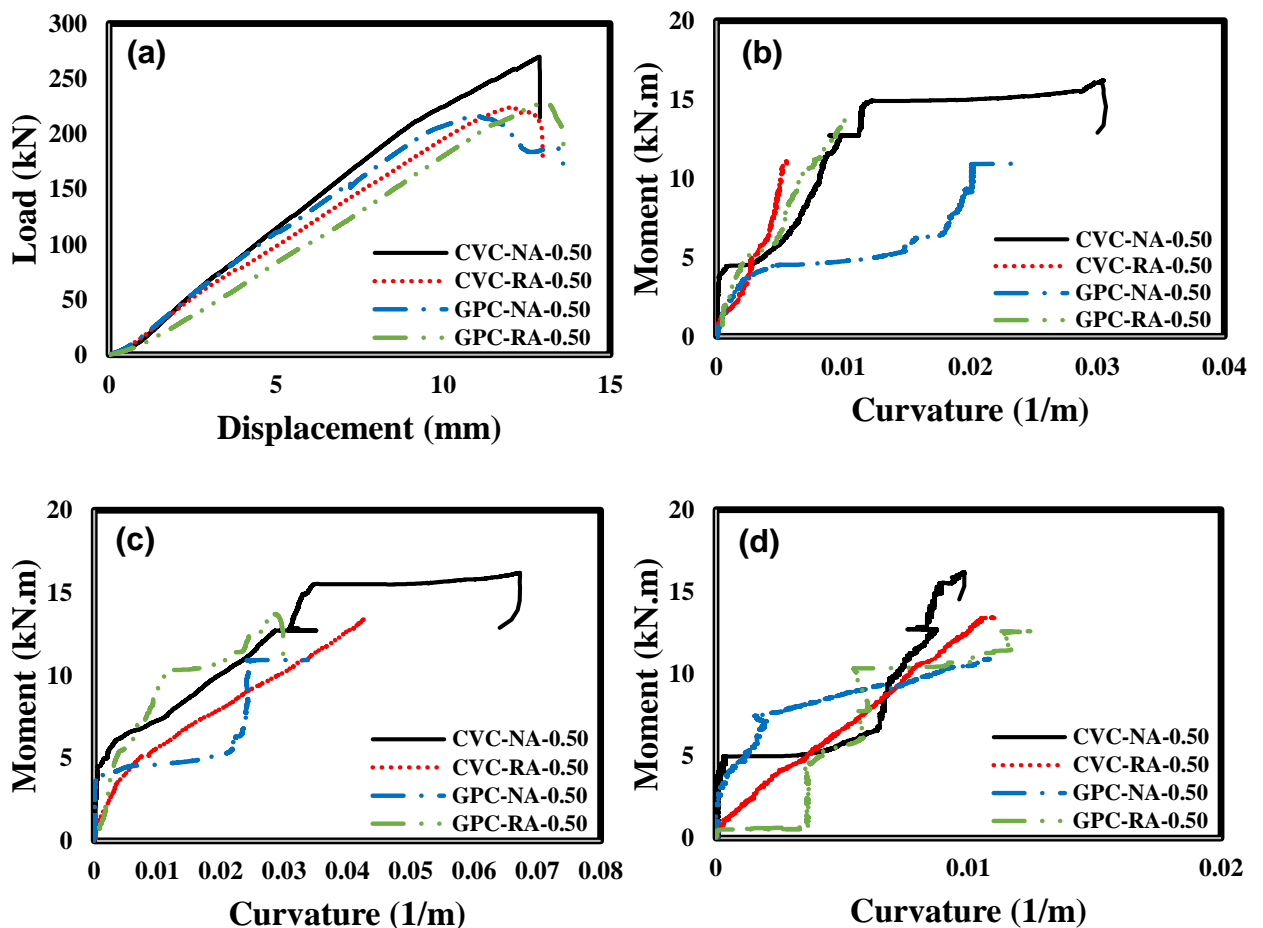


Figure 3-46 Test Results of Beam Specimens with  $a/d=0.50$ : (a) Total vertical load-midspan displacement, (b) the moment-curvature curve from left LVDTs, (c) the moment-curvature curve from mid-LVDTs, and (d) the moment-curvature curve from right LVDTs





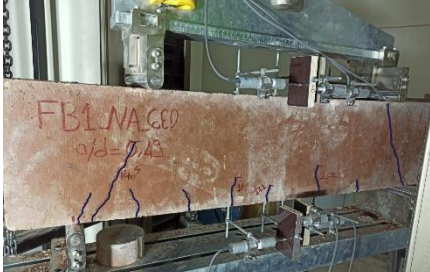

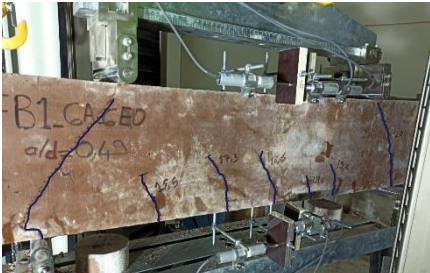

Specimen	Crack Initiation	Ultimate Stage
CVC – NA – 0.50		
CVC – RA – 0.50		
GPC – NA – 0.50		
GPC – RA – 0.50		

Figure 3-47 Observed Crack Patterns of Beam Specimens with  $a/d=0.50$

Table 3-13 Summary of Test Results

Parameters	<i>a/d = 0.50</i>				<i>a/d = 1.00</i>				<i>a/d = 1.65</i>			
	CVC-NA	CVC-RA	GPC-NA	GPC-RA	CVC-NA	CVC-RA	GPC-NA	GPC-RA	CVC-NA	CVC-RA	GPC-NA	GPC-RA
$F_y$ (kN)	230.11	204.51	205.85	220.08	165.10	168.81	165.98	170.06	99.16	98.91	99.08	99.18
$F_u$ (kN)	270.05	224.46	216.82	228.58	180.40	183.63	184.68	189.66	112.08	102.11	105.04	103.5
$M_y$ (kN.m)	NA	NA	NA	NA	18.26	16.18	18.91	19.65	18.86	16.49	19.89	18.96
$M_u$ (kN.m)	16.20	13.46	13.00	13.71	22.10	22.49	23.23	21.85	19.91	20.48	20.18	20.18
$u_y$ (mm)	10.09	11.60	8.20	12.00	9.16	11.25	11.16	10.45	9.16	8.16	9.81	9.96
$u_u$ (mm)	13.18	13.63	14.11	15.5	20.89	27.91	26.18	21.78	39.81	26.63	37.68	26.02
$\phi_y$ (1/m)	NA	NA	NA	NA	0.03	0.03	0.03	0.03	0.11	0.09	0.10	0.10
$\phi_u$ (1/m)	NA	NA	NA	NA	0.13	0.11	0.12	0.10	0.96	0.65	0.98	0.72
$\mu_u$	1.31	1.18	1.72	1.29	2.28	2.48	2.35	2.08	4.35	3.26	3.84	2.61
$\mu_\phi$	NA	NA	NA	NA	4.33	3.67	4.17	3.85	8.72	7.22	9.80	7.21
$E_t$ (kN.m)	1.90	1.69	1.87	1.88	4.23	3.67	4.43	3.00	3.53	2.31	3.23	2.27
$E_n$	1.64	1.42	2.22	1.43	5.60	3.87	4.78	3.37	7.77	5.72	6.65	4.60

### Test Results of Beam Specimens with $a/d = 1.00$

The total vertical load-midspan displacement and the moment-curvature responses of CVC-NA-1.00, CVC-RA-1.00, GPC-NA-1.00, and GPC-RA-1.00 are given in Figure 3-48. It could easily be inferred from Figure 3-48 that the response of all specimens is less brittle than previous specimens. In these tests, it was observed that GPC specimens failed with a limited or no post-yield response due to less amount of flexure cracks at the midspan. However, CVC specimens showed a mixed shear-flexure failure, resulting in more ductility. This observation was also validated by the determined crack patterns (Figure 3-49). The yield and ultimate loads, yield and ultimate displacements, and the ductility indices, were presented in Table 3-13.

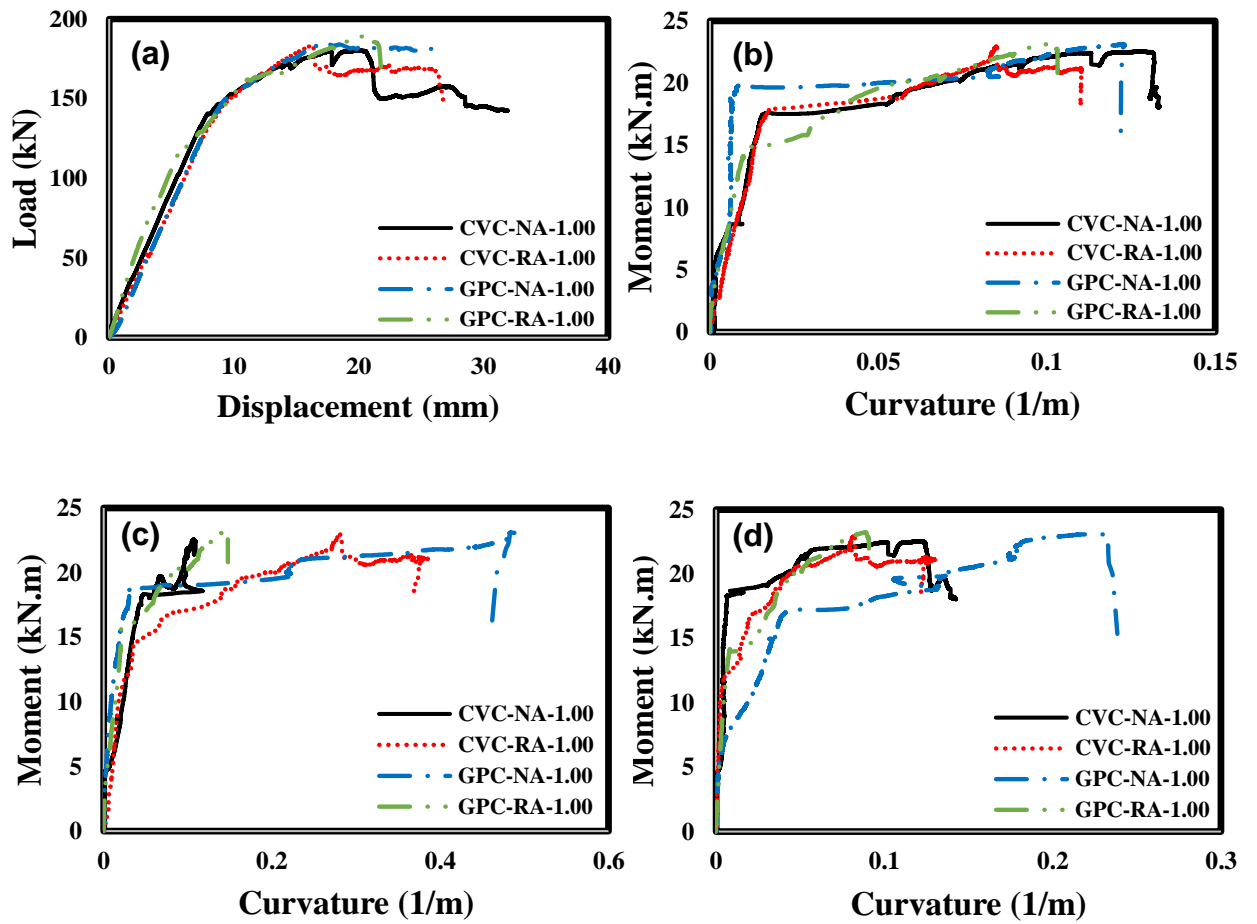


Figure 3-48 Test Results of Beam Specimens with  $a/d=1.00$ : (a) Total vertical load-midspan displacement, (b) the moment-curvature curve from left LVDTs, (c) the moment-curvature curve from mid-LVDTs, and (d) the moment-curvature curve from right LVDTs



Specimen	Crack Initiation	Ultimate Stage
CVC – NA – 1.00		
CVC – RA – 1.00		
GPC – NA – 1.00		
GPC – RA – 1.00		

Figure 3-49 Observed Crack Patterns of Beam Specimens with  $a/d=1.00$

### Test Results of Beam Specimens with $a/d = 1.65$

The total vertical load-midspan displacement and the moment-curvature responses of CVC-NA-1.65, CVC-RA-1.65, GPC-NA-1.65, and GPC-RA-1.65 are given in Figure 3-50. It could easily be inferred from Figure 3-50 that the response of all specimens is brittle. Limited or no post-yield response was observed. This observation was also validated by the determined crack patterns (Figure 3-51). It is apparent from Figure 3-51 that all specimens failed by a shear – crack reaching the support. The yield and ultimate loads, yield and ultimate displacements, and the ductility indices, are presented in Table 3-13.



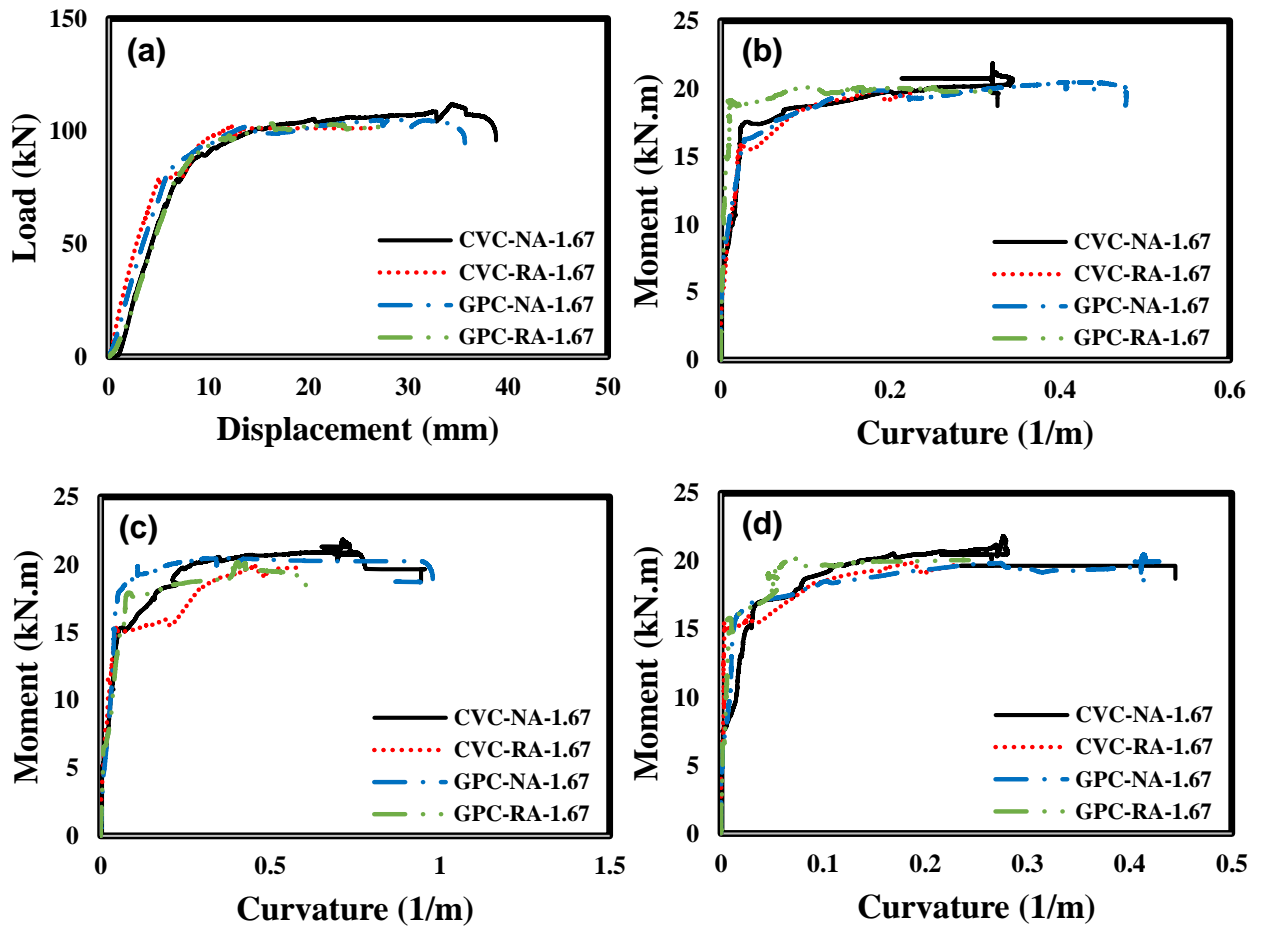


Figure 3-50 Test Results of Beam Specimens with  $a/d=1.65$ : (a) Total vertical load-midspan displacement, (b) the moment-curvature curve from left LVDTs, (c) the moment-curvature curve from mid-LVDTs, and (d) the moment-curvature curve from right LVDTs


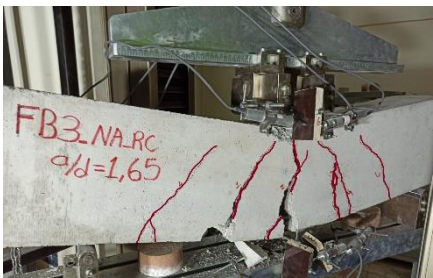



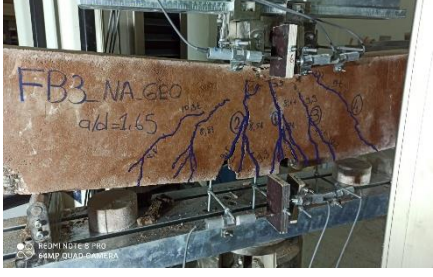


Specimen	Crack Initiation	Ultimate Stage
CVC – NA – 1.65		
CVC – RA – 1.65		
GPC – NA – 1.65		
GPC – RA – 1.65		

Figure 3-51 Observed Crack Patterns of Beam Specimens with  $a/d=1.65$

### 3.4.2.3 Discussion of Test Results

The first shear-span-to-depth ratio was selected as 0.50 in order to investigate the possible shear failure for these code-conforming beam specimens. As expected, all specimens, independent from the construction material chosen, failed in shear and showed brittle load-deflection and moment-curvature responses. Although the moment-curvature curves were not suitable to examine the behavior of reinforced concrete specimens due to the formation of inclined cracks between the load application point and the support, the change in the curvature response over the beam was also provided for the sake of completeness. It could easily be inferred from Figure 3-46 that geopolymer

concrete had very similar behavior compared to its conventional concrete counterparts in terms of load and deformation capacities. The failure patterns of all specimens were also detected to be similar (Figure 3-47). This observation proved that, for shear dominant behavior, i. the recycled aggregate had a very limited impact on the performance of concrete, and ii. the reinforced geopolymer concrete could perform nearly the same as the conventional reinforced concrete if the shear-dominant behavior was investigated. In addition, the displacement and curvature ductilities of all specimens (i.e., CVC-NA-0.50, CVC-RA-0.50, GPC-NA-0.50, and GPC-RA-0.50) were determined to be very low (Table 3.13). The other observation was that the normalized energy dissipation capacities of all specimens with recycled aggregates were also less than other specimens without recycled aggregates (Table 3.13).

The second shear-span-to-depth ratio (i.e.,  $a/d=1.00$ ) was used to determine the mixed shear-flexure failure for code-conforming reinforced beam specimens. All CVC specimens failed in shear-flexure combined action, manifesting itself by inclined cracks between the support and load application point and vertical cracks at the midspan. However, GPC specimens failed with a limited or no post-yield response due to fewer flexure cracks at the midspan. Unlike the first  $a/d$  ratio (i.e., 0.50), there exists some ductility, implied by the yield plateau in load-displacement and moment-curvature curves in Figure 3-48. It should be stated that the mid LVDTs attached to specimens CVC-NA-1.00 and GPC-RA-1.00 stopped recording at a load value of 81kN and 96kN, respectively. Therefore, the curvature ductility comparisons of all specimens were made by using left LVDTs. The curvature ductility values of each specimen ranged between 3.67 and 4.33. It was clear from Table 3.13 that geopolymer concrete had a curvature ductility of close to 4. If the curvature values determined from the mid LVDTs and left LVDTs were compared, the maximum curvature demand (i.e., mid LVDTs) at the midspan resulted in nearly three times the curvature demand at the left span (i.e., mid LVDTs). The reinforced geopolymer concrete could perform almost the same as the conventional reinforced concrete if the shear-flexure-dominant behavior was investigated. The other observation was that the normalized energy dissipation capacities of all specimens with recycled aggregates were also less than other specimens without recycled aggregates (Table 3.13). The decrease in normalized energy dissipation capacity for CVC and GPC specimens was 30.89% and 29.50%, respectively.

The last shear-span-to-depth ratio (i.e.,  $a/d=1.67$ ) was utilized to study the flexure-dominant failure for code-conforming reinforced beam specimens with different materials. All specimens failed in flexure-dominant action, manifesting themselves by nearly vertical cracks concentrated at the midspan. In all of these tests, there exists a significant amount of ductility, implied by the large yield plateau in load-displacement and moment-curvature curves in Figure 3-50. The curvature ductility comparisons of all specimens were made by using midspan LVDTs. The curvature ductility values of each specimen ranged between 7.21 and 9.80. It was clear from Table 3.13 that geopolymer concrete had a curvature ductility of close to 10, which is near twice the curvature ductility of specimens with an  $a/d$  ratio of 1.00. The failure patterns of all specimens were also detected to be similar (Figure 3-51). This observation proved that the reinforced

geopolymer concrete could perform nearly the same as the conventional reinforced concrete if the flexure-dominant behavior was investigated. However, the recycled aggregate had a negative effect on the performance of concrete, i.e., some reduction in ductility and hence energy dissipation capacity was observed (Table 3-13).

The capacity estimation performances of two current codes: ACI318-19 and TS500, were also investigated in the scope of this study. The nominal shear capacity and the nominal moment capacities of each specimen were calculated by using proposed equations in ACI318-19 and TS500 and are presented in Table 3-14. In Table 3-14, the estimated capacity ( $V_{cap}$ ) was obtained from the minimum of the nominal shear strength ( $V_n$ ) and the ratio of nominal moment capacity ( $M_n$ ) to moment arm. It could easily be inferred that the estimation performance of TS500 is slightly better than the estimation performance of ACI318-19. It should also be noted that the estimation performance of codes is independent of the material type and the use of recycled aggregates. Besides, the estimation performance is slightly better for shear-dominant failures.

Table 3-14 Estimation Performance of Code Proposed Equations

Specimens	Experiment			TS500 Estimations				ACI318-19 Estimations			
	$M_{max}$ (kN.m)	$F_{max}$ (kN)	$V_{max}$ (kN)	$M_n$ (kN.m)	$V_n$ (kN)	$V_{cap}$ (kN)	Error (%)	$M_n$ (kN.m)	$V_n$ (kN)	$V_{cap}$ (kN)	Error (%)
<b>CVC-NA-0.50</b>	16.2	270.1	135.0	15	91.6	91.60	- 32.15	12.7	89.2	89.2	- 33.93
<b>CVC-RA-0.50</b>	13.5	224.5	112.2	15.1	96.5	96.50	- 13.99	12.8	93.8	93.8	- 16.40
<b>GPC-NA-0.50</b>	13.0	216.8	108.4	15	95.1	95.10	- 12.27	12.8	92.5	92.5	- 14.67
<b>GPC-RA-0.50</b>	13.7	228.6	114.3	15	94.6	94.60	- 17.24	12.8	92.1	92.1	- 19.42
<b>CVC-NA-1.00</b>	22.1	180.4	90.2	15	91.6	61.22	- 32.12	12.7	89.2	51.84	- 42.53
<b>CVC-RA-1.00</b>	22.5	183.6	91.8	15.1	96.5	61.63	- 32.86	12.8	93.8	52.24	- 43.09
<b>GPC-NA-1.00</b>	22.6	184.7	92.3	15	95.1	61.22	- 33.67	12.8	92.5	52.24	- 43.40
<b>GPC-RA-1.00</b>	23.2	189.7	94.8	15	94.6	61.22	- 35.42	12.8	92.1	52.24	- 44.89
<b>CVC-NA-1.67</b>	21.9	112.1	56.0	15	91.6	38.46	- 31.32	12.7	89.2	32.56	- 41.85
<b>CVC-RA-1.67</b>	19.9	102.1	51.1	15.1	96.5	38.72	- 24.23	12.8	93.8	32.82	- 35.77
<b>GPC-NA-1.67</b>	20.5	105.0	52.5	15	95.1	38.46	- 26.74	12.8	92.5	32.82	- 37.48
<b>GPC-RA-1.67</b>	20.2	103.5	51.8	15	94.6	38.46	- 25.75	12.8	92.1	32.82	- 36.64

#### 3.4.2.4 Shear Behaviour

##### **Beam Specimens with a shear-span-to-depth ratio of 0.50**

The total vertical load-midspan vertical displacement and the moment-curvature responses of C-0.50, C-R-0.50, NGC-0.50, NGC-R-0.50 are presented in Figure 3.52. From Figure 3-52, it is clear that the flexural response of all specimens is observed to be brittle. The limited or no post-yield response was observed. This observation was also validated by the determined crack patterns (Figure 3-53). It is apparent from Figure 3-49 that all specimens failed by a shear – crack reaching the support. The yield and ultimate loads and yield and ultimate displacements, as well as the ductilities, are presented in



Table 3-15.

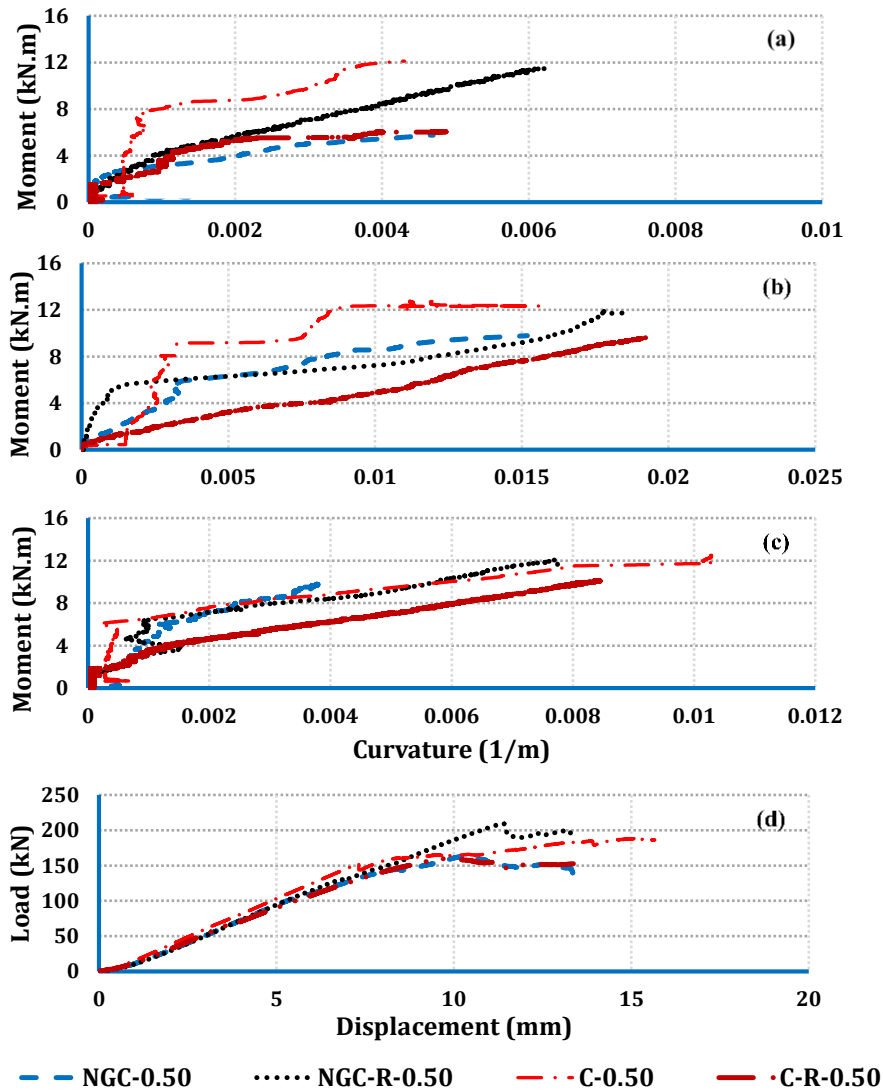


Figure 3-52 Test Results of Beam Specimens with  $a/d=0.50$ : (a) the moment-curvature curve from left LVDTs, (b) the moment-curvature curve from mid-LVDTs, (c) the moment-curvature curve from right LVDTs, and (d) Total vertical load-midspan vertical displacement

All specimens with an  $a/d$  ratio of 0.50 failed in shear, independent from the construction material. They, therefore, showed brittle load-deflection and moment-curvature responses. Similar findings were found in the literature that the arch mechanism was more dominant than the effect of matrix properties and type of the aggregate in the shear resistance contribution at lower  $a/d$  ratios. The failure of each specimen resulted from a large inclined crack in the shear span (Figure 3-53). Thus, the moment-curvature curves showed a limited deviation from the linear range. It could easily be stated from Figure 3-52 that the load and deformation capacities of all selected construction materials are similar. If the normalized energies are compared, it could be claimed that the inclusion of recycled aggregate results in a reduction in the energy dissipation capacities. In summary, the reinforced geopolymer concrete could perform nearly the same as the conventional reinforced concrete if the shear-dominant



behavior was investigated. Besides, the displacement and curvature ductilities of all specimens were determined to be very low (

Table 3-15).




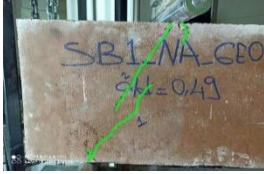



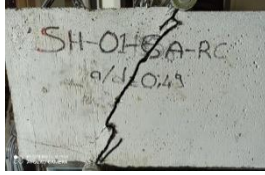


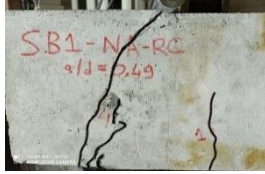

Test Specimen	Initial Crack	Crack	Final Stage
NGC-0.50			
NGC-R-0.50			
C-0.50			
C-R-0.50			

Figure 3-53 Observed Crack Patterns of Test Specimens with  $a/d=0.50$

Table 3-15 Summary of Test Results

Parameters	<i>a/d = 0.50</i>				<i>a/d = 1.00</i>				<i>a/d = 1.65</i>			
	C	C-R	NGC	NGC-R	C	C-R	NGC	NGC-R	C	C-R	NGC	NGC-R
$F_y$ (kN)	187.06	155.26	156.39	198.96	168.10	165.31	170.78	162.47	91.35	106.59	94.79	91.89
$F_u$ (kN)	195.24	159.94	164.18	206.32	190.03	191.49	192.4	190.4	94.93	110.82	98.63	103.89
$M_y$ (kN.m)	10.62	9.31	9.38	11.94	21.01	20.66	21.35	20.31	17.81	20.79	19.26	17.92
$M_u$ (kN.m)	11.71	9.60	9.85	12.38	23.75	23.94	24.05	23.80	18.51	21.61	19.04	20.26
$u_y$ (mm)	10.50	8.50	8.55	11.50	8.91	10.21	10.18	9.56	9.21	9.11	9.15	9.25
$u_u$ (mm)	15.18	13.78	13.89	13.86	13.18	16.47	19.05	15.34	14.41	30.57	14.51	35.05
$\phi_y$ (1/m)	0.0055	0.0198	0.0060	0.0031	0.017	0.020	0.021	0.019	0.031	0.035	0.035	0.052
$\phi_u$ (1/m)	0.0153	0.0198	0.0151	0.0181	0.076	0.096	0.103	0.092	0.181	0.206	0.175	0.231
$\mu_u$	1.45	1.62	1.62	1.21	1.48	1.61	1.87	1.60	1.56	3.36	1.59	3.79
$\mu_\phi$	2.78	1.00	2.52	5.84	4.47	4.80	4.90	4.84	5.84	5.89	5.00	4.44
$E_t$ (kN.m)	2.345	1.509	1.515	2.201	1.425	1.974	2.378	1.719	1.170	2.617	0.999	3.028
$E_n$	2.388	2.287	2.266	1.924	1.903	2.339	2.736	2.213	2.781	5.390	2.304	7.125

### Test Results of Beam Specimens with $a/d = 1.00$

The total vertical load-midspan displacement and the moment-curvature responses of C-1.00, C-R-1.00, NGC-1.00, and NGC-R-1.00 are given in Figure 3-54. It could easily be inferred from Figure 3-54 that the response of all specimens is brittle. Limited or no post-yield response was observed. This observation was also validated by the determined crack patterns (Figure 3-55). It is apparent from Figure 3-55 that all specimens failed by a shear – crack reaching the support. The yield and ultimate loads and yield and ultimate displacements, as well as the ductilities, are presented in Table 3.15.

Similar to previous tests, all specimens failed in shear-dominated action, manifesting themselves by inclined cracks between the support and load application point. However, these specimens showed slightly more curvature ductilities, implied by the yield plateau in moment-curvature curves in Figure 3-50. It should be stated that the right LVDTs attached to specimens C-1.00 had some problem at the initial stage, but they started recording after some time. The curvature ductility values of each specimen were very close to 5. The failure patterns of each test specimen were detected to be similar (Figure 3-55). The effect of the inclusion of recycled aggregate was seen to be negligible for these test specimens. Therefore, it could be concluded that the recycled aggregate had a very limited impact on the performance of concrete, and the

reinforced geopolymer concrete could perform nearly the same as the conventional reinforced concrete. Besides, the normalized energy dissipation capacity of the NGC specimen was significantly larger than others, but the remaining values were close to each other (

Table 3-15).

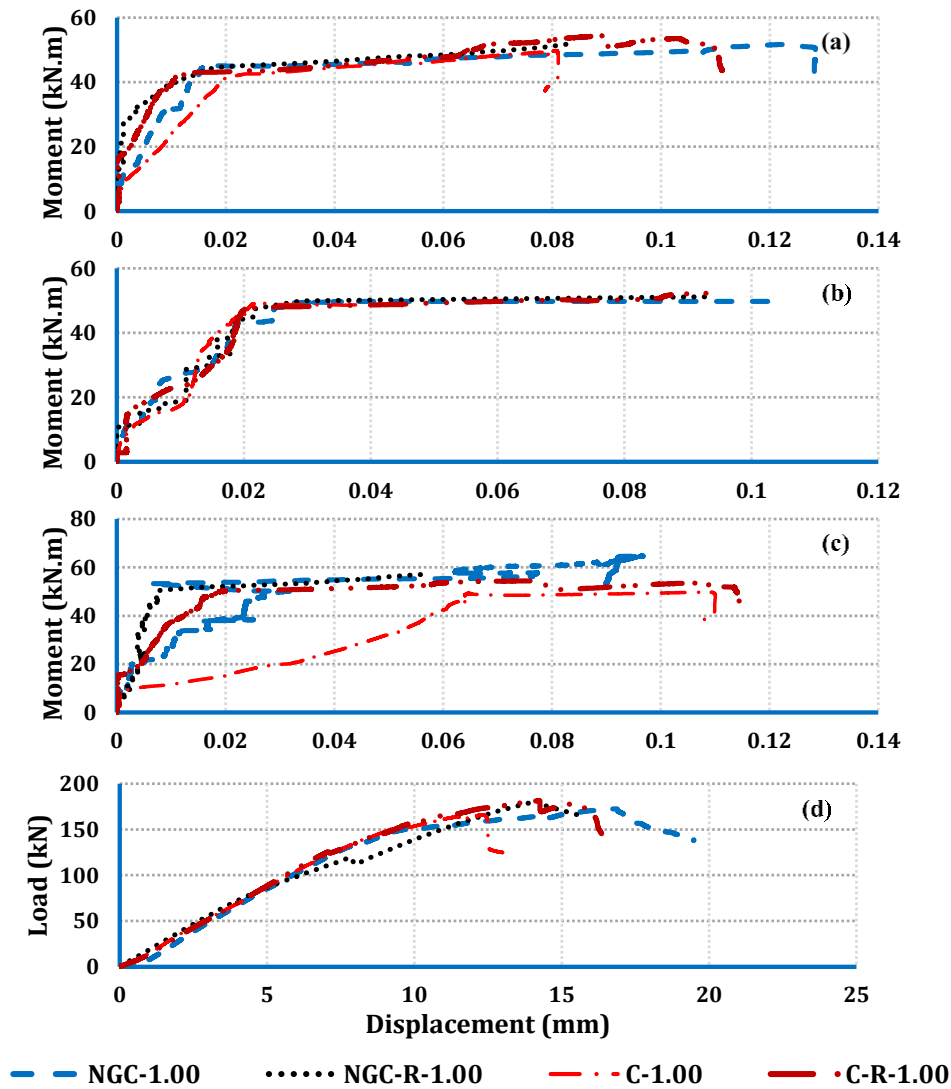


Figure 3-54 Test Results of Beam Specimens with  $a/d=1.00$ : (a) the moment-curvature curve from left LVDTs, (b) the moment-curvature curve from mid-LVDTs, (c) the moment-curvature curve from right LVDTs, and (d) Total vertical load-midspan vertical displacement

Test Specimen	Initial Crack	Crack	Final Stage
---------------	---------------	-------	-------------

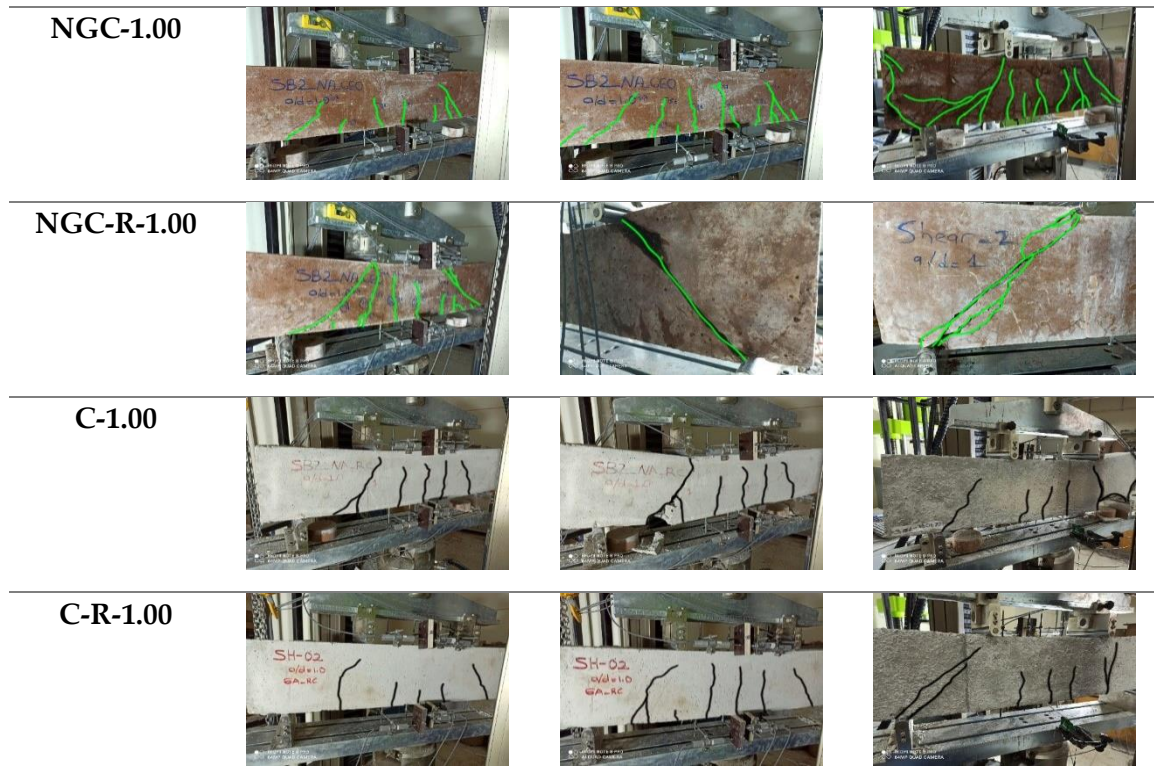


Figure 3-55 Observed Crack Patterns of Test Specimens with  $a/d=1.00$

### Test Results of Beam Specimens with $a/d = 1.65$

The total vertical load-midspan displacement and the moment-curvature responses of C-1.65, C-R-1.65, NGC-1.65, and NGC-R-1.65 are given in Figure 3-56. It could easily be inferred from Figure 3-56 that the response of all specimens is brittle. Limited or no post-yield response was observed. This observation was also validated by the determined crack patterns (Figure 3-57). It is apparent from Figure 3-57 that all specimens failed by a shear – crack reaching the support. The yield and ultimate loads and yield and ultimate displacements, as well as the ductilities, are presented in



Table 3-15.

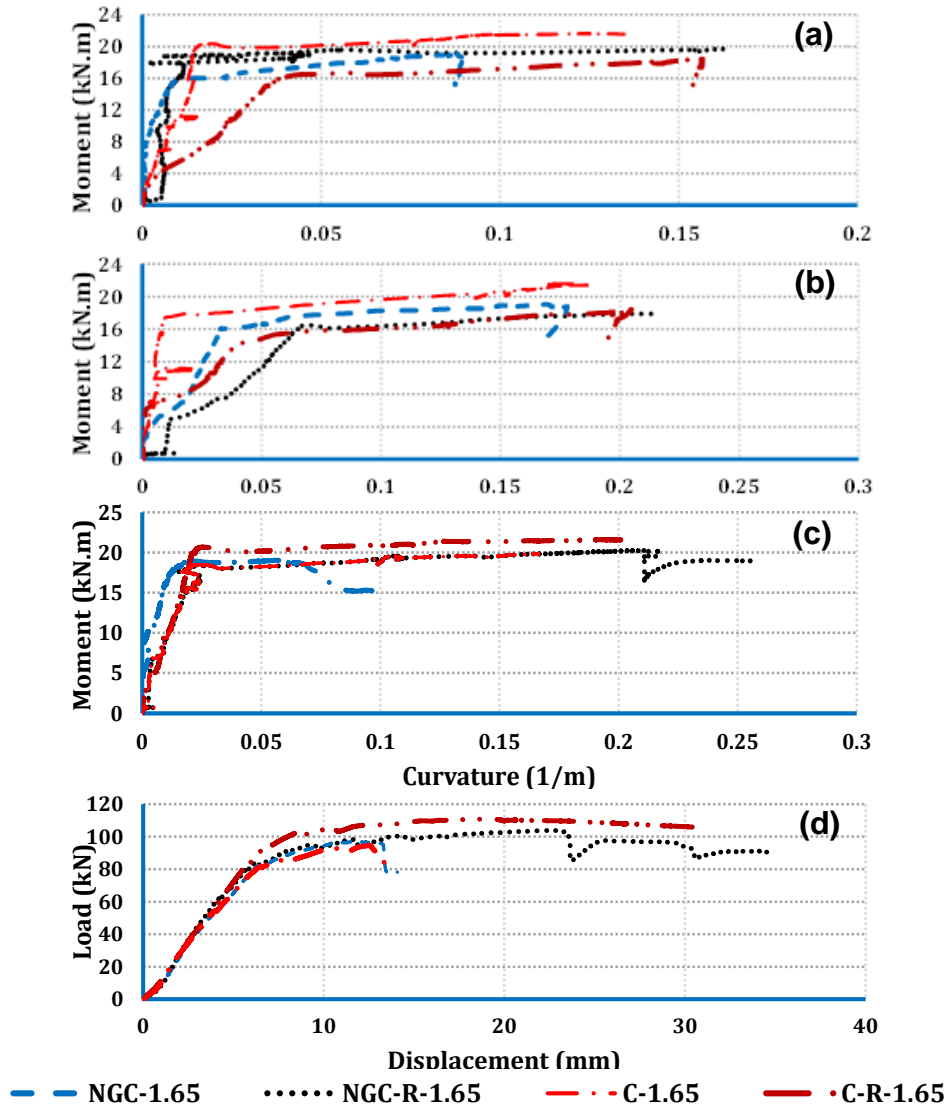


Figure 3-56 Test Results of Beam Specimens with  $a/d=1.65$ : (a) the moment-curvature curve from left LVDTs, (b) the moment-curvature curve from mid-LVDTs, (c) the moment-curvature curve from right LVDTs, and (d) Total vertical load-midspan vertical displacement

The shear-span-to-depth ratio of 1.65 was selected to study the possible shear-flexure failure. As expected, all specimens failed due to mixed shear and flexure cracks observed in the shear span and constant moment span, respectively. However, it should be noted that specimens lost their capacity due to the enlargement of inclined cracks. For this type of failure, the effect of recycled aggregates was significant. The inclusion of recycled aggregate resulted in a considerable reduction in the displacement ductility. However, the curvature ductility was not affected by the recycled aggregates significantly. Specimens without recycled aggregate showed a large yield plateau in load-displacement curves. However, specimens with recycled aggregates showed similar behavior to the specimens with an  $a/d$  ratio of 1.00. The normalized energy capacities of specimens without recycled aggregate were nearly two times their counterparts. Therefore, geopolymers have similar behavior to conventional concrete in the absence of recycled aggregates.

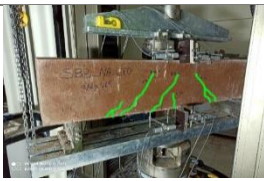

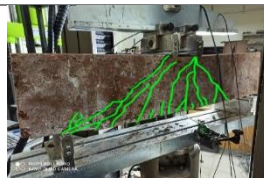
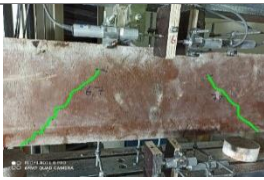



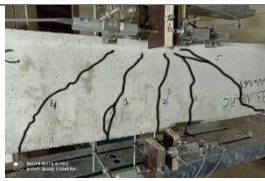




Test Specimen	Initial Crack	Crack	Final Stage
NGC-1.65			
NGC-R-1.65			
C-1.65			
C-R-1.65			

Figure 3-57 Observed Crack Patterns of Beam Specimens with  $a/d=1.65$

### 3.4.2.5 Discussion of Test Results

The test results of shear-critical beams revealed that the behavior of the geopolymer concrete specimens was similar to the conventional concrete specimens for all selected  $a/d$  ratios. In addition, except for specimens with an  $a/d$  ratio of 1.65, a large crack between the load application point and the support was observed, causing the failure of specimens. Besides, the observed shear cracks in those specimens were detected to be formed through the aggregates proving that the geopolymer paste was more robust than the used normal and recycled aggregates (Figures 3-58 & 3-59). Similar observations related to the shear crack mechanism existed for conventional concrete specimens. More importantly, the failure mechanism was insensitive to the inclusion of recycled aggregates for  $a/d$  ratios less than 1.65 (i.e., shear-dominated regions). This was mainly because the shear resisting mechanism of reinforced concrete specimens was not completely dependent on the tensile strength of concrete. The shear strength was a combination of different resistant mechanisms: Dowel action of the longitudinal reinforcement, uncrushed concrete in compression side, capacity of ties, aggregate interlock, and the tensile strength of concrete. Therefore, the effect of recycled aggregate was more pronounced in the flexure capacity.

On the contrary, the beam specimens with an  $a/d$  ratio of 1.65 showed different performances depending on the inclusion of recycled aggregates. The inclusion of the recycled aggregate caused a shift in the flexure-dominated behavior, implied by the enhanced ductility and normalized dissipated energies. This observation could be attributed to the secondary interfacial transition zone (ITZ) formation. It was claimed that the flexural ductility of beams depended on the bond strength between aggregate and paste, although failure mode was highly dependent on the  $a/d$  ratio. Since the most important factor affecting this bond strength is ITZ, a secondary ITZ formation was observed in mixtures with recycled aggregates due to former adhered mortar content surrounding the recycled aggregates. Less amount of ductility in the shear-flexure failure could be attributed to the weakness of the extra ITZ formed in the mixtures in the presence of recycled aggregates. This secondary ITZ formation reduced the flexural capacity, postponing the shear cracks. This observation was also proved by comparing the flexural strengths of mixtures with and without recycled aggregates (Table 3.12). It was apparent from Table 3.15 that approximately 10% reduction in the flexural strength of mixtures with recycled aggregates existed. It was, furthermore, known that the effect of ITZ depends significantly on the water/binder ratio of in mixtures using recycled aggregates, and the relatively high water/binder ratio in the Portland cement beams and free water in geopolymer beams was expected to produce a weaker ITZ formation.

In addition, the available capacity prediction equations are examined in this part. To this end, the experimental shear capacity of each specimen ( $V_{max}$ ) was calculated by taking the minimum of the recorded maximum shear force ( $F_{max}$ ) and the ratio of the recorded maximum moment and the shear span (i.e.,  $M_{max} / a$ ). Besides, the nominal moment capacity ( $M_n$ ) and the nominal shear capacity ( $V_n$ ) were calculated by the equations given in ACI 318-19 and TS500, respectively. The predicted nominal capacity ( $V_{cap}$ ) was taken as the minimum of the nominal shear capacity ( $V_n$ ) and the ratio of the nominal moment capacity and the shear span (i.e.,  $M_n / a$ ). These calculated values are presented in Table 5. It could easily be inferred that the estimation performance of both codes is very similar to each other, although the prediction of TS500 equations is slightly better. The absolute minimum percentage errors of ACI318-19 (TS500) equations for different  $a/d$  ratios are 61.68% (59.61%), 67.44% (65.77%) and 35.44% (33.04%), respectively. It should be noted that the code predictions resulted in over-conservative capacities for all specimens.





Figure 3-58 Close look-up to the final state of shear cracks of test specimens with an  $a/d$  ratio of 0.49



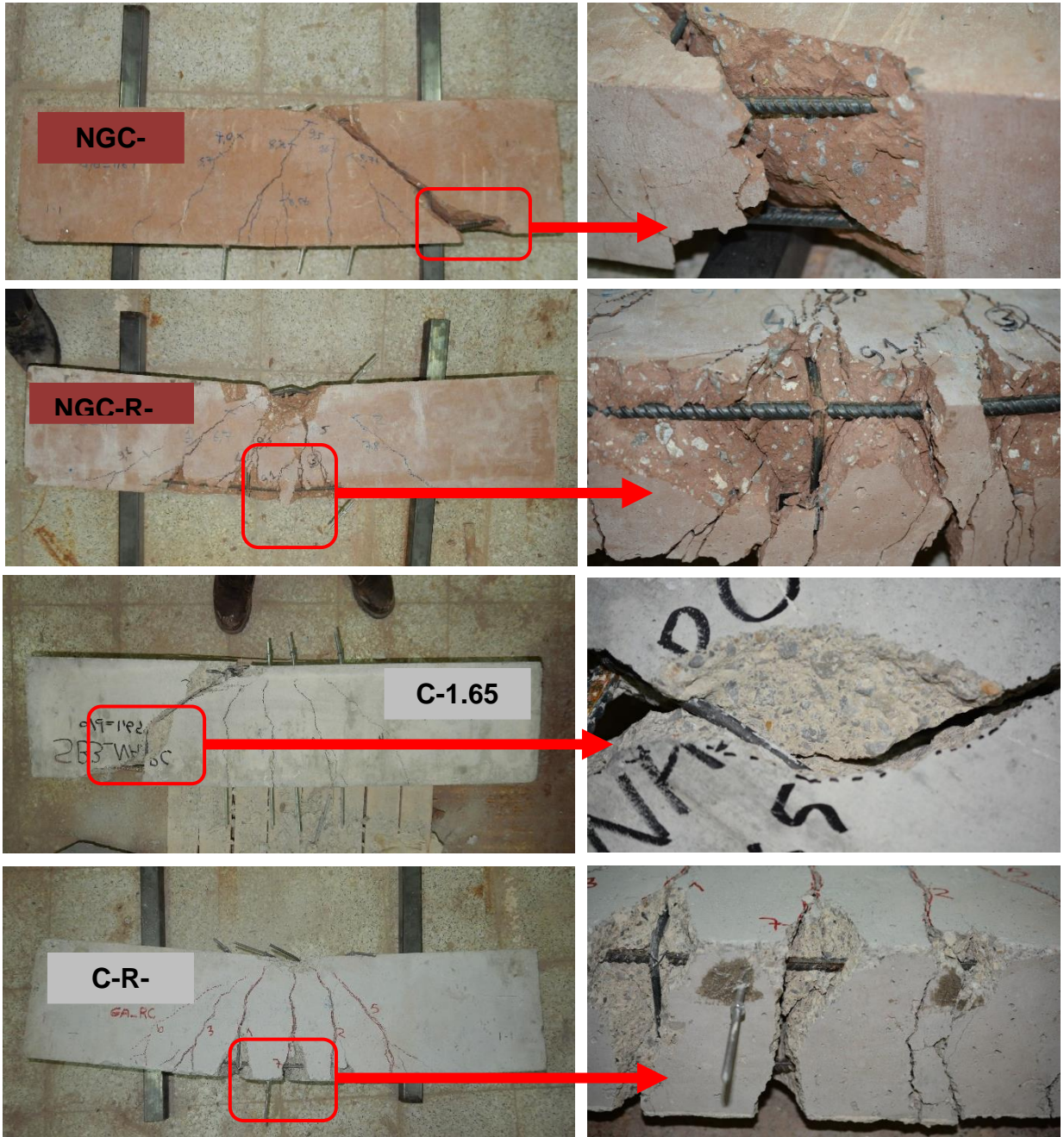


Figure 3-59 Close look-up to the final state of shear cracks of test specimens with an  $a/d$  ratio of 1.65



Table 3-16 Prediction Performance of Code Equations

Test Specimen	a/d	Experiment				TS500				ACI318-19			
		M <sub>max</sub> (kN.m)	F <sub>max</sub> (kN)	V <sub>max</sub> (kN)	M <sub>n</sub> (kN.m)	V <sub>n</sub> (kN)	V <sub>cap</sub> (kN)	Error (%)	M <sub>n</sub> (kN.m)	V <sub>n</sub> (kN)	V <sub>cap</sub> (kN)	Error (%)	
C	0.50	11.71	195.24	97.58	15.01	63.99	32.00	-67.21	12.76	60.73	30.36	-68.88	
C-R	0.50	9.6	159.94	79.97	15.10	64.61	32.30	-59.61	12.89	61.29	30.64	-61.68	
NGC	0.50	9.85	164.18	82.08	15.16	65.86	32.93	-59.88	12.98	62.43	31.21	-61.97	
NGC-R	0.50	12.38	206.32	103.16	15.08	65.37	32.69	-68.32	12.91	61.99	30.99	-69.96	
C	1.00	23.75	190.03	95.00	15.01	63.99	32.00	-66.32	12.76	60.73	30.36	-68.04	
C-R	1.00	23.94	191.49	95.75	15.10	64.61	32.30	-66.26	12.89	61.29	30.64	-67.99	
NGC	1.00	24.05	192.4	96.20	15.16	65.86	32.93	-65.77	12.98	62.43	31.21	-67.55	
NGC-R	1.00	23.8	190.4	95.20	15.08	65.37	32.69	-65.67	12.91	61.99	30.99	-67.44	
C	1.65	21.61	110.82	55.41	15.01	63.99	32.00	-42.25	12.76	60.73	30.36	-45.20	
C-R	1.65	18.51	94.93	47.46	15.10	64.61	32.30	-31.94	12.89	61.29	30.64	-35.44	
NGC	1.65	20.26	103.89	51.95	15.16	65.86	32.93	-36.61	12.98	62.43	31.21	-39.91	
NGC-R	1.65	19.04	97.63	48.82	15.08	65.37	32.69	-33.04	12.91	61.99	30.99	-36.51	

### 3.4.3 Details of numerical models

This section includes calibration studies for the numerical model to be created based on the test results presented in the previous sections. The numerical models were generated in the program ANSYS (2016). The 8-node solid element (i.e., Solid65), which has the ability to simulate both cracking and crushing of the concrete material, is assigned. Thus, the cracking behavior in the tensile zones and the crushing behavior in the compression zones of the geopolymer concrete could appropriately be simulated. In addition, the transverse and longitudinal reinforcements were represented by link elements (i.e., Link180). The selected link element has three translational degrees of freedom at each node.

The observations on the fact that the bonding behavior of geopolymer concrete is similar to that of conventional concrete. Like CVC, GPC is a nonlinear material with properties that change with time and pressure. Thus, the nonlinear behavior was mimicked by using the Drucker-Prager model combined with William-Warneke plasticity surface in the study. The cohesion ( $c$ ) and the internal friction angle ( $\phi$ ) values in the model were determined from the concrete compressive strength ( $f_{ck}$ ) and concrete tensile strength ( $f_{ctk}$ ) using Eqs. 1-2. The shear transfer coefficients for open and closed cracks had a significant impact on the estimations. Therefore, during the calibration phase, open-shear and close-shear coefficients were optimized, and the same value was utilized for all beams (Table 3-17). Besides, the steel reinforcement was characterized as an elastic-perfectly plastic material.

The numerical model is presented in Figure 3-60.

$$\phi = \text{asin} \left( \frac{f_{ck} - f_{ctk}}{f_{ck} + f_{ctk}} \right) \quad (1)$$

$$c = f_{ck} * \frac{1 - \sin(\phi)}{2 \cos(\phi)} \quad (2)$$

Table 3-17 Crack parameter values of geopolymer concrete

Concrete Parameters	
Open Shear Transfer Coefficient	0.2
Closed Shear Transfer Coefficient	0.8

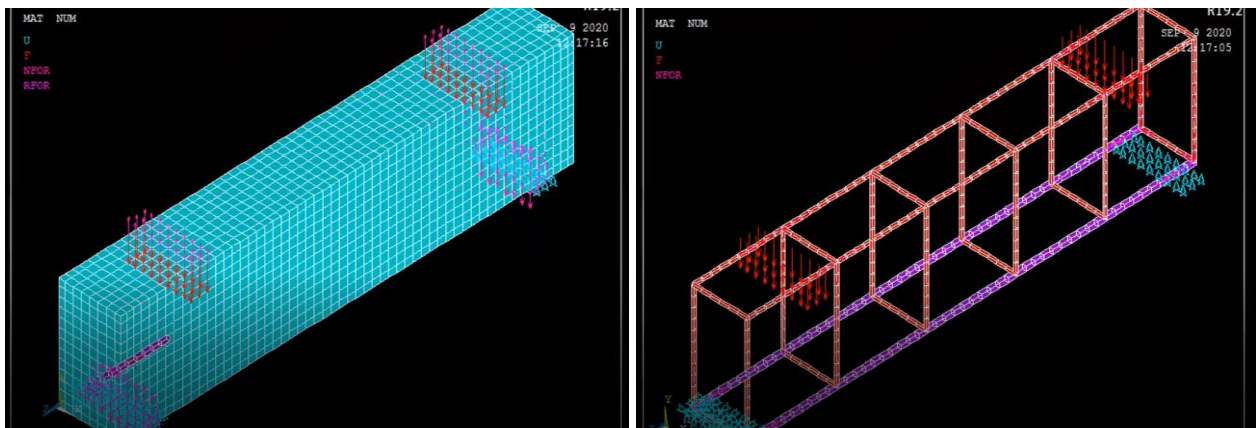


Figure 3-60 Numerical model: (a) 3D solid model and (b) Steel reinforcements

The boundary conditions of the models were assumed to be roller-supported and pin-supported at ends (Figure 3-60). The optimum mesh size was determined for numerical models. To this end, an initial mesh was selected, and the modal analysis was performed. Then, the mesh size was halved, and the model was solved again. When the difference in the estimated fundamental vibration period obtained successive models were detected to be below 1%, the coarse mesh (i.e., the mesh used in the previous analysis) was accepted as the optimum mesh (Figure 3-60). After numerous mesh sensitivity tests, it was determined that the most appropriate mesh sizes for beams were 20 mm since the difference in the estimated periods from numerical models with 10mm and 20mm maximum mesh sizes was 0.9%. The vertical load was applied using displacement-controlled loading similar to the conducted tests. The simulated beams were loaded from two points at a distance equal to the shear span.

### 3.4.3.1 Numerical Models of shear-critical beams

$a/d = 0.50$

The stirrup spacig in the geopolymer beam was taken as 200 mm, and the geopolymer shear beam with a shear span of 120 mm and an  $a/d$  ratio of 0.50 was numerically modeled as shown in Figure 3-61. The load-displacement curves obtained from experimental with the help of LVDT and numeric model were compared to each other (Figure 3-62). In addition, the estimated crack pattern was given in Figure 3-63.

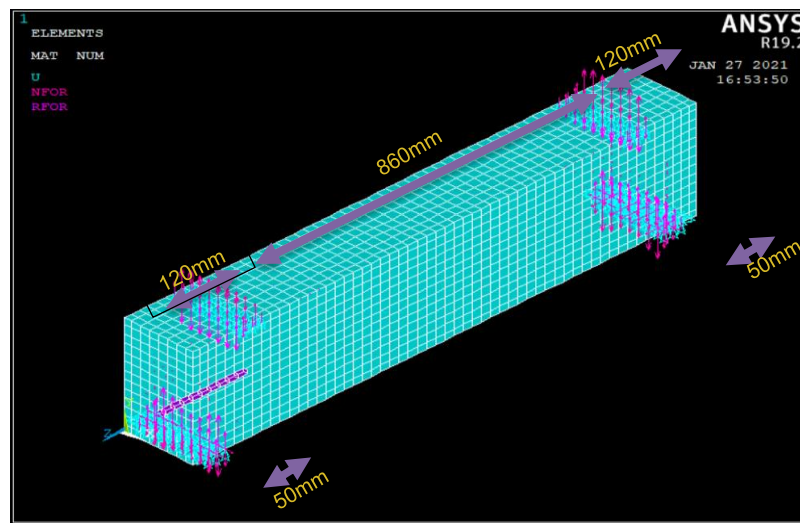


Figure 3-61 Numeric Model for  $a/d$  ratio = 0.50

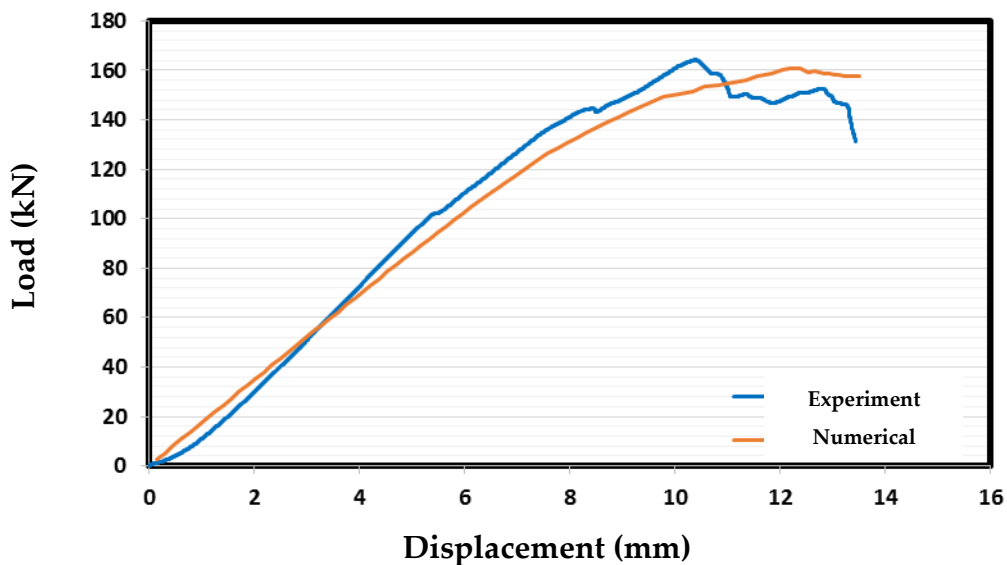


Figure 3-62 Load Displacement Curves ( $a/d = 0.50$ )

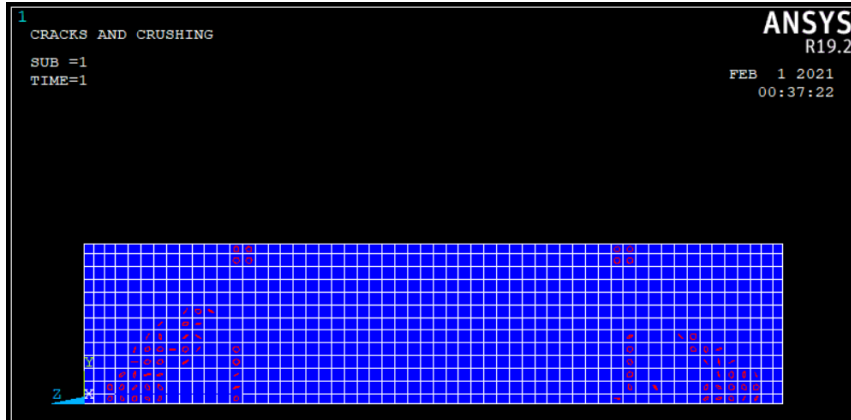


Figure 3-63 Estimated Crack Pattern ( $a/d = 0.50$ )

**$a/d = 1.00$**

The stirrup spacing in the geopolymer beam was taken as 200 mm, and the geopolymer shear beam with a shear span of 250 mm and an  $a/d$  ratio of 1.00 was numerically modeled as shown in Figure 3-64. The load-displacement curves obtained from experimental with the help of LVDT and numeric model were compared to each other (Figure 3-65). In addition, the estimated crack pattern was given in Figure 3-66.

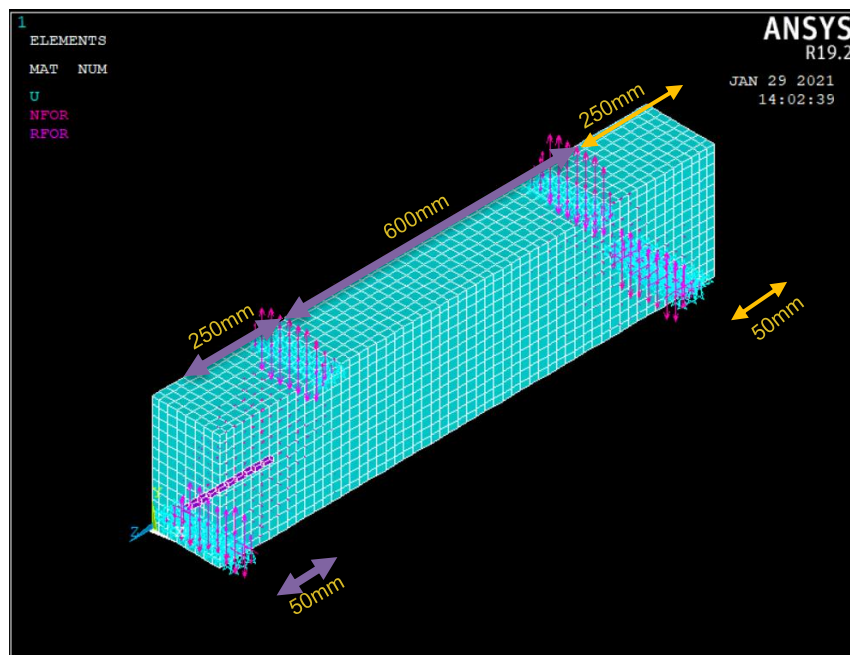


Figure 3-64 Numeric Model for  $a/d$  ratio = 1.00

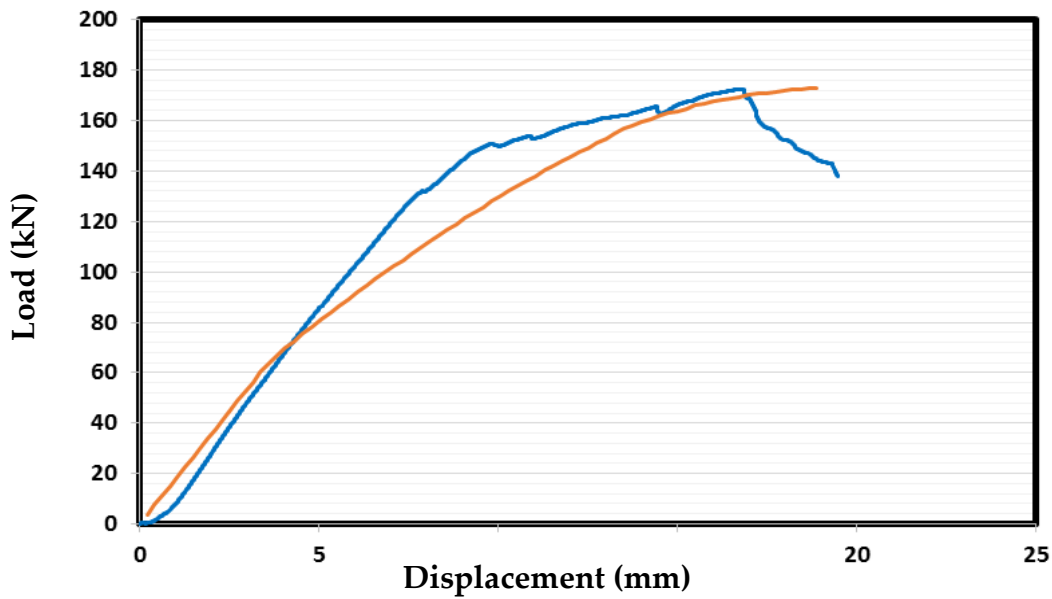


Figure 3-65 Load Displacement Curves ( $a/d = 1.00$ )

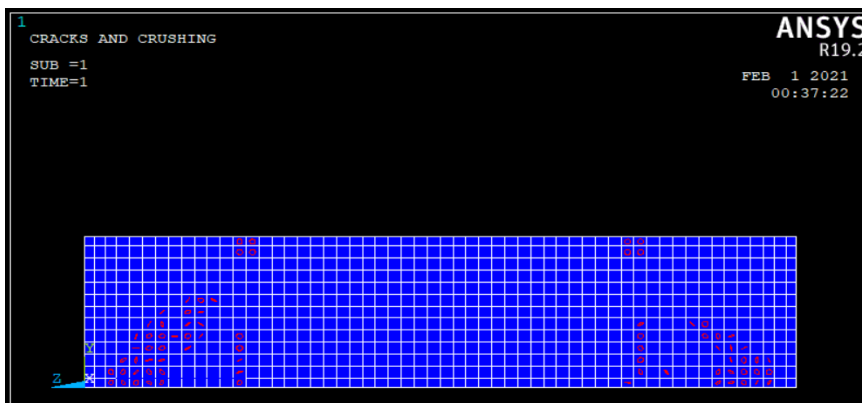


Figure 3-66 Estimated Crack Pattern ( $a/d = 1.00$ )

### $a/d = 1.65$

The stirrup spacing in the geopolymer beam was taken as 200 mm, and the geopolymer shear beam with a shear span of 390 mm and an  $a/d$  ratio of 1.65 was numerically modeled as shown in Figure 3-67. The load-displacement curves obtained from experimental with the help of LVDT and numeric model were compared to each other (Figure 3-68). In addition, the estimated crack pattern was given in Figure 3-69.

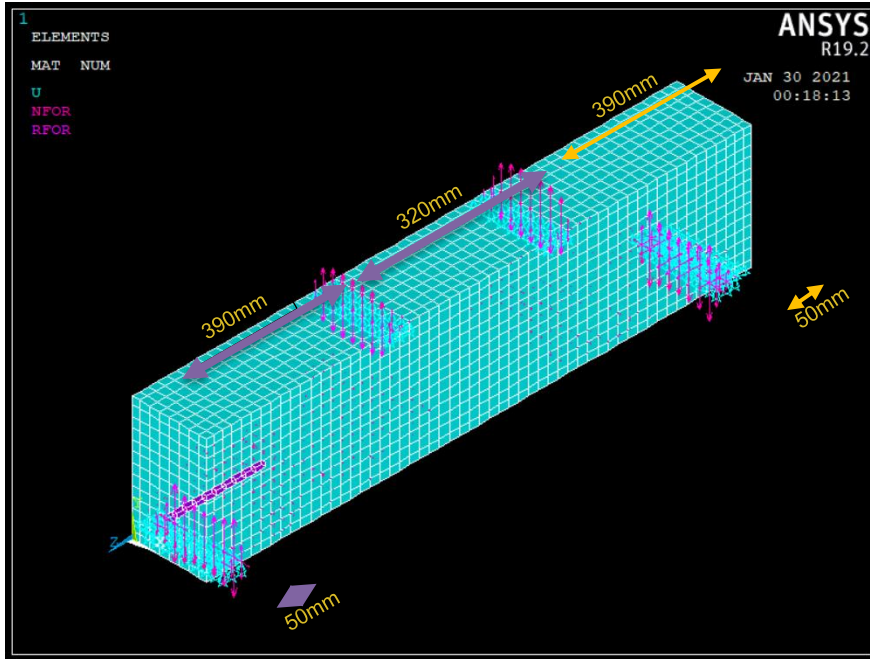


Figure 3-67 Numeric Model for  $a/d$  ratio = 1.65

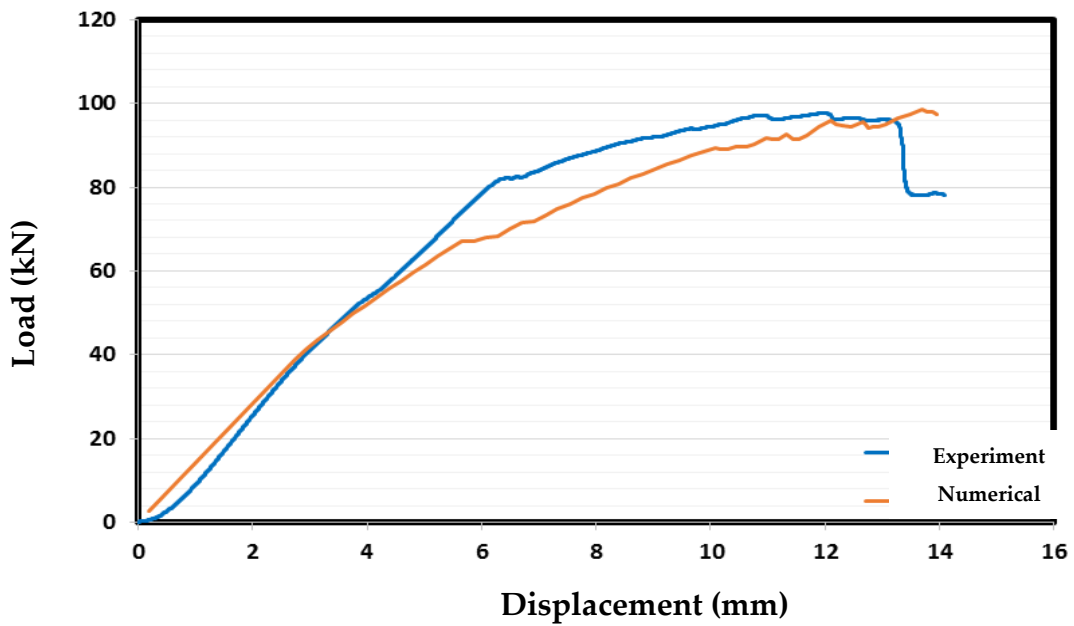


Figure 3-68 Load Displacement Curves ( $a/d = 1.65$ )



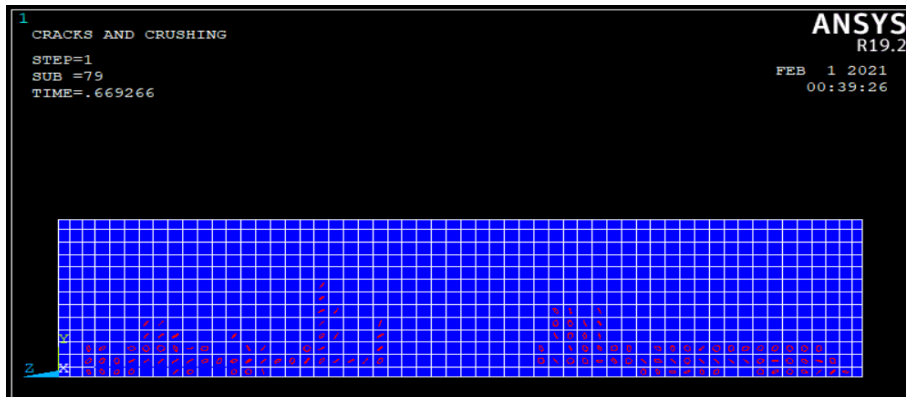


Figure 3-69 Estimated Crack Pattern ( $a/d = 1.65$ )

### 3.4.3.2 Numerical Models of flexure-critical beams

#### $a/d = 0.50$

The stirrup spacing in the geopolymer beam was taken as 100 mm, and the geopolymer shear beam with a shear span of 120 mm and an  $a/d$  ratio of 0.50 was numerically modeled. The load-displacement curves obtained from experimental with the help of LVDT and numeric model were compared to each other (Figure 3-70). In addition, the estimated crack pattern was given in Figure 3-71.

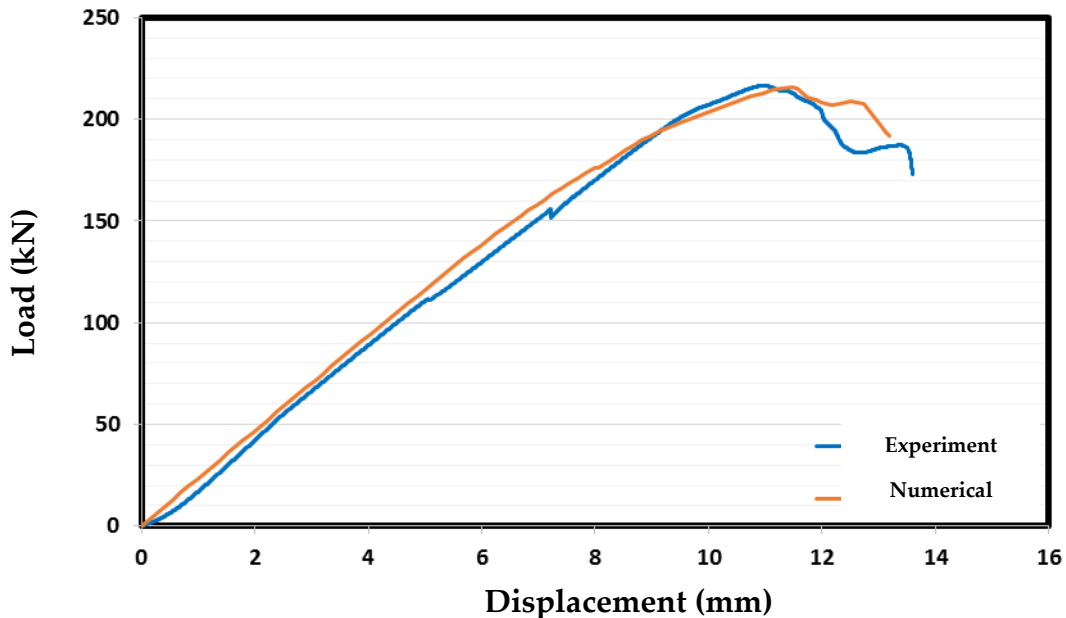


Figure 3-70 Load Displacement Curves ( $a/d = 0.50$ )

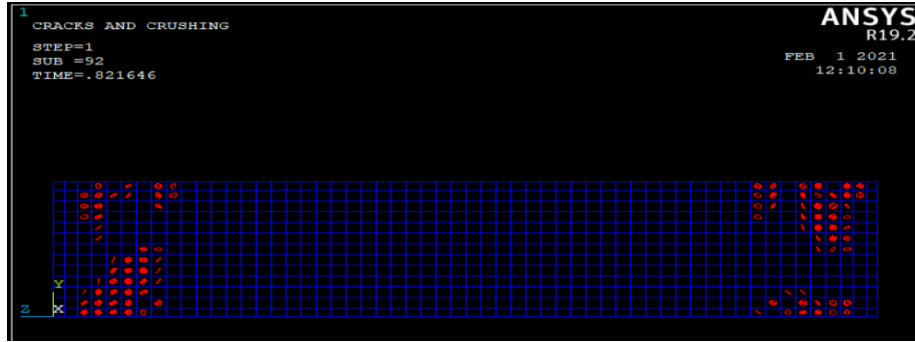


Figure 3-71 Estimated Crack Pattern ( $a/d = 0.50$ )

**$a/d = 1.00$**

The stirrup spacing in the geopolymer beam was taken as 100 mm, and the geopolymer shear beam with a shear span of 250 mm and an  $a/d$  ratio of 1.00 was numerically modeled. The load-displacement curves obtained from experimental with the help of LVDT and numeric model were compared to each other (Figure 3-72). In addition, the estimated crack pattern was given in Figure 3-73.

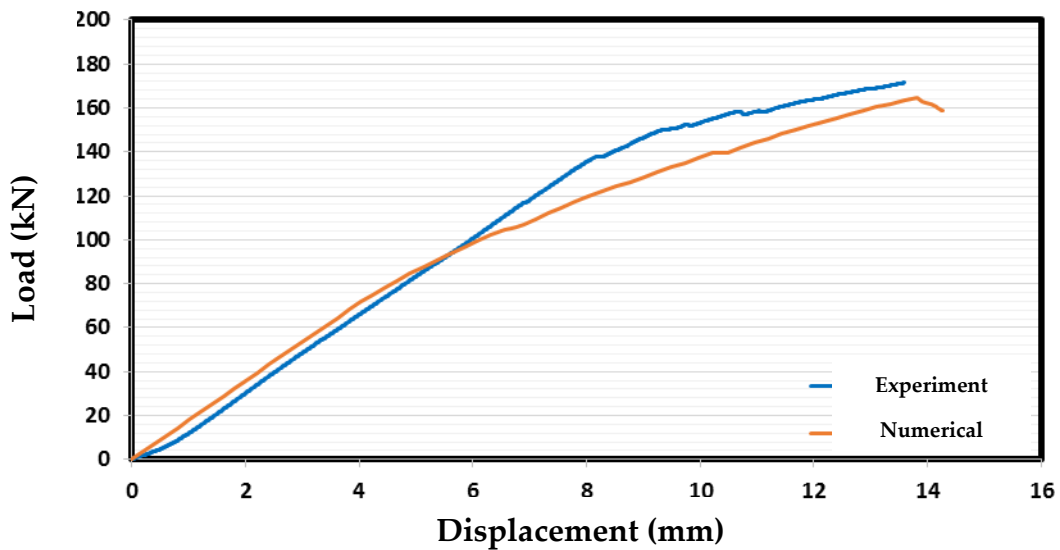


Figure 3-72 Load Displacement Curves ( $a/d = 1.00$ )

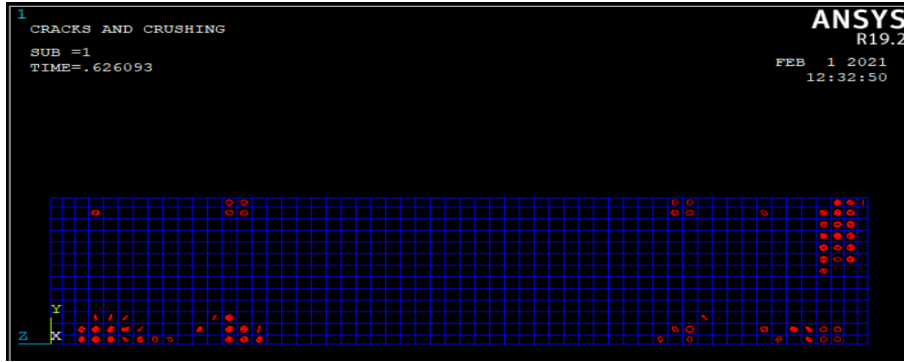


Figure 3-73 Estimated Crack Pattern ( $a/d = 1.00$ )

**$a/d = 1.65$**

The stirrup spacing in the geopolymer beam was taken as 100 mm, and the geopolymer shear beam with a shear span of 390 mm and an  $a/d$  ratio of 1.65 was numerically modeled. The load-displacement curves obtained from experimental with the help of LVDT and numeric model were compared to each other (Figure 3-74). In addition, the estimated crack pattern was given in Figure 3-75.

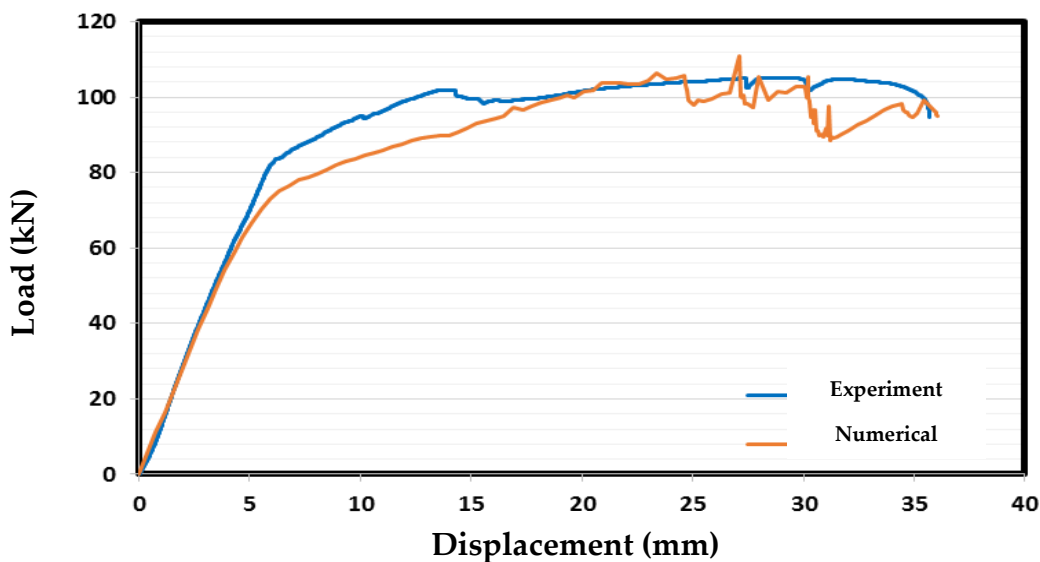


Figure 3-74 Load Displacement Curves ( $a/d = 1.65$ )

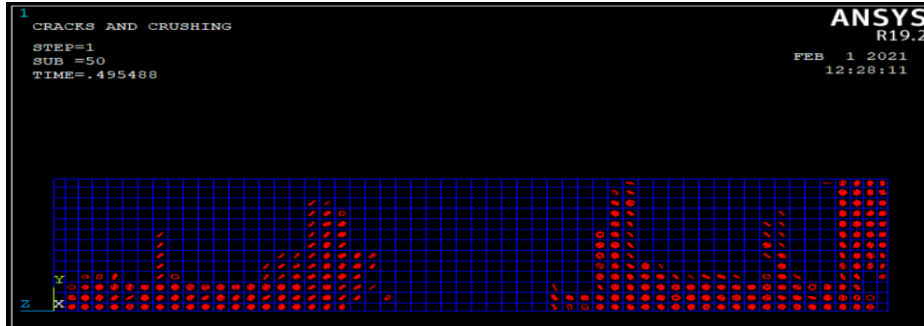


Figure 3-75 Estimated Crack Pattern ( $a/d = 1.65$ )

### 3.4.3.3 Summary of Numerical Estimations

#### Shear-critical beams

The estimated values of the ultimate displacement, maximum force capacity, energy and initial stiffness obtained for all shear-critical beams are shown in Table 3.18. The load-displacement curves are very similar to the experimentally obtained ones. The estimations of the numerical model for all specimens had an error of 2.96%, 2.98% and 0.86% for  $a/d = 0.50$ , 1.00 and 1.65, respectively. The initial secant stiffness values matched the experimental stiffness values with a maximum margin of error of 15% for shear beams. The energy absorption capacities of beam specimens were also calculated based on the area under the load-displacement graph. The energy absorption capacities obtained from the numerical models matched the experimental values for all shear beams with a maximum error rate of 7.29%.

Table 3-18 Summary of Numerical Estimations (Shear-critical beams)

$a/d = 0.50$	U(mm)	$F_y$ (N)	Energy (kN.m)	Rigidity (kN/m)
Max	13.508	160.672	1.379	17377.5
Perc. Error	2.615	2.146	4.312	4.266
$a/d = 1.00$	U(mm)	$F_y$ (N)	Energy (kN.m)	Rigidity (kN/m)
Max	18.909	172.994	2.151	17836
Perc. Error	2.976	-0.339	7.29	-15.069
$a/d = 1.65$	U(mm)	$F_y$ (N)	Energy (kN.m)	Rigidity (kN/m)
Max	13.96	98.531	0.917	14185.19
Perc. Error	0.863	-0.919	4.957	-13.523

### Flexure-critical beams

The estimated values of the ultimate displacement, maximum force capacity, energy and initial stiffness obtained for all flexural-critical beams are shown in Table 3.19. The load-displacement curves are very similar to the experimentally obtained ones. The estimations of the numerical model for all specimens had an error of 6.58%, -4.98% and -1.06% for  $a/d = 0.50$ , 1.00 and 1.65, respectively. The initial secant stiffness values matched the experimental stiffness values with a maximum margin of error of 12% for shear beams. The energy absorption capacities of beam specimens were also calculated based on the area under the load-displacement graph. The energy absorption capacities obtained from the numerical models matched the experimental values for all shear beams with a maximum error rate of 4.81%.

Table 3-19 Summary of Numerical Estimations (Flexure-critical beams)

$a/d = 0.50$	U(mm)	$F_y(N)$	Energy (kN.m)	Rigidity (kN/m)
Max	13.183	215.970	1.783	23479.649
Perc. Error	6.580	0.394	4.806	4.963
$a/d = 1.00$	U(mm)	$F_y(N)$	Energy (kN.m)	Rigidity (kN/m)
Max	14.273	164.560	1.440	17850.572
Perc. Error	-4.983	4.048	-2.746	-5.313
$a/d = 1.65$	U(mm)	$F_y(N)$	Energy (kN.m)	Rigidity (kN/m)
Max	36.067	111.013	3.088	14342.509
Perc. Error	-1.060	-5.685	4.424	-12.401

### 3.4.4 References

Zhang, Y., Lin, X., Zhou, J., Sun, H., & Ding, Z. (2021, April). Numerical simulation of mechanical properties of recycled concrete based on characterization of interfacial transition zone characteristics. In *Journal of Physics: Conference Series* (Vol. 1865, No. 3, p. 032013). IOP Publishing.

Zhu, F., Zhou, Q., Wang, F., & Yang, X. (2017). Spatial variability and sensitivity analysis on the compressive strength of hollow concrete block masonry wallettes. *Construction and Building Materials*, 140, 129-138.

LU, B., & LIU, B. K. (2013). Experiment study and numerical simulation on modification recycled aggregate concrete compressive strength. *Journal of Anhui Institute of Architecture & Industry (Natural Science)*, 02.

Xiao, J., Liu, Q., & Wu, Y. C. (2012). Numerical and experimental studies on fracture process of recycled concrete. *Fatigue & Fracture of Engineering Materials & Structures*, 35(8), 801-808.

## 4 Ultra-lightweight non-structural wall elements and green wood chip concrete panels

### 4.1 Introduction to lightweight concretes

#### 4.1.1.1 *Lightweight concrete*

The first use of Lightweight Aggregate Concrete (LWAC) dates back to 3000 BC. It is estimated that the first place of use was the Indus Valley. Its use as a building material in Europe appears in the Romans period in the 2000 BC. Today, it continues to be used for various purposes almost all over the world. Chandra et al., (2002) stated that LWAs, which make concrete light, were limited to materials obtained by natural means in the early days and that these materials were of volcanic origin such as pumice, scoria, tuff. With the increasing demand for lightweight concrete around the world, the use of fabricated aggregates, as well as natural-origin aggregates, began to become widespread.

The mechanical and chemical properties of the aggregate depend entirely on the characteristics of the raw material from which the aggregate is produced and the production methods. Concrete is generally thought to be a durable, rigid and



heavy material when the purpose of use is considered, but when the purpose of use changes, its color, strength and density can change. If we talk about the LWAC used in Pumice aggregate, it has a lighter and more porous structure than a normal concrete. Its biggest advantage is thermal insulation. While it is necessary to use normal concrete and thick walls to provide thermal insulation, it is possible to apply the same insulation with thinner walls when LWAC is used. This is one of the biggest benefits LWAC provides today (Yu et al., 2015; Chandra & Berntsson, 2002).

LWAC is still being researched and developed today. The applications of LWAC are not limited to insulation. It is used in structures in contact with liquids such as offshore structures, long bridges, or used in high-rise buildings. Loudon et al., (1979) studied the thermal properties of LWC. He reported that the concrete's density and moisture content are the main factors affecting the thermal conductivity. It has been determined that the aggregate used has an effect up to 25% on the thermal conductivity value of the concrete under similar density values.

Wasserman and Bentur et al., (1996) discovered that both the physical and chemical properties of the aggregate used to produce lightweight concrete affect the strength of the concrete due to the processes occurring in the interfacial transition zone of the concrete. Demirboğa and Gül et al., (2003) conducted various studies on the thermal conductivity and compressive strength of mineral reinforced expanded perlite aggregate concrete. After their experiments using silica fume and fly ash instead of cement, they observed that the thermal conductivity decreased to 15% and the compressive strength to 30%. TY Lo et al., (2007) conducted experiments on the strength of lightweight aggregate in terms of pipe strength. They revealed that the aggregate strength of LWCs is not directly related to the size (diameter) of the aggregate but is somehow related to the density of the aggregate.

In the various studies described above, we can see that the types of materials used and both the mechanical and chemical properties of these materials are examined. In particular, the results obtained in many thermal experiments show variations (Bogas et al., 2013). Some design methods have been proposed for lightweight concretes but most of them are based only on experimental results for a particular type of concrete and they depend on the specific properties of the selected materials, particularly the LWA type. (Grübl et al., 1979; Chandra & Berntsson, 2003)

The main focus of the current studies is the development of Ultra-Lightweight Concrete (ULWC), which has more advanced mechanical and chemical properties than LWC. In other words, it maintains the high strength expected from concrete, while at the same time it has more advanced thermal properties. The developed ULWC is a suitable product for a monolithic building. If it has high strength to be used in the carriers of the building, it will also eliminate the cost of making an extra insulation for the building. It provides a chance for more flexibility for those who design the building (Yu et al., 2013). Recently, in the production of ULWC, aggregates such as expanded recycled glass or micro silica have been

added to the concrete mix to produce building materials with the desired properties (Schlaich & Hückler, 2012). The dimensions of this glass or silica used are such that they replace sand and gravel in normal concrete. About 60% of the total volume is retained in small hollow particles. Concrete with a thermal conductivity of  $\lambda = 0.14 \text{ W/(mK)}$  can be obtained with a relatively high compressive strength of about  $10 \text{ N/mm}^2$ .

#### 4.1.1.2 Perlite

Perlite is a siliceous volcanic glass, which is made from pumice, has a glassy form of rhyolitic or dacitic magma and includes 2–5% water. The commercial product, known as expanded perlite, is made by heating the material to 760–1100°C, which converts the material's native water to vapor and causes it to expand to 4–20 times its original volume while producing lightweight high-porosity aggregates (Celik et al., 2013; Harben & Bates, 1990). Expanded perlite is the porous and light structure that results from this expansion. During expansion, the water in its structure, which is between 2% and 6%, evaporates. Perlite bursts when water is removed, resulting in its porous and light structure. It is chemically stable in nature since it does not include nitrates, phosphate, sulfates, heavy metals, or organic compounds (PS, 2019). Perlite is a material that can be used for insulation purposes in buildings, as it is a porous, light, fire-resistant and moisture-retaining material that provides sound and heat insulation (Topçu & Işıkdağ, 2007). Due to low density and lightweight properties of expanded perlite, it is suitable to produce lightweight concrete by utilizing that porous aggregate as a constituent (Sengul et al., 2011).

Sengul et al., (2011) investigated the effect of expanded perlite on the mechanical properties and thermal conductivity of lightweight concrete. The purpose of the study was to provide more data on the effects of expanded perlite on the mechanical properties and thermal conductivity of lightweight concrete. Mixtures were created in the experimental program by partially substituting natural aggregate with expanded perlite, resulting in unit weights of lightweight concretes in the fresh form ranging from 700 to 2000  $\text{kg/m}^3$ . The compressive strength and modulus of elasticity decreased as perlite content increased, according to basis of empirical evidence. Water absorption and sorptivity coefficient, on the other hand, increased when perlite content rise. Also, the test results indicated that using perlite improves thermal conductivity significantly and that there is a strong link between thermal conductivity and unit weight.

Jedidi et al., (2015) carried out this study to provide additional information about the impact of expanded perlite aggregate (EPA) dosage on the compressive strength and thermophysical characteristics of lightweight concrete at various ages. After choosing the proper mixing procedure for expanded perlite concrete (EPC), cubic and parallelepiped specimens were prepared at w/c ratio of 0.7 with different replacement percentages of sand by EPA varying from 0% to 80% by volume of sand. Over the period of the curing process, compressive strength, thermal conductivity, and thermal diffusivity were measured. The produced mixes

had unit weights ranging from 560 to 1510 kg/m<sup>3</sup>. When the perlite content was raised, researchers observed that the compressive strength was reduced. The test results showed that using EPA instead of natural aggregate boosted the lightweight concrete's thermal resistance and, as a result, improved thermal insulation.

Oktay et al., (2015) performed an experimental investigation for producing new cement-based with relatively high strength, low density and good thermal properties for energy efficient buildings. Within the scope of this research, various types of concretes containing silica fume (SF), superplasticizer (SP), and air-entrained admixtures are prepared with a constant water–cement ratio, and normal aggregates are replaced with lightweight aggregates (LWAs) such as pumice (PA), expanded perlite (EPA), and rubber aggregates (RA) at different volume fractions of 10%, 20%, and 30%. It is concluded that the addition of PA, EPA, and RA to the composite concretes reduced the bulk density and compressive strength of the material while improving the insulating properties.

#### 4.1.1.3 *Pumice*

Pumice is a type of lightweight aggregates that has been used in building for centuries. The outflow of gases from cooling magma during volcanic activity creates tiny hollow spaces, resulting in the porous structure of pumice (Parhizkar et al., 2012). It's a granulated version of a natural lightweight aggregate with a sponge-like structure. Pumice has numerous pores, from macro scale to micro scale, due to the sudden outflow of the gases in its body and its rapid cooling during its formation (Koçyiğit, 2016). Furthermore, due to semi-open or closed pores, there is no link between poor permeability and pores, hence heat and sound are well insulated in rocks (BSD, 2006).

Volcanic activity produces two types of pumice: acidic and basic pumice. Acidic pumice and basic pumice are the two types. Gündüz et al. (1998) name basic pumice basaltic pumice or scoria. Basic pumice has a grain density of more than 1.0 g/cm<sup>3</sup> in most cases. Brownish to red, dark gray to black are some of the colors available. In basic character pumice, the SiO<sub>2</sub> ratio is less than 50% and the Fe<sub>2</sub>O<sub>3</sub> ratio is larger than 5% in general. The most common and widely utilized variety of pumice on the planet is acidic pumice, which is lighter than basic pumice and has a particle density of less than 1.0 g/cm<sup>3</sup>. In acidic pumice, the SiO<sub>2</sub> ratio is greater than 50 and the Fe<sub>2</sub>O<sub>3</sub> ratio is less than 3% (Davraz, 2001).

Its hardness is 5 to 6 on the Mohs scale. Chemically, silica content of up to 75% can be found. General chemical composition of pumice; It consists of 60-75% SiO<sub>2</sub>, 13-17% Al<sub>2</sub>O<sub>3</sub>, 1-3% Fe<sub>2</sub>O<sub>3</sub>, 1-2% CaO, 7-8% Na<sub>2</sub>O - K<sub>2</sub>O and trace amounts of TiO<sub>2</sub> and SO<sub>3</sub>. The ratio of SiO<sub>2</sub> contained in the rock gives the rock abrasiveness. Due to this feature, it can exhibit a chemical structure that can easily corrode steel. Al<sub>2</sub>O<sub>3</sub> composition, on the other hand, provides high resistance to fire and heat. Na<sub>2</sub>O and K<sub>2</sub>O are known as minerals that give reaction properties in the textile industry.

Every year, 19.6 Mt of volcanic pumice (VP) is mined worldwide, with Turkey continuing to be the leading producer at 4.2 Mt each year (Crangle, 2010). Italy, Chile, Ecuador, Ethiopia, France, Germany, Greece, Spain, and the United States are the other prominent countries. Pumice concrete accounts for around 3% of total lightweight concrete usage in Europe, with Germany accounting for 70% of total consumption.

Pumice is employed in a variety of industries, including building, textiles, chemistry, agriculture, and health (Gündüz et al., 1998). It finds a wide range of applications in the construction and building industry due to superior properties such as low unit volume mass, high heat and sound insulation, air conditioning, easy plaster adhesion, excellent acoustic properties, elasticity against earthquake loads and behaviours, and being more cost-effective than alternatives (Sezgin vd., 2005).

Pumice aggregate may be found in a variety of locations across the world where volcanoes have existed. Pumice aggregates combined with Portland cement and water create a lightweight thermal and sound insulating, fire-resistant lightweight concrete for roof decks, lightweight floor fills, insulating structural floor decks, prefabricated or in-situ curtain wall systems, pumice aggregate masonry blocks, and a variety of other permanent insulating applications (Uğur et al., 2003).

Hossain, K. M. A., (2004) investigated the suitability of using volcanic pumice (VP) as cement replacement material and as coarse aggregate in lightweight concrete production. Tests were carried out on cement by substituting 0 percent to 25% of cement by weight and on concrete by replacing 0 percent to 100% of coarse aggregate by volume in accordance with this purpose. The physical and chemical properties of VP are examined in order to assess their potential impact on cement and concrete in both the fresh and hardened states. The VP concrete has sufficient strength and density to be regarded as structural lightweight concrete, according to the results. The VPC, on the other hand, has a lower modulus of elasticity and higher permeability and early surface absorption than control concrete.

Uysal et al., (2004) carried out a study to examine the effects of different cement dosages, slumps, and pumice aggregate ratios on the thermal conductivity and density of concrete. Thermal conductivity coefficients of different concrete mixtures containing pumice aggregate (PA) and normal aggregate were measured within this study. 5%, 50%, 75%, and 100% pumice ratios were substituted to normal aggregate by volume, 200, 250, 350, 400 and 500 kg/m<sup>3</sup> cement dosages, and 3 ± 1, 5 ± 1, and 7 ± 1 cm slumps were used to determine the effect of PA ratio, different cement dosage, and slumps on the thermal conductivity of concrete. The results of the tests show that PA reduced the density and thermal conductivity of concrete by up to 40% and 46%, respectively. The density and thermal conductivity of the concrete increased as the cement dose was increased in the combinations. Slump had a variable effect on density and thermal conductivity.

Hossain, K. M. A., (2011) studied mechanical and durability characteristics of lightweight concrete incorporating pumice based blended cement and aggregate. The development of lightweight volcanic pumice concrete (VPC) utilizing pumice-based ASTM Type I blended cement (PVPC) and aggregates is presented in the study (both coarse and fine). Fresh and mechanical characteristics of VPC mixes, such as slump, air content, compressive strength, tensile strength, density, and modulus of elasticity are examined. The addition of PVPC to VPC mixes had the positive effect of decreasing drying shrinkage and water permeability. Because of the formation of a high-quality interfacial paste-aggregate transition zone and the gradual internal curing in VPCs, the presence of coarse/fine/both VPA is also linked with reduced permeability. It is concluded that the development of low-cost, environmentally friendly VPC with adequate strength and durability properties might be highly beneficial for the long-term building and restoration of volcanic catastrophe regions all over the world.

#### 4.1.1.4 *Foam Concrete*

Another concrete that is in the foreground with its lightness and insulation feature, which is unusual in use, is Foam Concrete. It is a cement-based mortar produced by adding at least 20% foam per volume to the concrete mortar (Valore.,1954). Although it is called foam concrete, coarse aggregate is generally not used in its production. In fact, it would be correct to call it a mortar. Density of foam concrete generally takes values between 400 kg/m<sup>3</sup> and 1600 kg/m<sup>3</sup>. One of the most important factors that keeps the density at the desired level is the amount of fine aggregate. This amount is controlled by replacing it with foam. Foam concrete, like other lightweight concrete structures, is suitable for use in various building elements for insulation purposes. Thanks to the energy savings it provides, it offers economic and environmental solutions. Although it was seen for the first time in the world in the early 1920s in practice (Mindess., 2019), it is used in almost all countries today, especially as a filler class in buildings and road fillings (Tarasov et al., 2010; Mydin et al., 2011). Especially when we look at the last 20 years, higher quality superplasticizers and high-performance foaming agents that have been put on the market have allowed foam concrete to be used on even larger scales. Many studies have also been carried out to examine the properties and behavior of foam concrete.

Based on all the examinations made with foam concrete, we can say that the focus is not on the strength properties of foam concrete, but on the properties of its internal structure. The foam stabilization mechanism, which is tried to be provided in concrete, provides a uniform structure for the hardening process as well as providing a smooth geometry in the internal structure of the concrete. Although various tests have been carried out for the lowest density and highest strength, there is no standard method to determine the material mixing ratios for foam concrete. The parameters as the type of foam material used in the production of stable foam concrete, the proper distribution of the air bubbles created in the concrete, the preparation method of the foam material are decisive on the characteristics of foam concrete. In order to create a porous and hollow



structure in the concrete, it is appropriate to partially replace the cement with fly ash or silica fume or to use lightweight aggregates with low hydration heat. Thus, the amount of foaming agent used in the concrete will also be reduced (Weigler and Karl.,1980).

Activities that can be done in order to improve the material in the coming period can be listed as trying to examine the engineering properties of foam concrete (such as Poisson's Ratio, Modulus of Elasticity) more appropriately for concrete design, and to increase the fire resistance it has shown compared to conventional concrete. In order to improve its mechanical properties, detailing the properties of fiber-reinforced concrete, developing superplasticizers that do not have a negative effect on the stability of the foam and the non-decomposition of the mixture are also among the studies to be done (Amran et al.,2015).

#### 4.1.2 Materials and Methodology

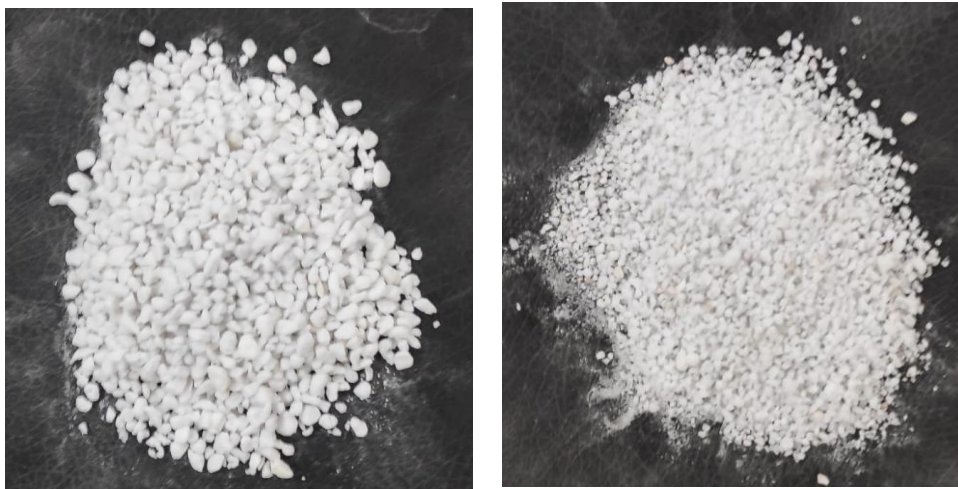
##### 4.1.2.1 *Materials*

##### **Eco-hybrid cement**

Within the scope of the ICEBERG study in subtask 3.3.3, eco-hybrid cement was used for the development and optimization of Ultra-lightweight non-structural wall elements. The chemical and physical properties of eco-hybrid cement were given in the previous section.

##### **Perlite**

Perlite aggregate with two different grain sizes (2-6 mm thick and 1-3 mm fine) was procured from a local supplier in Ankara. Images of perlite aggregate are presented in Figure 4-1.





(a)

(b)

Figure 4-1 Images of the coarse and fine perlite aggregate (a) coarse fraction, (b) fine fraction

### Pumice

The pumice used in this study was purchased from a local supplier in Ankara. The pumice aggregate used was divided into two phases as fine and coarse according to the particle size. The grain size of the fine pumice aggregate was between 3-7 mm, while the grain size of the coarse pumice aggregate was between 10-15 mm. Images of pumice aggregate are presented in Figure 4-2.

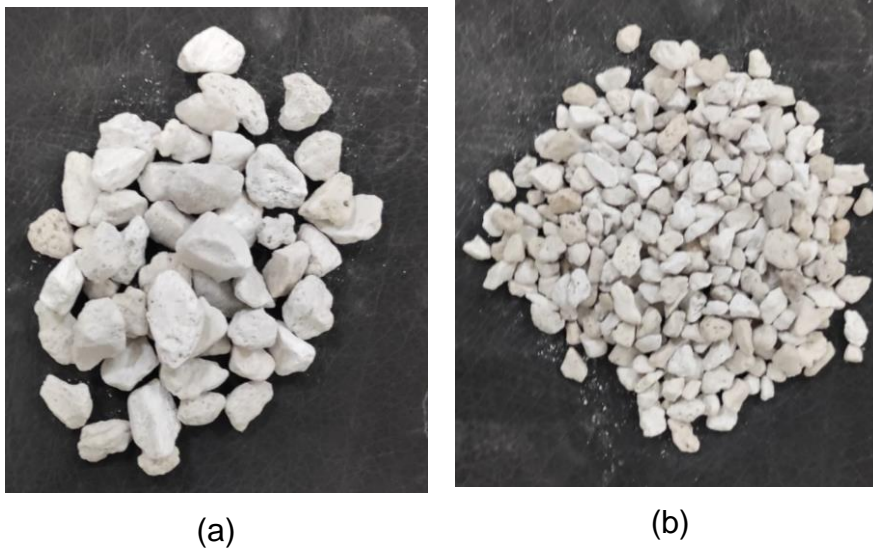


Figure 4-2 Images of the coarse and fine pumice aggregate (a) coarse fraction, (b) fine fraction

### Recycled aggregate

Since the properties of the recycling aggregates used in the mixtures within the scope of the study were presented in the previous sections, no additional information was given in this section.

### Foaming agent

A foaming agent, such as a surfactant or a blowing agent, is a substance that aids in the creation of foam and defined as air entraining agent. When present in tiny amounts, a surfactant lowers a liquid's surface tension and reduces the amount of effort required to make foam. The gaseous portion of the foam is formed by a blowing agent, which is a gas. When foaming chemicals are added to the mix water, discrete bubble cavities form, which can be then integrated into the cement or geopolymer paste.

There are two types of foaming agents: synthetic and protein foaming agents. Synthetic foaming agents are appropriate for densities of  $1000 \text{ kg/m}^3$  and higher, while protein foaming agents are ideal for densities of  $400 \text{ kg/m}^3$  to  $1600 \text{ kg/m}^3$ .

Animal proteins from horn, blood, cow bones, and other animal carcass remnants are used to make protein-based foaming agents. Chemicals are used to make synthetic foaming agents. Under sealed circumstances, synthetic foaming agents have a shelf life of roughly a year (Wan Ibrahim et al., 2015).

In this project, MasterRoc® SLF 30 was used as a foaming agent. A stable foam was formed by expanding the aqueous solution of the foaming agent with the help of air. This foaming agent can be used with a foam generator as well as foam can be created manually with the help of this agent. Technical properties of foaming agent are presented in Table 4.1.

Table 4-1 Technical properties of the foaming agent

<b>Technical Properties</b>	
<b>State</b>	Liquid
<b>Color</b>	Colorless
<b>Density (kg/m<sup>3</sup>) 20°C</b>	1035-1045
<b>Viscosity (mPa.s) 20°C</b>	100
<b>pH (5% solution) 20°C</b>	6.5-7.5
<b>Solubility in Water</b>	100%

#### 4.1.2.2 Methodology

##### Preparation of mixtures

While determining the design criteria of the mixtures, in first stage, it was aimed to evaluate the effect of perlite and pumice as lightweight aggregates on the density of the system. In this context, a control mixture containing only RCA was produced and the density changes of the mixtures were measured by performing different combinations of lightweight aggregate substitutions. At the same time, the effects of cement dosage and aggregate usage rate on the density of the system were investigated, as well. The steps of the procedure carried out to produce the said mixtures are as follows:

1. Weighing of dry elements of mixtures at specified rates
2. Mixing the weighed in dry condition with the mortar mixer for 60 seconds to ensure homogeneity
3. Adding the specified amount of water to the dry mix and mixing all the ingredients for 240 seconds
4. Determination of fresh densities of mixtures by placing them in molds and determining their fresh weight
5. After keeping the mixtures at ambient conditions for 24 hours, they are taken out of the molds and then left to cure under ambient conditions until the day when the relevant tests are performed

### Molding and curing

In the studies carried out to produce Ecohybrid cement-based ultra-lightweight non-structural wall elements, samples were produced using 15x15x4 cm molds in order to determine the fresh densities and thermal properties of the mixtures. All produced mixtures were cured under ambient conditions. Visuals of molds and a representative visual of the casted mixture are shown in Figure 4-3.



Figure 4-3 Image of the used molds for production of samples

### Testing

As part of the preliminary studies carried out to produce ultralight non-structural wall elements, fresh density measurements of the mixtures were carried out according to the ASTM C138 standard. In this context, immediately after the mixtures were produced, they were placed in the mold whose weight was determined before, and fresh densities were calculated by the weight obtained.

After the ultralight non-structural wall elements were produced, tests were performed on the samples with the LINSEIS HFM300 heat transfer coefficient measuring device and the thermal conductivity value was determined for each sample from the mixtures that were considered to have low fresh density. The technical specifications of the LINSEIS HFM300 device used are given in Table 4.2. The LINSEIS Heat Flow Meter provides a fast and easy-to-use hardware for determining the thermal conductivity properties of low thermal conductivity insulation panels as well as all other panels with high accuracy. The device is designed in accordance with ASTM C518, JIS A1412, ISO 8301 and DIN 12667 standards. The measurement principle is to place a sample between a hot and cold plate and measure the heat flow (LINSEIS Thermal Analysis, 2018). While the thermal conductivity tests are being completed, the upper plate is operated at 30 °C and the lower plate at 10 °C. After the sample is placed between the plates in the device, the thermal conductivity of the sample is measured.

Table 4-2 LINSEIS HFM300 device specifications

Parameter	Unit
Model type	HFM300/1
Temperature range of plates	0 - 40°C
Cooling System	Compressed Air
Plate Temperature Control	Peltier
Data Measurement Points	1
Sample Size	150x150x40 mm
Thermal Resistance Measurement Range	0.1 - 8.0 m <sup>2</sup> K/W
Thermal Conductivity Measurement Range	0.001 - 2.5 W/m.K
Repeatability	0.25%
Accuracy	± 1 - 3%
Variable Contact Pressure	0.25 kPa

In this report period, it is planned to measure the noise reduction levels of the mixtures produced within the scope of the production of ultralight non-structural wall element as a result of reaching the targeted density and thermal performances. For this reason, the sound insulation performances of the mixtures were not evaluated in this reporting period.

#### 4.1.3 Results and Discussion

All the results and discussion of the preliminary studies carried out within the scope of the project are presented in the sub-titles of the current section.

##### 4.1.3.1 Preliminary Studies 1<sup>st</sup> Group of Mixtures

Within the scope of the studies carried out for the production of ultra-lightweight non-structural wall elements, in the first stage, the main focus was the production of mortar mixtures in which Ecohybrid Cement forms the binder phase, and different types of lightweight aggregates were used. The density of the matrix was tried to be reduced by substituting perlite and pumice aggregates as lightweight aggregates with recycling concrete aggregate (RCA). In addition, to reduce the density of the system, another option, foam produced by foaming agent, was included in the system. Detailed mixing ratios are presented in Table 4.3. As seen in the table, in the first stage, a base mixture was prepared by adding 10% of the total aggregate content of perlite aggregate to the mixture whose aggregate phase consists of fine and coarse RCA. Then, based on this mixture, mixtures with varying cement dosage, perlite amount and water/binder ratio were derived. The visuals of the produced samples are presented in Figure 4-4.

Table 4-3 1<sup>st</sup> group samples produced within the scope of preliminary studies

	Mix 1.1	Mix 1.2	Mix 1.3	Mix 1.4	Mix 1.5	Mix 1.6	Mix 1.7	Mix 1.8
<b>Cement (g)</b>	400	500	621.6	621.6	400	350	300	250
<b>Water (g)</b>	280	400	350.8	340.8	340	310	310	270
<b>Perlite (g)</b>	104	200	112	143	200	250	250	282
<b>Pumice (g)</b>	0	0	0	0	334	350	400	0
<b>Fine RCA (g)</b>	367	0	367	0	0	0	0	0
<b>Coarse RCA (g)</b>	552	0	552	0	0	0	0	0
<b>Water/Binder</b>	0.7	0.8	0.56	0.55	0.85	1.13	0.89	1.08

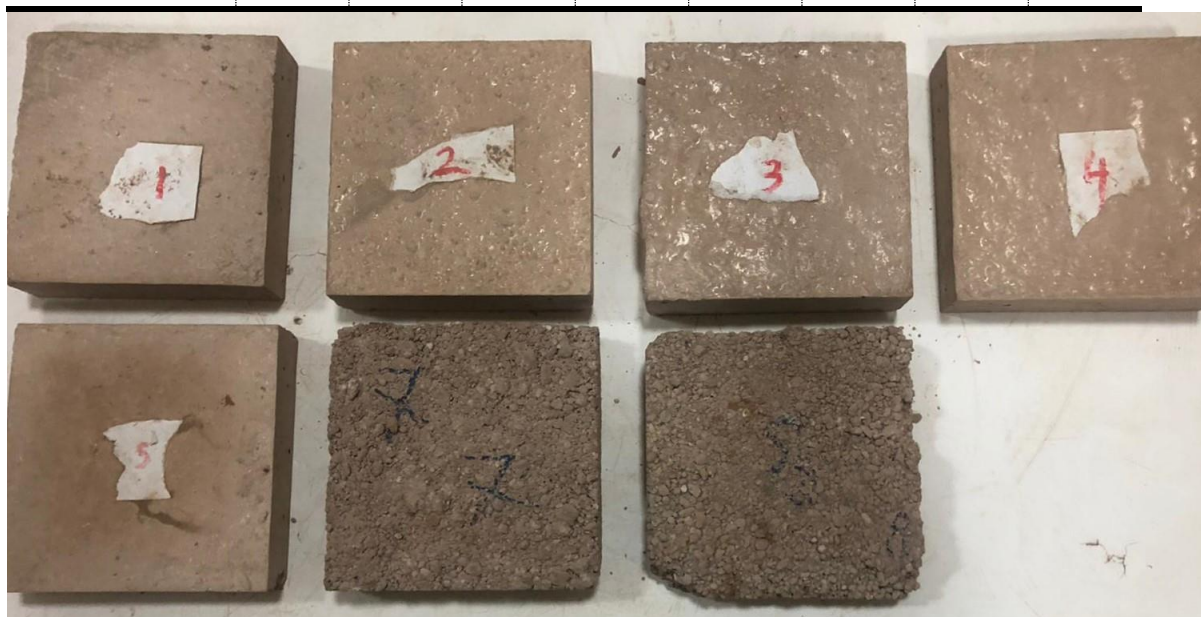


Figure 4-4 Images of the 1<sup>st</sup> group samples produced within the scope of preliminary studies

### Density Measurement

The fresh-dry density values of the produced samples are presented in Figure 4-5. When Mix 1.1 and Mix 1.2 are compared, the final density change seen as a result of the density differences of two different aggregates is clearly seen by using perlite instead of RCA. When Mix 1.1 and Mix 1.3 are compared, as a result of the substitution of perlite to RCA, the increase in cement dosage and the decrease in the water/binder ratio caused a relative increase in the density. For the same cement dosage and water/binder ratio, the effect of the combination of RCA and perlite aggregate in the system and the use of only perlite aggregate on the density can be seen with a noticeable decrease in Mix 1.4 compared to Mix 1.3. Although it is thought that increasing the cement dosage in order to ensure the mechanical performance of the system and its stability in the hardened state increases the density values (Altun & Aktaş, 2013), Mix 1.2 and Mix 1.4 showed almost the same density values. In the Mix 1.5 mixture, a perlite-pumice combination was used instead of the RCA-Perlite combination compared



to the Mix 1.1 mixture, and a notable change in the density values could not be obtained. Mix 1.6 and Mix 1.7 mixtures were produced by reducing the cement dosage of Mix 1.5 in order to reduce the density by decrease the cement dosage. As the water/binder ratio reached very high levels in the Mix 1.6 mixture, the mixture could not provide sufficient stiffening as a result of the hydration reactions and could not be removed from the mold. However, as a result of decreasing the water/binder ratio in the Mix 1.7 mixture and ensuring that the excess water of the mixture saturates the aggregates with the increased aggregate ratio, the mixtures reached the hardness that could come out of the mold, but weight measurement could not be performed due to the broken pieces. Mix 1.8, as the equivalent of Mix 1.7, which contains only perlite and has a lower cement dosage, has the lowest fresh and dry densities obtained in the preliminary studies. Although it is observed that the fresh and dry density for Mix 1.8 has decreased significantly in general, the failure of the sample to preserve its integrity reveals the necessity of various revisions in the mixing parameters.

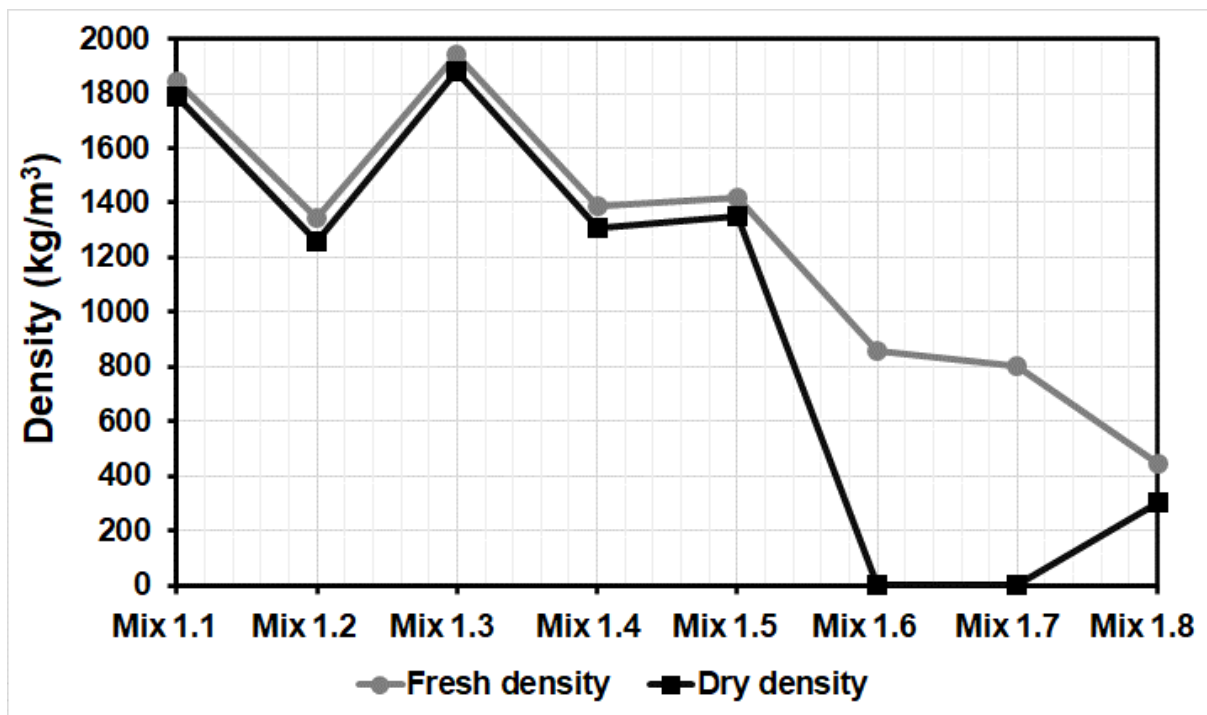


Figure 4-5 Density values of the 1<sup>st</sup> group samples produced within the scope of preliminary studies

### Thermal Analysis

No thermal analysis tests were carried out for the 1<sup>st</sup> group mixtures produced within the scope of the preliminary studies carried out for the production of ultra-lightweight non-structural wall elements. Failure to reach the desired density levels of the mixtures in question is the main factor in performing thermal analysis.



### 4.1.3.2 Preliminary Studies 2<sup>nd</sup> Group of Mixtures

#### Mixtures Produced with High Dosage of Foam Agent

In the second stage of the preliminary studies carried out for the production of ultra-lightweight non-structural wall elements, the mixtures were continued by using only perlite aggregate in the light of the data obtained from the 1<sup>st</sup> group samples. In order to reduce the densities of the mixtures effectively, foam concrete was produced at this stage. While preparing the mixtures, cement and water were mixed in the first stage, then the foaming agent was mixed with 1 liter of water with a drill at certain dosages and added to the cement paste. Finally, the mixture was completed by adding perlite aggregate to the system. In the 2<sup>nd</sup> group samples, the foaming agent ratio was chosen as 2.5% by weight for 1 liter of water in the first stage. The mixing ratios of the produced mixtures in first stage are presented in Table 4.4. Also the visuals of the mixtures are given in Figure 4-6. The analysis of the densities of the produced mixtures is detailed in a sub-title.

Table 4-4 First part of the 2<sup>nd</sup> group samples produced within the scope of preliminary studies

	Mix 2.1a	Mix 2.2a	Mix 2.3a	Mix 2.4a	Mix 2.5a	Mix 2.6a	Mix 2.7a
<b>Cement (g)</b>	700	500	500	500	500	500	500
<b>Water (g)</b>	350	250	250	200	200	200	200
<b>Perlite (g)</b>	50	50	75	75	50	100	100
<b>Foam (L)</b>	1.5 L	3 L	1.5 L	4.5 L	5.7 L	3 L	3 L
<b>Water/Binder</b>	0.5	0.5	0.5	0.4	0.4	0.4	0.4

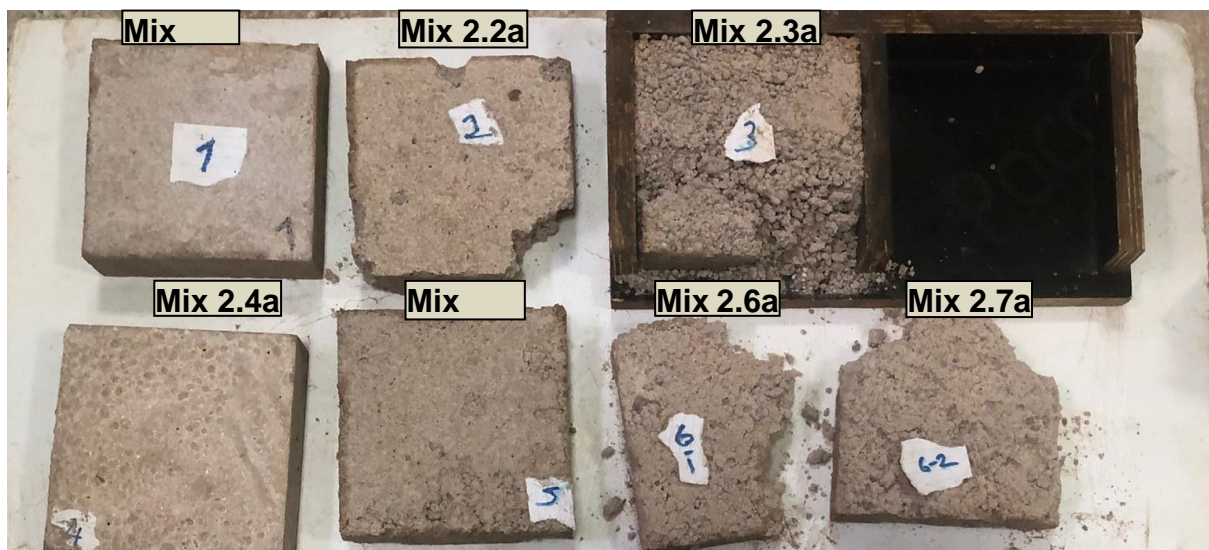


Figure 4-6 Images of the 2<sup>nd</sup> group samples produced with the foam generated by 2.5% foaming agent

#### Density Measurement

The second group of studies started with Mix 2.1a that has 0.5 water/binder content and 0.07 weight perlite content based on cement, and a fresh density value below 800 kg/m<sup>3</sup> was obtained with this mixture (Figure 4-7). Then, density reduction was made by decreasing the cement dosage and increasing the foam usage rate in the said mixture (Mix 2.2a). However, this mixture was shattered when demolding due to inadequate stiffness of the matrix. Considering that this situation is related to the inefficient hydration of the matrix due to the high rate of foam usage, the amount of foam was brought to the same level as Mix 2.1a and the perlite usage rate was increased from 0.10 to 0.15 (Mix 2.3a). Although the density value of the mixture in question decreased against Mix 2.1a, a higher density value than Mix 2.2a was obtained and the material was severely segregated due to low hydration and could not be removed from the mold. In Mix 2.4a, the water/binder ratio was reduced to 0.4 and the amount of foam usage was increased. It has a stiff and stable form, however the density of Mix 2.4a was quite high compared to other mixes. In Mix 2.5a, the perlite usage rate was reduced, and the amount of foam was increased to 5.7 L. As a result of these modifications, a significantly lower density was obtained compared to Mix 2.4a. Starting from this point, two mixtures with higher perlite content were produced with different densities of the produced foam and the effects of the density of the foam were investigated (Mix 2.6a-2.7a). The lower density foam at the top of the foam produced in a different container was used for Mix 2.6a, and the higher density foam at the bottom of the foam was used for Mix 2.7a. Although the density of the mixture produced with low density foam was reduced to lower levels (even the lowest density among all mixtures) compared to that produced with high density foam, neither sample had the stiffness that could be removed from the mold.

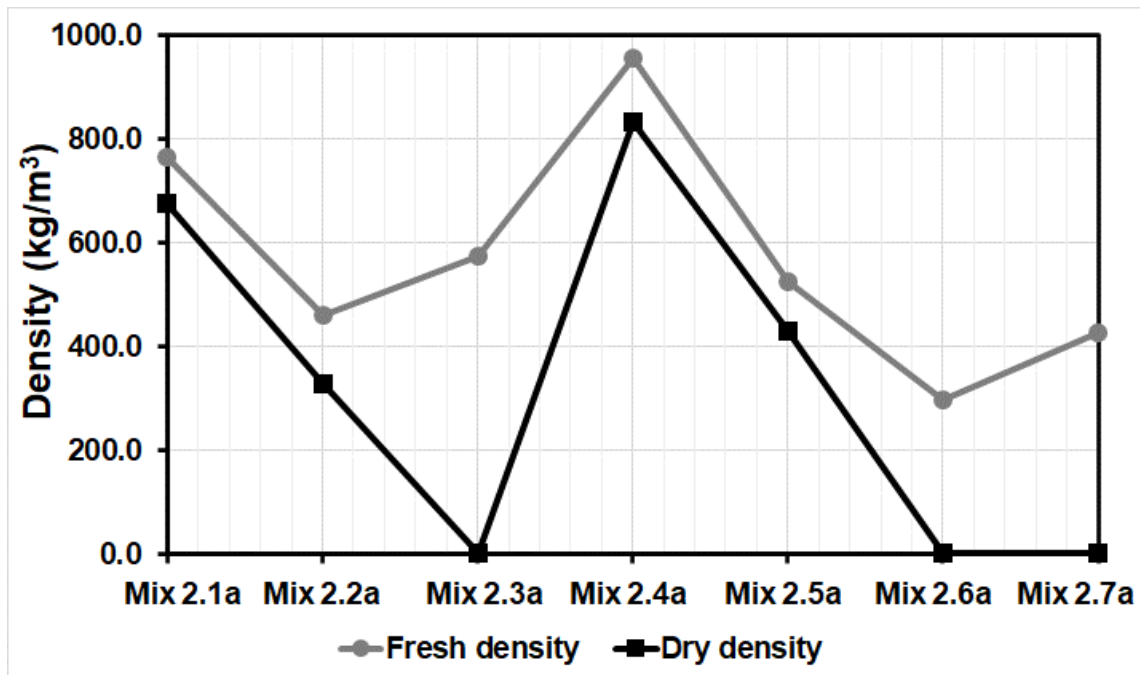


Figure 4-7 Density values of the 2<sup>nd</sup> group samples produced with the foam generated by 2.5% foaming agent

### Thermal Analysis

No thermal analysis tests were carried out for the first part of 2<sup>nd</sup> group mixtures produced within the scope of the preliminary studies carried out for the production of ultra-lightweight non-structural wall elements. Despite the fact that some of the mixtures in question can reach the desired density levels, their inability to maintain their shape stability is the main factor in thermal analysis.

### Mixtures Produced with Low Dosage of Foam Agent

Unlike the previous part of the study, in this part, the dosage of the foam agent was reduced to 0.5% by weight in 1 liter of water, and a more stable foam was tried to be produced, and the produced foam was directly added to the mixtures instead of water. The mixture proportions and visuals of related mixtures are given in Table 4.5 and Figure 4-8, respectively.

Table 4-5 Second part of the 2<sup>nd</sup> group samples produced within the scope of preliminary studies

	Mix 2.1b	Mix 2.2b	Mix 2.3b	Mix 2.4b	Mix 2.5b	Mix 2.6b	Mix 2.7b
<b>Cement (g)</b>	500	350	500	300	300	500	750
<b>Water (g)</b>	0	0	0	0	0	0	0
<b>Perlite (g)</b>	100	125	100	125	125	125	100
<b>Foam (L)</b>	3 L	4.5 L	4.5 L	2 L	3 L	4.5 L	4.5 L

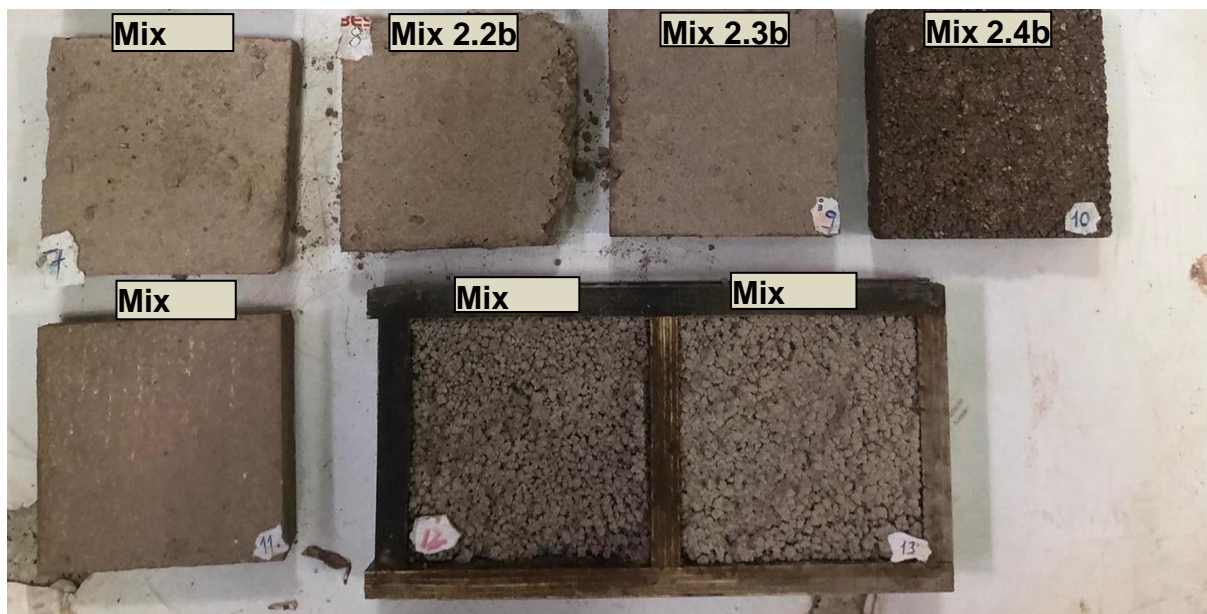


Figure 4-8 Images of the 2nd group samples produced with the foam generated by 0.5% foaming agent

### Density Measurement

To investigate the direct inclusion of the produced foam into mixtures instead of the water, as in the previous section, a base mix containing 500 g of Eco-hybrid cement and 100 g of perlite was produced using 3L foam at the first stage (Mix 2.1b). These mixtures had a fresh density below 620 kg/m<sup>3</sup> and dry density below 580 kg/m<sup>3</sup>. In order to further reduce the mixing density of Mix 2.1b, the cement dosage was reduced, and the amount of perlite was increased, and the fresh and dry density were reduced below 410 kg/m<sup>3</sup> and 300 kg/m<sup>3</sup>, respectively (Mix 2.2b) (Figure 4-9). However, due to the fact that the produced samples are open to degradation in hardened state, Mix 2.3b mixture was produced by increasing the foam amount to 4.5 L by keeping the cement dosage and perlite amount similar to Mix 2.1b. As a result, the density values of Mix 2.3b mixture decreased compared to Mix 2.1b, fresh density was decreased below 520 kg/m<sup>3</sup> and dry density was lowered below 420 kg/m<sup>3</sup>. Although Mix 2.3b has low-density values, the mixture was prone to deformation after hardening; thus, trying different options became necessary. For this reason, the Mix 2.2b mixture, which has a very low density, was reproduced with various modifications. At this point, the cement dosage was slightly reduced and Mix 2.4b, the version of Mix 2.2b produced with less foam, was produced. Although the mixture in question was stiffer than Mix 2.2b, its density was higher due to the reduced amount of foam. Mix 2.5b, produced by increasing the foam utilization rate of Mix 2.4b, exhibited the highest density results. In the ongoing studies, versions with more perlite (Mix 2.6b) and higher cement dosage (Mix 2.7b) were produced based on Mix 2.3b. Although lower densities were obtained for these two mixtures compared to Mix 2.3b, the mixtures could not reach the stiffness to be removed from the mold.

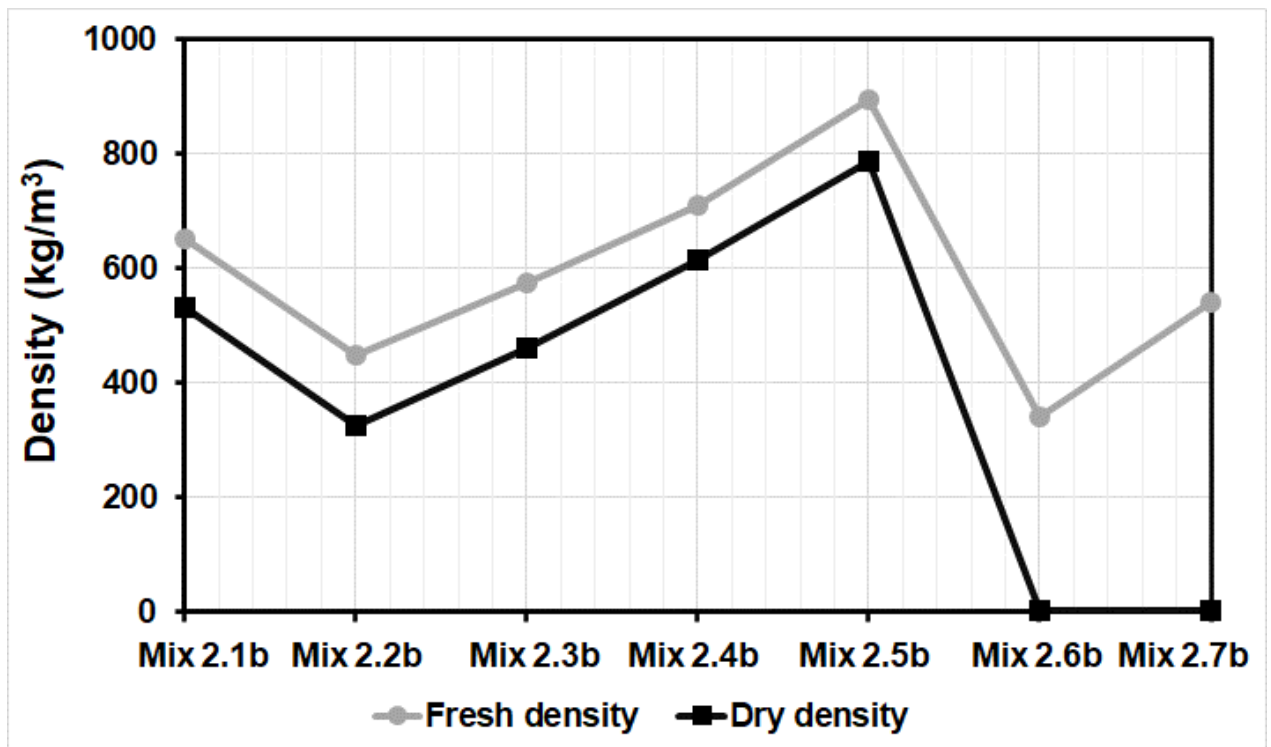


Figure 4-9 Density values of the 2<sup>nd</sup> group samples produced with the foam generated by 0.5% foaming agent



## Thermal Analysis

No thermal analysis tests were carried out for the second part of 2<sup>nd</sup> group mixtures produced within the scope of the preliminary studies carried out for the production of ultra-lightweight non-structural wall elements. Despite the fact that some of the mixtures in question can reach the desired density levels, their inability to maintain their shape stability is the main factor in thermal analysis.

### 4.1.3.3 *Preliminary Studies 3<sup>rd</sup> Group of Mixtures*

In the final stage of the preliminary studies, unlike the other stages, the foam was produced by incorporating the foaming agent directly into the cement paste at a certain dosage, instead of being produced separately from the mixture. The proportions of mixtures are presented in Table 4.6, and visuals of mixtures are shown in Figure 4-10.

Table 4-6 3<sup>rd</sup> group samples produced within the scope of preliminary studies

	Mix 3.1	Mix 3.2	Mix 3.3	Mix 3.4	Mix 3.5	Mix 3.6	Mix 3.7	Mix 3.8	Mix 3.9	Mix 3.10	Mix 3.11
<b>Cement (g)</b>	500	500	500	500	600	500	500	750	500	500	500
<b>Water (g)</b>	750	250	250	250	250	150	200	250	250	250	250
<b>Coarse Perlite (g)</b>	200	100	75	100	100	75	100	100	62.5	75	-
<b>Fine Perlite (g)</b>	-	-	-	-	-	-	-	-	62.5	-	75
<b>Foam</b>	150 g W + 5 g FA	150 g W + 2 g FA	150 g W + 2 g FA	150 g W + 2 g FA	150 g W + 2 g FA	150 g W + 2 g FA	150 g W + 2 g FA	150 g W + 3 g FA	100 g W + 2 g FA	50 g W + 2 g FA	150 g W + 2 g FA
<b>Super-plasticizer</b>	0	5	0	0	0	5	2.5	5	0	2.5	0
<b>Water/Binder</b>	1.50	0.50	0.50	0.50	0.50	0.30	0.40	0.33	0.50	0.50	0.50

Note: W represents water and FA represents foaming agent.

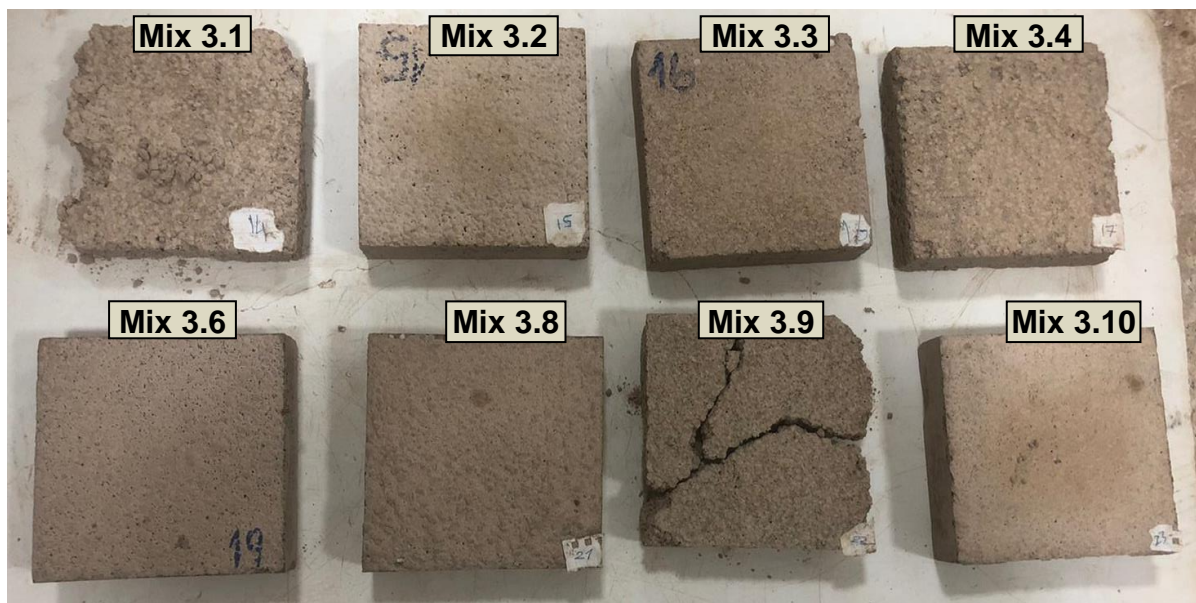


Figure 4-10 Images of the 3<sup>rd</sup> group samples produced within the scope of preliminary studies



## Density Measurement

As stated above the foaming agent was directly added to mixtures in this stage and process was conducted for specimen preparation of Mix 3.1 as followed; the water/binder ratio of 1.5 was chosen for Mix 3.1, after the cement was mixed with the required water, the foaming agent was mixed with 150 g of water and included in the mixture. Perlite aggregate was added to this mixture at the last step and this procedure was followed in all mixtures. For some mixtures, superplasticizer was added to increase the workability. While a very low fresh density below 310 kg/m<sup>3</sup> was obtained for this mixture, dry density measurements could not be performed due to the degradation of the mixture (Figure 4-11). Mix 3.2 mixture produced with lower water/binder and lower perlite usage ratio had a stiffer structure and higher density compared to Mix 3.1. In Mix 3.3, the perlite usage rate was further reduced and a decrease in density values was obtained. The effect of cement dosage was investigated in Mix 3.4 and Mix 3.5 mixtures and although the density of Mix 3.5 increased, it could not provide sufficient stiffness unexpectedly. Due to the fragile structure of Mix 3.4, Mix 3.5 was produced by reducing the amount of water and perlite, but similar results were obtained. It was planned to increase the amount of water and aggregate in the Mix 3.6 mixture to obtain fluidity with a superplasticizer. The fresh density values obtained for this mixture were at the targeted levels. Mix 3.7, the counterpart of Mix 3.6, produced with higher water and perlite content and using less superplasticizer, could not be removed from the mold, although it was at the desired level in terms of fresh density. Cement dosage, foaming agent usage rate and superplasticizer ratio were increased in Mix 3.8. Although a stiff and non-degradable sample was obtained as a result of increasing dosage, the dry density could be reduced to approximately 580 kg/m<sup>3</sup>. In Mix 3.10, which is the version of Mix 3.8 containing less cement and perlite, the foaming agent was included in the system with less water and the desired density values could not be reached. Finally, in Mix 3.9 and 3.11, perlite aggregate was included in the system in fine-coarse and only fine form, but the mixtures could not maintain their shape stability.

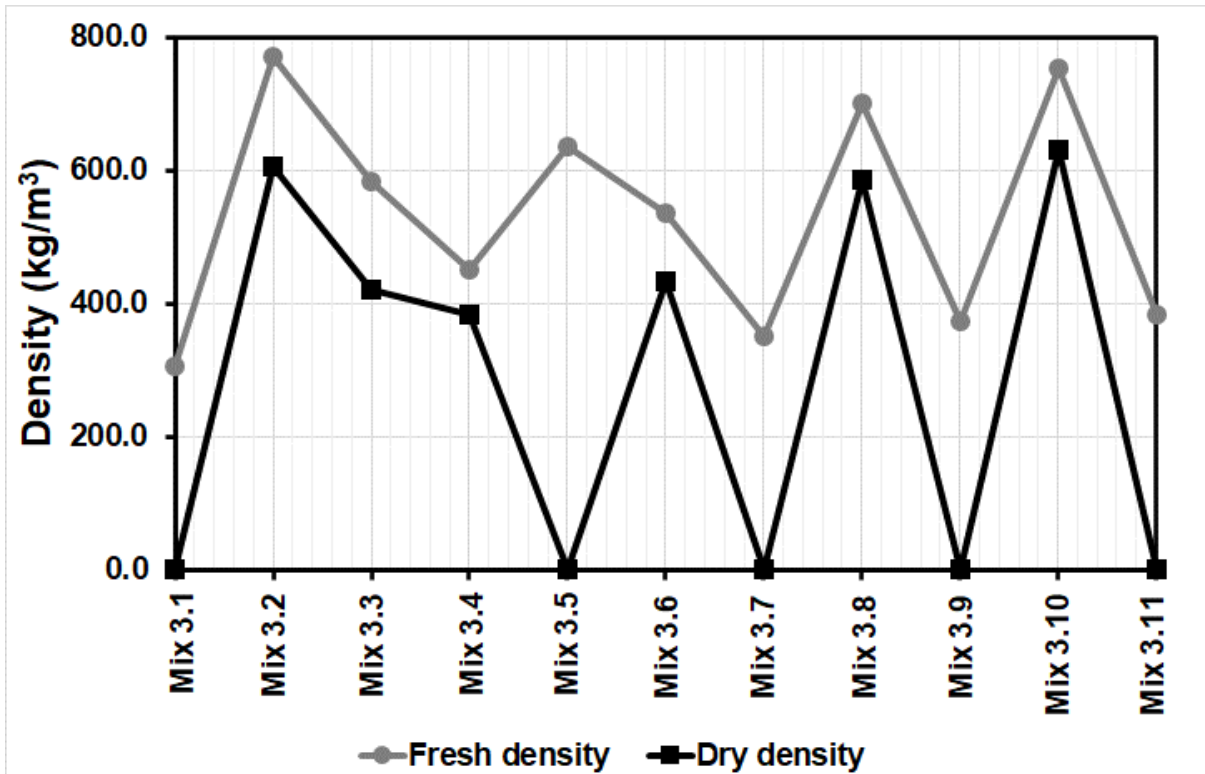


Figure 4-11 Density values of the 3<sup>rd</sup> group samples

### 3.3.2 Thermal Analysis

As a result of this study, 30x30 cm square specimens with a maximum thickness of 10 cm will be produced from some mixtures that have a sufficient level of performance and meet the project requirements, and thermal conductivity analysis will be carried out on these specimens. Thus, the effect of changing the mixture content on the thermal conductivity properties of the samples will be understood and will provide an idea for ongoing studies.

### 4.1.4 Conclusion

Within the project's scope, different types of lightweight mixture designs were produced using the existing version of Eco-hybrid cement for the work package aimed at producing ultra-lightweight non-structural wall elements. Since silica aerogel, which is planned to be used for the production of Ecohybrid cement-based ultra lightweight mixtures in the project proposal, has not yet been supplied in this reporting period, it is planned to reduce the densities of the mixtures with different methods. At this point, it is planned to reduce the densities of the mixtures by using perlite and pumice aggregates in the first place. Then, foams produced by different methods by means of foaming agent were included in the system in order to reduce the densities of the mixtures. As a result of the preliminary studies, the goal of reducing the densities of the mixtures produced

below the density values given in the project proposal was successfully achieved. In the current reporting period, thermal analyzes were carried out on certain samples, but the soundproofing performances of the mixtures were not examined. The outputs obtained are as presented below.

- The use of perlite aggregate instead of recycled aggregate in the mixtures significantly reduced the density values. In addition, the decrease in cement dosage also showed a significant effect on the decrease in density. However, under a certain cement dosage, the system was insufficient to maintain its stability in the hardened state.
- In the mixtures produced using foam, both fresh and dry density values were significantly reduced. However, if the volume of foam added and the amount of water in the system is high, it becomes very difficult to maintain the stability of the system, and hardened mixtures degrade easily.
- As a result of the inclusion of the produced foam in the system instead of water, the densities of the mixtures were significantly reduced, but the fact that the produced mixtures were open to degradation after hardening necessitated further studies.
- In the mixtures produced by mixing the foaming agent with some water into the system, it is possible to reach lower density values with stiffer samples, but more further studies are required to standardize this situation.

In general, studies will continue to produce stiffer, non-degradable, and lightweight mixtures in the later stages of the project. In addition, studies will be continued in order to examine and improve the noise reduction performance of the mixtures in the future.

#### 4.1.5 References

- Altun, F., & Aktaş, B. (2013). Investigation of reinforced concrete beams behavior of steel fiber added lightweight concrete. *Construction and Building Materials*, 38, 575-581.
- Amran, Y. M., Farzadnia, N., & Ali, A. A. (2015). Properties and applications of foamed concrete; a review. *Construction and Building Materials*, 101, 990-1005.
- Bogas, J. A., & Gomes, A. (2013). A simple mix design method for structural lightweight aggregate concrete. *Materials and Structures*, 46(11), 1919-1932.
- Celik, A. G., Kilic, A. M., & Cakal, G. O. (2013). Expanded perlite aggregate characterization for use as a lightweight construction raw material. *Physicochemical Problems of Mineral Processing*, 49.
- Chandra Berntsson, L. (2003). *Lightweight aggregate concrete science, technology and applications*. Norwich, NJ: Noyes Publications.
- Chandra, S., & Berntsson, L. (2002). *Lightweight aggregate concrete*. Elsevier.
- Chen, T. Y., Burnett, J., & Chau, C. K. (2001). Analysis of embodied energy use in the residential building of Hong Kong. *Energy*, 26(4), 323-340.

- Demirboğa, R., & Gül, R. (2003). Thermal conductivity and compressive strength of expanded perlite aggregate concrete with mineral admixtures. *Energy and Buildings*, 35(11), 1155-1159.
- Grübl, P. (1979). Mix design of lightweight aggregate concrete for structural purposes. *International Journal of Cement Composites and Lightweight Concrete*, 1(2), 63-69.
- Hammond, G. P., & Jones, C. I. (2008). Embodied energy and carbon in construction materials. *Proceedings of the Institution of Civil Engineers-Energy*, 161(2), 87-98.
- Harben, P. W., & Bates, R. L. (1990). Industrial minerals: geology and world deposits. *Metal Bulletin*.
- Hossain KMA, Lachemi M. Design, strength, durability and fire resistance of lightweight concrete with pumice aggregate. *ACI Materials Journal*, No. 5, 104(2007) 449-57.
- Hossain, K. M. A. (2004). Properties of volcanic pumice-based cement and lightweight concrete. *Cement and concrete research*, 34(2), 283-291.
- Hossain, K. M. A., Ahmed, S., & Lachemi, M. (2011). Lightweight concrete incorporating pumice based blended cement and aggregate: Mechanical and durability characteristics. *Construction and Building Materials*, 25(3), 1186-1195.
- Lo, T. Y., Tang, W. C., & Cui, H. Z. (2007). The effects of aggregate properties on lightweight concrete. *Building and Environment*, 42(8), 3025-3029.
- Loudon, A. G. (1979). The thermal properties of lightweight concretes. *International Journal of Cement Composites and Lightweight Concrete*, 1(2), 71-85.
- Mindess, S. (Ed.). (2019). *Developments in the Formulation and Reinforcement of Concrete*. Woodhead Publishing.
- Mydin, M. A. O., & Wang, Y. C. (2011). Structural performance of lightweight steel-foamed concrete–steel composite walling system under compression. *Thin-Walled Structures*, 49(1), 66-76.
- Oktay, H., Yumrutaş, R., & Akpolat, A. (2015). Mechanical and thermophysical properties of lightweight aggregate concretes. *Construction and Building Materials*, 96, 217-225.
- Parhizkar, T., Najimi, M., & Pourkhorshidi, A. R. (2012). Application of pumice aggregate in structural lightweight concrete.
- Perlit Kaynakları, 2019. Perlit URL <http://www.mta.gov.tr/v3.0/bilgimerkezi/perlit>. (Erişim tarihi:10. 02. 2021)
- Schlaich, M., & Hückler, A. (2012). Infraleichtbeton 2.0. *Beton-und Stahlbetonbau*, 107(11), 757-766.
- Sengul, O., Azizi, S., Karaosmanoglu, F., & Tasdemir, M. A. (2011). Effect of expanded perlite on the mechanical properties and thermal conductivity of lightweight concrete. *Energy and Buildings*, 43(2-3), 671-676.
- Tarasov, A. S., Kearsley, E. P., Kolomatskiy, A. S., & Mostert, H. F. (2010). Heat evolution due to cement hydration in foamed concrete. *Magazine of concrete research*, 62(12), 895-906.
- Topçu, İ. B., & Işıkdag, B. (2007). Manufacture of high heat conductivity resistant clay bricks containing perlite. *Building and Environment*, 42(10), 3540-3546.
- Uğur, İ. (2003). Improving the strength characteristics of the pumice aggregate lightweight concretes. In 18th International Mining Congress and Exhibition at Turkey-IMCET (Vol. 2003).

- Uysal, H., Demirboğa, R., Şahin, R., & Gül, R. (2004). The effects of different cement dosages, slumps, and pumice aggregate ratios on the thermal conductivity and density of concrete. *Cement and concrete research*, 34(5), 845-848.
- Valore, R. C. (1954, June). Cellular concretes part 2 physical properties. In *Journal Proceedings* (Vol. 50, No. 6, pp. 817-836).
- Wan Ibrahim, W. M., Hussin, K., Al Bakri, M. M. A., Kadir, A. A., & Binhussain, M. (2015). Development of Fly Ash-Based Geopolymer Lightweight Bricks Using Foaming Agent-A Review. In *Key Engineering Materials* (Vol. 660, pp. 9-16). Trans Tech Publications Ltd.
- Wasserman, R., & Bentur, A. (1996). Interfacial interactions in lightweight aggregate concretes and their influence on the concrete strength. *Cement and Concrete Composites*, 18(1), 67-76.
- Weigler, H., & Karl, S. (1980). Structural lightweight aggregate concrete with reduced density—lightweight aggregate foamed concrete. *International Journal of Cement Composites and Lightweight Concrete*, 2(2), 101-104.
- Yu, Q. L., Spiesz, P., & Brouwers, H. J. H. (2013). Development of cement-based lightweight composites—Part 1: mix design methodology and hardened properties. *Cement and concrete composites*, 44, 17-29.
- Yu, Q. L., Spiesz, P., & Brouwers, H. J. H. (2015). Ultra-lightweight concrete: Conceptual design and performance evaluation. *Cement and Concrete Composites*, 61, 18-28.
- Zhang, B., & Poon, C. S. (2018). Sound insulation properties of rubberized lightweight aggregate concrete. *Journal of Cleaner Production*, 172, 3176-3185.

## 4.2 Circular woodchip concrete panels to produce interior wall elements and roof slab

### 4.2.1 Introduction

The development of low cost and environmentally friendly products that combine high decorative and performance qualities are remain important [1-3]. Wood-chip concrete panels attract particular attention this regards. In many countries, the wood industries generate waste products. The low costs and the potential pollution from wood wastes have led to studies into the possible use of the wood chippings as fibers in concrete.

Wood-chip concrete panels are used in several applications in the construction industry as residential and commercial buildings such as accommodation building, office buildings, educational institutions for interior/ exterior walls. The benefits are, higher durability, lower maintenance cost and installation. The use of wood-chipping as fibers in cement composites increases toughness that is energy adsorption of materials, ductility that is enhance flexibility of the composite and, flexural capacity together with crack resistance.

Several investigations have been performed on the evaluation of physico-chemical properties and water absorption properties of wood-chip concrete composites. Bouguerra et al. [4] included wood chippings (3–8 mm) in a cement and clay matrix and tested the water adsorptivity: the macroporous wood aggregates reduced the capillary absorption inside the material.

Tamba et al. [5] described the physico-chemical properties of the wood chippings and the preparation procedure of this wood-based concrete, particularly the difficulty presented by the high water absorption properties of the wood.

There is a poor bonding strength between plant fibers and cement [6-8], because of anti -coagulant effect of dissolved substances and numerous polar hydroxyl groups existing in plant fibers. These reasons are affected cement hydration process and changes of volume such as dry shrinkage and wet expansion, it caused changes of pore structure and lower mechanical properties.

The purpose of this report is to determine and evaluate the results of recycle aggregates, eco-hybrid cement and chemical admixtures ( $Al_2(SO_4)_3$  -  $Na_2SiO_3$ ) at different ratio on flexural strength, compressive strength, and density value for wood-chip concrete panels.

### 4.2.2 Materials and methodology

#### 4.2.2.1 *Materials*

#### **Eco-hybrid cement**



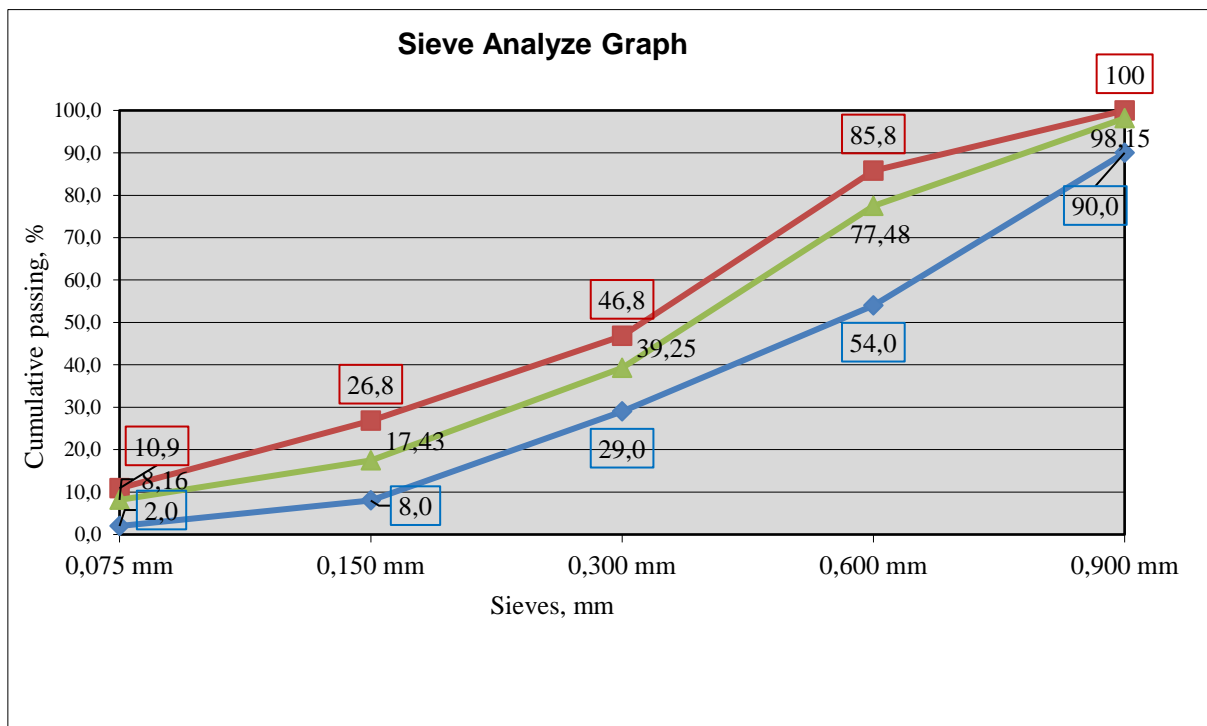
Eco-hybrid cement was used, manufactured by CIMSA (Mersin, Turkey). The properties and analysis of this cement is given previous chapters.

### Recycled aggregate

Recycle aggregate was used display a continuous grading between 0.9 and 0.075 mm (Table 4.7), obtained by BESE and manufactured by Hacettepe University.

Table 4-7 Sieve analysis table of recycle aggregates.

Sieves (mm)	Mass Retained	% Retained	Cumulative	
			Retained (%)	Passing (%)
0.9	1.85	1.85	1.85	98.15
0.6	20.67	20.67	22.52	77.48
0.3	38.23	38.23	60.75	39.25
0.15	21.82	21.82	82.57	17.43
0.075	9.27	9.27	91.84	8.16



**Note:** Blue line is indicated lower limit; Red line is indicated upper limit; Green line is indicated gradation of recycled aggregate

Figure 4-12 Result of sieve analysis of recycle aggregates.

## Wood Chippings

Pine wood chippings that are manufactured by TEPE BETOPAN display a continuous grading between 3 and 6 mm width.

The physical nature of the chippings is given Table 4.8.

Table 4-8 Properties of wood-chip fibers

Properties	Value
Length	5-25 mm
Width	3-6 mm
Thickness	0.3-0.4 mm



Figure 4-13 Wood-chip fibers

## Chemical Admixtures

Some chemical admixtures were used in wood-chip concrete panels. Firstly, there is aluminum sulphate ( $Al_2(SO_4)_3$ ) solution that accelerates cement hydration. Chemical properties of this admixtures given Table 4.9.

Table 4-9 Properties of aluminum sulphate ( $Al_2(SO_4)_3$ )

Properties	Value
% Water-Insoluble Substance Amount	0.13
pH	3.5

Another chemical admixture is sodium silicate ( $Na_2SiO_3$ ) solution that acts as glue between cement and chip and is given chemical properties in Table 4.10.

Table 4-10 Properties of sodium silicate ( $\text{Na}_2\text{SiO}_3$ )

Properties	Value
Density (at 20 C, $\text{gr/cm}^3$ )	1,377
Ph	11
Alkalinity	9,16
Weight Ratio ( $\text{SiO}_2/\text{Na}_2\text{O}$ )	3,14
Molar Ratio ( $\text{SiO}_2/\text{Na}_2\text{O}$ )	3,2
Viscosity (at 20 C)	111
$\text{Na}_2\text{O}$ (%)	8,6
$\text{SiO}_2$ (%)	27

#### 4.2.2.2 Methodology

##### Preparation of mixtures

In this experiment, effect of different water-cement, polymer-cement, fiber-cement ratios and have been investigated. According to experimental design, 10 different mixtures were prepared with wood chipping fiber in different amount of recycle aggregates, cement and chemical admixtures, which had same wood chipping fiber/chemical admixtures ratios. Firstly, three different mixtures with recycle aggregates were prepared. 10%, 12% and 15% were used these aggregates. Secondly, different cement ratios that were used 40%, 45%, 50% and 55% ratios were prepared and other mixtures that includes wood chipping fibers were used 13.3%, 16% and 20% ratios of chemical admixtures.

Table 4-11 Experimental designs and amount of materials used in mixtures

Mix	Wood-chipping fibers (%)	Chemical Admixtures (%)	Recycle Aggregate (%)	Eco-hybrid Cement (%)
Mix 1	33.5	15.1	10.1	41.3
Mix 2	32.8	14.8	12	40.4
Mix 3	31.7	14.3	15	39

<b>Mix 4</b>	34.2	15.5	10.3	40
<b>Mix 5</b>	31.4	14.2	9,4	45
<b>Mix 6</b>	28.5	12.9	8,6	50
<b>Mix 7</b>	25.7	11.6	7,7	55
<b>Mix 8</b>	29.5	13.3	11.2	46
<b>Mix 9</b>	36.8	16.6	9.2	37.5
<b>Mix 10</b>	44.3	20	7	28.7

In the route of production of wood-chip concrete specimens, first in order to the moisture of the wood chipping fibers, it is dried at 140 °C and the humidity rate is checked. The required amount of water is calculated so that the humidity of mixtures will be 47 percent. Raw materials are weighed according to mix design. These fibers have been mixed in concrete mixer (pan type) around thirty seconds and then, aluminum sulphate ( $Al_2(SO_4)$ ) diluted with calculated water is added to the mixture and mixed around sixty seconds. After, Sodium Silicate ( $Na_2SiO_3$ ) is added and mixed, Finally, aggregate and cement are added as solid ingredients and mixed.





### Molding and Curing

Cement bonded particle boards (CPB) specimens were put in the mold and pressed according to the following regime: 1 min – pressure rise up to 90 kg/cm<sup>2</sup>-

*Figure 4-14 a) concrete mixer (pan type) b) Mixing of wood-chip c) Adding aluminium sulphate (Al<sub>2</sub>(SO<sub>4</sub>)) solution d) adding sodium silicate (Na<sub>2</sub>SiO<sub>3</sub>) e) Adding recycle aggregate f) Adding eco-hybrid cement*

curing under pressure in hot water at a temperature of 85 °C; 24 hours. After specimens were placed at room temperature (23,2 °C) for 10 days for continued curing. Specimens with dimensions of 12x250x500 mm were cut three sampled CPB for flexural and compression test.







Figure 4-15 g) Press machine and pre-mold h) specimen before pressing i) specimen after pressing j) water curing at 85 °C k) cure pool l) specimen

## Testing

### Three-point flexural test

Flexural tests of specimens have been performed in BESMAK flexural machine. The dimensions of specimens used in three-point flexural tests are 12x50x250 mm. A specimen during three-point flexural test is shown in Figure 4-16m. The support span is 240 mm. Load (N), deflection (mm), stress (MPa), values have been obtained by these tests. Equation of flexural strength is given in Equation below;

$$\sigma = \frac{3xFL}{2xbd^2}$$

In this equation,

F= load at a given point on the load deflection curve (N)

L= Support span (mm)

b= Width of test beam (mm)

d= Depth or thickness of tested beam (mm)

σ= Stress in outer fibers at midpoint (MPa)

### Compression test

Compression tests of specimens have been performed in Yüksel Kaya Compression Machine from Hacettepe University. Equation of compressive strength is given in Equation below.



$$\sigma = \frac{F}{A_0}$$

F= Maximum load before cracking of specimen (N)

A<sub>0</sub>= Original specimen area

σ= Stress in WCP panels for 4 layers (MPa)

The dimensions of specimens used in compression tests are 48x50x50 mm specimens that consist of four layers. A specimen during compressive strength test is shown in Figure 4-16n.

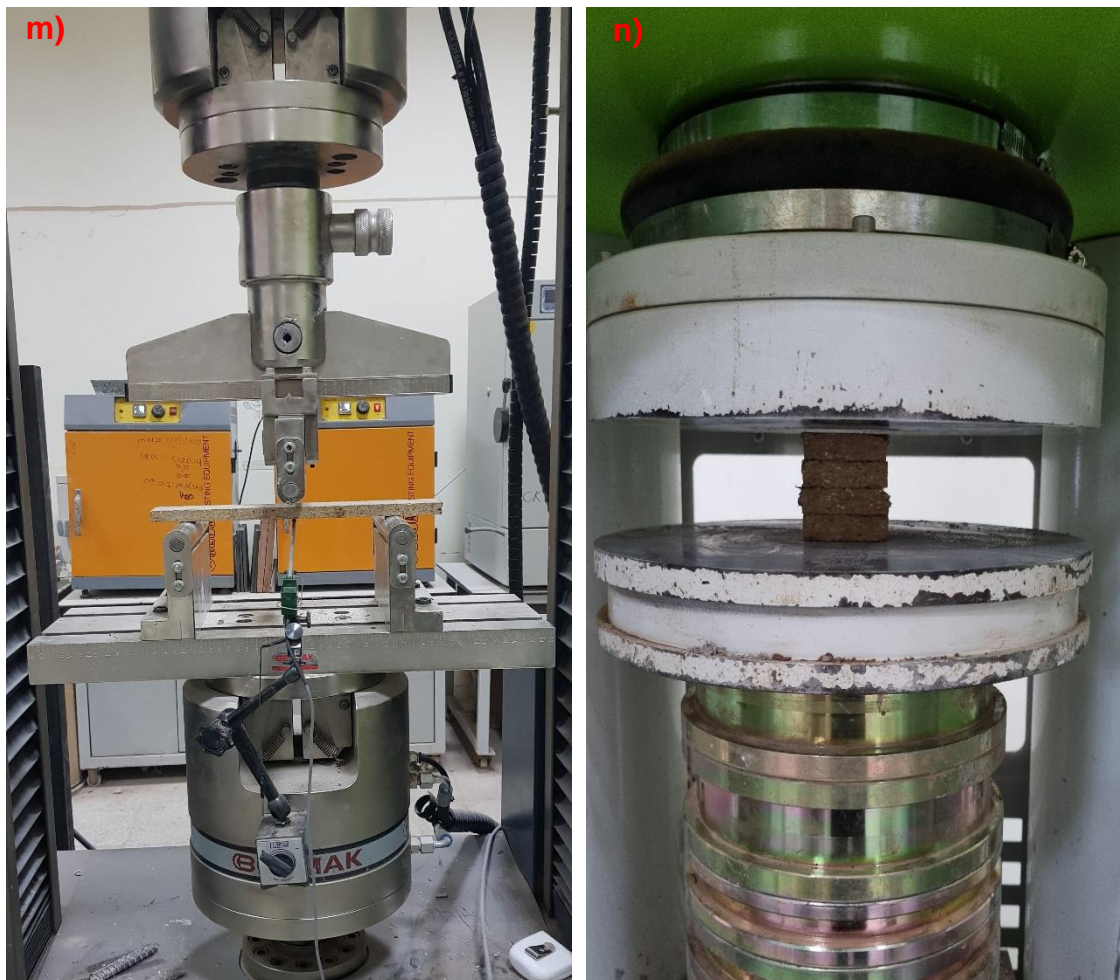


Figure 4-16 m) Three-point flexural test machine n) Compression test machine

## 4.2.3 Results and discussion

### 4.2.3.1 Experimental results of mixtures

## Flexural Strength

According to flexural test results, the highest flexural strengths have been achieved Mix 1, Mix 4 and Mix 9 that have got the same ingredients approximately, in three mixtures groups. It is observed that flexural strength slightly decreased when recycle aggregate contents increased by 10, 12 and 15% respectively, because of weak bond between wood-chip fibers and cement with decrease of other raw materials. Increasing the amount of cement in the mixtures caused a decrease in flexural strength. The reason for this decrease can be explained by the embrittlement of the mixtures with high cement ratio. When chemical admixture was used in different ratios, the best result was found at the rate of 16.6%. The low result of Mix 8 may be due to the weak bond between cement and wood-chipping fiber. Flexural strength of Mix 10 had low value because of low workability and inability to press.

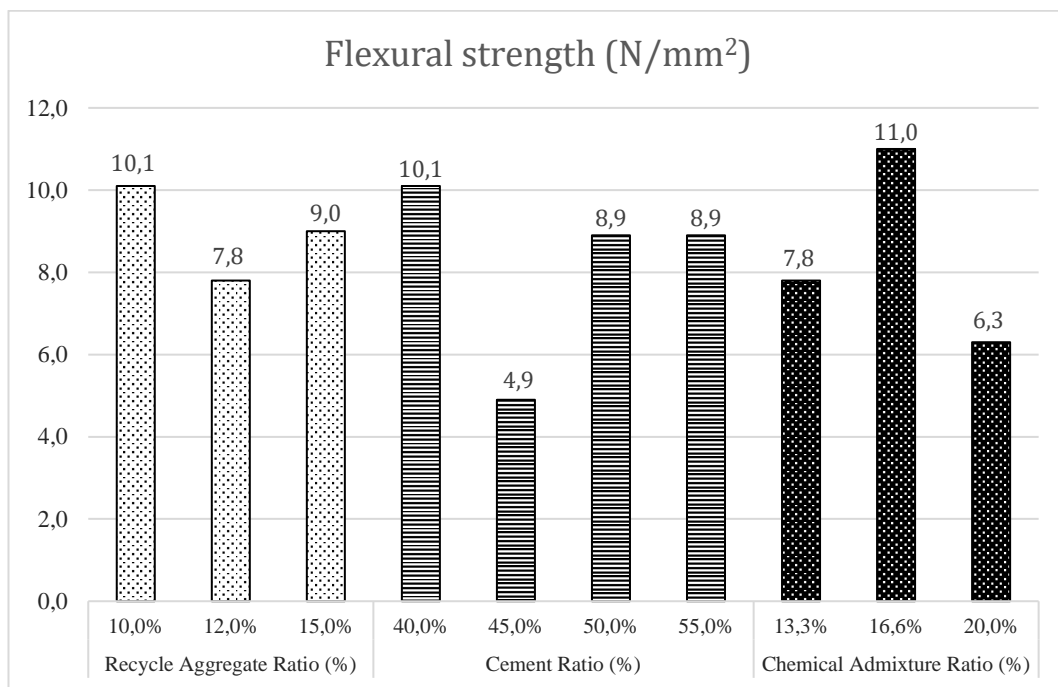


Figure 4-17 Results of three-point flexural tests

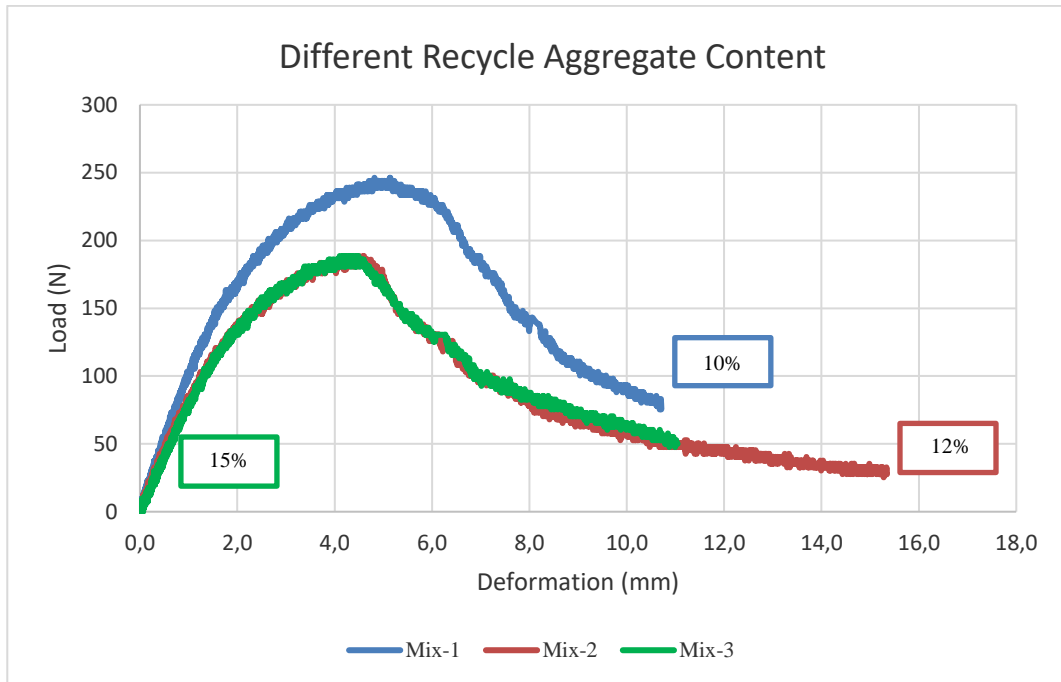


Figure 4-18 Flexural load-deformation curve of different recycle aggregate content.

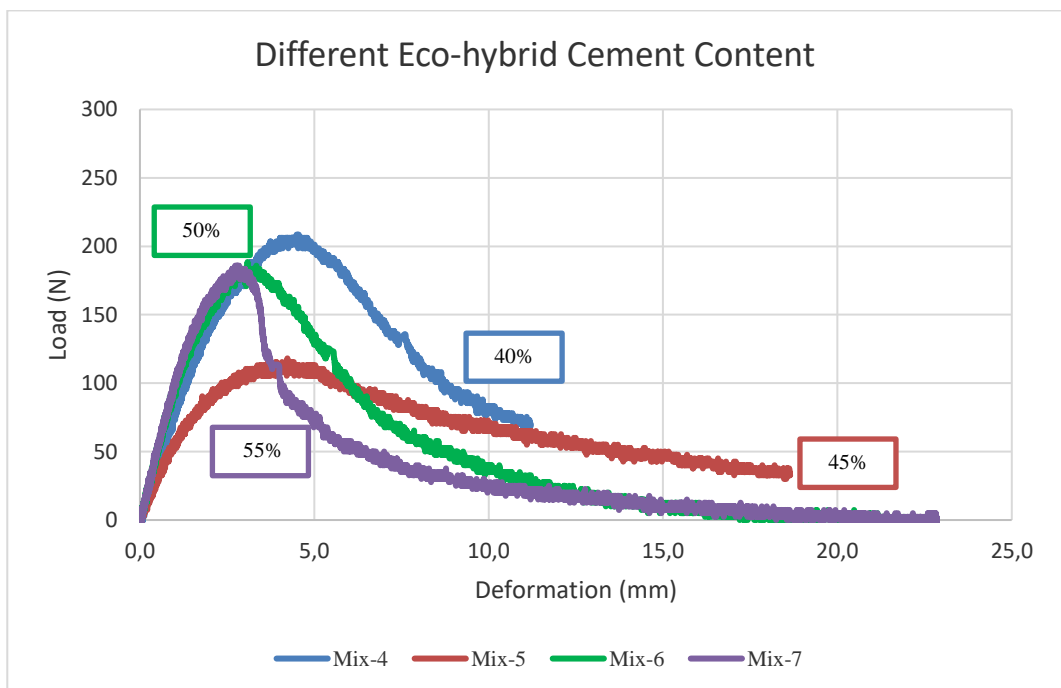


Figure 4-19 Flexural load-deformation curve of different eco-hybrid cement content.

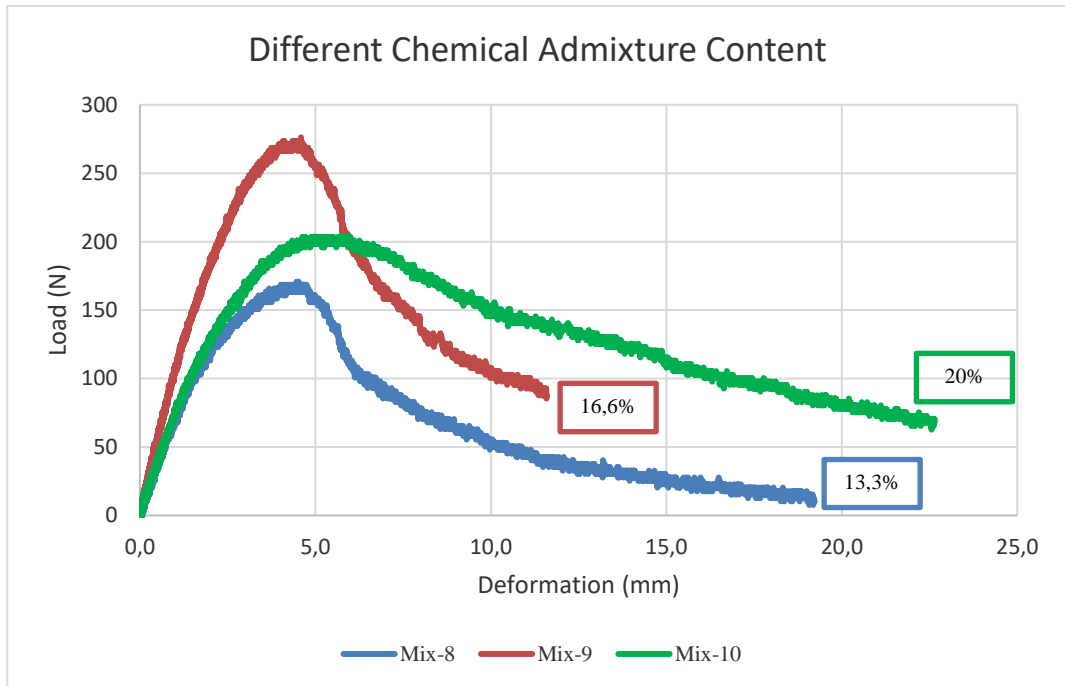


Figure 4-20 Flexural load-deformation curve of different chemical admixture content.

### Toughness

The toughness of the specimens was assessed by measuring the area under flexural stress-deformation curves. Results are shown in Figure 4-21. As can be seen, increasing recycle aggregates in mixtures give rise to less tough structure because of same result of flexural strength and the decrease in the toughness values of the mixtures used in different cement ratios was attributed to the brittle structure. Although a decrease in flexural strength was observed with the use of chemical admixtures in different ratios to the mixtures, it gained a tough feature because of the highest wood chipping fibers content of constant wood chipping fiber/chemical admixture ratio.

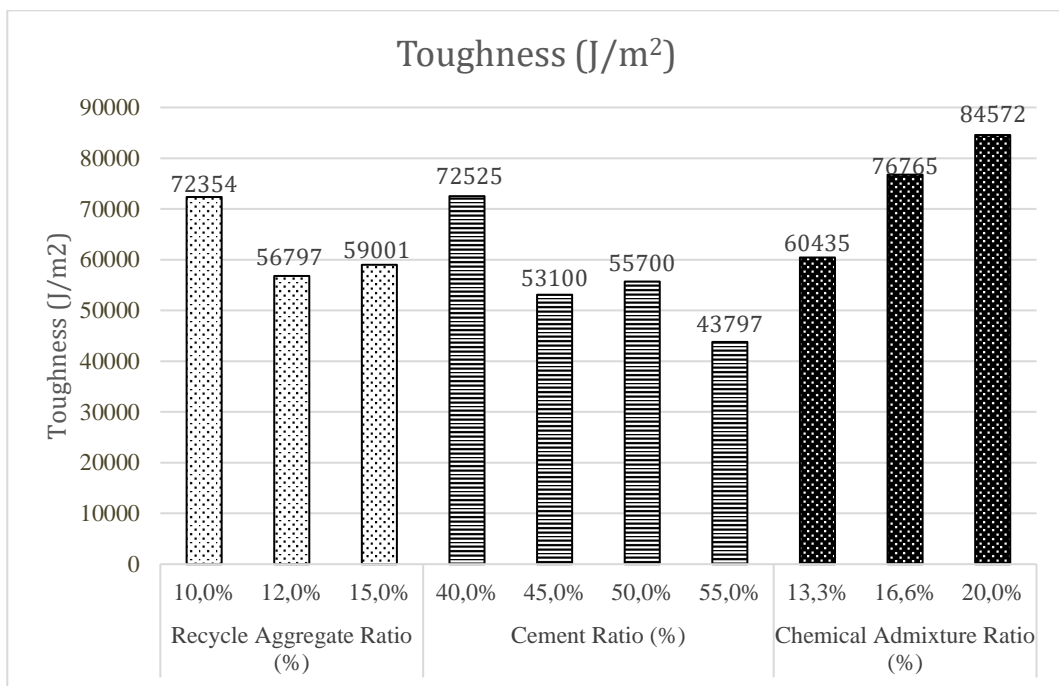


Figure 4-21 Results of toughness for flexural stress-deformation curve

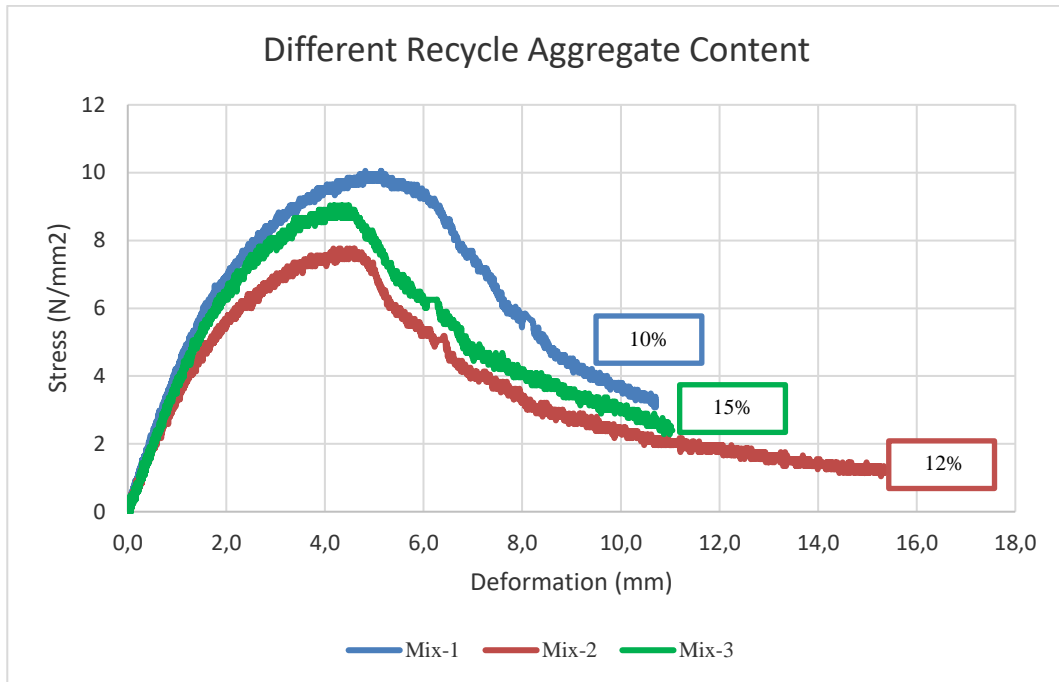


Figure 4-22 Flexural stress-deformation curve of different recycle aggregate content.

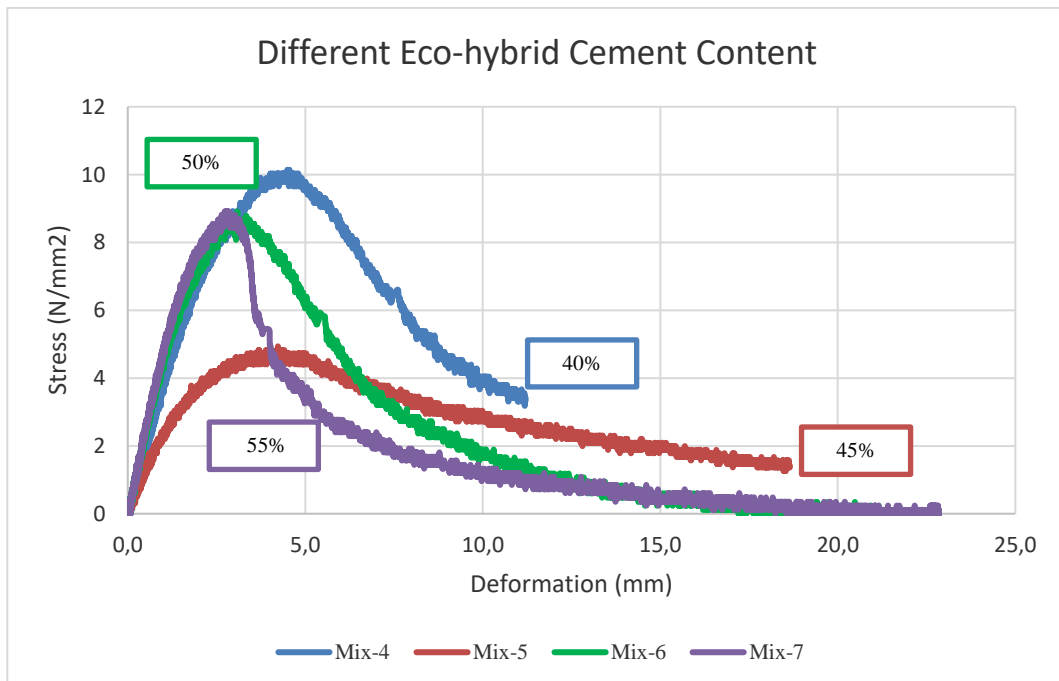


Figure 4-23 Flexural stress-deformation curve of different eco-hybrid cement content.



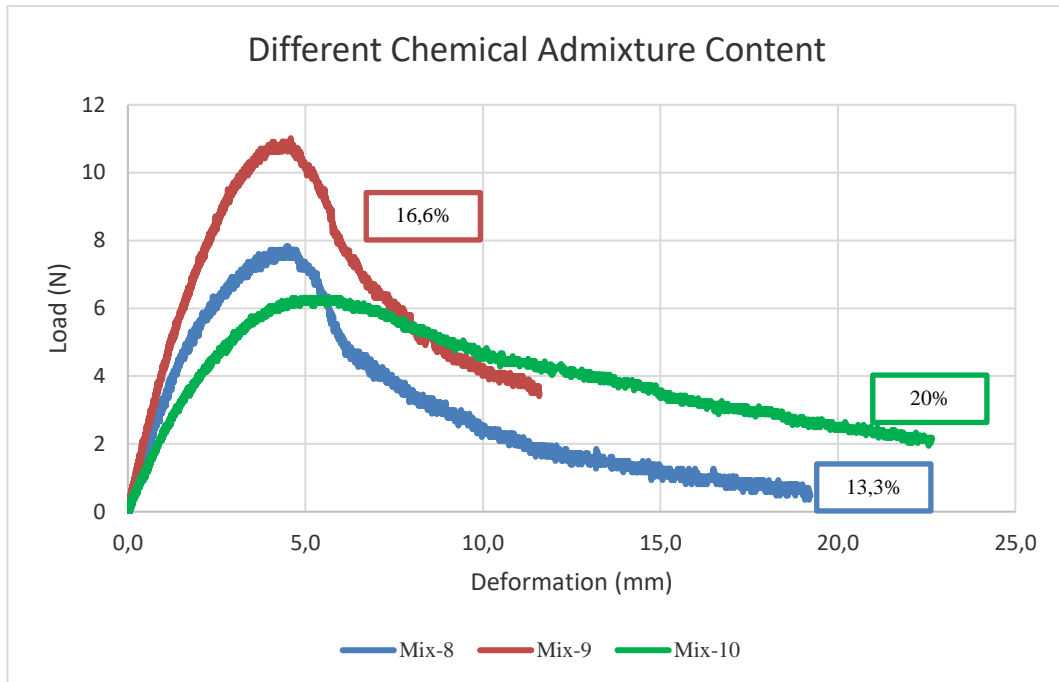


Figure 4-24 Flexural stress-deformation curve of different chemical admixture content.

### Compressive Strength

The pressure test was carried out by putting the 4 layers of the test specimens on top of each other and applying the force to the layered sample. According to compressive test results, the most strength mixture has been Mix 4. Increasing amount of cement has been decreased the compressive strength because the interoperability of different layers decreases and load transfer is not possible as the material becomes brittle.

However, in mixtures with different chemical admixtures content, as the content increases, the material will behave more ductile, so different layers work like a single layer and transfer the load to another layer properly.

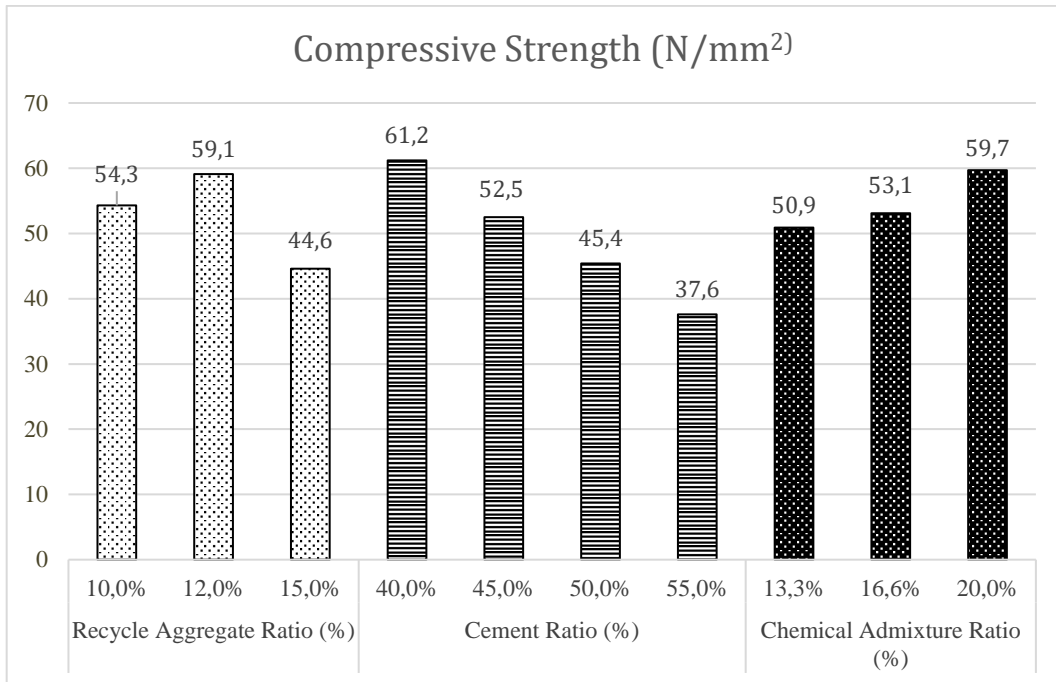


Figure 4-25 Results of compression tests

### Density

The density results of the mixtures showed that it was below the density limit value (1350 kg/m<sup>3</sup>) determined in the project. Increasing the amount of recycling aggregate by a small amount did not affect the density, while increasing the ratio of chemical admixtures caused a decrease in the density values with the increase in the amount of wood-chips due to the constant chemical admixtures/wood-chip ratio. It was observed that the density value became constant with the increase of cement ratio. This result may show that cement hydration is at the same levels.

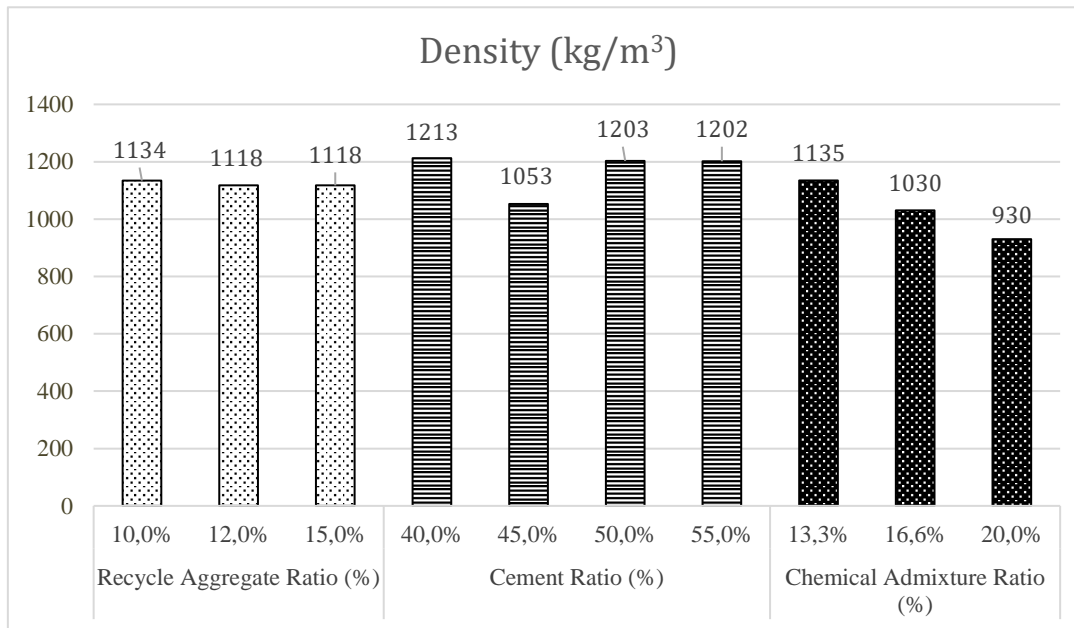


Figure 4-26 Results of density values

#### 4.2.4 Conclusion

First, the highest flexural strengths have been achieved Mix 1, Mix 4 and Mix 9 that have got the same ingredients approximately, in three mixtures groups. Increasing the amount of cement in the mixture result in a decrease in flexural strength because of embrittlement of the specimens and increasing aggregates contents caused weak bond between wood-chip fibers and cement matrix.

Second, Average toughness value trends after increasing amount of cement ratios different from the flexural strength trends because of brittle structure. Also, toughness results and flexural strength results are parallel. However, since the chip/chemical admixtures ratio is kept constant with the increase of chemical admixtures, the increase in the chip content causes results that are more toughness value but have lower bending strength in these samples.

Third, increasing amount of cement has been decreased the compressive strength because the interoperability of different layers decreases and load transfer is not possible as the material becomes brittle. However, in mixtures with different chemical additive content, as the content increases, the material will behave more ductile, so different layers work like a single layer and transfer the load to another layer properly.

It was observed that the density value became constant with the increase of cement ratio. This result may show that cement hydration is at the same levels.

Finally, the flexural, compressive strength and density values of CPB have been high. These results show that CPB can be good choice to mechanic properties. However, the development of the materials included in the project and the result of other tests will be effective in producing the best of these panels.

#### 4.2.5 References

- [1] Muhametrahimov R Kh, Galautdinov A R, Lukmanova L V, Khuzin A F, Lamberov A A and Egorova S R 2017 MATEC Web of Conferences 04005
- [2] Muhametrahimov R Kh and Izotov V S 2014 Stroitelnyye materialy 1-2 116
- [3] Muhametrahimov R Kh, Galautdinov A R and Lukmanova L V 2018 Izvestiya KGASU 3 (45) 210-19
- [4] Bouguerra A, Amiri O, Ai't-Mokhtar A, Diop MB. Water sorptivity and pore structure of wood cementitious composites. Mag Concrete Res 2002;54(2):103–12.
- [5] Tamba S, Jauberthie R, Lanos C, Rendell F. Lightweight wood fibre concrete. Concrete Sci Eng 2001;3:53–7.
- [6] Guozhong Li, Yanzhen Yu, Jianquan Li, Changchun Li, Yingzi Wang, Research on adaptability between crop-stalk fibers and cement, Cem. Concr. Res. 34(2004)1081-1085.
- [7] R. Narendar, K. Priya Dasan, Chemical treatments of coir pith: Morphology, chemical composition, thermal and water retention behavior, Compos. Part B. 56(2014) 770-779.
- [8] Sumit Chakraborty, Sarada Prasad Kundu, Aparna Roy, et al, Polymer modified jute fiber as reinforcing agent controlling the physical and mechanical characteristics of cement mortar, Constr. Build. Mater. 49(2013)214-222.

## 5 Demountable precast hollow-core blocks produced by accelerated carbonation.

### 5.1 Fine fraction upcycling

The crushing process of concrete waste produces recycled aggregates that are agglomerations of the original concrete's aggregates with adhered mortar. The crushing process will also produce fines from the mortar, the amount being controlled to a large extent by the strength of the original concrete, and to the used crushing technology. New crushing technologies have been developed to produce cleaner aggregates, i.e. aggregates with less adhered mortar. These technologies also generate more concrete fines. These are fines consisting mainly of hydrated cement paste and sand, i.e. old mortar. The fraction of adhered mortar (by volume of the sample) decreases with increasing size of the recycled aggregates (Hansen and Henrik, 1983; Parviz, 2012; Parthiban & Saravana Raja Mohan, 2017).

These concrete fines (0-4 mm) are up to now not valorized on a high level because of an elevated water absorption, higher fines content, and the presence of contaminations. Colman et al. (2020), sampled and characterized concrete fines from different recycling centers, and in nearly all samples the total amount of sulphate was found to exceed the limit specified in the European standard EN 206, meaning the concrete fines could not be reused in concrete complying with EN 206.

The waste concrete fines (0-4 mm) have in the last decade been identified as a feedstock for mineral carbonation. In the present study the carbonation of these concrete fines will be used to develop new construction materials. The goal of this study is to be able to use waste concrete fines without any additional binder to make hollow construction blocks using a vibro-press machine and mineral carbonation. These hollow blocks will be used to construct separation walls having a minimum strength of 5 MPa. In this report the objective is to better understand the parameters affecting the optimum bulk density obtained by compacting small solid bricks (dimensions: length: 160 mm, width:40 mm, height: 40 mm) with the vibro-press before upscaling to the full-size hollow blocks (dimensions: length:290 mm, width:90 mm, height: 190 mm). The thickness of the walls of these hollow blocks is 30 mm. Concrete fines from the recycling of waste concrete with the ADR-HAS technology (Gebremariam et al., 2020) was used as raw material. Two product streams were delivered by the TUDelft for this study: a recycled fine aggregate (RFA) (0.25–4 mm) and recycled concrete fines (RCF) (<0.25 mm). These fines were used as such without further treatment.

The concrete fractions were characterized (PSD, XRF, XRD, true density by He-pycnometry). In order not to waste limited material given, a screening test was used to investigate the carbonation potential and resulting strength by carbonating cylindrical samples of 23 mm diameter and 46 mm height made of the ECA and RFA. Water was added to the 'as received' RCF and RFA to obtain a moisture content of approximately 10%, which is necessary for a good

compaction of the material. The moisturized RCF and RFA were compacted and shaped in a cylindrical mold (diameter: 23.0mm, height: 46.0±0.5mm) by a hydraulic press with a compaction force of 150 kgf/cm<sup>2</sup>. The maximum compaction force was sustained for 30 seconds. The cylinders were subsequently carbonated in an autoclave reactor at a pressure of 3 barg CO<sub>2</sub>, and a temperature of 50°C, during 16 hours. This resulted in a compressive strength of 8.5±0.1 MPa for the RCF and 3.8± 0.1 MPa for the RFA. The CO<sub>2</sub> uptake was respectively 47.5 g CO<sub>2</sub>/kg RCF, and 33.1 g CO<sub>2</sub>/kg RFA. These results show the potential of the RCF and RFA to be used as a material for block production by mineral carbonation.



Figure 5-1. Carbonated cylinders made by hydraulic compaction of the RCF (left), RCA (right).

In a next step the compaction with a vibro-press was investigated. However, before attempting to make the hollow blocks, 40x40x160 mm moulds were used to regulate and optimize the RFA and RCF moisture content and the Vibro-press parameters to obtain proper sample height (40 mm) and maximize the bulk density, which will reflect on the compressive strength results (Figure 5-2). Once the prisms were made with the vibro-press, they were carbonated at 3 barg of CO<sub>2</sub>, and a temperature of 50°C, during 16 hours. After carbonation the prisms were cut to cubes and compressive strength test was carried out on the cubes (40 mm).

Summary of the results are shown in Figure 5-2. It can be clearly seen that for both RFA and RCF, the higher the wet density, and thus the higher the (dry) bulk density and the lower the porosity, the higher the compressive strength. In case of the RFA, the hydraulic compaction (at 150 kg/cm<sup>2</sup>) although it resulted in higher density (wet density 2.05 g/cm<sup>3</sup> and dry bulk density: 1.85 g/cm<sup>3</sup>), and lower porosity, its compressive strength is not significantly higher than the highest density (wet density: 1.98 and dry bulk density: 1.74 g/cm<sup>3</sup>) reached with the vibro-press which may indicate that the particle packing is better with the vibro-press. In case of the RCF, hydraulic compaction (at 150 kg/cm<sup>2</sup>) leads to higher density and thus higher compressive strength. For the RCF the correlation



between density and compressive strength seems to be the similar for the vibro-press and hydraulic compaction method. Additional experiments will be carried out to see if a better packing can be reached by using higher frequencies with the vibro-press. This needs to be further investigated, and reported.

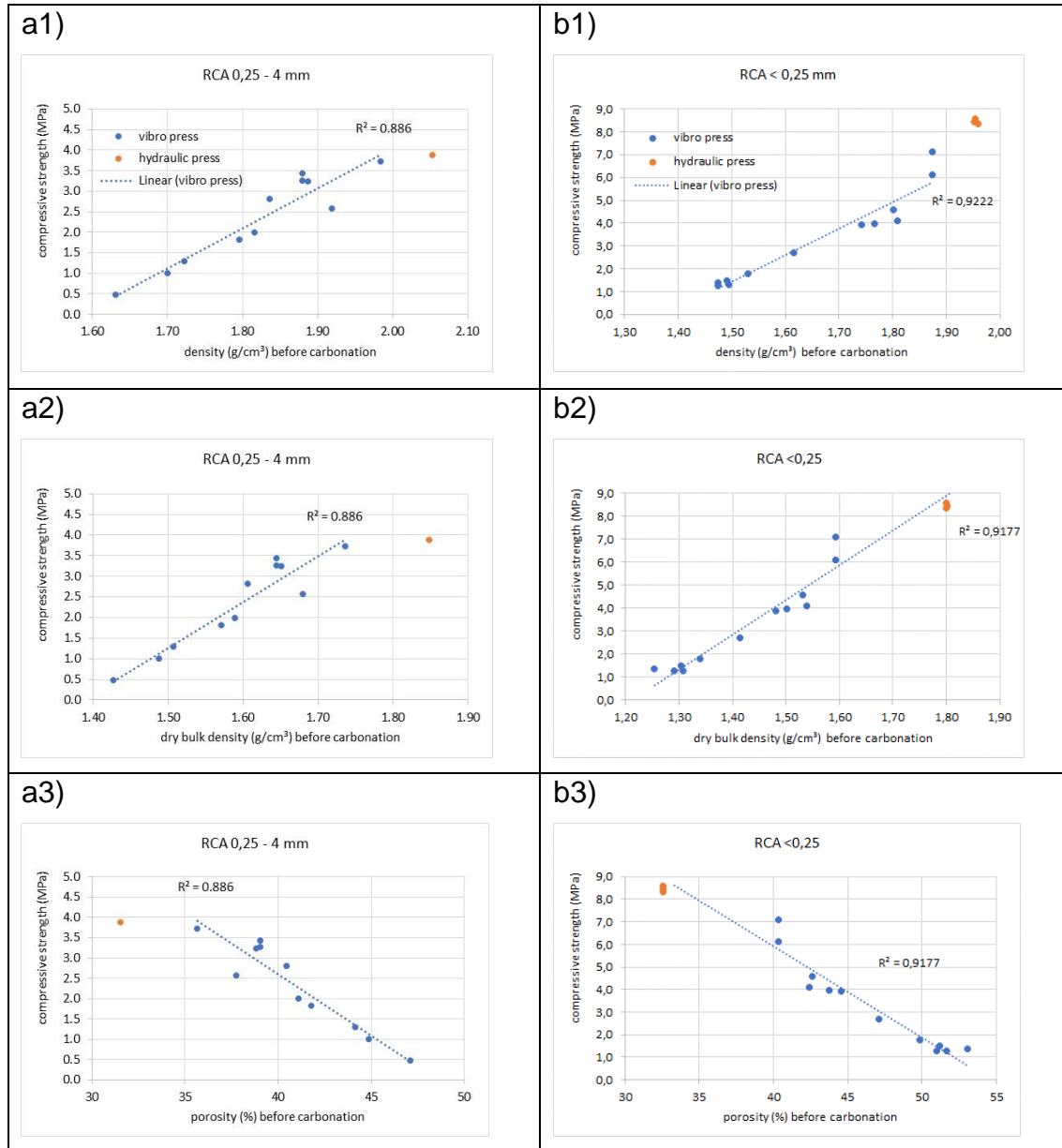


Figure 5-2 - Compressive strength (MPa) as function of density(g/cm<sup>3</sup>) before carbonation, dry bulk density (g/cm<sup>3</sup>) before carbonation, and porosity (%) for RCA and RCF prisms made with the Vibro-press. Figures in the left column are results associated with RCA, and the figures in the right column belong to the RCF.

## 5.2 References

Colman, Ch., D. Bulteel, S. Rémond, Z. Zhao, L. Courard (2020) Valorization of Fine Recycled Aggregates Contaminated with Gypsum Residues: Characterization and Evaluation of the Risk for Secondary Ettringite Formation. *Materials* 2020, 13, 4866. <https://doi.org/10.3390/ma13214866>

- Fang Y., J. Chang (2015) Microstructure changes of waste hydrated cement paste induced by accelerated carbonation. *Construction and Building Materials* 76 (2015) 360–365. <http://dx.doi.org/10.1016/j.conbuildmat.2014.12.017>
- Gebremariam A.T., F. Di Maio, A. Vahidi, P. Rem (2020) Innovative technologies for recycling End-of-Life concrete waste in the built environment. *Resources, Conservation and Recycling*, 163 (2020), 104911. <https://doi.org/10.1016/j.resconrec.2020.104911>
- Hansen, T.C., Narud, H., 1983. Strength of recycled concrete made from crushed concrete coarse aggregate. *Concr. Int.–Des. Constr.* 79–83.
- Nassar, R.U.D., P. Soroushian (2012) Strength and durability of RAC containing milled glass as partial replacement for cement. *Construction and Building Materials* 29, 368-377. <https://doi.org/10.1016/j.conbuildmat.2011.10.061>
- Nedunuri, A.S.S.S., A.Y. Mohammed, S. Muhammad (2021) Carbonation potential of concrete debris fines and its valorisation through mineral carbonation. *Construction and Building Materials*, 310 (2021), 125162. <https://doi.org/10.1016/j.conbuildmat.2021.125162>
- Parthiban, K., Saravana Raja Mohan, K., 2017. Influence of recycled concrete aggregates on the engineering and durability properties of alkali activated slag concrete. *Construction and Building Materials* 133, 65-72. <https://doi.org/10.1016/j.conbuildmat.2016.12.050>

## 6 Adjustment of formulations and pre-industrial prototypes of circular ceramic wall tiles

### 6.1 Description of the problem.

Currently, construction and demolition waste (CDW) represent the highest percentage of waste generation by economic activity and households in the EU, representing a mean of 35.9% of the total waste [1]. Moreover, despite the variability of type of material between CDW by country, all data available show that brick, tile and other ceramic material is the major waste type among them, excluding a low number of countries where metal waste is more representative. When it comes to the management of this ceramic waste in the EU, statistics show that they are normally accumulated in landfills having a particularly low recycling rate, especially in those developing countries [2]. Due to the policies that support a transition towards the reuse and recycling of CDW, added to the increasing demand of raw materials for construction materials, researchers in the field of recycling and materials engineering have put their efforts in alternative routes to get new value-added materials. Taking this into account, the target of this work package is to develop new ceramic product made from secondary raw material coming from high-grade sorted ceramic waste. Therefore, efforts are focused on demonstrate the technical and economic viability of circular ceramic wall tile containing at least 30 wt% of ceramic fractions recovered from CDW. Moreover, the objective is to upscale a novel process based on moderate sintering temperature (<800 °C in comparison with standard 1150 °C) to enable ~40% energy reduction.

### 6.2 State of the art/technology.

When focusing on the currently research trend of CDW applications, sand production, pavement/road construction, ready mix concrete, concrete blocks, cement, bricks, and low-cost adsorbent for wastewater treatment can be found [3]. However, no literature about new ceramic tiles from demolition wastes is available, being bricks the only ceramic material based on these wastes. Despite that, there exist other solid wastes that are being proposed to substitute partially or totally the ceramic tile raw materials. Among these wastes, ceramic tile polishing powder, sanitary stoneware waste, ceramic mud and red mud and different types of fly ash. The amounts in which they are added range between 10% and 100% and the temperatures they use range between 900-1300 °C. Moreover, these first scientific contributions show an improvement of the final ceramic pieces properties, such as higher flexural strength among others [4]. However, almost all of these recycled materials come from waste from the ceramic industry itself. In fact, in the last decades the ceramic industry has been recycling its own discarded products. Currently, these wastes have become raw materials, through their addition in the milling step of a wet milling process in floor tile and bricks manufacturing. Once more, this controlled addition represents an

improvement in the final quality and is considered the most efficient technique for the reutilization of this waste. Therefore, the technology here is based in this practice, changing the waste by high-grade purity sorted ceramic demolition waste.

### 6.3 Extended methodology

The current ceramic tile manufacturing process is explained below, while comparing it with the methodology here adopted. In general, the production flow of ceramic tiles consists of the selection and conditioning of raw materials, shaping of the raw piece and glazing and firing the piece. Within this general scheme, there may be different variations such as the shaping of the piece or the glazing process. On the one hand, shaping can be either by uniaxial pressing of the piece (floor or wall covering) or by extrusion of the material (rustic cladding). On the other hand, glazing can be done after the first firing (double firing) or directly on the green ceramic piece (single-firing). Finally, the piece can undergo additional treatments such as decoration by third fire, polishing, etc. This study is focused on the manufacture of ceramic covering tiles; therefore, the process of manufacturing tiles by uniaxial pressing will be described below without considering the glazing of the piece or subsequent finishing processes. Nevertheless, quality controls are here considered such as water absorption of the pieces and flexural strength.

The process begins with the selection and collection of virgin raw materials, coming from quarries near the factory. Consequently, the general composition of raw materials inherently depends on the area of manufacturing of the tiles, which can fluctuate even between areas of the same country. In general, the composition of these materials is based on feldspars, sands, carbonates and kaolins. These materials are used with minimal processing based on milling. This grinding can be made in two ways: dry (hammer mills) and wet (ball mills). The first case of grinding produces larger particle sizes (c.a. 300 microns) while the wet process produces particles smaller than 200 microns. In this study, both types of grinding have been combined to obtain a starting material of tens of microns, in order to facilitate the sintering process. A more detailed description of the importance of this process and the proposed processing of the raw material, in this case material from demolition and construction waste, is presented in previous deliverable D2.1 of this project.

Subsequently, the material that has been wet processed is controlled dry until the desired percentage of humidity by the atomization process. Atomization is a spray drying process by which the powder is sprayed in a drying chamber with a hot air flow, which after taking in the moisture from the particles, exits through the upper part of the cyclone, allowing the dry particles with spherical shape to exit through the bottom of it. The atomizers are industrial machines that work with tons, so to be able to reproduce this process on a small scale in the laboratory, the usual procedure is to moisten the powder by hand until the desired humidity percentage and sieve it to obtain spherical particles approximated to those of an industrial atomized.

Once the powder has been prepared, the pieces are shaped by dry pressing. In this procedure, the powder is mechanically compacted using hydraulic piston presses. Once the pieces are pressed, they are dried until the percentage of water is reduced to 2-5%. After this step, the pieces can be glazed or directly fired; in this case, they are directly conducted to the firing process. The pieces are sintered through a thermal cycle widely established and accepted by the industry, which is adapted to each composition and product. This cycle is made up of different controlled heating, sintering and cooling ramps to favour the desired crystallizations. For example, the conventional thermal cycle of porcelain tile reaches 1220 °C while the white or red body tile reaches lower temperatures of 1135 °C. The firing process have been optimized to be as fast as possible, being able to cook the pieces in cycles of up to less than 1 hour.

The technology proposed here does not differ from conventional industrial ceramic processing. In fact, it is worth to highlight that no logistical or material investment is required by ceramic companies to implement these techniques. The proposed process begins with grinding using the mills available in the industry, which are already used to grind the own ceramic waste produced during the production chain. This grinding is done until a powder size of microns is achieved. Once grounded, this powder is moistened using water in the same way as in industry, since no additive or solvent are needed. Finally, these pieces can be sintered using a conventional furnace, in fact, the maintenance of the pieces proposed is of the same duration as usual in these materials, 6 minutes, which would not affect the usual rhythm of production either.

## 6.4 Materials

For this study, common building materials have been chosen. For availability and reproducibility reasons, these studies were done on new, not used building materials. These materials can be classified in three different groups attending their chemical nature: ceramic, gypsum-based and cementitious materials. In the first group, five types of ceramics can be found, such as common brick, porcelain, roof, red body and white body tiles. There are two type of gypsums in the second one, plasterboard and plaster. Finally, two cementitious materials can be found in the third group: concrete (sidewalk curb), mortar (sidewalk tile). In Figure 6-1, pictures of each material, sorted by groups, are shown. For the preconditioning of the materials, they were cut with a circular saw, milled and sieved until a micrometric particle size was obtained, following the conventional milling process for these materials. A deeper description of the milling process as well as a deep characterization of these materials was provided in previous documents of the ICEBERG project, D2.1. The composition of the used materials is provided in terms of equivalent oxides in Table 6.1. Finally, the particle sizes obtained for this milling process were measured for each material and are shown in Table 6-2.

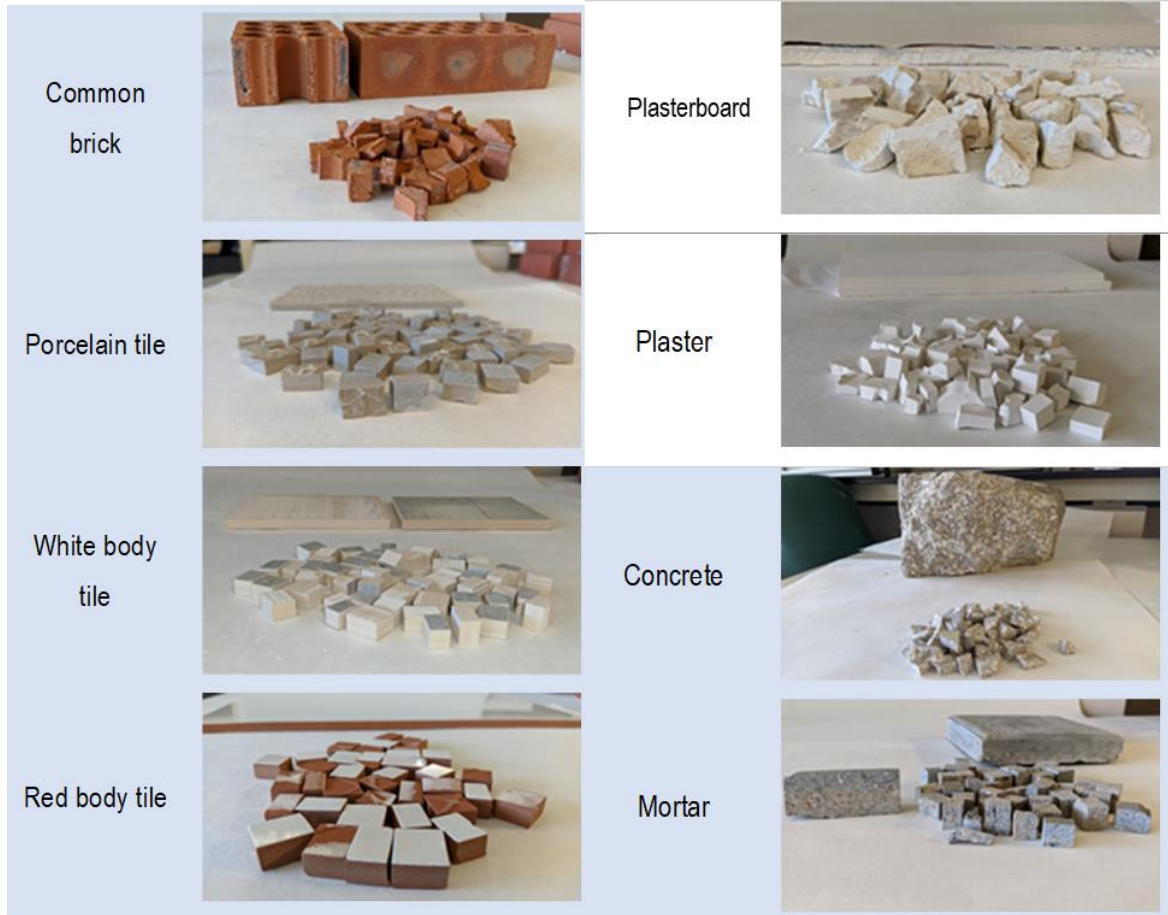


Figure 6-1. Pictures of the chosen construction materials: Ceramics, gypsums and cements groups.



Table 6-1. Composition in equivalent oxides of the materials obtained by XRF. N.d.: Non detected. Lol.: Loss-of-ignition.

	Brick (%)	Porcelain (%)	White body tile (%)	Roof tile (%)	Mortar (%)	Cement (%)	Plaster-board (%)	Plaster (%)	Red body tile (%)
CaO	1.05	0.78	8.93	3.22	25.4	36.1	31.7	39.3	8.52
Fe <sub>2</sub> O <sub>3</sub>	6.06	0.90	1.48	6.47	1.31	0.67	0.72	0.11	4.65
K <sub>2</sub> O	5.00	1.43	2.04	4.15	1.26	1.62	0.49	nd	3.61
MgO	4.54	0.46	0.31	2.62	2.50	0.45	0.44	0.81	1.80
Na <sub>2</sub> O	1.03	4.38	1.20	0.28	0.26	0.31	nd	nd	0.59
SiO <sub>2</sub>	62.4	71.6	67.0	64.3	42.4	30.5	7.70	1.13	64.5
TiO <sub>2</sub>	0.74	0.53	0.84	0.86	nd	nd	nd	nd	0.82
Al <sub>2</sub> O <sub>3</sub>	17.5	19.3	17.7	17.0	3.70	4.22	2.75	0.69	14.7
P <sub>2</sub> O <sub>5</sub>	0.22	0.14	0.065	0.11	0.050	0.046	nd	nd	0.13
SO <sub>3</sub>	0.082	nd	0.10	-	0.26	0.41	35.3	49.2	0.082
I.L.	1.11	--	--	0.81	22.8	25.6	20.3	8.40	--

Table 6-2. Particle size distributions ( $d_{50}$  and  $d_{90}$ ) of the pattern materials after conventional milling and sieving.

	Material	$d_{50}$	$d_{90}$	mode
Majority materials	Facade brick	5,53	21,49	bimodal
	Porcelain tile	4,97	21,01	bimodal
	Red body tile	4,88	19,34	bimodal
	White body tile	4,89	19,33	bimodal
Minority material	Drywall	5,64	22,33	monomodal
	Plaster	3,56	14,85	trimodal
	Concrete	5,43	26,30	monomodal
	Mortar	5,78	22,20	bimodal

In this project, a sorting line for high purity CDW is being developed, which is expected to have a sensitivity of 92%, however, sorted materials is not yet available. Therefore, in order to establish a theoretical approximation of the classified construction waste expected in the future, the following compositions and proportions of materials have been chosen. With this purpose, mixtures of

one ceramic (brick or porcelain tile) as majority material and one minority material (plaster, plasterboard, mortar or cement) were prepared in different proportions in weight: 80/20, 90/10 and 95/5. Moreover, with the aim of testing a real composition that approximates those available in a building demolition, the percentage of construction materials expected in a demolition has been calculated from a standard Spanish single-family house project. Then, these data have been extrapolated to only ceramic materials (Figure 6-2) with the composition: 81% brick, 14.4% red roof tile, 4.5% red body tile and 0.1% sanitary ware. Finally, the percentage of sanitary ware can be despised from the others, resulting in mixtures based on red ceramic.

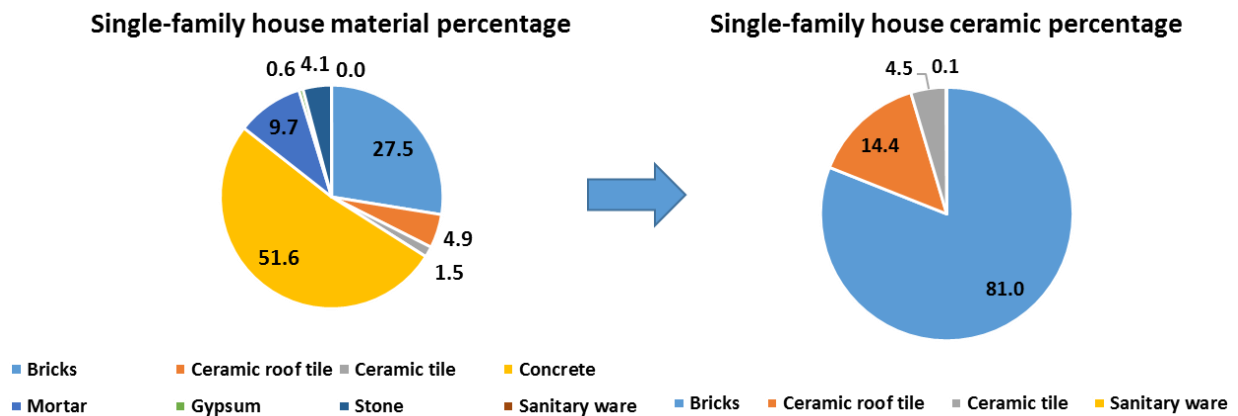


Figure 6-2. Single-house material proportion and only ceramic material proportion.

Finally, with the objective of improving the mechanical stability of the samples during pressing and handling of the samples two clays were selected, provided from Keraben Grupo. These two clays mainly differ in their content of Al<sub>2</sub>O<sub>3</sub> as well as their content in Ca<sup>2+</sup> and Na<sup>+</sup>, part of the composition, in terms of equivalent oxides are provided in Table 3, obtained by means of XRF spectroscopy. The first clay is a montmorillonite clay with origin in Ukraine, whilst the second one, is a kaolinitic clay, coming from Tarragona, Spain.

Table 6-3. Composition in equivalent oxides of the two industrial clays obtained by XRF. (In bold those present in >2%). Lol.: Loss-of-ignition.

	CaO	Fe <sub>2</sub> O <sub>3</sub>	K <sub>2</sub> O	MgO	Na <sub>2</sub> O	SiO <sub>2</sub>	TiO <sub>2</sub>	Al <sub>2</sub> O <sub>3</sub>	Lol
<b>Clay 1</b>	0.2	0.84	<b>2.3</b>	0.41	0.32	<b>55.5</b>	1.23	<b>22.5</b>	16.6
<b>Clay 2</b>	0.88	1.41	1.28	1.16	<0.10	<b>44.1</b>	0.23	<b>26.8</b>	24

## 6.5 Activities in progress

Firstly, a preliminary study was carried out in small scale in order to acquire general information about the mixtures of materials behavior under different sintering temperatures as well as discard any important incompatibility between them. With this purpose, different ceramic fractions with cementitious or gypsum-based materials and three sintering temperatures were chosen. Samples were prepared mixing the preconditioned powder of the principal material, ceramic (common brick or porcelain tile) with the minority material (mortar, concrete, plaster or plasterboard) using an electric grinder. The resulting 8 different compositions were prepared in 95/5, 90/10 and 80/20 proportions, being 24 samples for each thermal cycle. Then, the powder was moistened and pressed in a circular die, obtaining specimens of 1.5 cm in diameter and 0.4 cm in height. Pressed samples were thermally treated in a furnace that simulates the industrial thermal cycle. The chosen sintering temperatures were 900, 1000 and 1100 °C with dwelling time of 1 hour and a fast-cooling rate of 30 °C/min. Once the samples were sintered, they were studied by their density variation, linear contraction and mass loss. Final samples appearance are shown in Figure 6-3 and 6.4 and the mentioned measured parameters are provided in Figure 6-5 and 6.6 for brick and porcelain based samples respectively. Moreover, XRD patterns for some interesting samples were recorded in order to study the produced phase changes.

For **common brick mixtures**, densities of the materials on green are ~ 1.4 g/cm<sup>3</sup> and they remain almost unaltered after the thermal treatment at 900 and 1000 °C, without any noticeable linear contraction, as it can be seen in Figure 6-5. Specially, in the composition with less ceramic fraction, the density only increases in the high temperature cycle (1100°C), while in the lower cycles it decreases approximately 10%, with the exception of the composition with plaster, which remains unchanged in terms of density until the highest cycle. The most pronounced variation in density occurs for mortar and plasterboard compositions. As the fraction of brick material increases, the variation in density is attenuated, in fact, the compositions are practically unchanged in terms of density up to the highest cycle of 1100°C. These density changes can be explained by the shrinkage of the samples, since in the linear shrinkage graphs, it is observed how, again, the composition with less ceramic fraction is the one that contracts the most and that at temperatures of 900 and 1000 no shrinkage is observed in the pieces. Finally, an expansion is observed in the compositions containing plasterboard, because of the “bubbling” of the pieces due to the gases release. Finally, all the sintering temperatures and all the compositions and percentages show mass loss. Again, the mass loss decreases the higher the ceramic fraction, since the minority material has more water content and is generally less thermally stable than the ceramic one. Obviously, the higher the temperature cycle, the higher mass loss the samples experiment. Both, expansion of the mentioned samples and changes in colours can be appreciated in Figure 6-3. As it can be seen, the dark colour that appears after sintering at the highest temperature may be indicating overcooking of the sample. Therefore, temperatures between 950 and 1100 °C were chosen in following steps.

On the other hand, **mixtures containing porcelain tile** as a major component present lower densities when they are on green, c.a. 1.3 g/cm<sup>3</sup>. However, the mixtures containing materials from the gypsum group experiment shrinkage of c.a. 7 % even at 1000 °C. When the sintering temperature is reached at 1100 °C, the shrinkage is present in all the mixtures and proportions. Moreover, the samples presented in Figure 6-4 show a slight colour change as the sintering temperature rises. Based on the colour change, the shrinkage of these samples and the results of the thermochemical analyses of the porcelain tile material, 1100 °C is not an excessive temperature; therefore, it will be chosen as reference sintering temperature for further tests of mixtures of porcelain tile material. Finally, it should be highlighted that all samples on green, especially those containing gypsum materials, presented a very low mechanical stability, hindering the manipulation of the samples. Consequently, adding a plasticizer, such as clays, is considered to improve this property in the following tests.

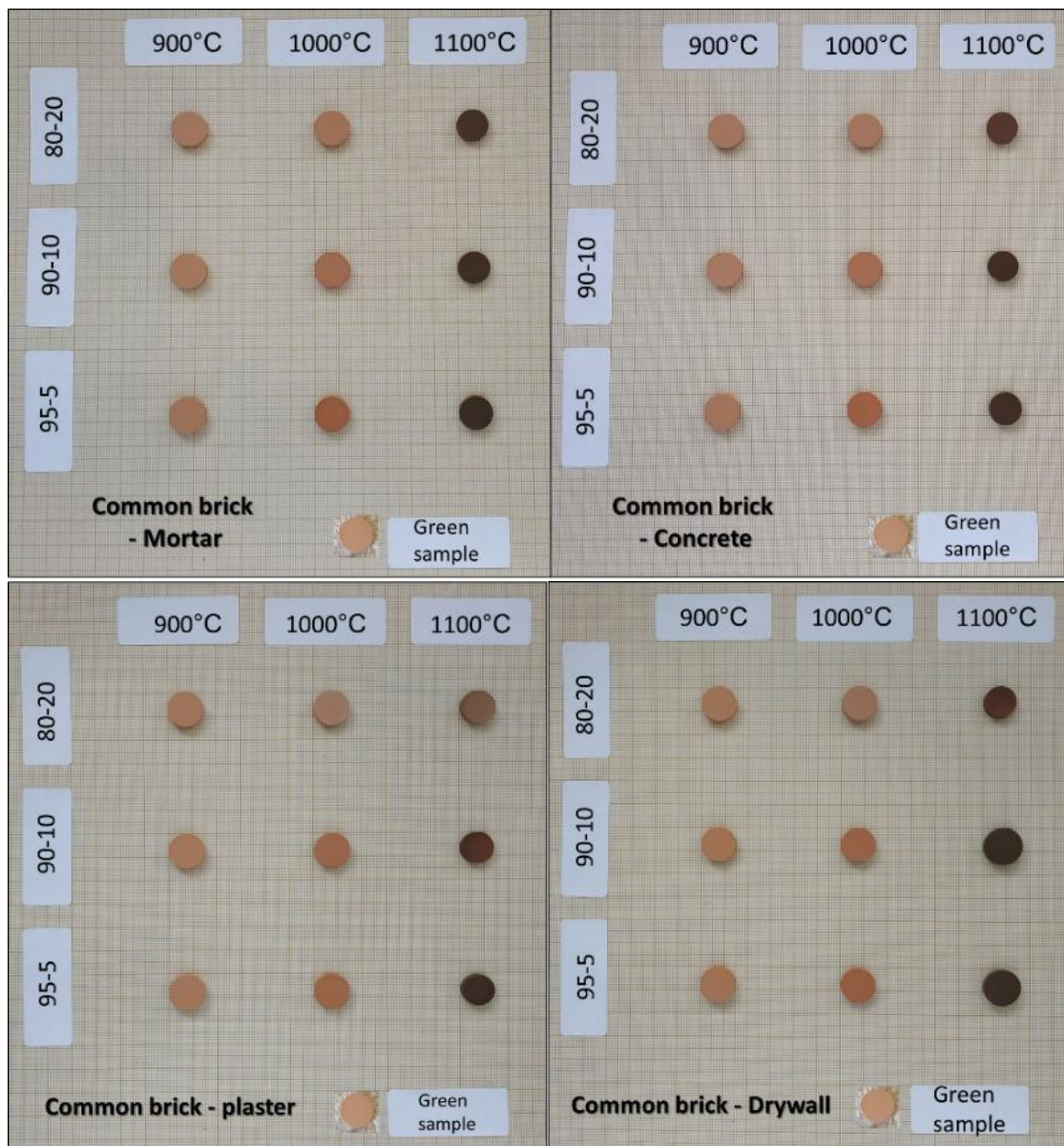


Figure 6-3: Sintered samples: mixtures containing common brick as ceramic fraction.



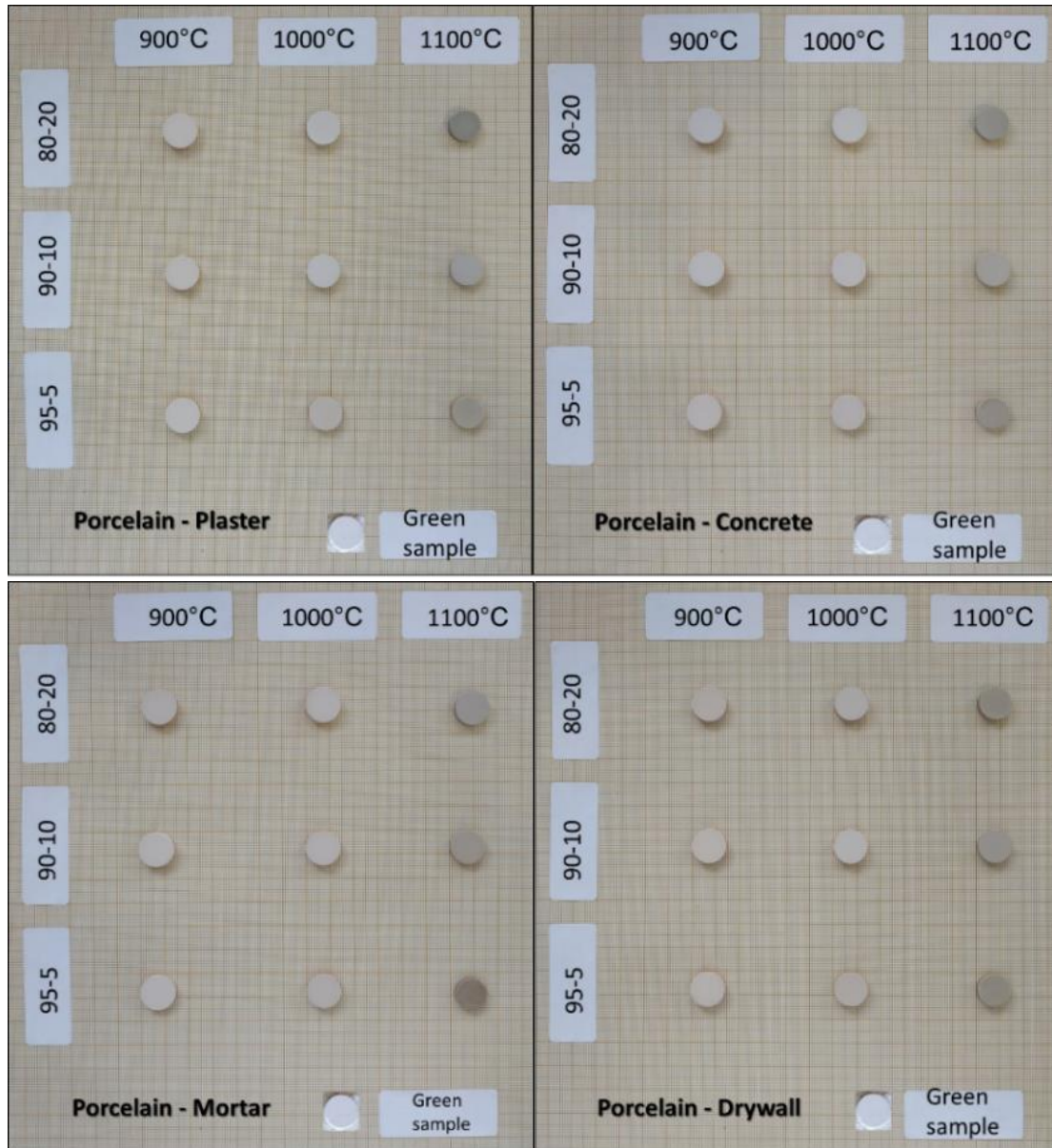


Figure 6-4 : Sintered samples: mixtures containing porcelain tile as ceramic fraction.

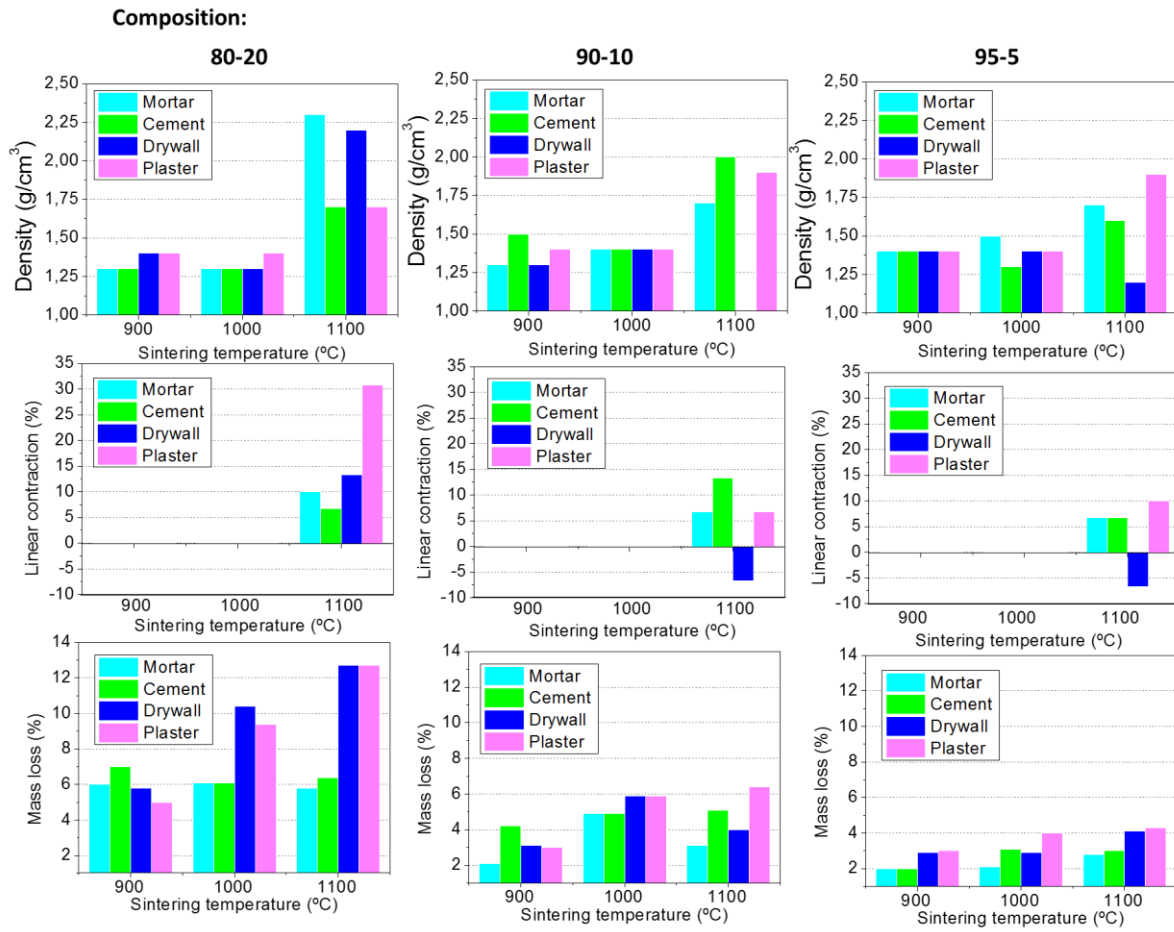


Figure 6-5. Final density, linear shrinkage and mass loss for brick-based samples containing 20, 10 and 5% of mortar, cement, drywall or plaster.



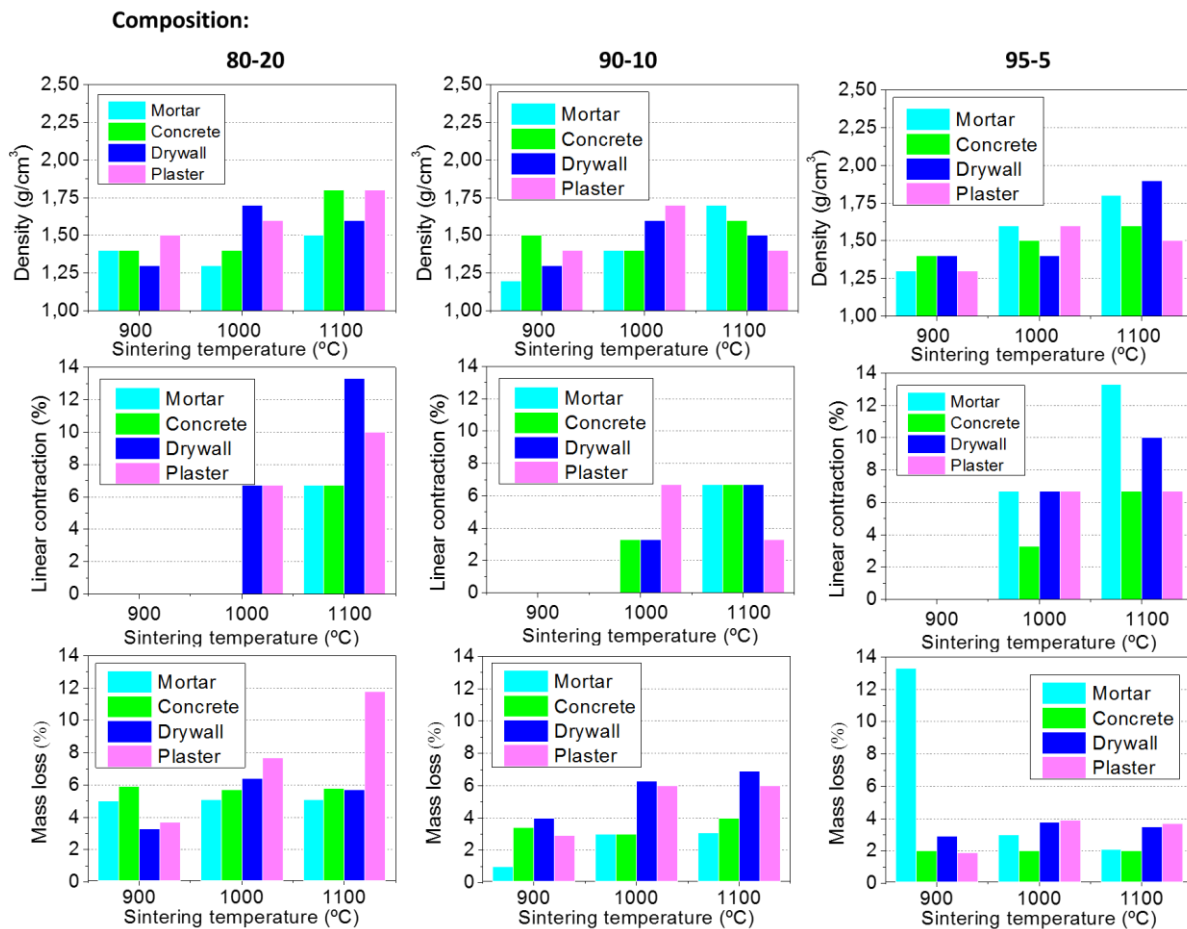


Figure 6-6. Final density, linear shrinkage and mass loss for porcelain tile-based samples containing 20, 10 and 5% of mortar, cement, drywall or plaster.

XRD analysis were carried out for all materials with a percentage of 80/20, for both 900 and 1100 °C sintering temperatures. Besides these samples, some interesting samples that experimented different contraction or colour change also were measured. XRD patterns of these materials are shown in Figure 6-7 for those containing brick as majority component, and Figure 6-8 for those containing porcelain tile. For comparative purposes, XRD patterns of the individual starting material are presented on the top of each graph. Moreover, the compositions are sorted by type of impurity: a) mortar, b) concrete, c) plaster and d) plasterboard. Firstly, it is seen that no reaction has undergone during the sintering process, since any new peaks are present in the mixture's XRD patterns. Besides that, all the mixtures present a similar behaviour, phases present in the ceramic fraction (common brick and porcelain tile) are still present in all the samples, while phases only present in the minor material, such as clinoenstatite and calcite in mortar, calcite in concrete, bassanite in plaster and gypsum in plasterboard, are not present in the sintered sample. This fact can be explained by the decomposition of the indicated phases at said temperature (as commented in previous report).

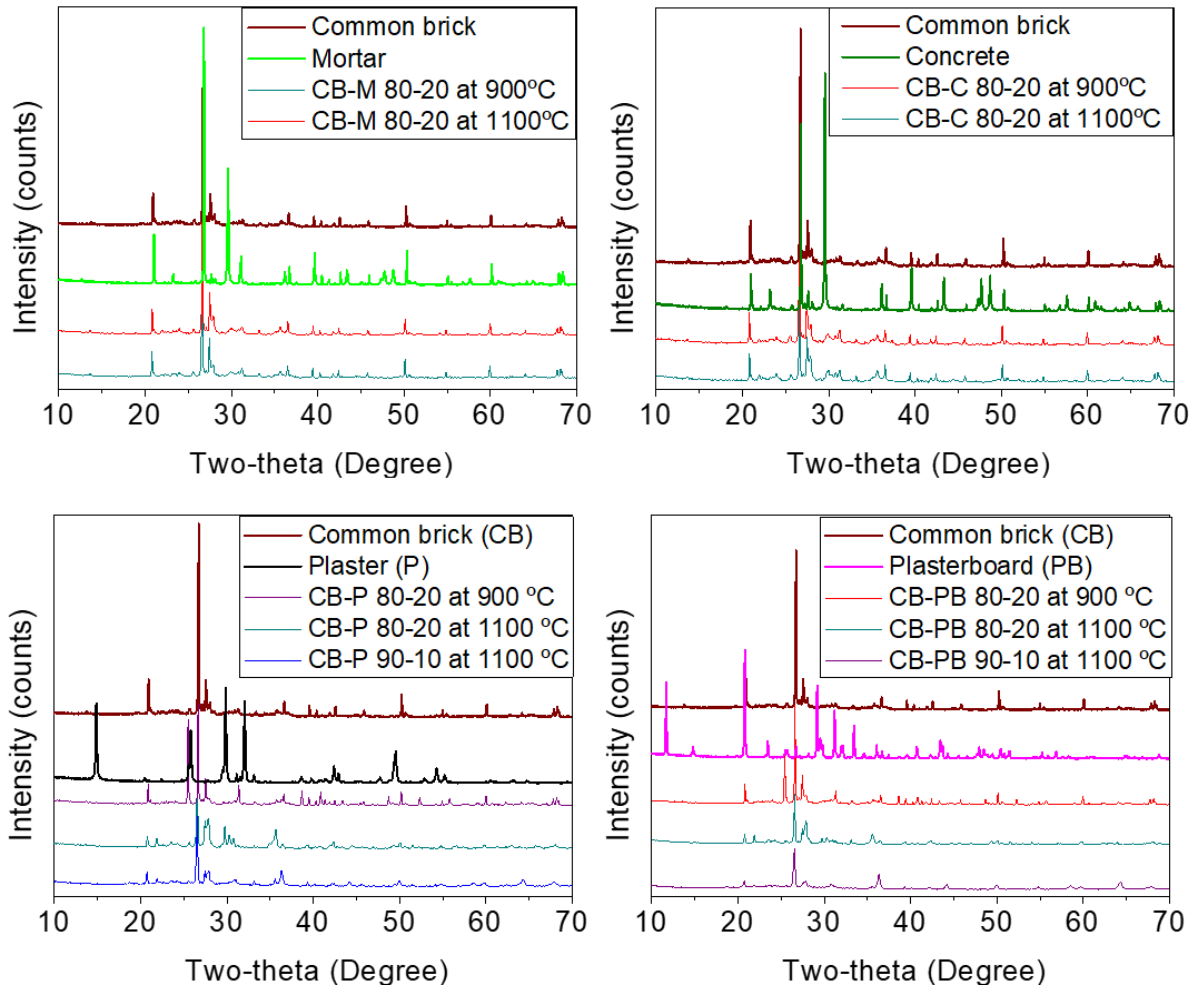


Figure 6-7 Comparison of XRD patterns of mixtures and individual starting material. Mixtures containing common brick as major material.

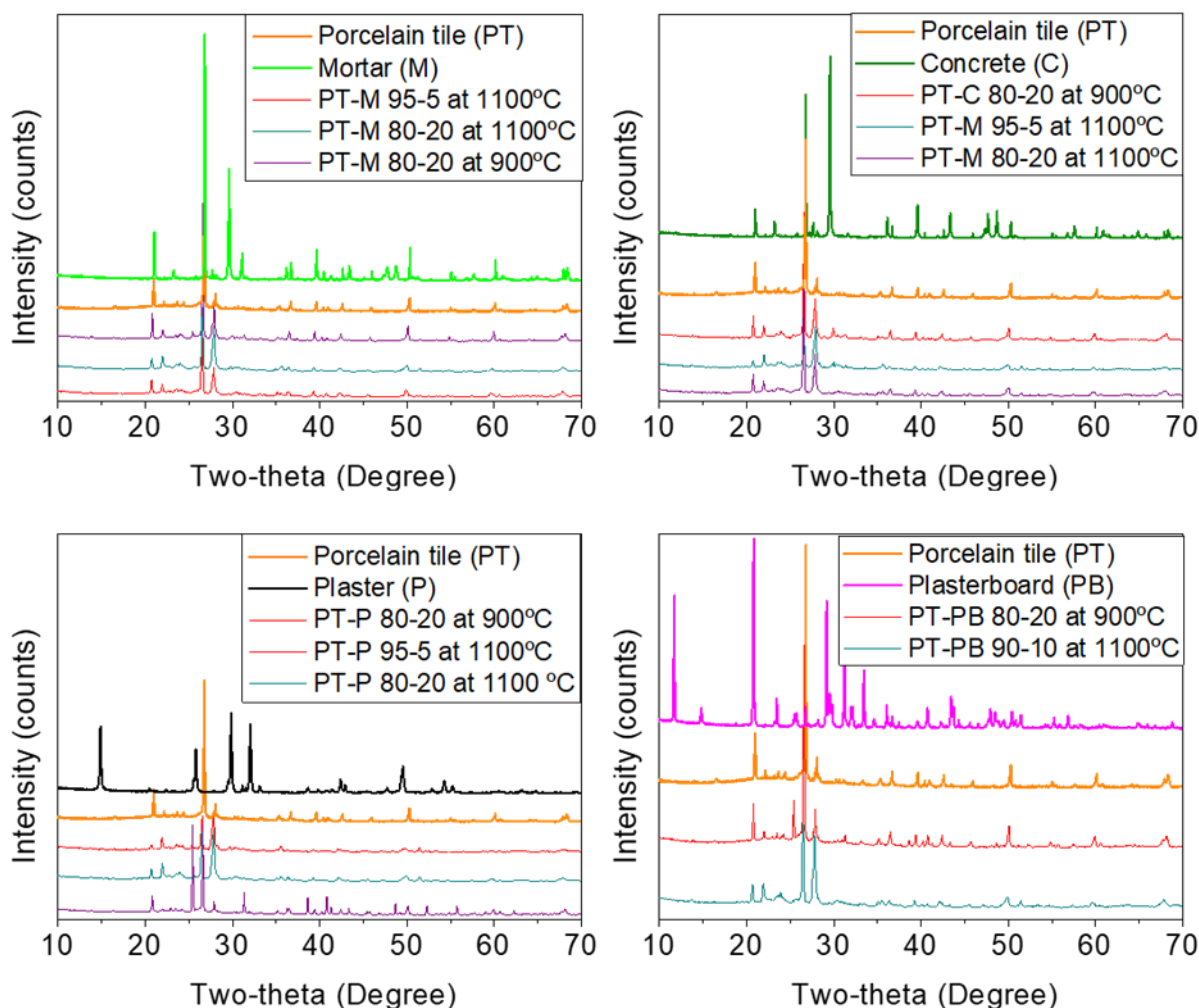


Figure 6-8. Comparison of XRD patterns of mixtures and individual starting material. Mixtures containing porcelain tile as majority material.

In the light of the results of this preliminary study, a larger scale test was carried out. For simplification reasons, one ceramic fraction 90%, with mortar and plasterboard and both at the same time as impurities, were chosen. The tested ceramics were common brick and porcelain tile. Finally, with the objective of improve the mechanical stability, two industrial clays, provided from Keraben Group, were added during the milling process in different fractions.

Briefly, for the preparation of the samples, the preconditioned powder material described in the 6.3 Materials section of this document was mixed in the desired proportions in an alumina ball mill for 20 min using water as solvent. Then, it was dried at 80 °C during 24 h and sieved under 100  $\mu\text{m}$ . Then, the powder was moistened and pressed at 450 kg/cm<sup>2</sup> by a rectangular die, obtaining samples of 80 mm x 3 mm x 0.4 mm. Pressed samples were thermally treated in a furnace that simulates the industrial treatments. Those mixtures based on brick material were treated at 950 and 1050 °C and those based in porcelain tile were treated at 1100 and 1150°C with dwelling time of 1 h and a fast-cooling rate of 30 °C/min.

Firstly, the clay fraction influence was studied in order to choose the type and content of clay for further experiments. With this objective, the two clays were added in 5, 10 and 30 wt% during the milling process of all compositions. For the sake of simplicity, only density results obtained for porcelain-based mixtures treated at 1150°C with a dwelling time of 1h are showed in Figure 6-9, assuming comparable results for the rest of materials. The clay content increases the green density, going from 1.6 g/cm<sup>3</sup> for the samples with lowest clay fraction (5%) to 1.8 g/cm<sup>3</sup> for those with the highest fraction (30%). Clay content is also related to linear shrinkage and mass loss of the sample. As it can be appreciated in Figure 6-10, the higher the clay content, the less shrinkage they experience. This result can be explained with the increase in volume by the formation of calcium and magnesium silicates with the temperature. At the same time, the weight loss increases with the clay content, probably due the high-water content of the clays, which is loss due the high temperature treatment. If the clay fraction increases the final volume and decreases the mass, lower densities could be expected, however, it is seen that in general, higher final densities are obtained. The higher green density of the sample can explain this apparent contradiction, which compensates these phenomena. When the two clays are compared, similar densities on green are shown, though, clay 2 experiments lower linear shrinkage with higher mass losses and better final densities are presented in general when clay 1 is used. In the light of these results, clay 1 in the lowest content was chosen for further experiments.

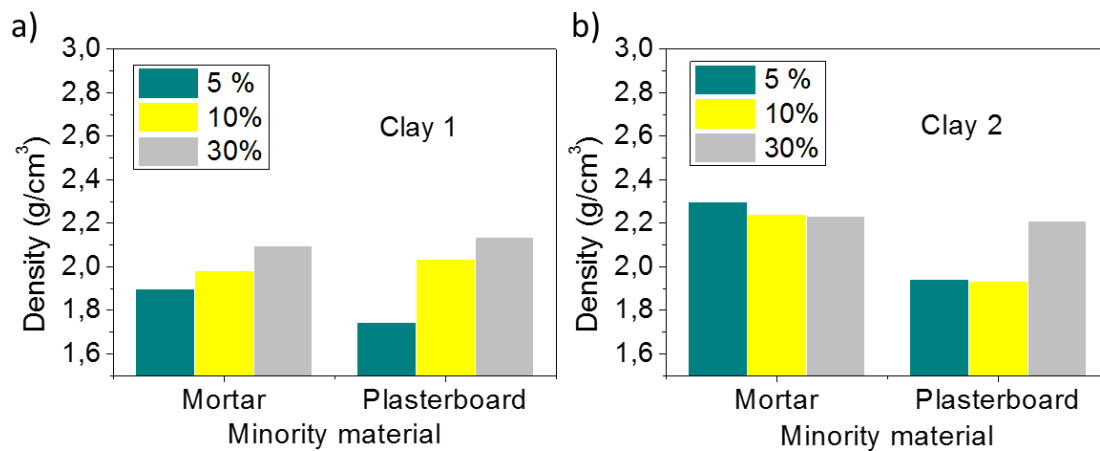


Figure 6-9 Final density (g/cm<sup>3</sup>) of the porcelain with mortar or plasterboard mixtures with 30, 10 and 5 % content of clay 1 and 2.

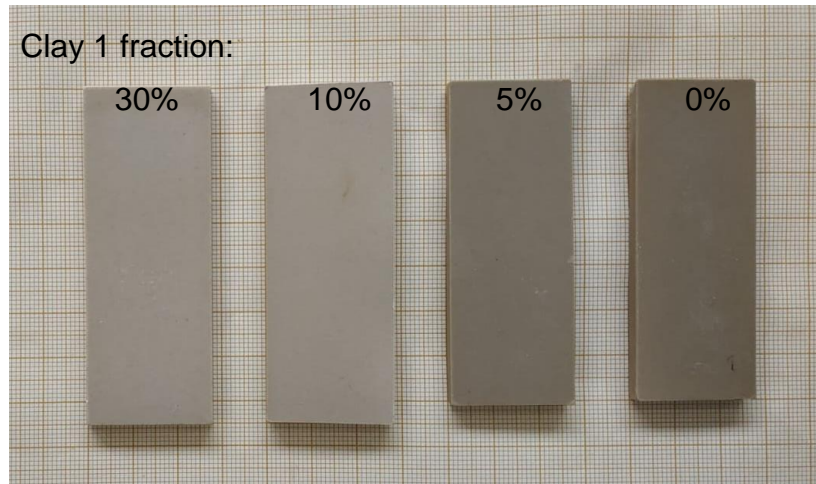


Figure 6-10 Photographic Image of Porcelain/mortar mixtures with clay 1 fractions of 30, 10, 5 % and no clay fraction, 0%, treated at 1150 °C with a dwelling time of 1 h.

Once the type and content of clay was stated, the optimal sintering temperature for each composition was studied. First, the strategy followed for brick-based materials is shown below. In order to choose the sintering temperature in the said range of 950 - 1100°C these brick-based compositions have been studied by means of hot-stage microscopy and ATD/TG analysis. A summary of the obtained results for these techniques is shown in Table 4, and 5 respectively. To start with, hot-stage microscopy results indicate that plasterboard mixtures start their densification slightly before than those containing mortar. However, their maximum densification point is approximately the same, c.a. 1150 °C. On the other hand, the clay dependence in the maximum densification temperature is too subtle to be relevant when it comes to industrial scale. The densification percentage of all these mixtures is similar, going from 35% to 41.5 % of area. Based on this, it could be concluded that for all the brick-bearing compositions, cycle temperature should be at least 950 °C, reaching the maximum at 1150 °C that is in concordance with the preliminary study results presented above.

Table 6-4 Temperatures of start of densification, maximum and densification percentage of brick with plasterboard or mortar mixtures, obtained by hot-stage microscopy.

Mixture	Clay	Start of densification (°C)	Max. densification T <sup>a</sup> (°C)	Densification % (% area)
<b>Brick/ plasterboard</b>	w/o			
	5% C1	1000	1150	38.3
	5% C2			
<b>Brick/mortar</b>	w/o		1143	35
	5% C1	950	1150	37.7
	5% C2		1155	41.5

In order to understand the limitation of temperature due to the gas release that those losses would provoke, the thermal characterization was carried out using Differential Thermal Analysis and Thermogravimetry (DTA-TG) by heating in air up to 1400 °C at a rate of 10 °C/min. A summary of mass loss percentage by means of ATD-TG is presented in Table 5. As it can be observed, the weight loss process to consider starts at ~ 1000 °C for those mixtures containing brick and plasterboard. This loss represents the 8 % of the sample mass, in contrast to ~ 3 and ~ 0.7% for those mixtures containing mortar and other ceramics respectively. This abrupt mass loss experimented for plasterboard-bearing samples could be translated into shrinkage, bending or breakage of ceramic pieces. Therefore, these problems are expected to compromise the samples containing gypsum above 1000 °C, however, lower temperatures could not be enough achieving the densification of the samples. On the other hand, mortar samples do not show these mass loss problems and remains stables above 750 °C.

Table 6-5 Percentage of mass loss and temperature range for brick with plasterboard or mortar mixtures, obtained by TG analysis.

Mixture	T <sup>a</sup> range (°C)	Mass loss (%)
<b>Brick/ plasterboard</b>	0-150	1.7 – 2
	150-660	3 – 3.7
	1000-1150	6.5 – 7.5
<b>Brick/mortar</b>	0-750	3.3 - 3.8

In the light of these results, the next step was the sintering of 3x8 cm ingots at different temperatures. For this purpose, samples adding 5% of clay 1 were prepared and treated of 1100 y 1150 °C for the porcelain-based materials and 950 y 1050 °C for the brick-based materials were chosen for the next step. The results in terms of final density are presented in the Figure 6-11a for the porcelain-based materials and 11b for the brick-based ones. As a comparative value, the commercial porcelain tile density is 2.3-2.4 g/cm<sup>3</sup>. Firstly, for both ceramics samples, density increases with the thermal treatment. For porcelain-based materials, final densities between 1.9 and 2.3 g/cm<sup>3</sup> are reached, being the higher those samples containing mortar treated at 1150 °C. Therefore, this temperature will be chosen for porcelain samples in further experiments. On the other hand, those samples containing brick as ceramic fraction present lower final densities of 1.4 – 1.9 g/cm<sup>3</sup>. These densities still too low and a temperature of 1100 °C will be tested in further experiments. It is worth to highlight that samples containing plasterboard present a low mechanical stability and some breakage or bending problems, as it is shown in Figure 6-10. However, when it is present in a 5% in those samples containing mortar and plasterboard at the same time, these problems are almost non-existent.



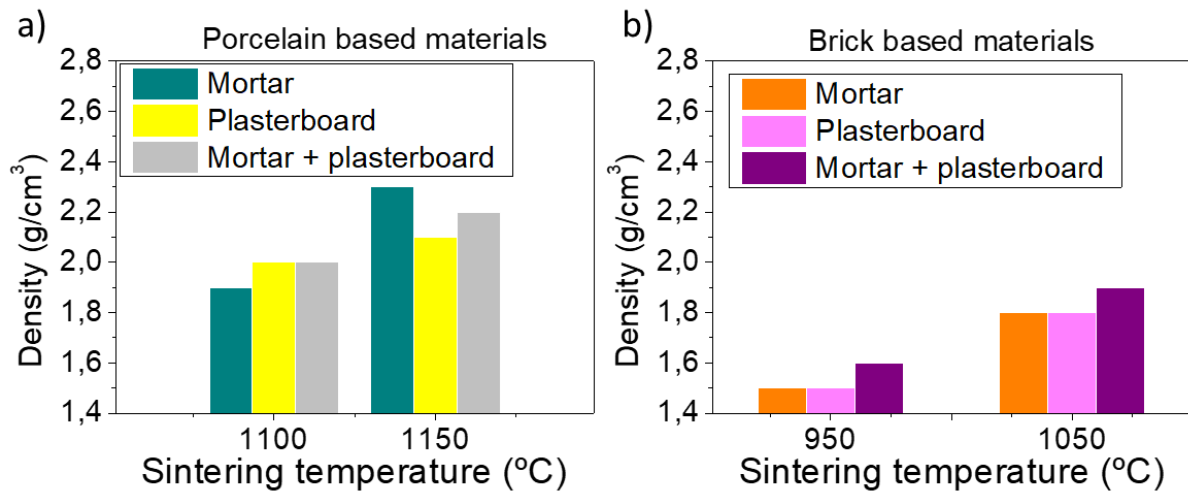


Figure 6-11 Density (g/cm<sup>3</sup>) of the porcelain (a) and brick (b) based materials with 5% of clay and 10% of the following impurities: mortar, plasterboard and mixture of mortar and plasterboard. Dwelling time = 1h.

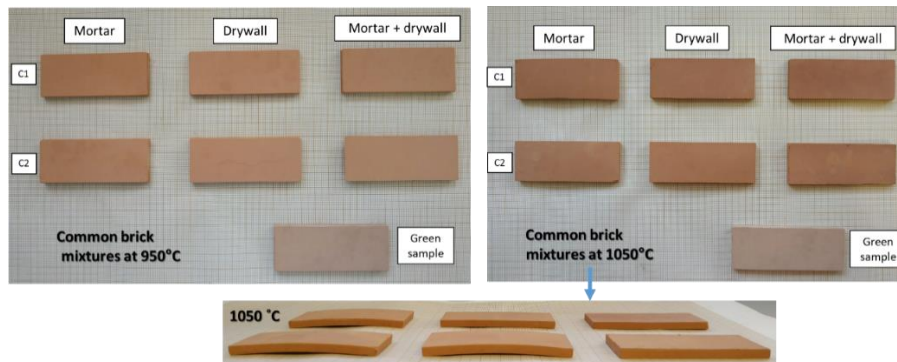


Figure 6-12 Brick based materials after thermal treatment at 950 and 1050 °C with a dwelling time of 1 h.

Finally, once the sintering temperatures were chosen (1150 °C for porcelain-based samples and 1100 °C for brick-based ones), samples were reproduced in a shorter dwelling time of 6 minutes. Moreover, with the objective to test the behaviour of these samples when more than one type of ceramic is present, the following mixtures were prepared; porcelain material was mixed in equal proportion with white body tile and brick was mixed with other red ceramic, imitating the composition of the hypothetical demolition of a single-family house as explained in Materials subsection of this document. Finally, in order to test the quality of these samples, water absorption and strength measurements were carried out. Moreover, samples with only ceramic fraction and no impurity content were done for comparative reasons. Results of these measurements are presented in Figure 6-11 and a picture of the materials is shown in Figure 6-12. Firstly, the obtained final densities are higher than those obtained for samples sintered during 1 h. In all materials, the presence of non-ceramic fraction worsens the results, especially for those samples containing plasterboard. Except for the brick and porcelain + white body tile, which present better densities when mortar fraction is added. When it comes to water absorption, the trend is to increase with the impurity fraction presence, again in a more pronounced way in the case of plasterboard presence. However, all the samples present acceptable water absorption values for wall tiles, which are normally around 8-10 %DM. Moreover,

those samples containing only ceramic fraction or mortar as impurity present excellent water absorption values  $< 0.5\%$ , acceptable for even exterior floor tiles with frost resistant capacities, except for the porcelain and white body sample, which is out of the range. The addition of a porous material such as white body tile to the porcelain samples worsen the properties of the samples in a noticeable way, however, the presence of impurities improves the quality of the sample.

Finally, the flexural strength results show that all the pieces with the exception of brick/ plasterboard and porcelain+white body tile present values above  $40\text{ N/cm}^2$ , which would correspond to typical values for floor covering tiles. In addition, some of these pieces present exceptionally high values, such as porcelain material with mortar, which presents fracture hardness values of  $70\text{ N/cm}^2$ . It is worth noting that these values were measured with the unglazed piece, which means that values higher than these would appear after the glazing process.

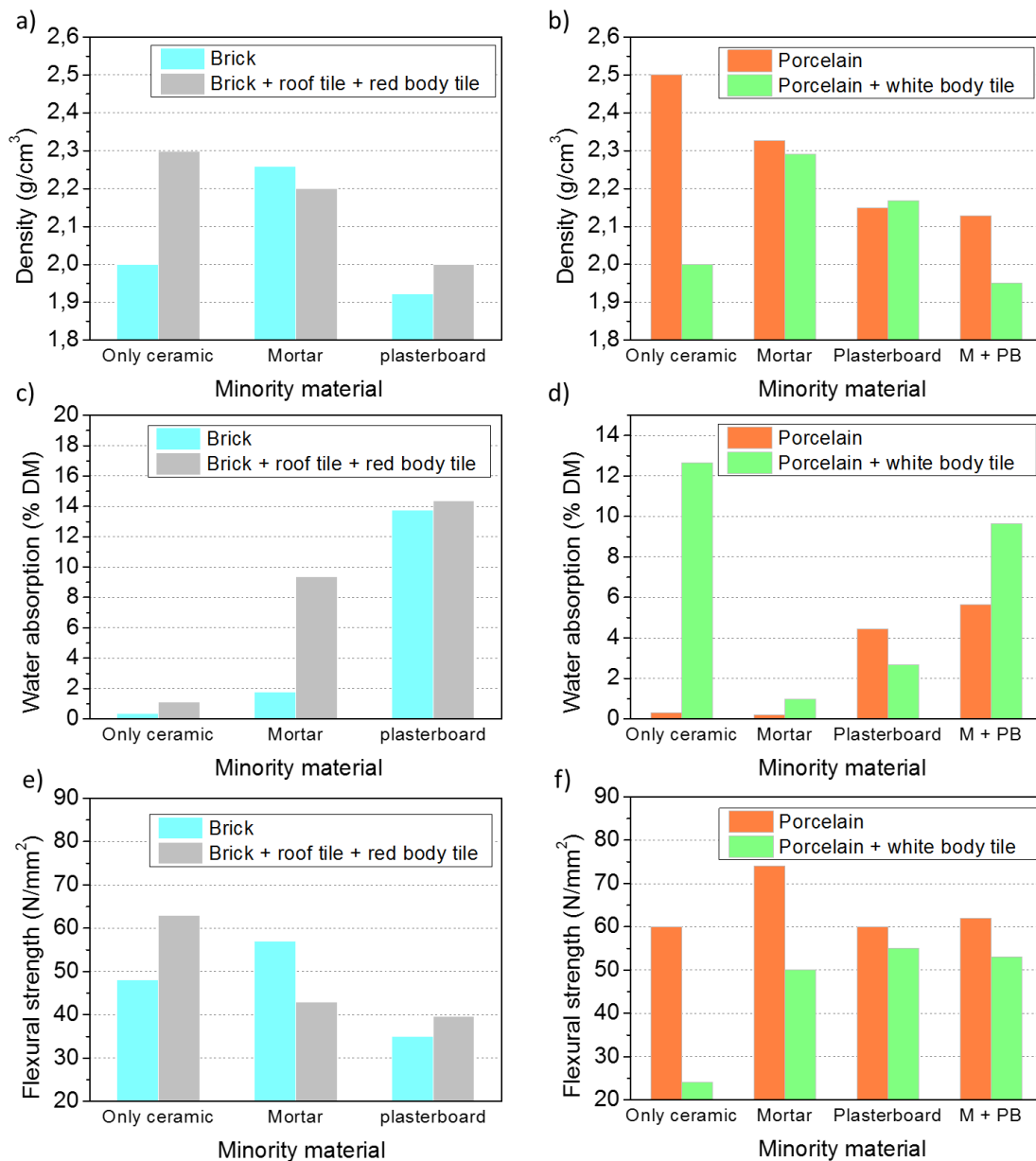


Figure 6-13 Density variation, water absorption and flexural strength for brick-based materials (left) and porcelain based ones (right).

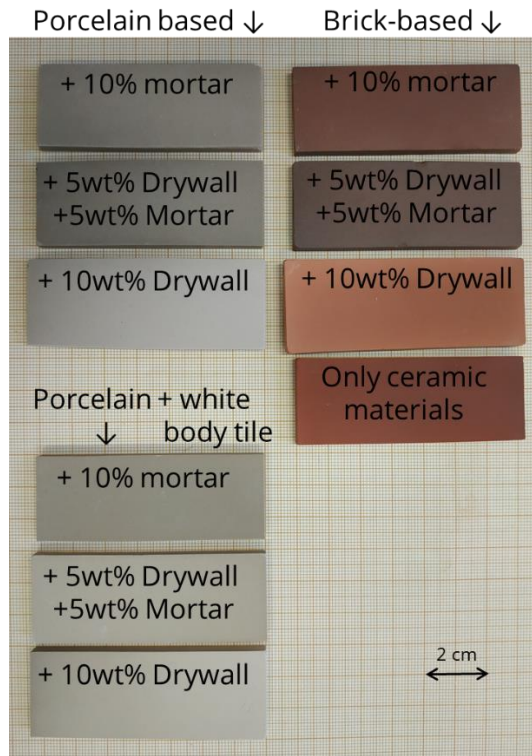


Figure 6-14 Photographic image of porcelain-based and brick-based materials after the sintering at 1150 and 1100 °C during 6 min respectively.

## 6.6 Planning for the rest of the activities

Based on the presented results, it is possible to produce wall and floor tiles made from EBM. Therefore, the next step would be to scale the process to pre-industrial level. For this objective, the first step would be the atomization of 0.1-1 ton of ceramic EBM in Keraben Grupo. Once the material is prepared, it would be pressed and thermally sintered as described for the materials. Obviously, this process cannot be possible without the sorted EBM. However, there is not any EBM supply up to date. Therefore, a provisional solution would be to apply for construction materials in the recycling plants nearby. Once the pre-industrial pieces have undergone the quality controls, the successful prototypes will be produced at industrial scale in a 1-5 trial. Finally, the following drivers will be evaluated in order to account for the feasibility and sustainability of the new process proposed: reduction of raw material consumption by introducing >30 wt% EBM in the ceramic tiles and reduction of emissions due tile sintering temperature reduction.

On the other hand, an innovative methodology is currently being developed for the production of ceramic materials with materials from construction and demolition waste using low temperature. This technology is known as cold sintering and could reduce the sintering temperature following the project objective. The first results of this task are already being obtained with very

good projections. Therefore, the efforts are focusing on the development of this technique. Once the parameters of this technique are established and optimized at the laboratory level, the industrial escalation of the process will be designed and tested.

As explained above, the planning for the rest of the activities depends on the availability of CDW. Therefore, it is difficult to estimate the dates in which this task can be carried out. However, an approximate Gant diagram with the planning for the next months, divided in the following subtasks is provided in Table 6.

- i) Cold-sintering process development.
- ii) Wet milling and atomization of 0.5-1 ton of ceramic EBM and manufacture of green ceramic pieces by uniaxial pressing and sintering of the pieces.
- iii) Validation of the process and prototypes through quality control standards used in the ceramic industry.
- iv) Production of the material at a pre-industrial scale in a trial of 1-5 ton.
- v) Evaluation of the feasibility and sustainability of the process.

Table 6-6 Gant diagram with the planning for the rest of activities.

Task	m18	m19	m20	m21	m22	m23	m24	m25	m26	m27	m28
I											
li											
lii											
Iv											
v)											

## 6.7 Preliminary conclusions

The proposed activities of the project are being carried out in the estimated time. Moreover, no important deviation of the initial planning has been occurred, despite the lack of ceramic EBM supply. However, this setback has been provisionally solved by using new construction material, as an approximation until this supply is available. Following this estimation, different ceramic materials have been mixed with cementitious and gypsum base materials for their sintering for the manufacture of ceramic tiles. The results show that the production of tiles is possible, even reducing slightly the sintering temperature in 100 °C without any additive. The quality controls confirm that these pieces have excellent properties of flexural strength and water absorption, being possible to manufacture frost resistant floor tiles using porcelain tile as ceramic fraction with a 10% of mortar impurities. On the other hand, red ceramic-based prototypes show lower

qualities, however, the measured properties are included in the ceramic wall tile classification. Nevertheless, gypsum-based materials such as plaster or plasterboard need to be discarded for this procedure due to the bending and breakage experimented problems. However, gypsum-based materials will be recovered for cold-sintering process, where calcium supply is necessary. Finally, it is worth to mention that ceramic EBM supply is needed for the continuation of the procedure in the next months.

## 6.8 References

- [1] *Waste statistics - statistics explained*. (2021, abril). Eurostat. Rev: Sept 2021. [https://ec.europa.eu/eurostat/statistics-explained/index.php?title=Waste\\_statistics#Total\\_waste\\_generation](https://ec.europa.eu/eurostat/statistics-explained/index.php?title=Waste_statistics#Total_waste_generation)
- [2] Deloitte, Resource Efficient Use of Mixed Wastes Improving management of construction and demolition waste Final report Final report, 2017.
- [3] G.S. Dos Reis, M. Quattrone, W.M. Ambrós, B.G. Cazacliu, C.H. Sampaio, Current applications of recycled aggregates from construction and demolition: A review, *Materials (Basel)*. 14 (2021) 1–21. doi:10.3390/ma14071700.
- [4] S.S. Hossain, P.K. Roy, Sustainable ceramics derived from solid wastes: a review, *J. Asian Ceram. Soc.* 8 (2020) 984–1009. doi:10.1080/21870764.2020.1815348.

## 7 Adjustment of formulations and pre-industrial prototypes of circular wooden based panels

### 7.1 Phenolic resin formulation and up-scale production using the bio-oil

One of the objectives of Task 3.5 is the development of a phenolic resin formulation using the bio-oil produced by VTT. In this regard, initial lab-scale synthesis experiments of phenol formaldehyde resin were performed without using bio-oil in order to serve as reference for the bio-oil containing resins. Thus, several parameters of the phenol formaldehyde synthetic protocol were examined and optimized. More specifically, the impact of utilizing solid paraformaldehyde or formaldehyde solution as a reagent for the synthesis, NaOH molar ratio towards phenol and formaldehyde, and the addition rate of NaOH during the course of the reaction were investigated to assess their impact on the final resins' properties. The last parameter, i.e. the addition rate of NaOH solution seems to play an important role in the synthesis of the resin, as the reaction between formaldehyde and the phenoxide which is formed by the deprotonation of phenol from NaOH, is rather exothermic. This exothermic reaction, during the



synthesis of phenol formaldehyde resin, requires constant monitoring of the reaction temperature, as it is important to maintain it around 90 °C.

When the resin synthesis is completed, a series of characterization is performed in the final product. Such characterization includes the determination of free formaldehyde, pH value of the final resin, viscosity (Brookfield), solid content, and IR spectra.

The bio-oil based formaldehyde resin was synthesized according to the optimum reaction conditions that were determined during the synthesis of phenol formaldehyde resins. The addition of NaOH during synthesis of the resin, as described above, is a critical step. During the addition of NaOH solution, the reaction temperature is being constantly monitored and maintained in the area of 90°C. It is of interest that, by increasing the ratio of phenol substitution with lignin bio-oil, the reaction temperature increases at a lower rate. This fact indicates that the phenoxides of lignin being formed from the deprotonation with the NaOH solution are less reactive compared to the phenoxides deriving from the deprotonation of phenol by NaOH. Despite this lower activity of lignin phenoxides species, the amount of free formaldehyde in the final bio-oil based resins was determined to be low, similar to the level of phenol formaldehyde resins.

The pH of the produced resins is alkaline and, depending on the synthetic conditions, varies from 9.54 to 10.90. The substitution of phenol with lignin bio-oil does not seem to have a significant impact on the pH value of the final resin, as the bio-oil based formaldehyde resins exhibit small differences in the pH values compared to the phenol-formaldehyde resins.

On the other hand, the viscosity of bio-oil based resins is higher than that of the phenol formaldehyde resins. Resins with higher bio-oil lignin content show higher viscosities. A fact that affects the viscosity of the final resin proved to be the reaction conditions and more specifically the atmosphere under which the resin is prepared. The use of nitrogen aims to prevent possible oxidations (e.g. the oxidation of formaldehyde) during the synthesis reaction of resin. The experimental results showed that under nitrogen atmosphere the final resins had increased values of viscosity.

The non-volatile content of the produced resins is the range of 42 to 52.5%. The utilization of lignin bio-oil in resin synthesis seems to cause a slight decrease of the non-volatile content of the final product. This can be a result of the water contained in the bio-oil.

Free formaldehyde content is low for all the prepared resins and is not affected by the replacement of phenol with lignin bio-oil.

The gel times of the resins produced with bio-oil seem to be affected by the viscosity and the content of lignin. Generally, gel times tend to decrease for resins with higher lignin content but this is considered for resins with similar viscosities.

Finally, the addition of lignin bio-oil affects the appearance of the final resin. Phenol-formaldehyde resins have a dark red color, while lignin bio-oil containing resins have a dark brown color, which is more intense for higher lignin concentrations.



The experimental results from the characterization of the produced resins are summarized in table 7-1.

Table 7-1 Characterization results of resins.

a/a	Sample Name	Lignin wt%	Non Volatiles (N.V.%)	Free Formaldehyde	Viscosity	pH	Gel Time 150 °C (sec)
1	ICB_03	0	44,17	1,68	71 cP	9,70	-
2	ICB_04	0	42,47	1,68	41 cP	9,54	-
3	ICB_05	0	50,15	0,39	74,8 cP	10,40	-
4	ICB_06	0	52,20	0,41	229 cP	10,55	-
5	ICB_07	0	50,95	0,02	103 cP	10,51	-
6	ICB_08	0	51,48	0,18	136,2 cP	10,61	-
7	ICB_09	8,85	48,47	0,05	1142 cP	10,25	195
8	ICB_10	17,7	49,04	0,09	162 cP	10,64	175
9	ICB_11	26,55	47,70	0,05	82,5 cP	10,23	160
10	ICB_12	35,4	48,40	0,09	161,5 cP	10,17	150
11	ICB_13	8,85	49,90	0,54	13520 cP	10,90	165
12	ICB_14	10	48,80	0,32	542 cP	10,90	160
13	ICB_15	20	48,70	0,36	142 cP	10,41	170
14	ICB_16	30	48,76	0,27	6820 cP	10,20	180
15	ICB_17	40	49,66				150
	ICB_17a		24,38	0,14	194 cP	10,20	180
16	ICB_18	50	49,76				125
	ICB_18a		24,18	0,18	110 cP	9,78	165
17	ICB_19	30	48,46	0,31	1570 cP	10,20	165

Samples ICB\_17a and ICB\_18a were diluted with 50% H<sub>2</sub>O due to the high viscosity of the final resin.

Samples of the resins containing lignin bio-oil were sent to Tecnalía for further characterisation such as tensile shear strength. The next steps will be dedicated to the further optimization of the synthesis protocol so as to include the maximum content of lignin possible (50%) in the resin formulation and collaboration with the partners involved in this Task to select the best performing resin for up-scaling synthesis trials according to the agreed timetable.

## 7.2 Thermal insulation panels containing >50 wt% of high-quality recovered wood fibers and 2.5 wt% of biophenolic resin

### 7.2.1 C&D waste wood for defibrating operation in insulation fiber board process

The second objective of Task 3.5 is the development of thermal insulation wood fiber board that contains at least 50% of wood coming from recovery.

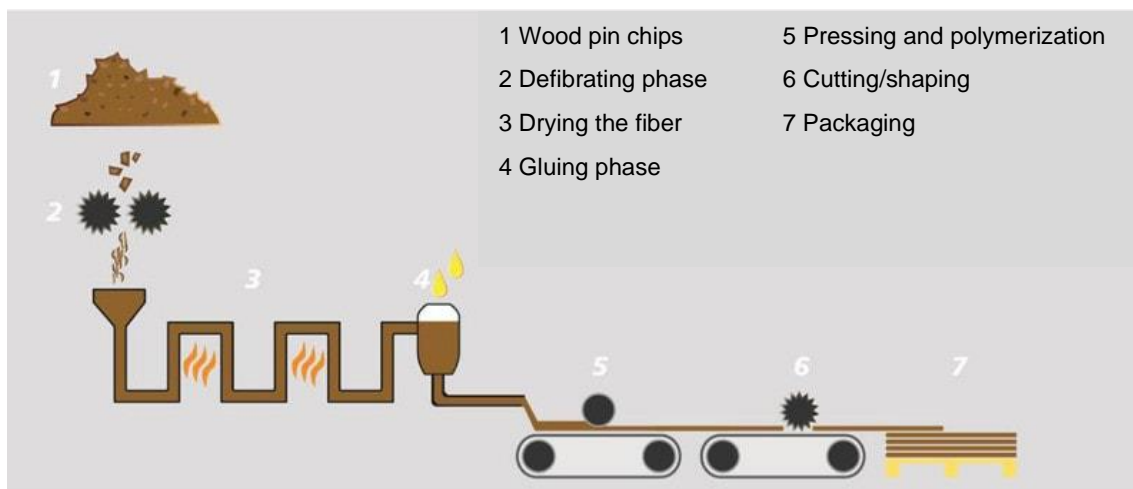


Figure 7-1. Synthetic view of the wood insulation fiberboard process.

Actually, the defibrating phase (n°2 above), uses only fresh soft wood pin chips. Depending of the summer weather, it is known that when the wood raw material is not fresh enough, the quality of fiber gets not the best level to produce suitable insulation board. The average moisture level of standard raw material pin chips is between 40 and 60 wt %.

If we talk about C&D Wood, the moisture content will not be so “fresh” as standard soft wood pin chips coming from saw-mill’s industry as a by-product. In fact, moisture content of C&D waste wood will be more around 20wt%. Thus, suitability for such wood to be defibrated is not the same. It is really necessary to test on lab scale the defibrating of C&D raw materials.

### 7.2.2 First specimens from C&D raw materials.

At the end of 2020, first C&D wood waste shredded specimen were send to Pavatex (Fig 7-2 below). The objective was to see which one could be the best candidate for producing wood fiber, at lab scale first.



Figure 7-2 The first six kind of shredded C&D wood waste sample send from VTT.

After discussion, we have indicated that the shape of these raw materials were not suitable for defibrating phase. By comparison to the standard fresh soft wood pin chips used commonly in production, the initial shape and geometry is not at all the same (Fig 7-3, with same photo scale as in Fig 7-2). The initial shape of pin chips gets a lot of influence on the final size of fiber.



Figure 7-3. At left standard soft wood pin chips; at right wood fiber obtained from standard raw material.

By the same way, the homogeneity on size of raw material is also important. That will be necessary to make trials with raw materials that contains the minimum dust or fine particle. Thus, the defibrating phase could be really done with homogeneous results on fiber.

A set of 2 kg of standard fresh wood pin chips was sent to VTT in order they can look after the best way to produce C&D wood waste pin chips.

### 7.2.3 New development of C&D wood waste shredding for getting pin chips

Purkupiha delivered the sample load of mixed demolition wood to Tiihonen from demolition site (Figure 7-4). Material samples have been produced for pyrolysis oil (cf.) and insulation material tests.



Figure 7-4. At left Raw materials from Purkupiha, at right mixed C&D wood waste

Coarse sorting between clean wood and painted/glued wood products was done by a grapple loader during the pre-crushing process. Metals and mineral particles were removed from the pre-crushed material by magnetic and gravitational separation unit.

For insulation material tests, samples have been made from pre-crushed and cleaned material with disc refiner, double stream impact mill and hammermill. Further tests with hammermill are ongoing to produce suitable particle size and shape for insulation material production. The figure 7.5 show the kind of new raw materials obtained from C&D wood waste.



Figure 7-5. At left sorting and pre-crushing; on center and right, sort of Pin chips obtained for defibrating.

A preparation of two new set of raw materials (with different settings) will be produced in Week 42. Delivery will be done directly to Pavatex in order to choose the best of the two materials, in order to prepare the defibrating phase at lab scale.



## 8 Formulations and pre-industrial prototype of circular plasterboards

### 8.1 Assessment of the industrial impact of increasing the recycled gypsum content to 35 wt% from a productivity standpoint

The ICEBERG circular plasterboard produced by GYPS with their manufacturing process (Figure 8-1), will be characterized by an increase of the recycled gypsum content to 35 wt%. It is anticipated that any variations to the production process can be controlled and managed so that there will be no industrial impact on the productivity of the plasterboard manufacturing process.

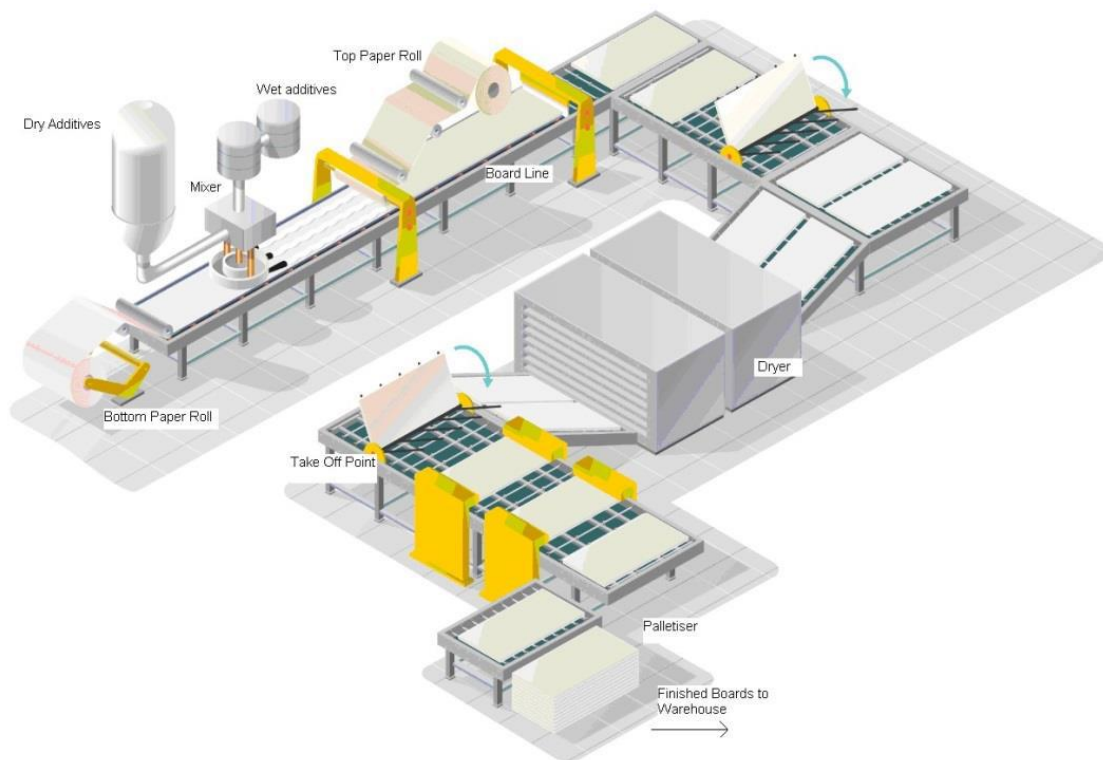


Figure 8-1. Flow diagram of the plasterboard manufacturing process at British Gypsum (GYPS), adapted from the Environmental Product Declaration document (<https://www.british-gypsum.com/products/gyproc-wallboard?tab0=1>).

The main impact of increasing the recycled gypsum content to 35 wt% will be lower use of natural gypsum, and therefore, lower costs for its transportation and reduced emissions. The ongoing gypsum purification testing will provide insight into the suitability of the recycled gypsum and determine if there will be any additional testing requirement prior to production. It is believed that there will be no need to do additional quality control of the incoming recycled gypsum or reject part of the material because its purity will be 96 wt% or higher. It is envisaged

that it could be difficult sourcing the required amounts of waste gypsum to maintain the 35 wt% share of recycled gypsum in the plasterboard. This is due to uncertainties of LU's refurbishment program due to the impact of COVID19 on the LU's Estates and Facilities Management operations and budget. Failing that, both GYPS and ENVA have confirmed that EoL plasterboard could be sourced through their clients.

## 8.2 Evaluation of productivity and rejection percentage with 10 wt% recycled content gypsum plasterboards

The compositions of the ICEBERG circular plasterboard with 35 wt% recycled gypsum and the business-as-usual (BAU) standard plasterboard manufactured by GYPS that contains on average 10 wt% recycled gypsum are presented in Table 8-1. The main impacts of increasing the recycled gypsum content to 35 wt% will be a 20 wt% reduction in the use of natural gypsum. No rejects will be produced during the manufacturing process of either ICEBERG or BAU plasterboards because any trimmings will be recycled back into the process.

*Table 8-1 Composition and amount of rejected products for the new ICEBERG plasterboard (35 wt% recycled gypsum) and BAU plasterboard (10 wt% recycled gypsum on average).*

	New ICEBERG plasterboard (35 wt% recycled gypsum)	Gyproc wallboard standard plasterboard (10 wt% recycled gypsum on average)
Natural gypsum (wt%)	60	81
Additives (wt%)	<1	1.1
Paper liner (wt%)	4	3.6
Gypsum from scrap (wt%)	0	14.3

## 8.3 Assessment for circular plasterboard including circular silica aerogels to enhance thermal properties of the product.

It is envisaged that the introduction of circular silica aerogels in new ICEBERG plasterboards will lower the thermal conductivity of the plasterboard without impacting the productivity of the manufacturing process. However, further testing will be conducted to establish if there are any factors that affect the standard production process. Furthermore, circular silica aerogels could potentially be



difficult to separate during the recycling process, and therefore, accumulate in waste gypsum from EoL plasterboard after several recycling cycles. This could potentially have an impact on the productivity of the manufacturing process, as the properties of the circular plasterboard might be affected that could require corrective measures for the process and/or final product.

### 8.4 Assessment and optimization of the binding system used to attach the plasterboard to the wall to facilitate assembly and disassembly

Currently, the binding systems used to attach the plasterboard to wall and ceilings and facilitate its assembly and disassembly are metal screws (metal and timber frame) and drywall adhesive (gypsum-based product). Screws can be easily removed from EoL plasterboard using magnetic separators. Drywall adhesive is attached to the plasterboard’s paper surface that needs to be chipped away, which might cause contamination of the EoL plasterboard with pieces of masonry. The use of metal screws could be used regardless of the percentage of recycled gypsum in the plasterboard. Additionally, using drywall adhesive should be unaffected as the effect use of adhesive is primarily affected by the suction level of the paper lining, which is not expected to change with the higher percentage of recycled gypsum.

### 8.5 Characterization of the ICEBERG plasterboards

Table 8-2 presents available data for the properties of the new ICEBERG plasterboards with and without silica aerogel and BAU plasterboard. The geometric regularity of the plasterboards should be able to be managed within the production process and should not be affected by the share of recycled gypsum. However, there is no prior data or experience of including silica aerogels within plasterboards. Therefore, while it is believed that the productivity will be unaffected, this requires data collection from testing.

*Table 8-2 Properties of the new ICEBERG plasterboard (35 wt% recycled gypsum), with and without circular silica aerogel, and BAU plasterboard (10 wt% recycled gypsum on average).*

Property	New ICEBERG plasterboard (35 wt% recycled gypsum)	New ICEBERG plasterboard (35 wt% recycled gypsum) containing circular silica aerogel	Gyproc wallboard standard plasterboard (10 wt% recycled gypsum on average)

	TARGET VALUES	TARGET VALUES	CURRENT VALUES (British Standard EN 520)
Geometric regularity	<b>Width:</b> nominal width +0 -4 mm <b>Length:</b> nominal length +0 -5 mm <b>Thickness:</b> nominal thickness +0.5 -0.5 mm <b>Squareness of ends:</b> below 2.5 mm per meter of width	<b>Width:</b> nominal width +0 -4 mm <b>Length:</b> nominal length +0 -5 mm <b>Thickness:</b> nominal thickness +0.5 -0.5 mm <b>Squareness of ends:</b> below 2.5 mm per meter of width	<b>Width:</b> nominal width +0 -4 mm <b>Length:</b> nominal length +0 -5 mm <b>Thickness:</b> nominal thickness +0.5 -0.5 mm <b>Squareness of ends:</b> below 2.5 mm per meter of width
Surface hardness ≤ 15 (BS EN 15283)			There is no current requirement at GYPS for surface hardness testing for standard Wallboard
Thermal conductivity ( $\lambda < 0.076$ W/mK)	0.19W/mk	0.076W/mk	0.19 W/mK

## 9 Adjustment of formulations and pre-industrial prototypes of circular PU based products.

### 9.1 Circular PU-based granular aerogels

KEEY has developed a PU based aerogel product aiming the best synergy between the thermal conductivity and mechanical properties. Due to a meticulous engineering of the fine porous structure with our expertise in lean aerogel manufacturing technology, the PU aerogel products can be tailored to show different performances matching with various application requirements: low-thermal conductivity ( $\lambda = 0.015$  W/m.K), good mechanical properties, improved sound insulation (100-300 m/s), cost effective, easy to handle, no dust release and suitable for 3D shaping.

Polyols are one of the most important raw material for PU based aerogel production which contribute to the properties such as pore structure, flexibility, and mechanical properties etc. Recently, RAMPF developed a method for PU recycling called Glycolysis. The glycols react with the urethane group of used polyurethane products under the specific reaction conditions with higher reactivity during the addition of a catalyst resulted in recycled polyols. This could be an advantage to produce cost effective PU aerogel from recycled polyols.

The objective of this task is to optimize and industrial scale up of PU based aerogel ( $\lambda < 0.018$  W/mK) using the recycled polyols from RAMPF (> 10wt.%).

The methodology of research approach is described as follows;

#### 9.1.1 Pre-screen recycled polyols by analysing their molecular weight, functional group, purity and solubility

In this preliminary study, KEEY obtained 3 different types of polyols from RAMPF. The specifications of each polyols are shown in the Table 1. In general, the properties of polyols are comparable to commercial products except the water and MDA content which are slightly higher than the aim specification. We observed some particles non-soluble in PUR\_V4 before using it as shown in Tab 9-1.

Table 9-1 The specifications of each polyols

	Specification aim	Commercial	PUR_V4	PIR_V8	PIR-V9-2
Hydroxyl-Value	550± 50	380	482	505	486

(mg KOH / g)					
Acid-Value (mg KOH / g)	-	-	-	6.67	1.68
Viscosity (mPa*s @ 25 °C)	2500 ± 2500	-	9938	5500	4390
Water content (wt.%)	< 0.1	<0.1	0.44	0.31	0.19
MDA content (wt.%)	< 0.1	N/A	0.3	2.61	1.51



Figure 9-1 Polyols PUR\_V4

### 9.1.2 Integration of selected recycled polyols (>10 wt%) in the current formulation of PU aerogel

Polyurethane gels were synthesized through a sol-gel route based on polyaddition reactions between polyols and polyisocyanates according to the following classical chemical scheme for generic diol and di-isocyanate as presented in Figure 9-2. The different types of recycled polyols from RAMPF were integrated in the synthesis. The reactants were first dissolved in a suitable organic solvent in which both monomers and the growing polyurethane particles are soluble.

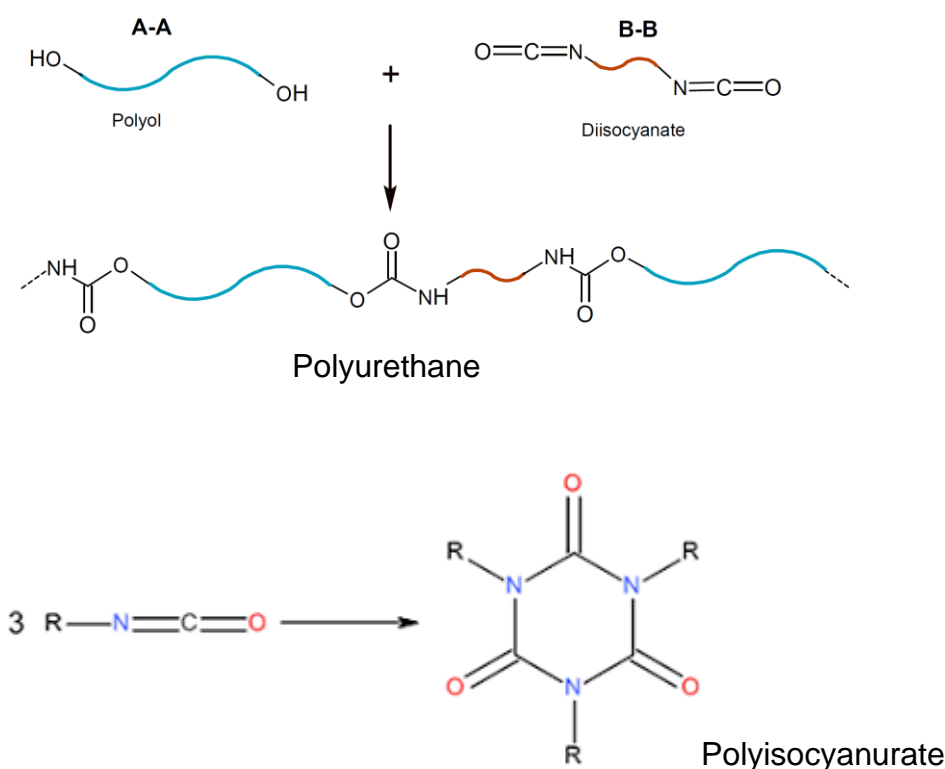


Figure 9-2 Polyaddition between polyols and polyisocyanates

At the beginning, the polyols from RAMPF were dissolved in commonly used solvents for polyurethane aerogel such as methylethylketone (MEK) and acetone. It was observed that the polyols were soluble in MEK but not in acetone. There were some precipitations even when the polyols were highly diluted in acetone. According to these results, MEK will be used as a solvent for PU aerogel synthesis.

PU aerogels were prepared in 60 ml polypropylene containers using different types of polyols (22 wt.%), diisocyanate, and catalyst. The reactions were carried out at the same reaction conditions (temperature, liquid/solid ratio, NCO/OH ratio, and catalyst). Both polyols and isocyanates were diluted in MEK and well mixed, the catalysts were added and the gelation time was noted. MEK was added on the PU gels surface to prevent the gels from drying and kept standing at room temperature overnight. PU gels were washed several times in MEK to remove some organic residue and then dried using Low temperature supercritical drying process with Carbon Dioxide as solvent. The process was carried out at homogeneous conditions of supercritical carbon dioxide and MEK. Dynamic drying time varied with the thickness of the samples for each batch. Depressurization was carried out at a max. speed of 0.3 bar/min.

During the synthesis, some precipitations were found in samples PUR\_V4 and PIR\_V9-2 and some parts of PIR\_V8 were not well dissolved. The gelation time of samples PUR-V4, PIR\_V8, and PIR\_V9-2 were 4, 2, and 11 minutes respectively. The appearance of the PU aerogels are shown in Figure 9-3. PU aerogels showed slightly shrinkage. The density of PU aerogel was calculated from the mass divided by the volume of each sample. The values were between

0.12-0.13 g/cm<sup>3</sup> which are in the range of PU aerogel. PUR\_V4 and PIR\_V9 were dense and homogeneous while PIR\_V8 was foam-like. The monolith PU aerogel with dimension 10 x 10 x 1 cm. will be prepared to measure the thermal conductivity at Tecnalia. As the lower thermal conductivity of aerogel may occur when the density increases resulted in the decreasing of gas conduction and radiation heat transfer. However, as the density increases the conductivity of the solid clearly becomes the dominant heat conduction mechanism, and consequently, the thermal conductivity values of aerogel increase. It's necessary to vary the density of PU aerogel to find the optimum point where achieve the lowest thermal conductivity.

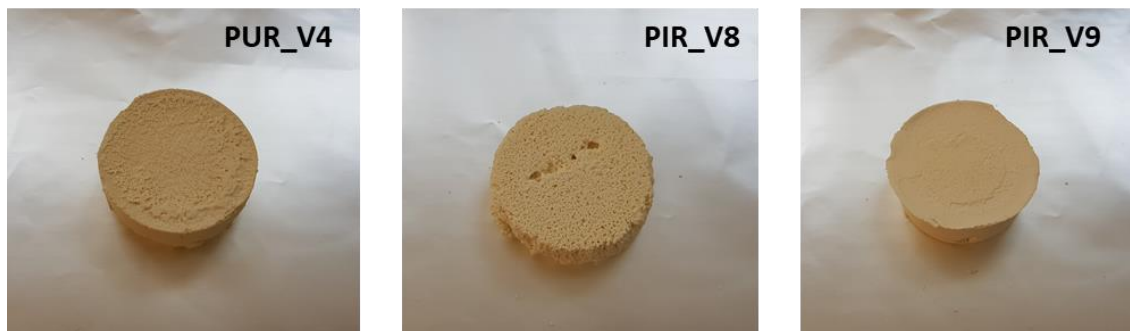


Figure 9-3 Obtained PU aerogels with different polyols

### 9.1.3 Optimization of the reaction conditions of recycled polyol-based PU aerogels

In this step, the reaction conditions will be optimized to obtain the lowest thermal conductivity. The solid content (weight % of reactant per weight of solvent) can play an important role in term of density, physical properties resulted in the different in thermal conductivity. The effect of %solid content on the PU aerogel properties were investigated. The polyols PIR\_V9\_2 was chosen for this study because it has less water content and the obtained PU aerogel was dense and homogeneous. PU aerogels were prepared by dissolving the reactive components in MEK as a solvent at a given weight percentage % solid. The compositions of PU aerogel were the same. The results of PU aerogels prepared with different % solid content are shown in Table 2. It was observed that the gelation time depends strongly on the solid content. By increasing MEK amount resulted in longer gelation time. The density of aerogel increases with increasing %solid content. It was suggested that the final aerogel density can be controlled by varying the quantities of reactant and solvent. Please note that the samples is still under supercritical drying process (SCD).



Table 9-2 The conditions of PU aerogels prepared by varying the solid content

Sample	%solid content	Gelation time (min.)	Density (g/cm <sup>3</sup> )	Characteristic after SCD
PIR_V9-S10	10	13	n/a	under SCD
PIR_V9-S15	15	11	“	“
PIR_V9-S20	20	8	“	“
PIR_V9-S25	25	5.30	“	“

#### 9.1.4 Adjustment of the percentage of recycled polyols in the formulation for PU aerogel

In this step, the reaction conditions will be optimized to obtain the lowest thermal conductivity. The solid content (weight % of reactant per weight of solvent) can play an important role in terms of density, physical properties resulted in the different in thermal conductivity. The effect of %solid content on the PU aerogel properties were investigated. The polyols PIR\_V9\_2 was chosen for this study because it has less water content and the obtained PU aerogel was dense and homogeneous. PU aerogels were prepared by dissolving the reactive components in MEK as a solvent at a given weight percentage % solid. The compositions of PU aerogel were the same. The results of PU aerogels prepared with different % solid content are shown in Table 9-3. It was observed that the gelation time depends strongly on the solid content. By increasing MEK amount resulted in longer gelation time. The density of aerogel increases with increasing %solid content. It was suggested that the final aerogel density can be controlled by varying the quantities of reactant and solvent. Please note that the samples is still under supercritical drying process (SCD).

Polyols are the other important components for PU aerogel synthesis which contribute in properties of PU aerogel such as flexibility and softness etc. We studied the effect of polyols content on the properties of PU aerogel. The total volume of aerogel was constant, and the composition between polyols (PIR\_V9-2) and diisocyanate were varied. It was found that the gelation time slightly decreases as the weight content of polyols increased. It was suggested that there are more OH group which reacted with isocyanate. For the properties of obtained PU aerogels, the increasing of % polyols did not show a significant effect on the density of aerogel but it effects in terms of flexibility. At higher %polyols, the PU aerogels became harder and denser. It may be related to the increase of polyurethane in the formulation. Please note that the synthesis will be repeated the check the reproducibility in synthesis and SCD process.

Table 9-3 The conditions of PU aerogels prepared by adjusting the wt.% of polyols

Sample	wt.% PIR_V9-2	Gelation time (min.)	Density (g/cm <sup>3</sup> )	Characteristic after SCD
PIR_V9-W23	23	8	0.155	Flexible and more shrinkage
PIR_V9-W28	28	8	0.156	Flexible
PIR_V9-W34	34	7	0.132	Hard and less shrinkage
PIR_V9-W45	45	5	0.165	Hard and more shrinkage

The properties of PU aerogel at different conditions will be characterized. The BET surface area, pore volume, average pore size, and pore size distribution were measured by using liquid nitrogen absorption method. Microstructures were measured by using a field-emission scanning electron microscope. Thermal conductivity at a single mean temperature of 23 °C was measured using hot plate method.

### 9.1.5 Characterization of the recycled polyol-based PU aerogels

The continuous aerogel production using jet cutting has been validated in lab scale. The formulation of recycled polyols-based PU aerogel with the lowest thermal conductivity will be selected for the optimization. The process conditions such as solvent, temperatures, and cutting parameters will be optimized in November.

### 9.1.6 Validation and large batch manufacturing

This part did not start yet. The meeting between partners (KEEY, RAMPF and SOPREMA) will be determined to discuss in detail for the production of PU aerogel. The final properties, quantities of recycled polyols from RAMPF will be specified. The properties of PU aerogel will be required from SOPREMA, so KEEY will produce the suitable PU aerogels for the applications.

## 9.2 Circular PU-based panels

### 9.2.1 Establish a polyol book of specifications containing the desired physical and chemical characteristics.

Keeping in mind the production step of the circular PU-based panels, a polyol book of specifications has been established (Figure 9-4). The aim is to introduce into standards formulations, polyols resulting from chemical recycling of polyurethane panels. By the results, specifications for the eco-sourced polyols are similar to standards polyols commonly used in production.

For standard productions, two types of polyols are used: polyether polyols with an OH value between 500 and 600 mgKOH.g<sup>-1</sup> and polyester polyols with an OH value between 150 and 250 mgKOH.g<sup>-1</sup>. Polyether polyols are used for PUR formulations and polyester polyol are used for PIR formulations.

Regarding viscosity, due to processability matters, it must be between 1000 and 5000 mPa.s at 25 °C.

Acid value and water content must be close to the polyols commonly used in production and should not vary from one batch to another because those two parameters have an impact on the reactivity of the polyurethane formulation. Consequently, acid value is set to 3 ± 0.5 mgKOH.g<sup>-1</sup> and water content must be lower than 0.4 wt %.

Eventually, due to regulation matters, amine or MDA content must be lower than 0.1 wt %.

**Viscosity:** 1000 – 5000 mPa.s at 25°C

**Acid value:** 3 ± 0.5 mgKOH.g<sup>-1</sup>

**OH value:** 500-600 mgKOH.g<sup>-1</sup>  
or 150-250 mgKOH.g<sup>-1</sup>

**Water content:** <0.4 w%

**MDA content:** <0.1 w%

Figure 9-4. Polyol book of specifications

### 9.2.2 Screen different polyol iterations to identify the most suitable candidates via lab foam trials

According to the polyol book of specifications, several polyols were synthesized by RAMPF. 3 types of polyols were produced, resulting from PIR panels recycling, PUR panels recycling or a PUR and PIR mix panels recycling. Up to now 15 polyols were synthesized (Table 9-4).

Table 9-4. Properties of the recycled polyols synthesized

		<b>OH value</b> (mgKOH.g <sup>-1</sup> )	<b>Viscosity</b> (mPa.s)	<b>MDA content</b> (%)
From PIR panels	ICE-PIR-V2	668	1780	2.27
	ICE-PIR-V3	655	1700	2.19
	ICE-PIR-V4	678	1590	1.97
	ICE-PIR-V8-2	502	5100	2.09
	ICE-PIR-V9	496	4250	1.10
	ICE-PIR-V14	503	3530	0.154
From PUR panels	ICE-PIR-V15	541	4600	0.107
	ICE-PUR-V1	460	8220	0.42
	ICE-PUR-V2	475	8430	0.54
	ICE-PUR-V3	470	8640	0.62
	ICE-PUR-V4-2	515	8180	0.36
	ICE-PUR-V7	560	2395	0.101
From PIR/PUR panels	ICE-PUR-V9	565	2500	0.096
	ICE-PUR/PIR-Mix-V2	524	3530	0.105
	ICE-PUR/PIR-MIX-V4	574	3010	0.105

Polyols were received in 3 series:

- The first series includes 6 polyols:
  - o ICE-PIR-V2, ICE-PIR-V3, ICE-PIR-V4, ICE-PUR-V1, ICE-PUR-V2 and ICE-PUR-V3.
- The second series includes 6 polyols:
  - o ICE-PIR-V8-2, ICE-PIR-V9, ICE-PIR-V14, ICE-PUR-V4-2, ICE-PUR-V7 and ICE-PUR/PIR-Mix-V2.
- The third series includes 3 polyols:
  - o ICE-PIR-V15, ICE-PUR-V9 and ICE-PUR/PIR-Mix-V4.

All polyols appeared as brown viscous liquid (Figure 9-5).

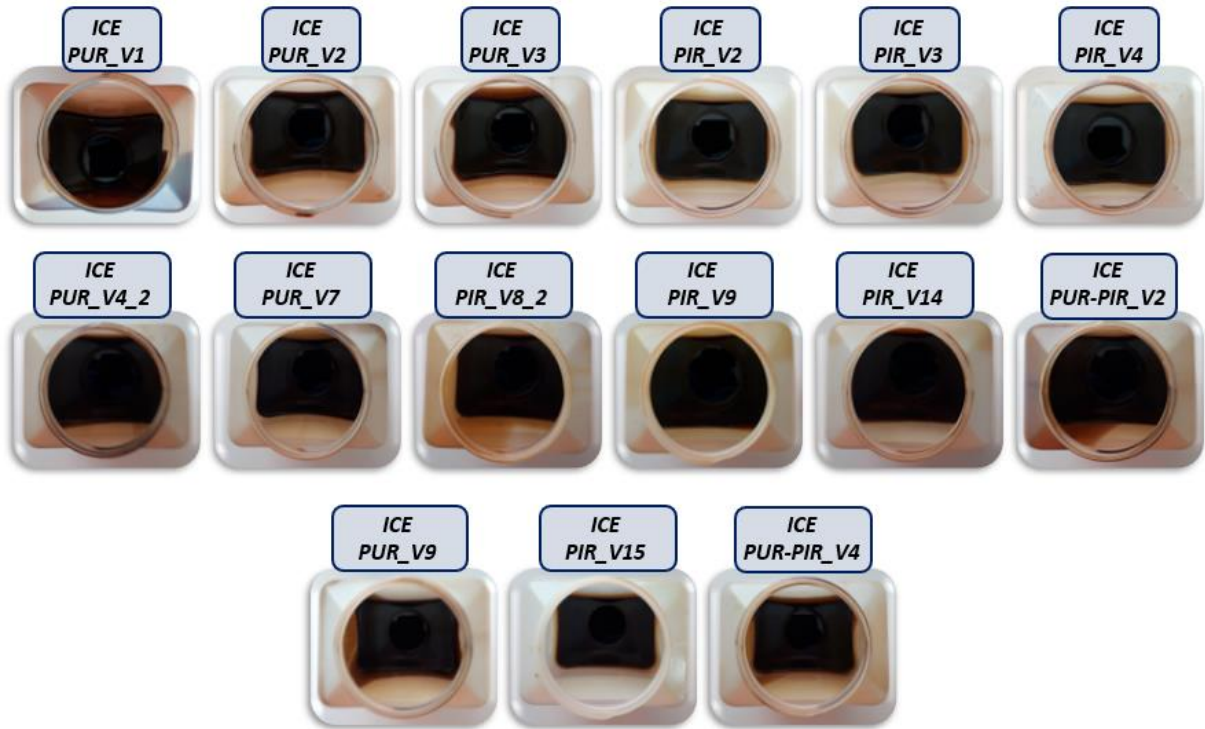


Figure 9-5. Pictures of the polyols synthesized by RAMPF

- **Viscosity measurements**

The viscosities of the first series of 6 polyols were measured (Figure 9-6). According to the results, polyols resulting from the recycling of the same type of foam showed similar behavior. Polyols based on PUR foam show viscosities much higher compared to the viscosity of the reference polyol. At 25 °C, viscosities are between 10 000 mPa.s and 15 000 mPa.s. PIR-foam based polyols exhibits similar viscosities compared to the reference polyether polyol.

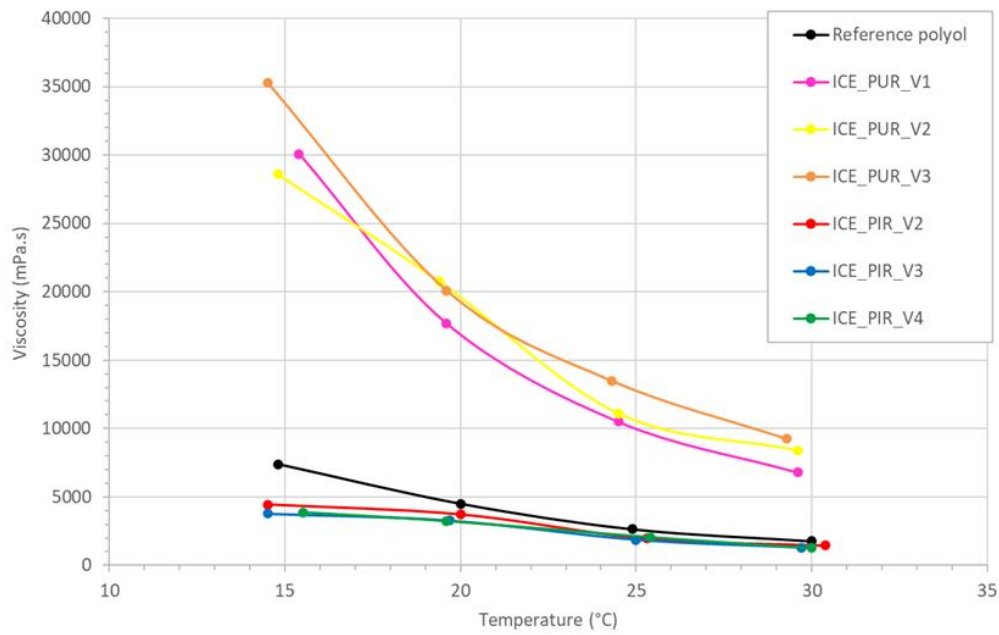


Figure 9-6. Viscosity measurements of the first series of 6 polyols received

Regarding the viscosities of the second series of 6 polyols, at 25 °C, ICE\_PUR\_V7 polyol, has the closest viscosity to the reference polyether polyol. ICE\_PIR\_V14, ICE\_PUR-PIR-mix\_V2 and ICE\_PIR\_V9 have higher viscosities but still remaining below 5000 mPa.s. ICE\_PUR\_V4-2 et ICE\_PIR\_V8-2 have higher viscosities at 25 °C, between 7000 and 9000 mPa.s (Figure 9-7).

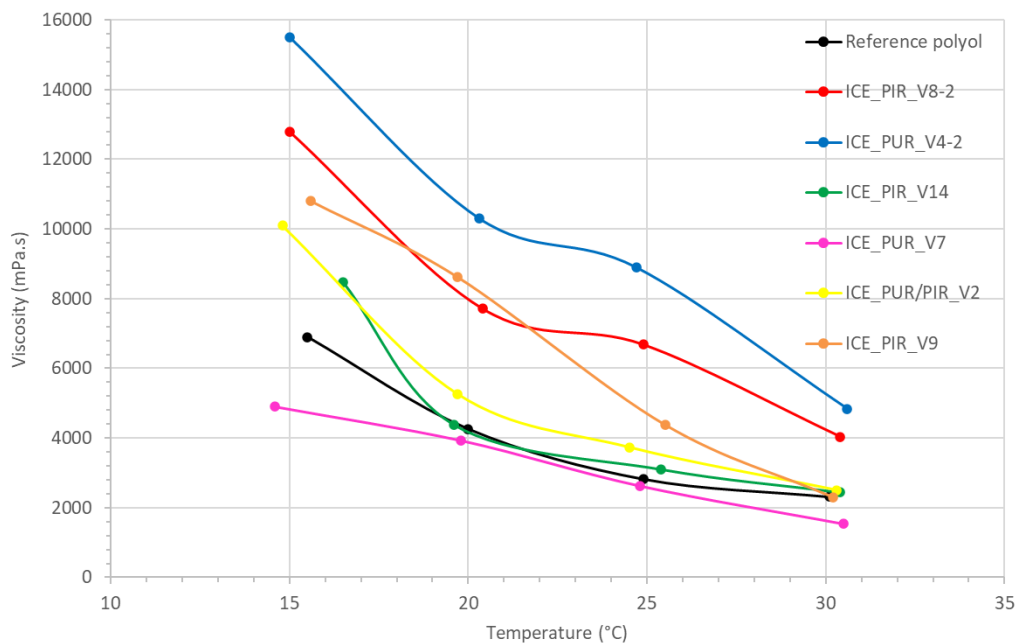


Figure 9-7. Viscosity measurements of the second series of 6 polyols received



For a first evaluation, indeed, the OH value of all the polyols synthesized is above 450 so all polyols were tested in PUR formulation. Expansion profile and reactivity were carried out keeping the index of the formulation constant. 10, 25 and 50 % substitutions of the reference polyether polyol for each polyol were tested.

- **Reaction times**

Reaction times of **the first series of 6 polyols** were determined (Table 9-5). The kinetic times of the test formulations are faster than the reference formulation. In addition, the increase in substitution leads to a decrease of the kinetic times. At the same percentage of substitution, the formulations made with polyols based on PUR foam give slower kinetic times. For polyols based on PIR foam, the 50% substitution study was not possible due to high reactivity.

Table 9-5. Reaction times of the first series of 6 polyols

	Poly ether polyol Reference	ICE_PUR_V1				ICE_PUR_V2			ICE_PUR_V3			ICE_PIR_V2		ICE_PIR_V3		ICE_PIR_V4	
		10%	25%	50%	50%	10%	25%	50%	10%	25%	50%	10%	25%	10%	25%	10%	25%
Cream Time (s)	12	11	10	9	11	10	9	10	10	9	10	8	10	8	10	8	
Gel Time (s)	46	46	38	28	40	34	33	40	37	29	37	25	40	32	35	25	
Tack-free Time (s)	69	58	49	38	55	48	44	54	49	39	51	38	53	40	49	36	

Regarding **the second series of 6 polyols**, it appeared that polyols are less reactive than the first series of polyols but still more reactive than the reference. A decrease in kinetic times was measured from 10% substitution. Unlike it was observed in the first series of polyols, the nature of the recycled foam does not seem to have an impact on reactivity because all polyols have similar behaviour for the same percentage of substitution.

Table 9-6. Reaction times of the second series of 6 polyols

	Reference polyol	ICE_PUR_V4_2			ICE_PIR_V8_2			ICE_PIR_V9			ICE_PUR_V7			ICE_PIR_V14			ICE_PUR/PIR-Mix_V2		
		10%	25%	50%	10%	25%	50%	10%	25%	50%	10%	25%	50%	10%	25%	50%	10%	25%	50%
Cream Time	13	11	11	9	11	10	9	11	11	10	11	11	10	11	11	11	12	12	9
Gel Time	49	43	38	32	43	37	38	42	38	32	46	39	33	42	35	34	42	39	31
Tack-free Time	64	57	49	39	61	48	45	55	51	41	54	54	43	62	49	45	52	52	42

- **Expansion profiles**

Expansion curves were obtained using a Foamat equipment (Figure 9-8). This equipment allows to follow and study the foam expansion. Thanks to all the sensors, this equipment gives temperature, foam height curve and expansion rate curves.

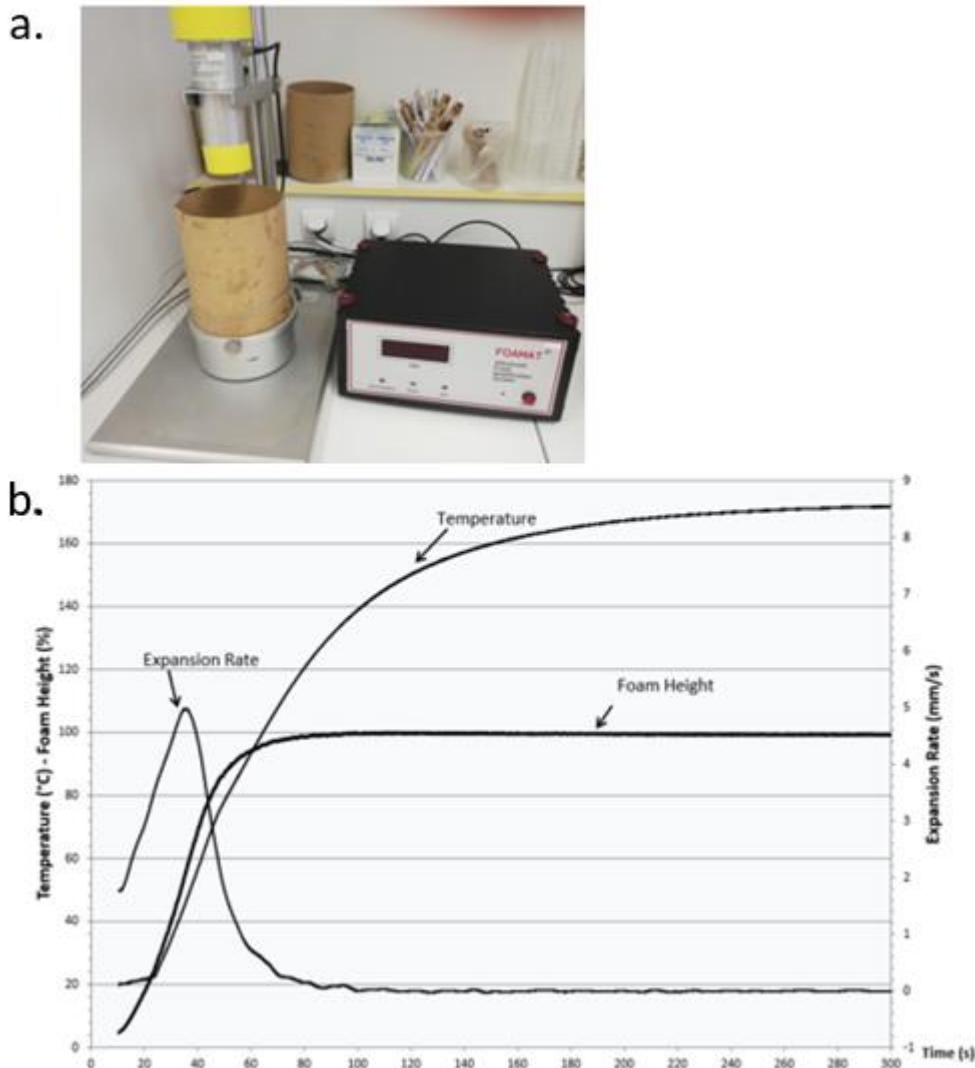


Figure 9-8. a. Foamat equipment and b. example of curves obtained

Expansion profiles of **the first series of 6 polyols** were determined. An example of the curves obtained for one polyol resulting from the recycling of PUR foam and one polyol resulting from the recycling of PIR foam is given Figure 9-9. Polyols resulting from the recycling of the same type of foam (PUR or PIR) have very similar behaviour. Polyols synthesized with PIR foams appeared to be more reactive than the polyols synthesized with PUR foams. For the same percentages of substitutions, the expansion curves are similar.

**At 10 % substitution**, differences are observed on the expansion rate curve (Figure 9-10). The peaks are slightly shifted towards faster times compared to the reference formulation. The maximum expansion rate values are higher than the reference formulation for all the tests but more importantly for the formulations using PIR-foam based polyols.

**At 25 % substitution**, differences made at 10 % substitution on the expansion rate curves are more marked at 25% substitution (Figure 9-11). Other differences

appear: the maximum height of the tests is reached more quickly, and the maximum temperature is higher. These differences are more noticeable for the substituted tests based on polyol obtained from PIR foam.

**At 50 % substitution**, the same differences as for the 25% substitution are observed but even more importantly (Figure 9-12).

Pictures of the corresponding foams resulting from the evaluation of the first series of 6 polyols is given Figure 9-13.

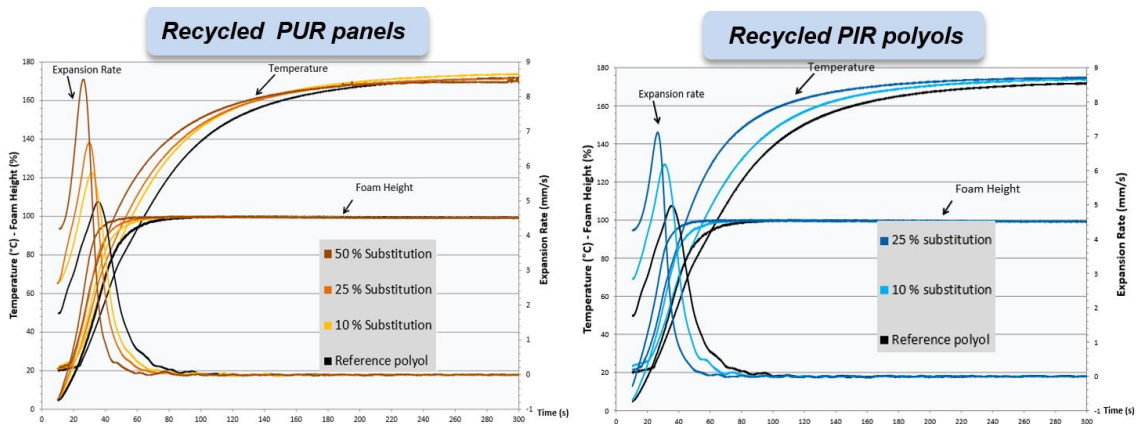


Figure 9-9. Examples of expansion curves obtained from the recycling of PUR and PIR foams.

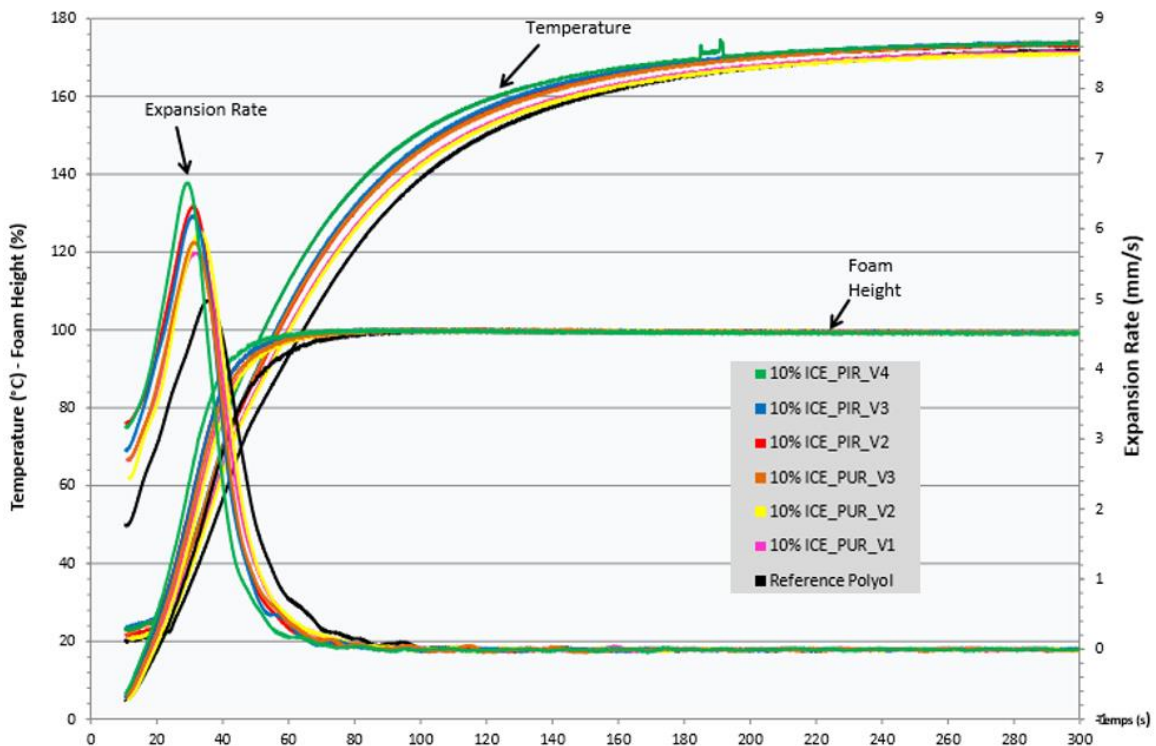


Figure 9-10. Expansion curves of the first series of polyols at 10 % substitution

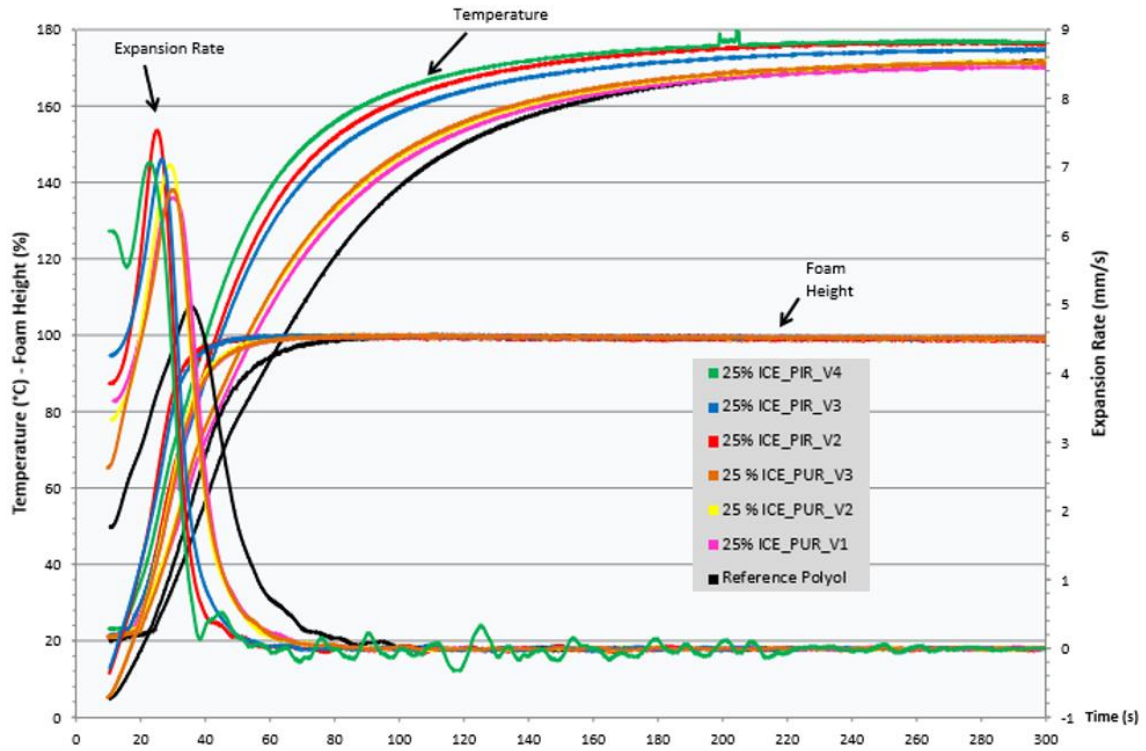


Figure 9-11. Expansion curves of the first series of polyols at 25 % substitution

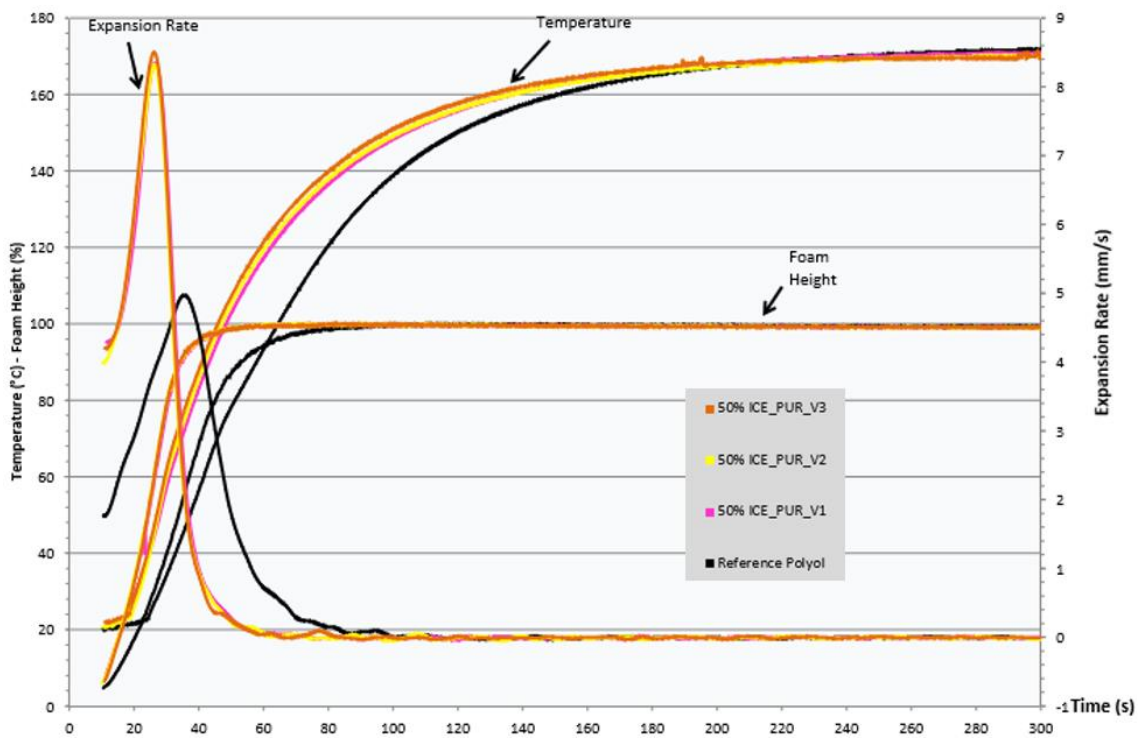


Figure 9-12. Expansion curves of the first series of polyols at 50 % substitution



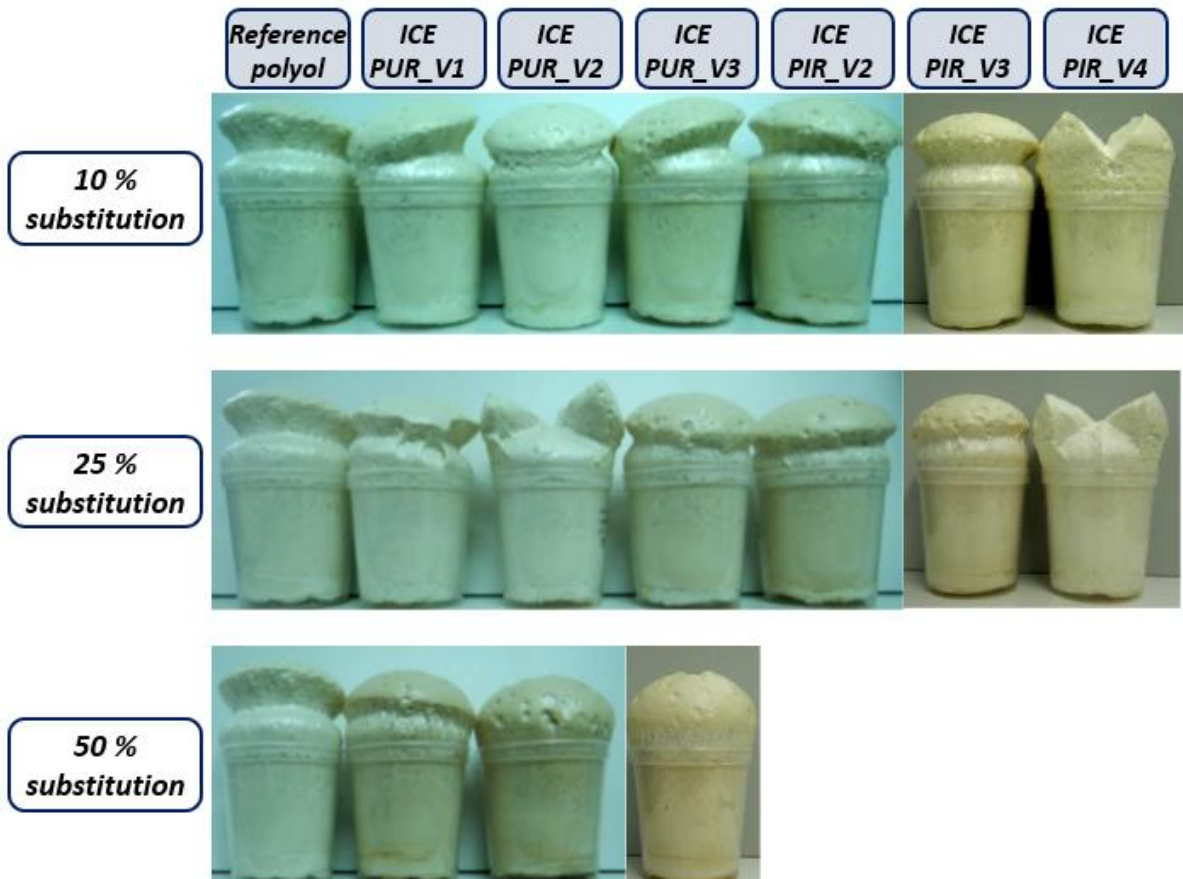


Figure 9-13. Pictures of the foams resulting from the evaluation of the first series of 6 polyols

Regarding **the second series of polyols**, as for the kinetic study, polyols based on PIR or based on PUR foams have similar behaviour. Results confirmed that polyols of the second series are less reactive than the first series of polyols

**At 10 % substitution**, the foamat curves of the polyols tested are similar to those of the reference formulation (Figure 9-14). A slight shift of the peak towards faster times was observed and the rate of expansion was more important.

**At 25 % substitution**, the tests still behave similarly to each other (Figure 9-15). An increase in reactivity compared to the reference was observed:

- The temperatures reached by the tested polyols are higher
- The maximum heights are reached more quickly
- The peak is shifted to faster times and the expansion rate increased.

**At 50 % substitution**, regarding ICE\_PIR\_V8-2, the differences to the reference formulation remain close to the 25 % substitution. But differences are much more marked for the other polyols evaluated (Figure 9-16).

Pictures of the corresponding foams resulting from the evaluation of the second series of 6 polyols is given Figure 9-17.

**The study of the third series of polyol is in progress.**

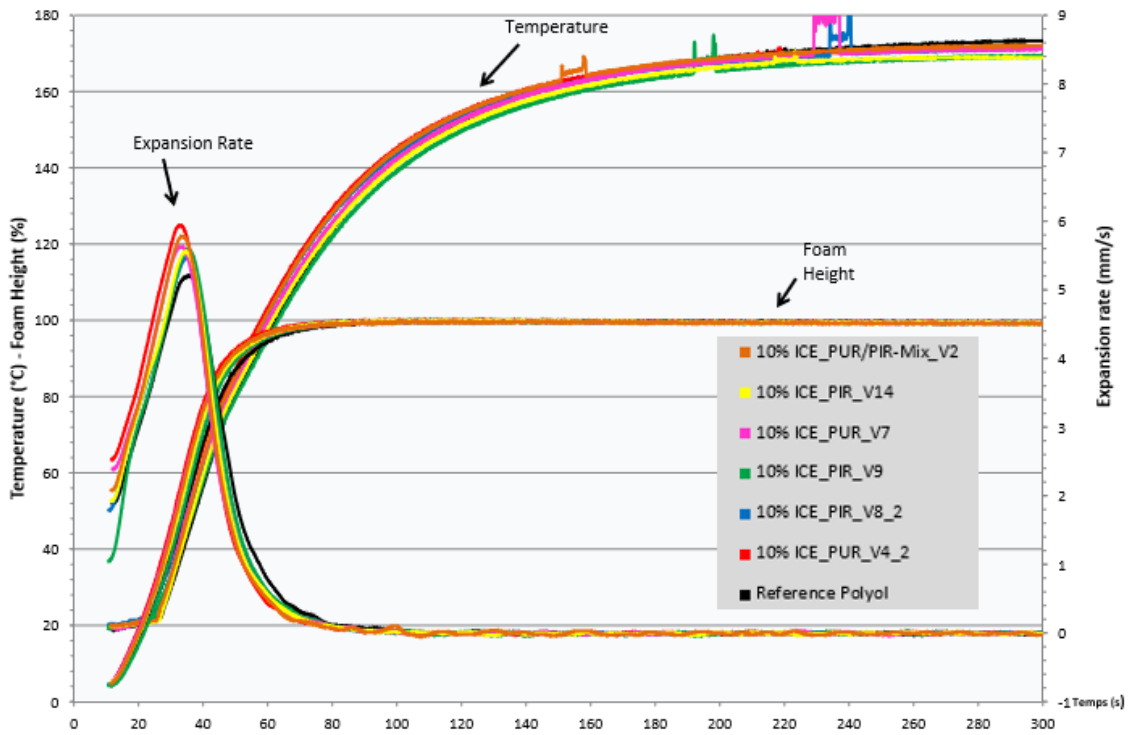


Figure 9-14. Expansion curves of the second series of polyols at 10 % substitution

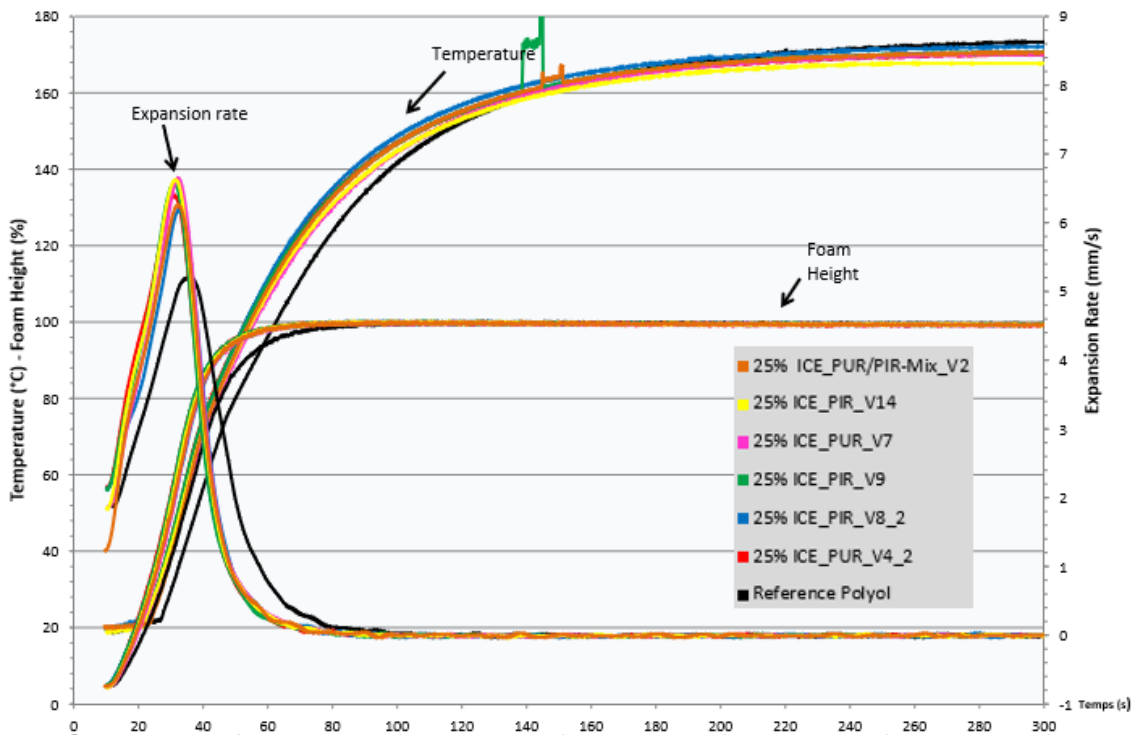


Figure 9-15. Expansion curves of the second series of polyols at 25 % substitution



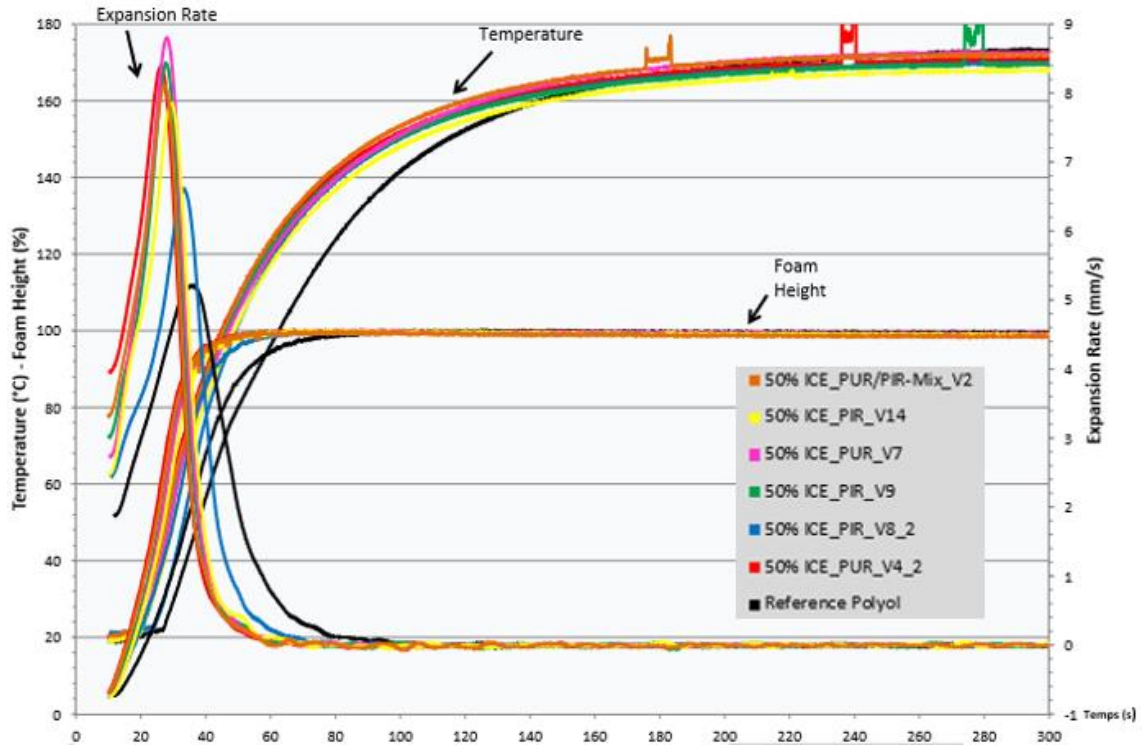


Figure 9-16. Expansion curves of the second series of polyols at 50 % substitution

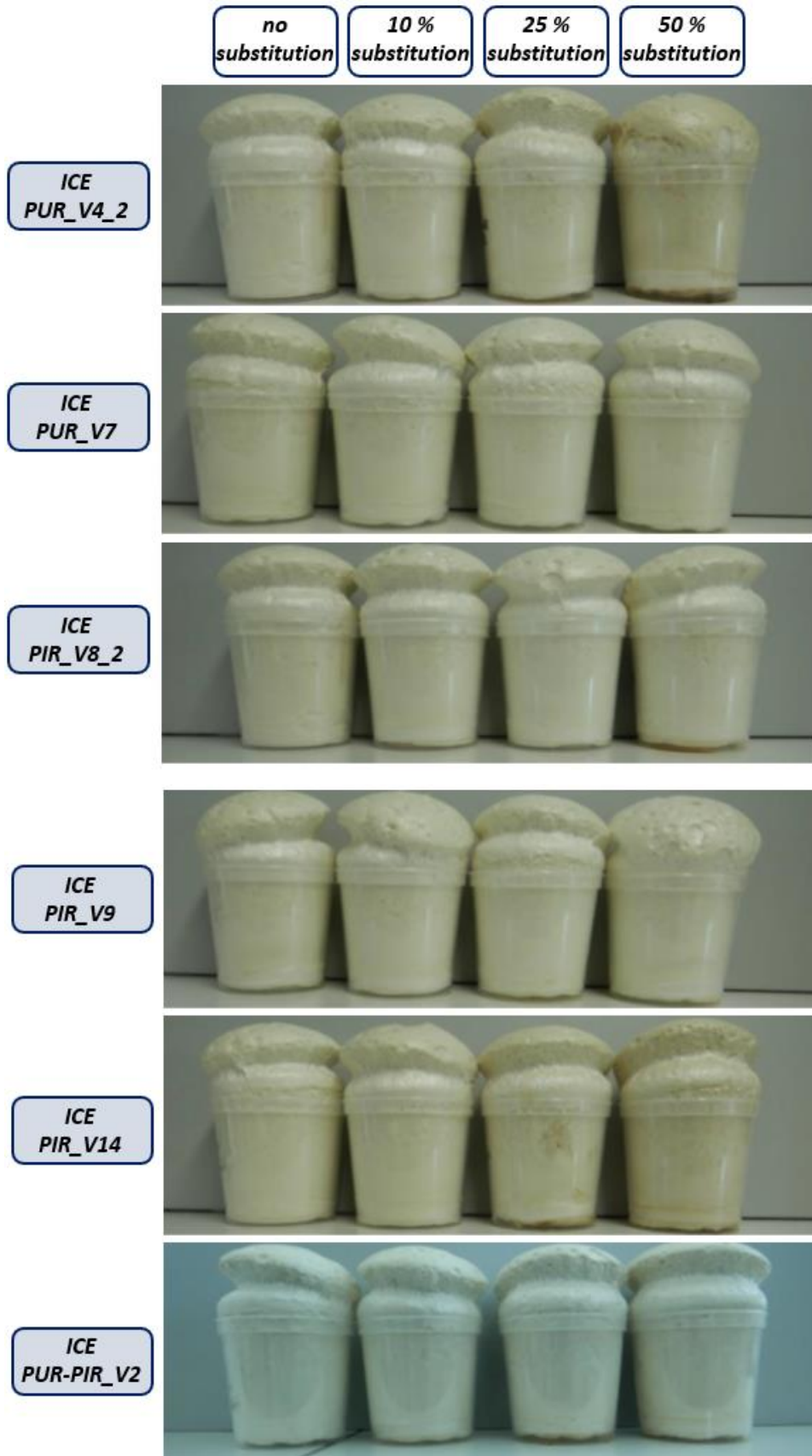


Figure 9-17. Pictures of the foams resulting from the evaluation of second series of 6 polyols

### 9.2.3 Results and Discussions

- **Selection of the most suitable candidate:**

**One polyol will be selected to continue the study. But currently, the evaluation study continues in order to select the right polyols.**

Up to now, **ICE-PUR-V7** polyol appears to be best candidate. Indeed, the polyols of the second series appear to have a closer reactivity to the reference polyol than polyols of the first series. Among the other polyols, ICE-PUR-V7 appears to be a good candidate because it showed a viscosity and a reactivity close to that of the reference polyol.

The next step will be to produce a lab sample on a larger scale in order to characterize the foam.

Also, we wait for still some samples from RAMPF. These polyols should be have a better performance for our application.